

Multimodal nanoparticles for quantitative imaging

Citation for published version (APA):

Vries, de, A. (2011). *Multimodal nanoparticles for quantitative imaging*. [Phd Thesis 1 (Research TU/e / Graduation TU/e), Biomedical Engineering]. Technische Universiteit Eindhoven.
<https://doi.org/10.6100/IR719507>

DOI:

[10.6100/IR719507](https://doi.org/10.6100/IR719507)

Document status and date:

Published: 01/01/2011

Document Version:

Publisher's PDF, also known as Version of Record (includes final page, issue and volume numbers)

Please check the document version of this publication:

- A submitted manuscript is the version of the article upon submission and before peer-review. There can be important differences between the submitted version and the official published version of record. People interested in the research are advised to contact the author for the final version of the publication, or visit the DOI to the publisher's website.
- The final author version and the galley proof are versions of the publication after peer review.
- The final published version features the final layout of the paper including the volume, issue and page numbers.

[Link to publication](#)

General rights

Copyright and moral rights for the publications made accessible in the public portal are retained by the authors and/or other copyright owners and it is a condition of accessing publications that users recognise and abide by the legal requirements associated with these rights.

- Users may download and print one copy of any publication from the public portal for the purpose of private study or research.
- You may not further distribute the material or use it for any profit-making activity or commercial gain
- You may freely distribute the URL identifying the publication in the public portal.

If the publication is distributed under the terms of Article 25fa of the Dutch Copyright Act, indicated by the "Taverne" license above, please follow below link for the End User Agreement:

www.tue.nl/taverne

Take down policy

If you believe that this document breaches copyright please contact us at:

openaccess@tue.nl

providing details and we will investigate your claim.

Multimodal Nanoparticles for Quantitative Imaging

Anke de Vries

Financial support for the publication of this thesis was provided by:

Bioscan, Inc.



The Bio-Molecular Engineering group of Philips Research Laboratories,
Eindhoven, the Netherlands

Philips Innovative Laboratories, Philips Research Aachen, Germany



All are kindly acknowledged for their contribution.

A catalogue record is available from the Library Eindhoven University of
Technology

ISBN: 978-90-386-2929-2

Printed by: Ipskamp, Enschede, The Netherlands

Cover Design: Joost Rooze

Multimodal Nanoparticles for Quantitative Imaging

PROEFSCHRIFT

ter verkrijging van de graad van doctor aan de
Technische Universiteit Eindhoven, op gezag van de
rector magnificus, prof.dr.ir. C.J. van Duijn, voor een
commissie aangewezen door het College voor
Promoties in het openbaar te verdedigen
op dinsdag 13 december 2011 om 16.00 uur

door

Anke de Vries

geboren te Eindhoven

Dit proefschrift is goedgekeurd door de promotoren:

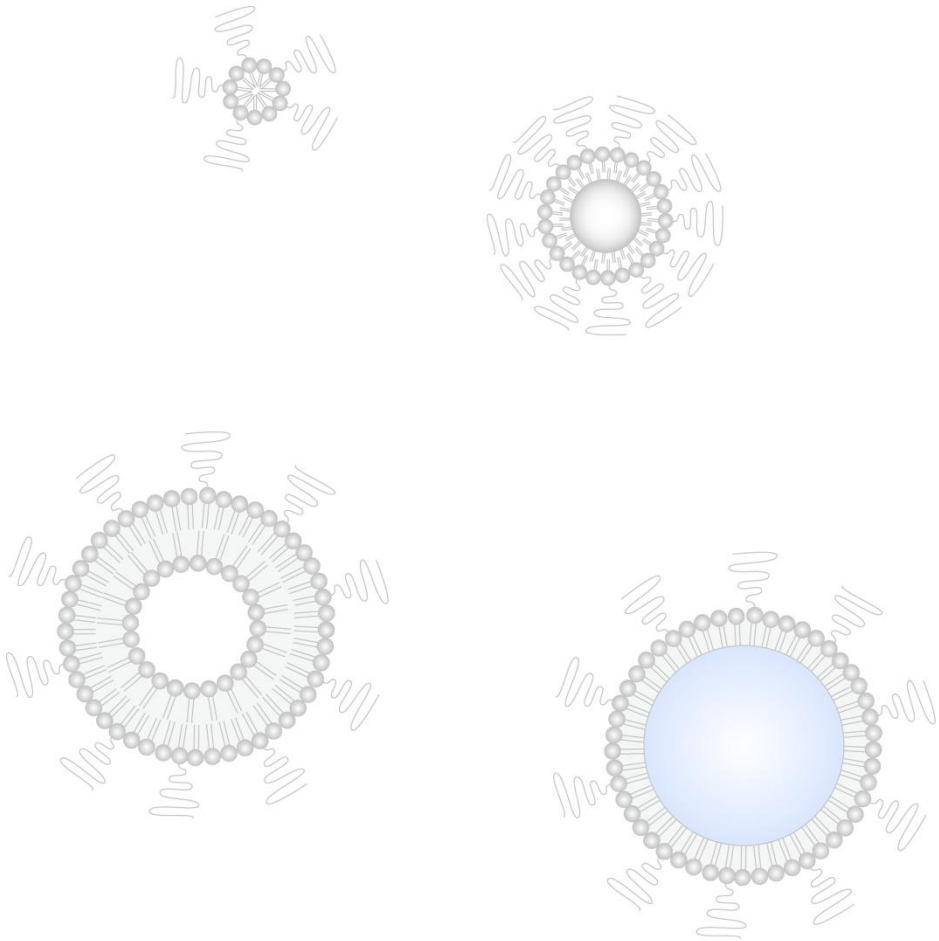
prof.dr. H. Gröll
en
prof.dr. K. Nicolay

Contents

Chapter 1:	Introduction: Nanoparticles for quantitative imaging	1
Chapter 2:	Block-copolymer-stabilized iodinated emulsions for use as CT contrast agents	25
Chapter 3:	Alternating biodistribution of blood pool CT contrast agents by a co-injection of rapid RES-uptake material	45
Chapter 4:	Quantitative Spectral K-edge imaging	73
Chapter 5:	Dual-isotope $^{111}\text{In}/^{177}\text{Lu}$ SPECT imaging as a tool in molecular imaging tracer design	91
Chapter 6:	Multimodal liposomes for SPECT/MR imaging as a tool for <i>in situ</i> relaxivity measurements	111
Chapter 7:	Relaxometric studies of gadolinium-functionalized perfluorocarbon nanoparticles for MR imaging	129
Chapter 8:	Future perspectives	149
	Summary	155
	List of Publications	160
	Conference Proceedings	161
	Curriculum Vitae	163
	Dankwoord	174

Introduction

Nanoparticles for quantitative imaging



1.1. Imaging modalities

Diagnostic imaging such as computed tomography (CT), magnetic resonance imaging (MRI), ultrasound and nuclear imaging is an integral part of modern clinical care and plays a crucial role in disease diagnosis, staging and follow up [1,2]. Image generation exploits the interaction of biological tissue with a number of different types of waves (e.g. electromagnetic or acoustic) leading to different sensitivity, spatial and temporal resolution for each imaging modality. Building on their respective strengths, each imaging modality evolved into their own specialism with dedicated medical applications.

1.1.1. Computed tomography (CT)

In radiographic techniques (conventional X-ray or CT) patients are exposed to X-ray photons that are emitted by a broadband X-ray source with energies in the range of 25-150 keV. A photon sensitive detector captures the transmitted photons, leading to an image as a result from the attenuation of these X-ray photons by the body. In CT, pictures taken at different angles allow the reconstruction of a tomographic 3D image. Contrast differences are generated by variations in electron densities that scale in first approximation with tissue densities. As all soft tissue is similar in density, the intrinsic contrast in organs such as the liver, kidneys, muscles and fat is low and similar, while calcified structures like bones have a high CT contrast [3]. Modern techniques like multi-slice CT detectors provide higher image quality and high volume per scan speed at lower costs [4-6], making CT the modality of choice when rapid diagnosis is required for e.g. trauma patients [7]. Though the resolution of CT scanners is in theory very high, it is in clinical practice limited by the radiation dose for the patient. The use of ionizing radiation is a disadvantage of CT and the exposure of the patient should be kept at a minimum [8-11].

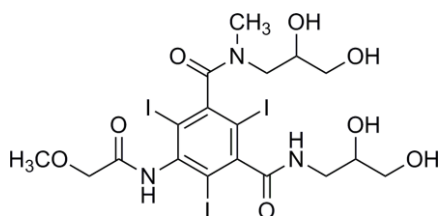


Figure 1. Chemical structure of iopromide.

For improved X-ray and CT imaging, contrast agents can be administered to the patient in order to enhance the existing contrast of the images. Efficient atoms for use as CT contrast agents are high-Z elements like iodine and barium, as their high electron densities leads to an efficient absorption of X-ray photons. Iodine-based CT contrast agents generally consist of a benzene ring substituted with three iodine atoms and two

or three hydrophilic side groups that determine solubility, osmolarity and pharmacokinetic properties [12-14]. An example is iopromide (Fig. 1) and is clinically used in urography [15,16], brain scans and angiography [17-20].

Spectral CT is an extension of the CT technology, which makes use of an energy resolved detector [21]. Such a detector allows photon counting within defined energy bins along the range of 25-150 keV and allows identifying different elements based on their absorption characteristics. For example, high-Z elements show a discontinuity in X-ray absorption at energies, which is sufficient to ionize electrons located on the K-shell of the element. Figure 2A shows a typical absorption spectrum of iodine having a K-edge at 30.2 keV. As the K-edge is characteristic to each element, Spectral CT allows distinguishing different high-Z elements. Furthermore, the K-edge absorption is directly proportional to the tissue concentration of the respective element, turning Spectral CT into a quantitative imaging technique [22,23].

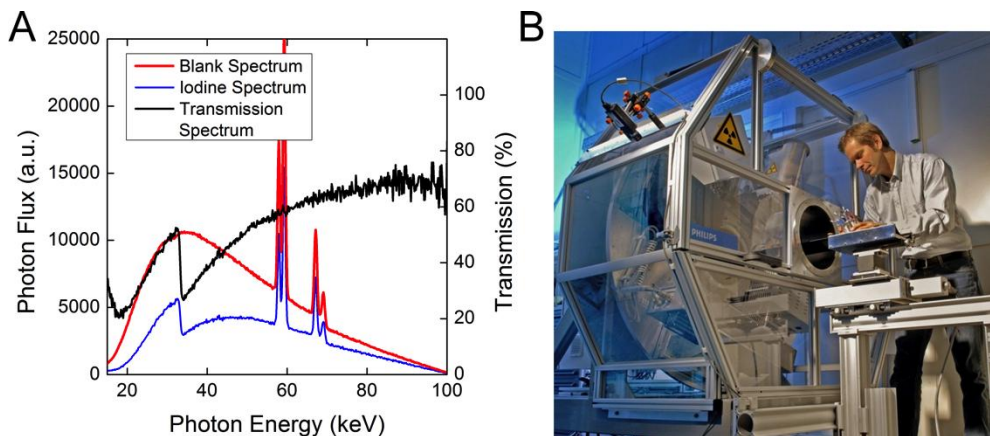


Figure 2. A) Photon flux of an X-ray tube, showing in red the initial spectrum, in blue the spectrum after passage through iodine and in black, the transmission caused by iodine (%) showing a pronounced K-edge at 30.2 keV. B) The first prototype Spectral CT scanner located at Philips Research in Hamburg, Germany.

Many clinical applications may benefit from this technique, since it is now possible to distinguish between sources of high absorption in body tissue such as calcifications in plaque and the absorption coming from intravenously administered contrast agents. The quantification may also aid in the accurate characterization of diseases such as pancreatic [24] or hepatocellular carcinomas (HCC) [25,26] since the dynamic properties of contrast agent concentrations are required for exact staging. The first Spectral CT scanner is made by Philips Research in Hamburg and is currently in development for preclinical use, later on to be extended to a clinical device.

1.1.2. Magnetic Resonance Imaging (MRI)

An MR image is based on the relative response of specific nuclei to absorbed radio frequency energy (1-100 MHz). Like radiography, this image is a function of density and the magnetic properties of the nucleus that is being observed. Image contrast is furthermore influenced by other physical factors, including differences in the ability to re-emit the absorbed radio frequency signal (relaxation), and flow phenomena. As MRI is able to provide excellent soft tissue contrast with extreme high resolutions, it is often used to image organs, tendons and ligaments [27], as well as the spinal cord [28] and different types of tumors (e.g. brain tumors) [29,30]. MRI is a very versatile but relatively costly technique and requires long scanning times (30-60 minutes). No motion is allowed during acquisition, which, together with claustrophobic feelings some patients develop inside the narrow bore of the system, makes it a relatively uncomfortable modality for the patient.

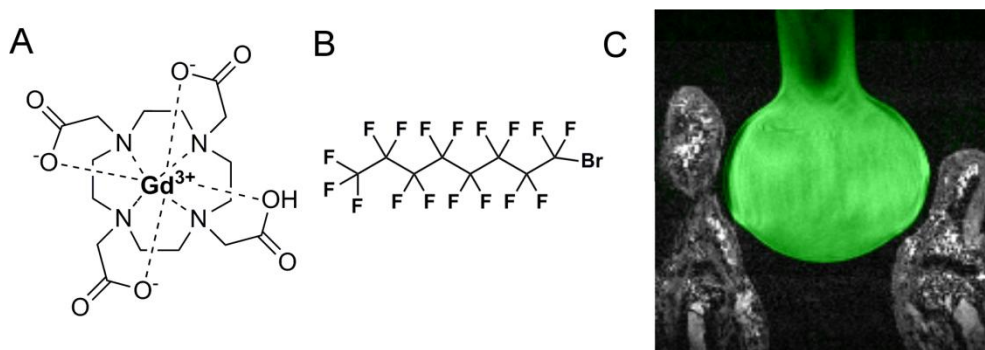


Figure 3. The chemical structure of A) a Gd-DOTA chelate and B) perfluoro octylbromide; C) The combination of 2 MRI scans, visualizing two fingers (proton MRI) holding the fluorinated contrast agent perfluoro octylbromide (fluorine MRI) in a small flask (green).

MRI contrast agents are usually based on paramagnetic metal ions with gadolinium (Gd) being most commonly used. As its free form is toxic, they are coordinated with a chelate like DTPA or DOTA (see Fig. 3A for Gd-DOTA (Dotarem®)) [31,32]. Contrast agents for MRI act like catalysts, speeding up the magnetic relaxation of different nuclei in close vicinity. Applications involve amongst others dynamic contrast enhanced perfusion studies or MR angiography. Most MR images, certainly in clinical practice, are visualizing the hydrogen nucleus because of its relative high abundance in the body, but also other nuclei such as fluorine can be imaged by tuning the MRI scanner to the specific Larmor frequency of the measured compound [33]. As fluorine is almost absent in the human body, fluorinated contrast agents such as perfluoro octylbromide (Fig. 3B) are required to produce an image of the contrast agent and are often combined with proton MRI for spatial localization (Fig. 3C) [34-36].

1.1.3. Ultrasound

Images can furthermore be produced using high frequency acoustic waves also known as ultrasound. Ultrasound waves (2-20 MHz) are reflected by internal interfaces of structures in the body, resulting in backscattered waves (echo's) that are processed into an image. In ultrasound imaging, the wavelength of sound is the fundamental limit of spatial resolution, i.e. at 3.5 MHz, the resolution in soft tissue is about 0.50 mm. Ultrasound provides real time image generation during an exam and has no side effects as no ionizing radiation is used. Most common applications are in prenatal, abdominal or vascular imaging [37-41]. Ultrasound is limited by the availability of a clear acoustic window between the external surface and the region of interest. This is especially restrictive in thoracic imaging where bone and lung tissue overlap. Contrast enhanced ultrasound imaging mainly involves echocardiography using 2-5 micron sized stabilized gas bubbles (Optison®, Sonovue®) [42-45].

1.1.4. Nuclear imaging

Nuclear imaging is the most sensitive of all imaging modalities and furthermore, the only modality where contrast agents are a prerequisite for image generation [46]. Both single photon emission computed tomography (SPECT) and positron emission tomography (PET) utilize radiolabeled tracers to produce images of the *in vivo* radiotracer distribution. Radiopharmaceuticals for PET contain positron emitters (i.e. ^{18}F , ^{11}C) and decay under emission of a positron that annihilates with an electron in the surrounding tissue (ca. 0.8 - 2 mm) of a patient. This creates two 511 keV gamma-rays emitted back-to-back under an angle of 180° that are detected for quantification and localization of the tracer. In the clinic, by far the most PET scans use 2-deoxy-2- ^{18}F fluoro-D-glucose (FDG), a glucose analog that is rapidly taken up by cells with a high rate of glucose metabolism, which is characteristic for malignant cells [47-49] and inflammations [50-52].

In SPECT imaging, radiopharmaceuticals are labeled with isotopes (e.g. Technetium ($^{99\text{m}}\text{Tc}$), Indium (^{111}In)) emitting characteristic and isotope specific γ -photons in the energy range of 80 - 250 keV. As the detector is able to resolve the energy of the measured photons, different radionuclides can be measured simultaneously (dual-isotope) and visualized simultaneously in the body. One of the drawbacks of SPECT compared to PET is its lower sensitivity caused amongst others by the detection technology using collimators. SPECT isotopes on the other hand have longer decay halftimes and can be visualized over a longer time span as most PET isotopes, allowing targeted imaging using long-circulating radiolabeled ligands. For example, radiolabeled antibodies target receptors expressed on cancer cells but as this targeting process takes several days to result in a sufficient tumor to blood ratio, imaging and

quantification of the tumor are only feasible using isotopes with decay times matching the circulation time of the ligand (Fig. 4). Targeted imaging using SPECT made it possible to image head and neck cancer using Rhenium(^{186}Re)-labeled monoclonal antibodies U36 [53,54], or OncoScint® for the detection of colorectal carcinomas [55-57]. Currently, one of the most frequently used clinical applications of SPECT however, is in cardiology to image myocardial perfusion imaging using i.e. $^{99\text{m}}\text{Tc}$ -sestamibi [58-60]

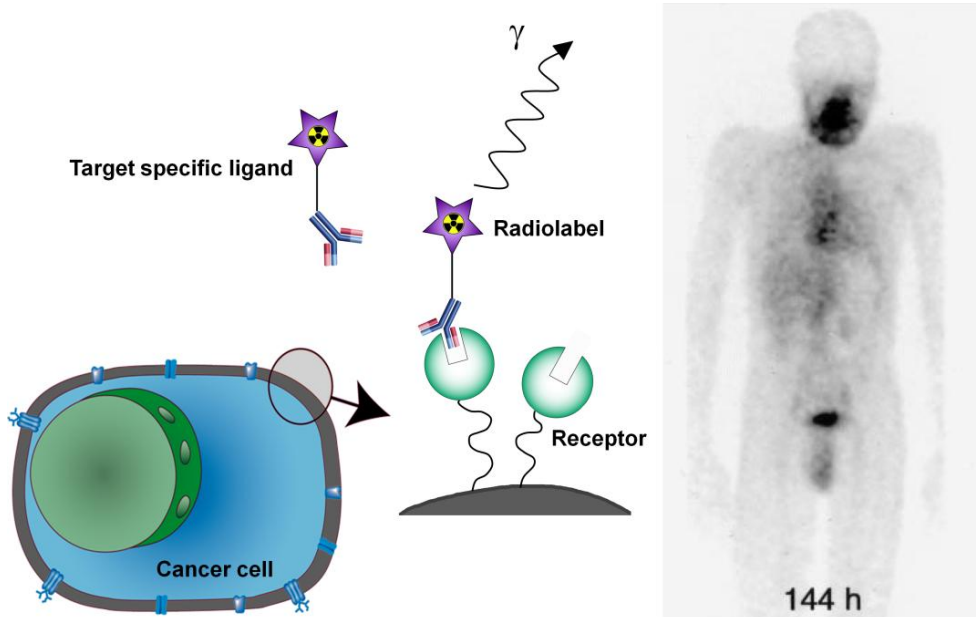


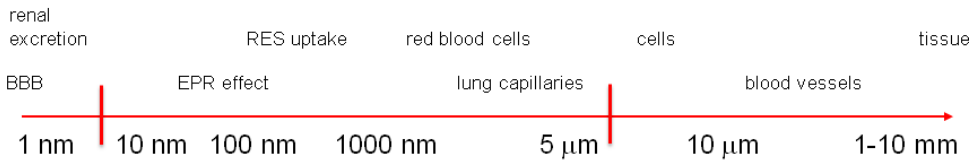
Figure 4. Targeted imaging of cancer using radiolabeled antibodies, for example in head and neck cancer. The whole body scan is reprinted with permission from Colnot *et al.* [53].

1.2. Lengthscales *in vivo*

The size of intravenously administered contrast agents is of great importance as it determines to a large extent the biodistribution and excretion pathways (Fig. 5). Clinically approved contrast agents for MRI, CT, and nuclear imaging are small molecules with sizes well below 5.5 nm and are rapidly excreted *via* the kidney. This 5 nm approximates the cut-off for renal filtration [61]; compounds below this size are excreted from blood into the urine, while compounds larger than 5.5 nm will eventually be taken up in the liver and spleen. The upper limit of contrast agent size is determined by the capillaries in the lung that have a diameter of roughly 5 μm , allowing passage of red blood but anything larger than 5 μm may clog the arteries and induce a lung embolism. The differences of contrast agents in their clearance pathway have medical implications and need to be tuned according to their application.

Additionally, size is of great essence in the uptake of nanoparticulate or macromolecular contrast agents or drugs into tumor tissue *via* the enhanced permeability and retention (EPR) effect [62-64]. The EPR effect is a consequence of poorly aligned endothelium cells in tumor neovasculature, causing gaps in the endothelium wall through which macromolecules can pass. Additionally, the lymphatic drainage is not well developed, which causes contrast agents that have passed through the vessel walls to be retained or trapped in the tumor tissue, while they cannot penetrate through normal tissues with well-aligned endothelium. This passive targeting is only feasible if the size of the contrast agent is optimal. If the molecule is too small, it can rapidly leak out of the tumor tissue and will not be retained, while large molecules or particles may not even penetrate through the leaky vessels into the tumor tissue. Nanoparticles with sizes of 50 - 200 nm have been found optimal for targeting via the EPR effect and have been utilized for the imaging of C26 colon carcinomas using SPECT [65] and IGROV-1 tumors using MRI and fluorescence microscopy [66]. The EPR effect is nowadays clinically utilized for passive tumor targeting of the drug delivery system Doxil (Caelyx). Doxil is a 100 nm sized nanoparticulate formulation of doxorubicin and is used as a chemotherapeutic agent for various tumors. Doxorubicin is an anti-cancerous drug and when injected in its free form has a renal excretion due to its small size. This small size also leads to a rapid extravasation from blood vessels into all tissues, thereby inducing cardiac toxicity, which limits its use in high dosages [67-69]. When encapsulated into a nanoparticle, the cardiac side effects are severely reduced and the effective drug delivery to the tumor region is increased due to the EPR effect [70,71]. This example demonstrates the strong benefit of nanoparticles and, besides drug delivery systems, have been extensively investigated as imaging agents.

Biology



Chemistry

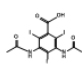

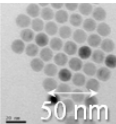
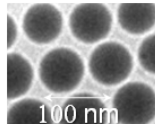
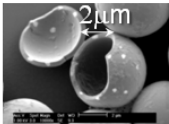
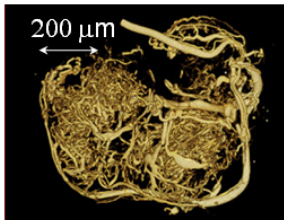
					
classical MRI, CT, nuclear agents	anti- bodies	blood pool agents, iron oxides	molecular imaging agents, drug delivery agents	ultrasound microbubbles	μ -CT of tumor vasculature

Figure 5. Lengthscales related to contrast agents. BBB: blood brain barrier; EPR: enhanced permeability and retention; RES: reticuloendothelial system.

1.3. Nanoparticles

The last decade has witnessed a rapid development in research of novel multifunctional nanoconstructs for applications in imaging and treatment such as dendrimers [72,73], nanocontainers [74], nanocrystals, etc. as well as modified endogenous agents based on proteins, antibodies, lipoproteins or viruses. Especially well-known are the self-assembling nanoparticles that are formed by the self-association of amphiphilic molecules.

1.3.1. Morphology

Amphiphiles, also referred to as surfactants, consist of a hydrophobic and a hydrophilic moiety. In water, these molecules dissolve molecularly below a critical concentration that is determined by the molecular weight of the hydrophobic and hydrophilic part. Above the critical concentration, the free enthalpy drives the formation of aggregates, where the hydrophobic parts maximize their contact areas with the hydrophilic parts being located at the interface to water.

By varying the masses of the hydrophilic group ($Mass_{phil}$) and hydrophobic group ($Mass_{phob}$) and thereby its f_{eo} -ratio of the surfactant, one can tune the three dimensional structure of the final formed aggregate [75].

$$f_{eo} = \frac{Mass_{phil}}{Mass_{phil} + Mass_{phob}}$$

This principle can be used to prepare different morphological nanostructures using either lipids or amphiphilic di-block polymers as a surfactant. For example, a high value of f_{eo} ($f_{eo} > 0.5$) resembles a surfactant with a large hydrophilic head group and a relatively small hydrophobic chain, leading to a cone-like structure. When these molecules are aligned next to each other when they self-assemble in water, a highly curved shape will form: a micelle. Contrary, an intermediate value of f_{eo} leads to a straighter surfactant. Alignment of these molecules leads to less curved shapes, such as cylindrical micelles ($0.4 < f_{eo} < 0.5$) and vesicles ($0.25 < f_{eo} < 0.4$) (Fig. 6). Furthermore, poly-ethylene glycol-phospholipids (pegylated lipids) are often incorporated as a surfactant for stabilization of the nanoparticles. Having an f_{eo} -ratio of ~ 0.8 , pegylated lipids by themselves will assemble into micelles [76]. Values of f_{eo} lower than 0.2 are expected to form inverted structures.

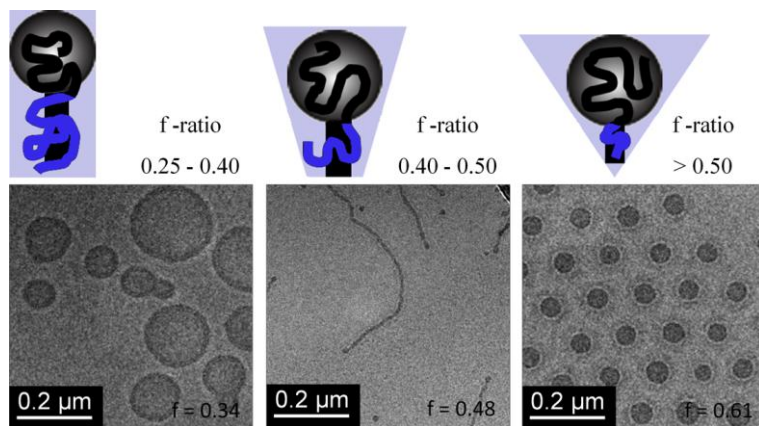


Figure 6. Schematic representation of the shape of nanoparticles with hydrophilic f_0 -ratios of 0.34 (PBD-PEO $M_{w,PEO}=1300$ g/mol; $M_{w,PBD}=2500$), 0.48 (PBD-PEO $M_{w,PEO}=5000$ g/mol; $M_{w,PBD}=5500$) and 0.61 (PBD-PEO $M_{w,PEO}=1900$ g/mol; $M_{w,PBD}=1220$). The corresponding cryo-TEM images visualize the structures formed after self-assembly in water. Samples were measured at Philips Research (MiPlaza) by dr. M.A. Verheijen.

1.3.2. Micelles

Lipid micelles (Fig. 7A) have, depending on the phospholipid used, sizes that vary between 5 and 50 nm, which result in a relatively long circulation time in blood. Different types of micellar contrast agents can be prepared for instance by incorporating paramagnetic lipids as MR agents or radiolabeled lipids as agents for SPECT imaging. Micelles have been used as diagnostic agents in numerous studies such as atherosclerotic plaque detection [77-79]. However, the one drawback of these systems is that micelles composed of low molecular weight surfactants such as lipids have a high critical micelle concentration (CMC), typically in the micromolar range [80,81]. Above this CMC, micelles are formed but below this lipid concentration, the lipids are dissolved in solution as individual molecules. For *in vivo* application, the stability of micelles presents a problem, as the concentration can drop upon injection and subsequent dilution in the blood below the CMC, causing the micelle to dissolve. In contrast, amphiphilic polymers are more favorable for *in vivo* use, as their high number of hydrophobic monomers leads to a strong decrease of the CMC leading to more stable micelles [75]. Polymeric micellar contrast agents have been developed for CT [82], MRI [83,84] and SPECT [85].

Within the hydrophobic core of a micelle, other hydrophobic entities can be incorporated, such as nanocrystals having a hydrophobic surface or hydrophobic drugs (Fig. 7B). This concept can be extended to build multifunctional nanoparticles, for example by adding fluorescent lipids or paramagnetic lipids to the lipid monolayer for

multimodal optical/MR imaging [86]. Also other types of hydrophobic nanocrystals such as gold nanoparticles [87-89] or iron oxides (Fig. 7B) [90,91] can be incorporated as previously demonstrated by van Tilborg *et al.* who further functionalized micellar iron oxides with Annexin V as a targeting moiety for the MR detection of apoptotic cells [92]. Nanocrystal contrast agents typically have sizes between 4 and 50 nm depending on the incorporated crystal and the respective surface coating.

1.3.3. Liposomes and polymersomes

Spherical capsules of well-defined size enclosing an aqueous interior can be made by exploiting the self-assembling nature of naturally occurring amphiphilic phospholipids entitled initially as multilamellar smectic mesophases, later to be known as liposomes (Fig. 7C) [93]. The size of liposomes depends on their preparation and can vary from around 50 nm to larger than 1 μm in diameter. To increase liposome stability towards the action of the physiological environment, cholesterol is incorporated into the liposomal membrane (sometimes up to 50% mol). Plain liposomes are rapidly cleared from the blood (usually within 30 min) as they are recognized by opsonizing proteins and subsequently sequestered by cells of the reticuloendothelial system (RES) [94]. Klibanov *et al.* [95] found that pegylated lipids act as a steric barrier for attachment of plasma proteins and slows down the particles clearance rate, resulting in a general use of pegylated lipids (5-10 mol%) in the liposomal composition. When polymers are used as a surfactant, vesicles named polymersomes are formed that are generally more stable than liposomes. Additionally, the membrane properties can be tuned by choosing and modifying the hydrophobic polymer block according to the needs [75].

1.3.4. Emulsions

When a third hydrophobic oil phase is added to water and a surfactant usually emulsions or microemulsions are formed. While microemulsions are thermodynamically stable and form spontaneously, emulsions present a thermodynamically unstable dispersion of oil droplets in water. Here, the surface tension at the oil/water interface is lowered by the presence of surfactants, in this context also called emulsifiers, leading to a kinetically metastable system. The stability of the emulsion is determined by the different surface tensions depending of the nature of the oil and emulsifiers (Fig. 7D). Emulsion droplets have generally sizes of 50 - 500 nm, which depends amongst others on the surfactant and oil used. Initially, emulsions for medical applications were developed for parenteral nutrition [96] as they can contain large amounts of hydrophobic oil (10 - 20 % soybean or safflower oil) in an aqueous solution and are moreover well accepted as delivery systems for either lipophilic or hydrophobic drugs. Furthermore, hydrophobic contrast agents can be incorporated in the nanoparticle core, using emulsions as a convenient vehicle for formulating hydrophobic particles or molecules for *in vivo* use. Similar to liposomes, the blood circulation of emulsion

particles can be further prolonged by incorporating a pegylated surfactant in the surface layer (e.g. 10 mol% pegylated lipids or 100 mol% pegylated polymer).

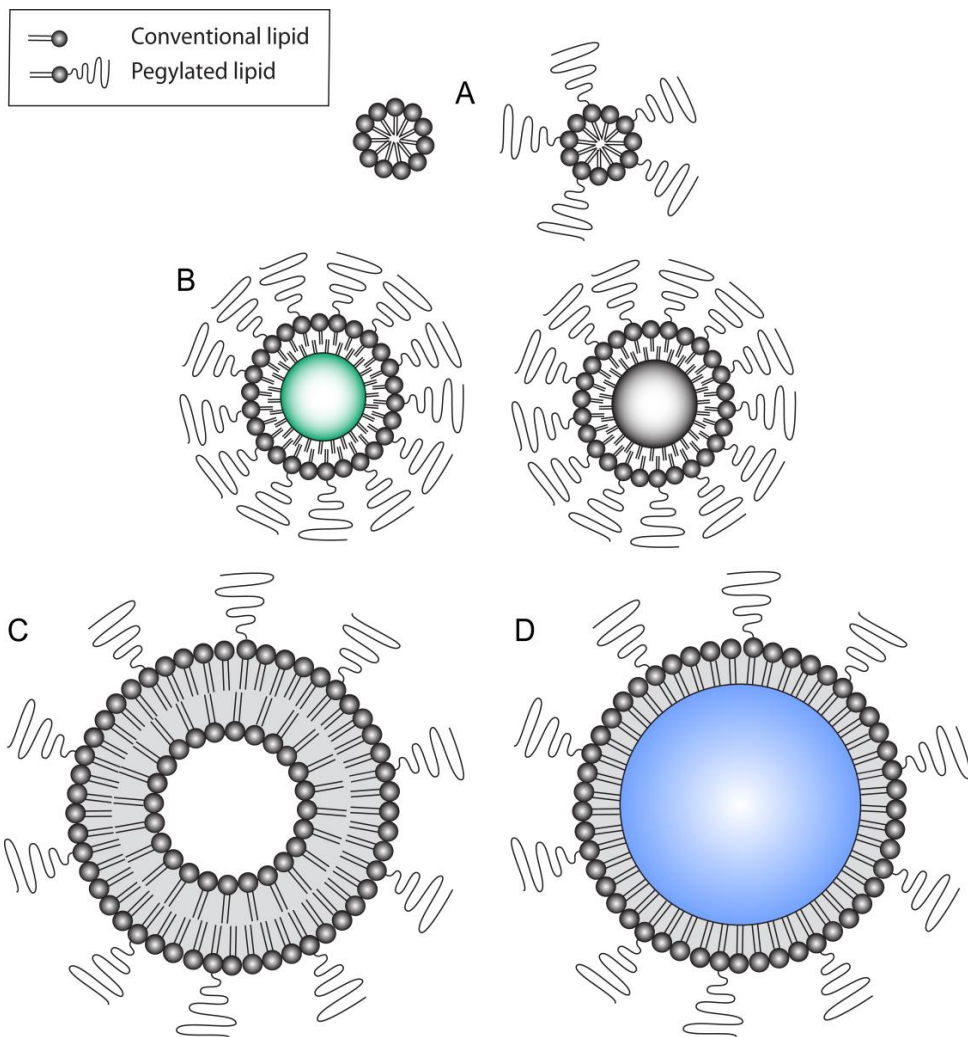


Figure 7. Schematic representation of self-assembled amphiphilic molecules forming well-defined structures as A) Micelles; B) Lipid-modified quantum dot and iron oxide nanoparticle; C) Liposome; D) Emulsion.

1.4. Multifunctional nanoparticles

Molecular imaging aims to perform *in vivo* characterization and measurement of biologic processes at the cellular and molecular level [97]. Molecular imaging therefore requires imaging probes to visualize pathophysiological changes, which is challenging as disease-related markers typically have expression levels in the pM to nM range [98]. Nuclear imaging techniques have sensitivities high enough to perform targeted imaging when a single imaging probe (or less) is attached per ligand. However, imaging techniques as CT and MRI have sensitivities in the 10-100 μ M range and the clinically available contrast agents would therefore not provide enough signal to noise to image these low expressed molecular markers when a 1:1 ratio of contrast agent per targeting ligand is used.

Nanoparticles can bridge the gap for CT and MRI. As nanoparticles are relatively large in size (typically 50 - 200 nm), they can be used as carriers and can accommodate a high payload of contrast agent per particle on its surface or inside the particle. For instance, a 200 nm sized liposome with 25 mol% of paramagnetic lipid in the lipid bilayer, contains over 100.000 gadolinium chelates per particle. This increase of contrast agent concentration per particle is a necessity to be able to perform molecular imaging studies with MRI or CT.

The nanoparticulate surface can be utilized to incorporate any desirable molecule. An example is the previously mentioned pegylated lipids that were utilized to prolong the nanoparticle blood circulation time. Furthermore, targeting ligands can be attached to the nanoparticle surface that target molecular markers of interest (Fig. 8). Also the incorporation of multiple imaging probes for different imaging modalities is possible. Nanoparticles have also been investigated extensively for drug delivery, as drugs can be incorporated inside the nanoparticle or in the surfactant layer.

Despite the wide range of possibilities, there are currently only 2 agents that qualify as nanoparticulate contrast agents and are FDA approved for human application. Iron oxide nanoparticles (Resovist) with sizes around 20-40 nm find application as MR contrast agents. In ultrasound imaging, gas filled bubbles stabilized by lipids or polymers with sizes up to 2-4 μ m are used as contrast agents (Optison®, Sonovue®, Definity®).

Though nanoparticles offer many possibilities, their size presents at the same time a limitation, as they are inevitably taken up by the RES system in the liver and spleen [94,99,100]. Some nanoparticles show a subsequent slow hepatobiliary excretion, while

others are bio-inert and exhibit prolonged tissue retention. Possible long term side effects and toxicity is therefore a major concern [101,102].

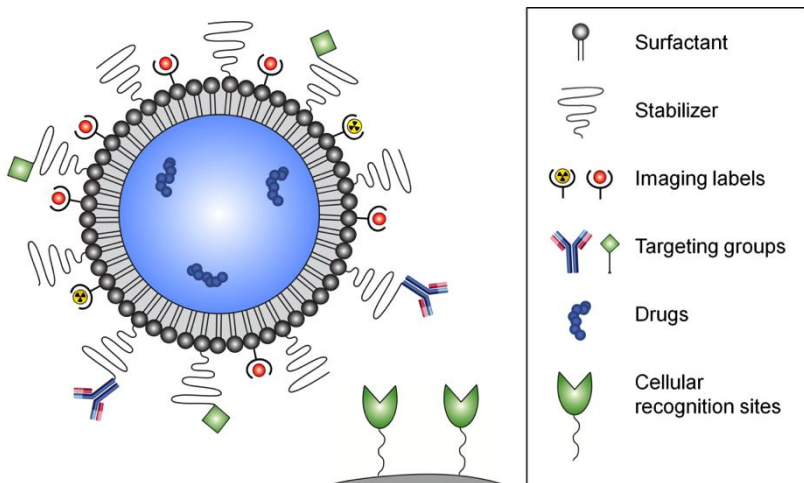


Figure 8. Schematic representation of a multifunctional multimodal nanoparticle.

1.5. Research using nanoparticles

1.5.1. Liposomes

Liposomes have been previously reported as carriers for SPECT, PET, CT and MRI contrast agents for various applications, e.g. angiography for the visualization of blood vessels [103-105] or liver imaging [106,107]. Other way around, incorporation of imaging agents into the liposomes allows to follow non-invasively the biodistribution of liposomes, which is of interest in the development of liposomal drug formulations [108]. The introduction of targeting groups onto the liposomal surface allowed numerous studies to utilize liposomes for molecular imaging. For instance, antibody-conjugated paramagnetic liposomes (LM609) were designed by Sipkins *et al.* to achieve *in vivo* targeted MR imaging of molecules expressed on vascular endothelium [109].

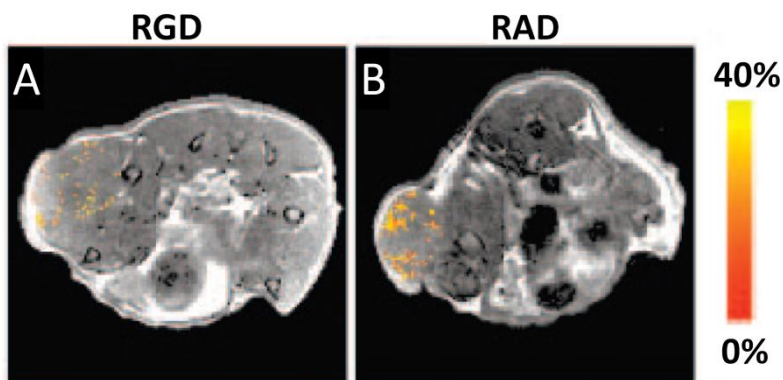


Figure 9. *In vivo* localization of paramagnetic liposomes in the middle of the tumor of an animal 35 min post-injection of A) RGD-liposomes; B) RAD-liposomes. Only a small number of voxels showed contrast enhancement. The color indicates the % of signal enhancement according to the pseudo-color scale on the right. No quantitative numbers can be attributed to the amount of uptake. Reprinted with permission from [110].

Furthermore, Mulder *et al.* [110] demonstrated the use of a paramagnetic liposomal MR contrast agent containing the targeting peptide cyclic-RGD (RGD), which can specifically target the $\alpha_v\beta_3$ -integrin. The $\alpha_v\beta_3$ -integrin is identified as a marker of angiogenic vascular tissue and is expressed i.e. during tumor growth. RGD-liposomes accumulated mainly at the rim of the tumor as they targeted the $\alpha_v\beta_3$ -integrin moieties of the newly formed blood vessels. Control liposomes conjugated with RAD were found through the whole tumor and were non-specifically taken up in the tumor *via* the EPR effect. Though the uptake mechanisms of these two types of liposomes are quite different, the degree of signal enhancement is similar (Fig. 9). However, in MRI, the degree of signal enhancement *in vivo* is not necessarily linearly related to nanoparticle concentration. In the work of Kok *et al.* [111] it was shown that targeted liposomes are

internalized in cells with a faster kinetic and into subcellular structures of a larger size compared to a negative control or non-targeted liposomes. Inside these subcellular structures, there is a restricted water exchange and the paramagnetic contrast agents have a limited access to water protons to increase their relaxivity. As a result, internalization leads to a reduced relaxivity. Especially, for *in vivo* application, it becomes difficult to relate an observed change in contrast to the absolute uptake of paramagnetic liposomes in the tumor. This technique is therefore unable to give a measure of quantitative uptake of the liposomes in the tumor.

1.5.2. Emulsions

Emulsions are investigated as contrast agents for CT and MRI. The underlying reason is twofold. First, due to their size, emulsions stay in the vascular system and, providing an appropriate surface coating is used, they show a long circulation time comparable to liposomes. Secondly, the hydrophobic core can be formed by a contrast providing hydrophobic oil such as an iodinated oil for CT imaging or a fluorinated oil for ^{19}F MR imaging.

In the continuous search for long-circulating blood pool CT contrast agents, nanoparticles have been proposed such as iodinated liposomes [107,112], micelles [82, 113], as well as emulsions. CT is in general not a sensitive imaging method and its increase in contrast relies mostly on the concentration of high-Z elements. High concentrations of CT contrast can be obtained using emulsions and several lipid-based emulsions have therefore been developed and tested in preclinical studies. For example, FenestraTM vascular contrast (VC; ART, Quebec, Canada) is based on iodinated triglyceride - poly ethylene glycol (ITG-PEG) [114,115]. Fenestra has a relatively low iodine concentration (50 mg l/mL, in comparison to the clinical use of 300 mg/l/mL of Iopromide) but shows a long blood circulation half-time of over 7 hours (for an injected dose of 500 mg l/kg) [116]. Besides CT also Spectral CT requires the use of CT contrast agents, preferably blood pool contrast agents to circumvent extravasation.

The use of fluorinated emulsions as contrast agents *in vivo* goes back to the research on fluorinated emulsions as an artificial blood substitute [117,118]. Perfluorocarbons consist of various hydrocarbon derivatives in which all hydrogen atoms have been replaced with fluorine (Fig. 3B). Not surprisingly, this brings substantial changes in the behavior of the molecule. Fluorine has 9 electrons as compared to only one electron for hydrogen, and are packed in a proportionally less space which creates a very electron dense cloud. Fluorine also has a higher ionization potential, a larger electron affinity and a lower polarizability than hydrogen. The latter directly translates into low van der Waals interactions between perfluorocarbons and consequently only low intermolecular forces are present. Perfluorocarbons are therefore very much like gas-like fluids as they

can easily dissolve substances with a similar low cohesivity such as gases (e.g. O₂, CO₂, N₂). For that reason, the potential of perfluorocarbons for oxygen delivery was recognized early [119]. The main challenge was to formulate the hydrophobic perfluorocarbon oil into a stable emulsion for *in vivo* use. The need to follow the *in vivo* biodistribution of these fluorinated emulsions triggered their use as contrast agents. It was recognized that perfluorocarbons can be used as contrast agents for X-ray [120], ultrasound [121] and MRI [122-124].

Perfluorocarbons are very suitable for fluorine MRI since the ¹⁹F nucleus has a 100 % natural abundance, a nuclear spin of ½ and a sensitivity comparable to that of hydrogen. The lack of background signal favors fluorine for contrast agent quantification *in vivo*. Contrast agents as perfluorocarbon emulsions are required providing high local densities of ¹⁹F to reach detectable ¹⁹F concentrations [36, 125,126]. Over the last decade, the group of Wickline has performed extensive studies on perfluorocarbon nanoparticles demonstrating their use amongst others in quantitative molecular imaging of fibrin-targeted clots in atherosclerosis [36], α_vβ₃-targeting of angiogenesis in diseased aortic valve leaflets [127] and angiogenic switch in Vx-2 tumors. However, sensitivity remains an issue as the ¹⁹F concentration (or amount) by far cannot approach the ¹H content in the human body.

1.6. Aim and outline of this thesis

The aim of this thesis is to explore nanoparticles for quantitative imaging. There are two reasons for this. First of all, the combination of quantification and nanoparticles aids in our understanding about biological processes as nanoparticles can be used as blood pool agents, as targeted- or passive imaging probes in diseased areas. Moreover, novel drug delivery systems are under development that require information about the drugs biodistribution and fate. Quantification of the local concentration of contrast agents can give relevant information about the fate of the drug and the effectiveness of the method.

The combination of quantitative imaging and high resolution imaging would integrate the advantages of two techniques such as the high spatial resolution of MRI and the high sensitivity of SPECT. Ultimately, the introduction of target-specificity does allow the imaging of molecular markers for early disease recognition. Only a limited number of preclinical multimodal quantitative contrast agents have been developed that provide quantitative images with high resolution scans.

In this thesis, we investigate several novel nanoparticles for quantitative imaging. In chapter 2, the synthesis, formulation, characterization and preclinical performance of an iodinated emulsions is described for CT imaging. In chapter 3, the dose dependent biodistribution is investigated as well as strategies to vary the biodistribution. In chapter 4, the iodinated emulsion is further developed into a radiolabeled multimodal particle for SPECT and Spectral CT imaging. This study shows the use of a multimodal nanoparticle to investigate and demonstrate quantitative imaging of spectral CT.

In chapter 5 a dual-isotope SPECT imaging protocol has been developed as a tool for pre-clinical testing of new molecular imaging tracers. New molecular targeting probes are consistently investigated as a tool to enable target specific binding of nanoparticles to cellular surfaces of interest. Single-isotope SPECT can be used for a quantitative mapping of a tracer's organ distribution and to investigate its target specificity. However, when a good comparison between two tracers needs to be made, dual-isotope SPECT can be used in which the biodistribution of two different ligands labelled with two different radionuclides can be studied in the same animal, thereby excluding experimental and physiological inter-animal variations. The developed dual-isotope protocol was tested using a known angiogenesis specific ligand (cRGD peptide) in comparison to a potential non-specific control (cRAD peptide).

One of the major challenges of MR imaging is the quantification of local concentrations of paramagnetic contrast agents. As the MR contrast depends on the water exchange between water interacting with the contrast agent and its surrounding, any interference of the biological environment on the water exchange process can lead to a loss of the relation between contrast agent concentration and MR signal intensity. In chapter 6, we propose a multimodal radiolabeled paramagnetic liposomal contrast agent that allows simultaneous imaging with SPECT and MRI. While SPECT allows quantifying the nanoparticle concentration, MRI can now be used to get an indirect read-out of the water exchange, which in return reveals insights in biological processes and environments. This multimodal contrast agent furthermore unites the strengths of multiple imaging modalities within one nanoparticle.

One other possibility to perform quantification in combination with MRI is ^{19}F MR. In the past, fluorine nanoparticles have been proposed that serve as molecular imaging tracers in e.g. atherosclerotic plaque detection or angiogenesis. One of the major drawbacks of quantitative ^{19}F MR is its high detection limit (in the mM range). As a result, high concentrations of fluorine are required at the site of interest to be able to visualize the diseased area, but achieving these levels of concentration is not always feasible. Chapter 7 describes a study that investigates the use of special designed paramagnetic lipids to increase the ^{19}F MR signal per particle.

The thesis ends with a general discussion on future perspectives and conclusions.

1.7. References

- [1] Iyer RB, Silverman PM, Tamm EP, Dunnington JS, DuBrow RA. Diagnosis, staging, and follow-up of esophageal cancer. *AJR Am J Roentgenol.* 2003;181:785-93.
- [2] Sohaib SA, Koh DM, Husband JE. The role of imaging in the diagnosis, staging, and management of testicular cancer. *AJR Am J Roentgenol.* 2008;191:387-95.
- [3] Kalender WA. X-ray computed tomography. *Phys Med Biol.* 2006;51:R29-43.
- [4] McCollough CH, Zink FE. Performance evaluation of a multi-slice CT system. *Med Phys.* 1999;26:2223-30.
- [5] Mollet NR, Cademartiri F, van Mieghem CA, Runza G, McFadden EP, Baks T, et al. High-resolution spiral computed tomography coronary angiography in patients referred for diagnostic conventional coronary angiography. *Circulation.* 2005;112:2318-23.
- [6] Fuchs T, Kachelriess M, Kalender WA. Technical advances in multi-slice spiral CT. *Eur J Radiol.* 2000;36:69-73.
- [7] Huber-Wagner S, Lefering R, Quick LM, Korner M, Kay MV, Pfeifer KJ, et al. Effect of whole-body CT during trauma resuscitation on survival: a retrospective, multicentre study. *Lancet.* 2009;373:1455-61.
- [8] Morin RL, Gerber TC, McCollough CH. Radiation dose in computed tomography of the heart. *Circulation.* 2003;107:917-22.
- [9] Hunold P, Vogt FM, Schmermund A, Debatin JF, Kerkhoff G, Budde T, et al. Radiation exposure during cardiac CT: effective doses at multi-detector row CT and electron-beam CT. *Radiology.* 2003;226:145-52.
- [10] Brenner DJ, Hall EJ. Computed tomography--an increasing source of radiation exposure. *N Engl J Med.* 2007;357:2277-84.
- [11] Li X, Samei E, Segars WP, Sturgeon GM, Colsher JG, Toncheva G, et al. Patient-specific radiation dose and cancer risk estimation in CT: part II. Application to patients. *Med Phys.* 2011;38:408-19.
- [12] Bourin M, Jolliet P, Ballereau F. An overview of the clinical pharmacokinetics of x-ray contrast media. *Clin Pharmacokinet.* 1997;32:180-93.
- [13] Stacul F. Current iodinated contrast media. *Eur Radiol.* 2001;11:690-7.
- [14] Christiansen C. X-ray contrast media--an overview. *Toxicology.* 2005;209:185-7.
- [15] Newhouse JH, Landman J, Lang E, Amis ES, Goldman S, Khazan R, et al. Efficacy and safety of iopromide for excretory urography. *Invest Radiol.* 1994;29:S68-73.
- [16] O'Connor OJ, Maher MM. CT urography. *AJR Am J Roentgenol.* 2010;195:W320-4.
- [17] Cademartiri F, Mollet NR, van der Lugt A, McFadden EP, Stijnen T, de Feyter PJ, et al. Intravenous contrast material administration at helical 16-detector row CT coronary angiography: effect of iodine concentration on vascular attenuation. *Radiology.* 2005;236:661-5.
- [18] Nieman K, Oudkerk M, Rensing BJ, van Ooijen P, Munne A, van Geuns RJ, et al. Coronary angiography with multi-slice computed tomography. *Lancet.* 2001;357:599-603.
- [19] Johnson PT, Pannu HK, Fishman EK. IV contrast infusion for coronary artery CT angiography: literature review and results of a nationwide survey. *AJR Am J Roentgenol.* 2009;192:W214-21.
- [20] Weininger M, Barraza JM, Kemper CA, Kalafut JF, Costello P, Schoepf UJ. Cardiothoracic CT angiography: current contrast medium delivery strategies. *AJR Am J Roentgenol.* 2011;196:W260-72.
- [21] Barber W, Nygard E, Iwanczyk JS, Zhang M, Frey EC, Tsui BMW, et al. Characterization of a novel photon counting detector for clinical CT: count rate, energy resolution, and noise performance. *Proceedings of SPIE.* 2009;7258:725824-1 - 725824-9.
- [22] Roessl E, Proksa R. K-edge imaging in x-ray computed tomography using multi-bin photon counting detectors. *Phys Med Biol.* 2007;52:4679-96.
- [23] Schlomka JP, Roessl E, Dorscheid R, Dill S, Martens G, Istel T, et al. Experimental feasibility of multi-energy photon-counting K-edge imaging in pre-clinical computed tomography. *Phys Med Biol.* 2008;53:4031-47.
- [24] Catalano C, Laghi A, Fraioli F, Pediconi F, Napoli A, Danti M, et al. Pancreatic carcinoma: the role of high-resolution multislice spiral CT in the diagnosis and assessment of resectability. *Eur Radiol.* 2003;13:149-56.
- [25] Zhao H, Yao JL, Wang Y, Zhou KR. Detection of small hepatocellular carcinoma: comparison of dynamic enhancement magnetic resonance imaging and multiphase multirow-detector helical CT scanning. *World J Gastroenterol.* 2007;13:1252-6.
- [26] Ippolito D, Sironi S, Pozzi M, Antolini L, Ratti L, Alberzoni C, et al. Hepatocellular carcinoma in cirrhotic liver disease: functional computed tomography with perfusion imaging in the assessment of tumor vascularization. *Acad Radiol.* 2008;15:919-27.

- [27] O'Connor EE, Dixon LB, Peabody T, Stacy GS. MRI of cystic and soft-tissue masses of the shoulder joint. *AJR Am J Roentgenol.* 2004;183:39-47.
- [28] Leitch JK, Figley CR, Stroman PW. Applying functional MRI to the spinal cord and brainstem. *Magn Reson Imaging.* 2010;28:1225-33.
- [29] Kransdorf MJ, Jelinek JS, Moser RP, Jr., Utz JA, Brower AC, Hudson TM, et al. Soft-tissue masses: diagnosis using MR imaging. *AJR Am J Roentgenol.* 1989;153:541-7.
- [30] Nelson SJ. Analysis of volume MRI and MR spectroscopic imaging data for the evaluation of patients with brain tumors. *Magn Reson Med.* 2001;46:228-39.
- [31] Caravan P, Ellison JJ, McMurry TJ, Lauffer RB. Gadolinium(III) Chelates as MRI Contrast Agents: Structure, Dynamics, and Applications. *Chem Rev.* 1999;99:2293-352.
- [32] Raymond KN, Pierre VC. Next generation, high relaxivity gadolinium MRI agents. *Bioconjug Chem.* 2005;16:3-8.
- [33] Samaratunga RC, Pratt RG, Zhu Y, Massoth RJ, Thomas SR. Implementation of a modified birdcage resonator for 19F/1H MRI at low fields (0.14 T). *Med Phys.* 1994;21:697-705.
- [34] Bulte JW. Hot spot MRI emerges from the background. *Nat Biotechnol.* 2005;23:945-6.
- [35] Ruiz-Cabello J, Walczak P, Kedziorek DA, Chacko VP, Schmieder AH, Wickline SA, et al. In vivo "hot spot" MR imaging of neural stem cells using fluorinated nanoparticles. *Magn Reson Med.* 2008;60:1506-11.
- [36] Morawski AM, Winter PM, Yu X, Fuhrhop RW, Scott MJ, Hockett F, et al. Quantitative "magnetic resonance immunohistochemistry" with ligand-targeted (19)F nanoparticles. *Magn Reson Med.* 2004;52:1255-62.
- [37] Kenny JF, Plappert T, Doubilet P, Saltzman DH, Cartier M, Zollars L, et al. Changes in intracardiac blood flow velocities and right and left ventricular stroke volumes with gestational age in the normal human fetus: a prospective Doppler echocardiographic study. *Circulation.* 1986;74:1208-16.
- [38] Wilson N, Goldberg SJ, Dickinson DF, Scott O. Normal intracardiac and great artery blood velocity measurements by pulsed Doppler echocardiography. *Br Heart J.* 1985;53:451-8.
- [39] Allan LD, Chita SK, Al-Ghazali W, Crawford DC, Tynan M. Doppler echocardiographic evaluation of the normal human fetal heart. *Br Heart J.* 1987;57:528-33.
- [40] Kaufmann BA. Ultrasound molecular imaging of atherosclerosis. *Cardiovasc Res.* 2009;83:617-25.
- [41] Bazzocchi A, Filonzi G, Ponti F, Sassi C, Salizzoni E, Battista G, et al. Accuracy, reproducibility and repeatability of ultrasonography in the assessment of abdominal adiposity. *Acad Radiol.* 2011;18:1133-43.
- [42] Tu J, Hwang JH, Matula TJ, Brayman AA, Crum LA. Intravascular inertial cavitation activity detection and quantification in vivo with Optison. *Ultrasound Med Biol.* 2006;32:1601-9.
- [43] Li T, Tachibana K, Kuroki M. Gene transfer with echo-enhanced contrast agents: comparison between Albunex, Optison, and Levovist in mice--initial results. *Radiology.* 2003;229:423-8.
- [44] Schneider M. SonoVue, a new ultrasound contrast agent. *Eur Radiol.* 1999;9:S347-8.
- [45] Correias JM, Bridal L, Lesavre A, Mejean A, Claudon M, Helenon O. Ultrasound contrast agents: properties, principles of action, tolerance, and artifacts. *Eur Radiol.* 2001;11:1316-28.
- [46] Massoud TF, Gambhir SS. Molecular imaging in living subjects: seeing fundamental biological processes in a new light. *Genes Dev.* 2003;17:545-80.
- [47] Okada J, Yoshikawa K, Imazeki K, Minoshima S, Uno K, Itami J, et al. The use of FDG-PET in the detection and management of malignant lymphoma: correlation of uptake with prognosis. *J Nucl Med.* 1991;32:686-91.
- [48] Schoder H, Meta J, Yap C, Ariannejad M, Rao J, Phelps ME, et al. Effect of whole-body (18)F-FDG PET imaging on clinical staging and management of patients with malignant lymphoma. *J Nucl Med.* 2001;42:1139-43.
- [49] Quon A, Gambhir SS. FDG-PET and beyond: molecular breast cancer imaging. *J Clin Oncol.* 2005;23:1664-73.
- [50] Rudd JH, Myers KS, Bansilal S, Machac J, Pinto CA, Tong C, et al. Atherosclerosis inflammation imaging with 18F-FDG PET: carotid, iliac, and femoral uptake reproducibility, quantification methods, and recommendations. *J Nucl Med.* 2008;49:871-8.
- [51] Spier BJ, Perlman SB, Reichelderfer M. FDG-PET in inflammatory bowel disease. *Q J Nucl Med Mol Imaging.* 2009;53:64-71.
- [52] de Prost N, Tucci MR, Melo MF. Assessment of lung inflammation with 18F-FDG PET during acute lung injury. *AJR Am J Roentgenol.* 2010;195:292-300.
- [53] Colnot DR, Quak JJ, Roos JC, van Lingen A, Wilhelm AJ, van Kamp GJ, et al. Phase I therapy study of 186Re-labeled chimeric monoclonal antibody U36 in patients with squamous cell carcinoma of the head and neck. *J Nucl Med.* 2000;41:1999-2010.

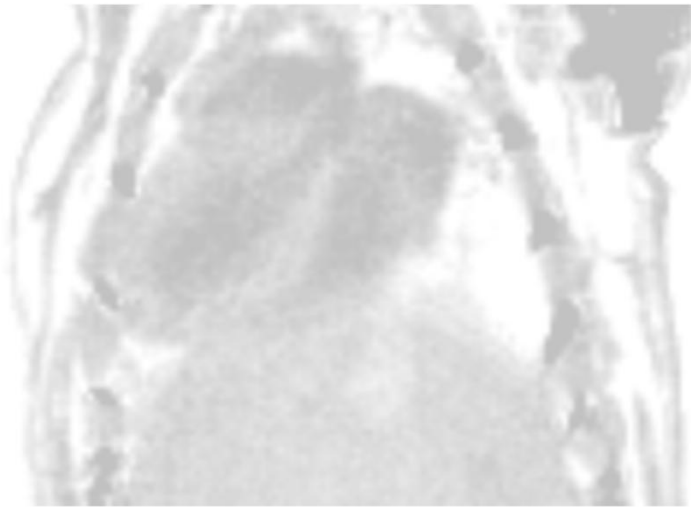
- [54] Postema EJ, Borjesson PK, Buijs WC, Roos JC, Marres HA, Boerman OC, et al. Dosimetric analysis of radioimmunotherapy with ¹⁸⁶Re-labeled bivatuzumab in patients with head and neck cancer. *J Nucl Med.* 2003;44:1690-9.
- [55] Abdel-Nabi H, Doerr RJ, Chan HW, Balu D, Schmelter RF, Maguire RT. In-¹¹¹In-labeled monoclonal antibody immunoscintigraphy in colorectal carcinoma: safety, sensitivity, and preliminary clinical results. *Radiology.* 1990;175:163-71.
- [56] Abdel-Nabi HH, Chan HW, Doerr RJ. Indium-labeled anti-colorectal carcinoma monoclonal antibody accumulation in non-tumored tissue in patients with colorectal carcinoma. *J Nucl Med.* 1990;31:1975-9.
- [57] Hladik P, Vizda J, Bedrna J, Simkovic D, Strnad L, Smejkal K, et al. Immunoscintigraphy and intra-operative radioimmunodetection in the treatment of colorectal carcinoma. *Colorectal Dis.* 2001;3:380-6.
- [58] Zanco P, Zampiero A, Favero A, Borsato N, Chierichetti F, Rubello D, et al. Prognostic evaluation of patients after myocardial infarction: incremental value of sestamibi single-photon emission computed tomography and echocardiography. *J Nucl Cardiol.* 1997;4:117-24.
- [59] Schillaci O, Lagana B, Danieli R, Gentile R, Tubani L, Baratta L, et al. Technetium-99m sestamibi single-photon emission tomography detects subclinical myocardial perfusion abnormalities in patients with systemic lupus erythematosus. *Eur J Nucl Med.* 1999;26:713-7.
- [60] Mannting F, Zabrodina YV, Dass C. Significance of increased right ventricular uptake on ^{99m}Tc-sestamibi SPECT in patients with coronary artery disease. *J Nucl Med.* 1999;40:889-94.
- [61] Choi HS, Liu W, Misra P, Tanaka E, Zimmer JP, Itty Ipe B, et al. Renal clearance of quantum dots. *Nat Biotechnol.* 2007;25:1165-70.
- [62] Maeda H, Wu J, Sawa T, Matsumura Y, Hori K. Tumor vascular permeability and the EPR effect in macromolecular therapeutics: a review. *J Control Release.* 2000;65:271-84.
- [63] Iyer AK, Khaled G, Fang J, Maeda H. Exploiting the enhanced permeability and retention effect for tumor targeting. *Drug Discov Today.* 2006;11:812-8.
- [64] Kaasgaard T, Andresen TL. Liposomal cancer therapy: exploiting tumor characteristics. *Expert Opin Drug Deliv.* 2010;7:225-43.
- [65] Lin YY, Li JJ, Chang CH, Lu YC, Hwang JJ, Tseng YL, et al. Evaluation of pharmacokinetics of ¹¹¹In-labeled VNB-PEGylated liposomes after intraperitoneal and intravenous administration in a tumor/ascites mouse model. *Cancer Biother Radiopharm.* 2009;24:453-60.
- [66] Kamaly N, Kalber T, Ahmad A, Oliver MH, So PW, Herlihy AH, et al. Bimodal paramagnetic and fluorescent liposomes for cellular and tumor magnetic resonance imaging. *Bioconjug Chem.* 2008;19:118-29.
- [67] Boucek RJ, Jr., Dodd DA, Atkinson JB, Oquist N, Olson RD. Contractile failure in chronic doxorubicin-induced cardiomyopathy. *J Mol Cell Cardiol.* 1997;29:2631-40.
- [68] Carver JR, Schuster SJ, Glick JH. Doxorubicin cardiotoxicity in the elderly: old drugs and new opportunities. *J Clin Oncol.* 2008;26:3122-4.
- [69] Singal PK, Iliskovic N. Doxorubicin-induced cardiomyopathy. *N Engl J Med.* 1998;339:900-5.
- [70] Gabizon A, Catane R, Uziely B, Kaufman B, Safra T, Cohen R, et al. Prolonged circulation time and enhanced accumulation in malignant exudates of doxorubicin encapsulated in polyethylene-glycol coated liposomes. *Cancer Res.* 1994;54:987-92.
- [71] O'Brien ME, Wigler N, Inbar M, Rosso R, Grischke E, Santoro A, et al. Reduced cardiotoxicity and comparable efficacy in a phase III trial of pegylated liposomal doxorubicin HCl (CAELYX/Doxil) versus conventional doxorubicin for first-line treatment of metastatic breast cancer. *Ann Oncol.* 2004;15:440-9.
- [72] Langereis S, DeLussanet QG, van Genderen M, Backes WH, Meijer EW. Multivalent contrast agents based on Gd-DTPA-terminated poly (propylene imine) dendrimers for Magnetic Resonance Imaging. *Macromolecules.* 2004;37:3084-91.
- [73] Kobayashi H, Brechbiel MW. Nano-sized MRI contrast agents with dendrimer cores. *Adv Drug Deliv Rev.* 2005;57:2271-86.
- [74] Popovic Z, Otter M, Calzaferri G, De Cola L. Self-assembling living systems with functional nanomaterials. *Angew Chem Int Ed Engl.* 2007;46:6188-91.
- [75] Discher DE, Ahmed F. Polymersomes. *Annu Rev Biomed Eng.* 2006;8:323-41.
- [76] Johnsson M, Edwards K. Liposomes, disks, and spherical micelles: aggregate structure in mixtures of gel phase phosphatidylcholines and poly(ethylene glycol)-phospholipids. *Biophys J.* 2003;85:3839-47.
- [77] van Tilborg GA, Vucic E, Strijkers GJ, Cormode DP, Mani V, Skajaa T, et al. Annexin A5-functionalized bimodal nanoparticles for MRI and fluorescence imaging of atherosclerotic plaques. *Bioconjug Chem.* 2010;21:1794-803.

- [78] van Bochove GS, Paulis LE, Segers D, Mulder WJ, Krams R, Nicolay K, et al. Contrast enhancement by differently sized paramagnetic MRI contrast agents in mice with two phenotypes of atherosclerotic plaque. *Contrast Media Mol Imaging*. 2011;6:35-45.
- [79] Mulder WJ, Strijkers GJ, Briley-Saboe KC, Frias JC, Aguinaldo JG, Vucic E, et al. Molecular imaging of macrophages in atherosclerotic plaques using bimodal PEG-micelles. *Magn Reson Med*. 2007;58:1164-70.
- [80] Lichtenberg D, Robson RJ, Dennis EA. Solubilization of phospholipids by detergents. Structural and kinetic aspects. *Biochim Biophys Acta*. 1983;737:285-304.
- [81] Ashok B, Arleth L, Hjelm RP, Rubinstein I, Onyuksel H. In vitro characterization of PEGylated phospholipid micelles for improved drug solubilization: effects of PEG chain length and PC incorporation. *J Pharm Sci*. 2004;93:2476-87.
- [82] Torchilin VP, Frank-Kamenetsky MD, Wolf GL. CT visualization of blood pool in rats by using long-circulating, iodine-containing micelles. *Acad Radiol*. 1999;6:61-5.
- [83] Grogna M, Cloots R, Luxen A, Jérôme C, Passirani CL, N, Desreux J, et al. Polymer micelles decorated by gadolinium complexes as MRI blood contrast agents: design, synthesis and properties. *Polymer Chemistry*. 2010;1:1485-90.
- [84] Nakamura E, Makino K, Okano T, Yamamoto T, Yokoyama M. A polymeric micelle MRI contrast agent with changeable relaxivity. *J Control Release*. 2006;114:325-33.
- [85] Torchilin VP. PEG-based micelles as carriers of contrast agents for different imaging modalities. *Adv Drug Deliv Rev*. 2002;54:235-52.
- [86] Starmans LW, Kok MB, Sanders HM, Zhao Y, Donega Cde M, Meijerink A, et al. Influence of cell-internalization on relaxometric, optical and compositional properties of targeted paramagnetic quantum dot micelles. *Contrast Media Mol Imaging*. 2011;6:100-9.
- [87] Cai QY, Kim SH, Choi KS, Kim SY, Byun SJ, Kim KW, et al. Colloidal gold nanoparticles as a blood-pool contrast agent for X-ray computed tomography in mice. *Invest Radiol*. 2007;42:797-806.
- [88] Cormode DP, Skajaa T, van Schooneveld MM, Koole R, Jarzyna P, Lobatto ME, et al. Nanocrystal core high-density lipoproteins: a multimodality contrast agent platform. *Nano Lett*. 2008;8:3715-23.
- [89] Boisselier E, Astruc D. Gold nanoparticles in nanomedicine: preparations, imaging, diagnostics, therapies and toxicity. *Chem Soc Rev*. 2009;38:1759-82.
- [90] Huang HC, Chang PY, Chang K, Chen CY, Lin CW, Chen JH, et al. Formulation of novel lipid-coated magnetic nanoparticles as the probe for in vivo imaging. *J Biomed Sci*. 2009;16:86.
- [91] Fan C, Gao W, Chen Z, Fan H, Li M, Deng F. Tumor selectivity of stealth multi-functionalized superparamagnetic iron oxide nanoparticles. *Int J Pharm*. 2011;404:180-90.
- [92] van Tilborg GA, Geelen T, Duimel H, Bomans PH, Frederik PM, Sanders HM, et al. Internalization of annexin A5-functionalized iron oxide particles by apoptotic Jurkat cells. *Contrast Media Mol Imaging*. 2009;4:24-32.
- [93] Bingham AD, Standish MM, Watkins JC. Diffusion of univalent ions across the lamellae of swollen phospholipids. *J Mol Biol*. 1965;13:238-52.
- [94] Drummond DC, Meyer O, Hong K, Kirpotin DB, Papahadjopoulos D. Optimizing liposomes for delivery of chemotherapeutic agents to solid tumors. *Pharmacol Rev*. 1999;51:691-743.
- [95] Klibanov AL, Maruyama K, Torchilin VP, Huang L. Amphipathic polyethyleneglycols effectively prolong the circulation time of liposomes. *FEBS Lett*. 1990;268:235-7.
- [96] Benita S, Levy MY. Submicron emulsions as colloidal drug carriers for intravenous administration: comprehensive physicochemical characterization. *J Pharm Sci*. 1993;82:1069-79.
- [97] Weissleder R, Mahmood U. Molecular imaging. *Radiology*. 2001;219:316-33.
- [98] Blankenberg FG. Molecular imaging: The latest generation of contrast agents and tissue characterization techniques. *J Cell Biochem*. 2003;90:443-53.
- [99] Harashima H, Sakata K, Funato K, Kiwada H. Enhanced hepatic uptake of liposomes through complement activation depending on the size of liposomes. *Pharm Res*. 1994;11:402-6.
- [100] Ishida T, Ichihara M, Wang X, Kiwada H. Spleen plays an important role in the induction of accelerated blood clearance of PEGylated liposomes. *J Control Release*. 2006;115:243-50.
- [101] Medina C, Santos-Martinez MJ, Radomski A, Corrigan OI, Radomski MW. Nanoparticles: pharmacological and toxicological significance. *Br J Pharmacol*. 2007;150:552-8.
- [102] Maurer-Jones MA, Bantz KC, Love SA, Marquis BJ, Haynes CL. Toxicity of therapeutic nanoparticles. *Nanomedicine (Lond)*. 2009;4:219-41.
- [103] Tilcock C, Yap M, Szucs M, Utkhede D. PEG-coated lipid vesicles with encapsulated technetium-99m as blood pool agents for nuclear medicine. *Nucl Med Biol*. 1994;21:165-70.
- [104] Goins B, Phillips WT, Klipper R. Blood-pool imaging using technetium-99m-labeled liposomes. *J Nucl Med*. 1996;37:1374-9.

- [105] Howles GP, Ghaghada KB, Qi Y, Mukundan S, Jr., Johnson GA. High-resolution magnetic resonance angiography in the mouse using a nanoparticle blood-pool contrast agent. *Magn Reson Med.* 2009;62:1447-56.
- [106] Fosheim SL, Colet JM, Mansson S, Fahlvik AK, Muller RN, Klaveness J. Paramagnetic liposomes as magnetic resonance imaging contrast agents. Assessment of contrast efficacy in various liver models. *Invest Radiol.* 1998;33:810-21.
- [107] Montet X, Pastor CM, Vallee JP, Becker CD, Geissbuhler A, Morel DR, et al. Improved visualization of vessels and hepatic tumors by micro-computed tomography (CT) using iodinated liposomes. *Invest Radiol.* 2007;42:652-8.
- [108] Gabizon A, Tzemach D, Mak L, Bronstein M, Horowitz AT. Dose dependency of pharmacokinetics and therapeutic efficacy of pegylated liposomal doxorubicin (DOXIL) in murine models. *J Drug Target.* 2002;10:539-48.
- [109] Sipkins DA, Cheresh DA, Kazemi MR, Nevin LM, Bednarski MD, Li KC. Detection of tumor angiogenesis in vivo by $\alpha v \beta_3$ -targeted magnetic resonance imaging. *Nat Med.* 1998;4:623-6.
- [110] Mulder WJ, Strijkers GJ, Habets JW, Bleeker EJ, van der Schaft DW, Storm G, et al. MR molecular imaging and fluorescence microscopy for identification of activated tumor endothelium using a bimodal lipidic nanoparticle. *Faseb J.* 2005;19:2008-10.
- [111] Kok MB, Hak S, Mulder WJ, van der Schaft DW, Strijkers GJ, Nicolay K. Cellular compartmentalization of internalized paramagnetic liposomes strongly influences both T1 and T2 relaxivity. *Magn Reson Med.* 2009;61:1022-32.
- [112] Mukundan S, Jr., Ghaghada KB, Badea CT, Kao CY, Hedlund LW, Provenzale JM, et al. A liposomal nanoscale contrast agent for preclinical CT in mice. *AJR Am J Röntgenol.* 2006;186:300-7.
- [113] Trubetskov VS, Gazelle GS, Wolf GL, Torchilin VP. Block-copolymer of polyethylene glycol and polylysine as a carrier of organic iodine: design of long-circulating particulate contrast medium for X-ray computed tomography. *J Drug Target.* 1997;4:381-8.
- [114] Weichert JP, Lee FT, Jr., Longino MA, Chosy SG, Counsell RE. Lipid-based blood-pool CT imaging of the liver. *Acad Radiol.* 1998;5:S16-9; discussion S28-30.
- [115] Wisner ER, Weichert JP, Longino MA, Counsell RE, Weisbrode SE. A surface-modified chylomicron remnant-like emulsion for percutaneous computed tomography lymphography: synthesis and preliminary imaging findings. *Invest Radiol.* 2002;37:232-9.
- [116] Ford NL, Graham KC, Groom AC, Macdonald IC, Chambers AF, Holdsworth DW. Time-course characterization of the computed tomography contrast enhancement of an iodinated blood-pool contrast agent in mice using a volumetric flat-panel equipped computed tomography scanner. *Invest Radiol.* 2006;41:384-90.
- [117] Riess JG, Krafft MP. Fluorinated materials for in vivo oxygen transport (blood substitutes), diagnosis and drug delivery. *Biomaterials.* 1998;19:1529-39.
- [118] Riess JG. Oxygen carriers ("blood substitutes")-raison d'etre, chemistry, and some physiology. *Chem Rev.* 2001;101:2797-920.
- [119] Zuck TF, Riess JG. Current status of injectable oxygen carriers. *Crit Rev Clin Lab Sci.* 1994;31:295-324.
- [120] Mattrey RF, Long DM, Peck WW, Slutsky RA, Higgins CB. Perfluorooctylbromide as a blood pool contrast agent for liver, spleen, and vascular imaging in computed tomography. *J Comput Assist Tomogr.* 1984;8:739-44.
- [121] Schutt EG, Klein DH, Mattrey RM, Riess JG. Injectable microbubbles as contrast agents for diagnostic ultrasound imaging: the key role of perfluorochemicals. *Angew Chem Int Ed Engl.* 2003;42:3218-35.
- [122] Mattrey RF. Perfluorooctylbromide: a new contrast agent for CT, sonography, and MR imaging. *AJR Am J Roentgenol.* 1989;152:247-52.
- [123] Long DM, Long DC, Mattrey RF, Long RA, Burgan AR, Herrick WC, et al. An overview of perfluorooctylbromide-application as a synthetic oxygen carrier and imaging agent for X-ray, ultrasound and nuclear magnetic resonance. *Biomater Artif Cells Artif Organs.* 1988;16:411-20.
- [124] Thomas SR, Clark LC, Jr., Ackerman JL, Pratt RG, Hoffmann RE, Busse LJ, et al. MR imaging of the lung using liquid perfluorocarbons. *J Comput Assist Tomogr.* 1986;10:1-9.
- [125] Neubauer AM, Caruthers SD, Hockett FD, Cyrus T, Robertson JD, Allen JS, et al. Fluorine cardiovascular magnetic resonance angiography in vivo at 1.5 T with perfluorocarbon nanoparticle contrast agents. *J Cardiovasc Magn Reson.* 2007;9:565-73.
- [126] Srinivas M, Morel PA, Ernst LA, Laidlaw DH, Ahrens ET. Fluorine-19 MRI for visualization and quantification of cell migration in a diabetes model. *Magn Reson Med.* 2007;58:725-34.
- [127] Waters EA, Chen J, Allen JS, Zhang H, Lanza GM, Wickline SA. Detection and quantification of angiogenesis in experimental valve disease with integrin-targeted nanoparticles and 19-fluorine MRI/MRS. *J Cardiovasc Magn Reson.* 2008;10:43.

Chapter 2

Block-copolymer-stabilized iodinated emulsions for use as CT contrast agents



Based on

Block-copolymer-stabilized iodinated emulsions for use as CT contrast agents
A. d. Vries, E. Custers, J. Lub, S. v.d. Bosch, K. Nicolay and H. Gröll
Biomaterials (31) 2010, p. 6537-6544

Abstract

The objective of this study was to develop radiopaque iodinated emulsions for use as CT blood pool contrast agents. Three hydrophobic iodinated oils were synthesized based on the 2,3,5-triiodobenzoate moiety and formulated into emulsions using either phospholipids or amphiphilic polymers, i.e. Pluronic F68 and poly(butadiene)-*b*-poly(ethylene glycol) (PBD-PEO), as emulsifiers. The size, stability and cell viability was investigated for all stabilized emulsions. Three emulsions stabilized with either lipids or PBD-PEO were subsequently tested *in vivo* as a CT blood pool contrast agent in mice. While the lipid-stabilized emulsions turned out unstable *in vivo*, polymer-stabilized emulsions performed well *in vivo*. In blood, a contrast enhancement of 220 Hounsfield Units (HU) was measured directly after intravenous administration of 520 mg I/kg. The blood circulation half-life of a PBD-PEO stabilized emulsion was approximately 3 hours and no noticeable *in vivo* toxicity was observed. These results show the potential of above emulsions for use as blood pool agents in contrast enhanced CT imaging.

2.1. Introduction

X-ray and computed tomography (CT) are the most frequently used diagnostic imaging technologies in the clinic. Recent technological advances, such as fast digital X-ray detectors or spiral and multi-slice CT [1,2], in combination with the approval of improved iodinated CT contrast agents, opened a plethora of new applications in radiology. With X-ray and CT moving forward into the interventional care, such as stent placement, balloon dilatation, vascular surgery, and electrophysiology procedures, there is a clear need for CT contrast agents that allow sharp blood vessel delineation and have a long circulation time to avoid multiple contrast agent injections [3,4]. Current contrast agents used in X-ray and CT applications are usually iodinated molecules with a low molecular weight (< 2000 Da) resulting in a rapid renal excretion and a high free volume of distribution as they rapidly equilibrate between the blood compartment and the extracellular, extravascular compartment [5,6]. One strategy to improve the current generation of CT contrast agents is to design a blood pool CT contrast agents having sizes larger than ca. 5.5 nm to prohibit rapid renal excretion and extravasation [7]. Blood clearance of these agents occurs *via* uptake in the reticuloendothelial system (RES) followed by metabolism and/or excretion *via* the hepatobiliary pathway. Long circulation times can be achieved by designing a stealth coating on the agents' surface to avoid rapid opsonization followed by macrophage uptake. Moreover, it is desired that the CT contrast agent has a high iodine payload to avoid injection of a large volume. The latter is of special interest for preclinical studies using CT contrast agents as the maximum volume that can be injected intravenously into mice is generally restricted to ~200 μ L.

Whereas most CT contrast agents are based on the high-Z element iodine, also other high-Z elements have been explored for their radiopaque properties in preclinical studies. For example, nanoparticles based on bismuth sulphide (10-50 nm) or gold (38 nm) with blood half-lives of 140 ± 15 minutes and 14.6 ± 3.3 hours respectively were investigated in mice [8,9]. So far, a detailed study on the toxicity of bismuth-based nanoparticles is lacking, however, several studies report on the potential toxic effect of gold nanoparticles [10-12], which hampers their translation into the clinic. Most investigations on new CT contrast agents focus on iodine due to similarities with the already clinical approved agents. Margel and coworkers designed solid nanoparticles of 30.6 ± 5 nm for X-ray imaging based on polymers of 2-methacryloyloxyethyl(2,3,5-triiodobenzoate) [13-15], which is a similar approach taken by Hyafil *et al.* [16]. Besides highly radiopaque solid nanoparticles, also iodinated polymeric micelles of MPEG-iodolysine block-copolymers [17,18] and emulsions of iodinated triglycerides were investigated [19]. The latter is commercially available for preclinical use (Fenestra VC

(ART, Saint-Laurent, Canada)), however, the low iodine concentration of 50 mg I/mL hampers its use in small animals due to restrictions on the injectable volume.

In our work, we explored highly iodinated nano-emulsions as a possible class of blood pool CT contrast agent. The radiopaque core of the emulsions consists of a hydrophobic iodinated oil, e.g. octan-2-yl 2,3,5-triodobenzoate (**oil 1**), 3,7-dimethyloctyl 2,3,5-triodobenzoate (**oil 2**), or 2,3,5-triodobenzyl 2-methylheptanoate (**oil 3**). These oils were emulsified using three types of surfactants, namely 1,2-distearoyl-*sn*-glycero-3-phosphocholine (DSPC; a phospholipid), poly(ethylene oxide)-*b*-poly(propylene oxide)-*b*-poly(ethylene oxide) (PEO-PPO-PEO; Pluronic F68) or poly(butadiene)-*b*-poly(ethylene oxide) (PBD-PEO) (Fig. 1). The obtained CT contrast agents were characterized in great detail using dynamic light scattering, Coulter Counter, and Cryo-TEM. MTT toxicity assays were performed to test for acute cell toxicity. Finally, the best candidate emulsions (DSPC, **oil 1**; PBD-PEO, **oil 1**; PBD-PEO, **oil 2**) were taken into *in vivo* tests to study blood half-life and contrast generation in CT imaging of mice.

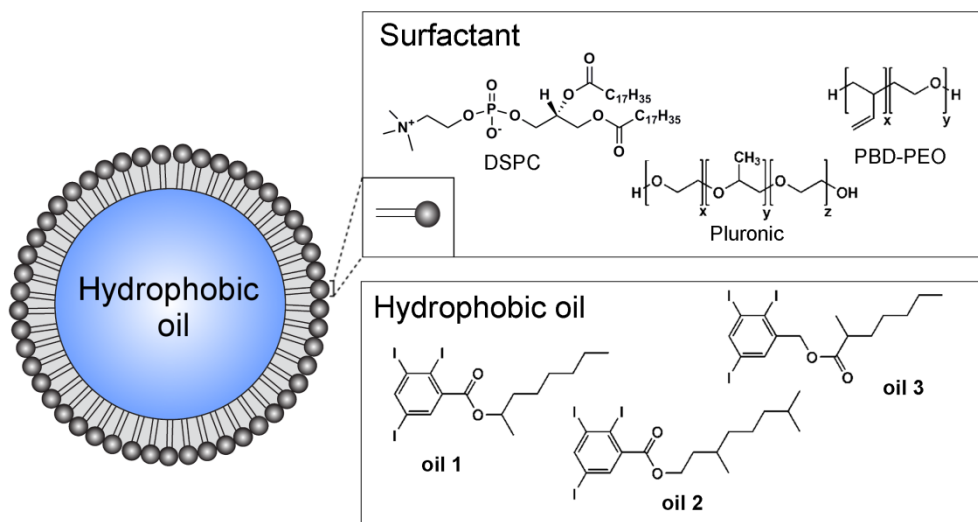


Figure 1. Schematic representation of a stabilized emulsion as a CT contrast agent showing the different types of surfactant and hydrophobic oils.

2.2. Materials and Methods

2.2.1. Materials

All solvents were obtained from Merck. 2-Methyl heptanoic acid was obtained from Acros. 1,2-Distearoyl-*sn*-glycero-3-phosphocholine (DSPC), 1,2-distearoyl-*sn*-Glycero-3-phospho-ethanolamine-*N*-[methoxy(polyethyleneglycol)-2000] (DSPE-PEG₂₀₀₀) were purchased from Lipoid and cholesterol (Chol) was purchased from Avanti Polar Lipids. Pluronic F-68 (PEO-PPO-PEO: $M_{w,PEO}=3360$ g/mol; $M_{w,PPO}=1680$ g/mol; $M_{w,PEO}=3360$ g/mol) [20] was purchased from Sigma-Aldrich. Poly(butadiene(1,2-addition)-*b*-ethylene oxide) (P-6088; $M_{w,PEO}=2033$ g/mol; $M_{w,PBD}=1305$ g/mol) was obtained from Polymer Source. All other commercial chemicals were purchased from Sigma-Aldrich in the highest available quality.

2.2.2. Synthesis

2.2.2.1. 2,3,5-Triiodobenzoyl chloride (**1**)

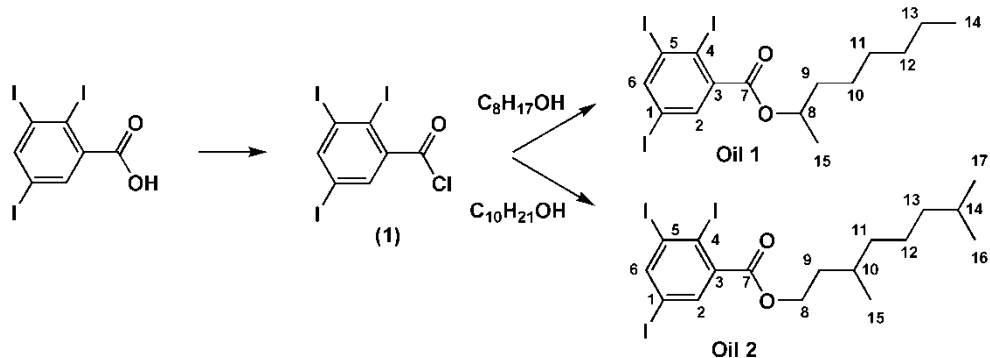
A mixture of 2,3,5-triiodobenzoic acid (100.1 g, 0.20 mol) and of thionyl chloride (200 mL, 1.74 mol) was refluxed for 3 hrs. The gases generated were neutralized by passing them through a Na₂CO₃ solution. After cooling, the excess of thionyl chloride was evaporated at 60°C *in vacuo* and tetrachloromethane (100 mL) was added. The crude mixture was heated to 65°C and was left at 4°C to obtain brownish crystals (90.8 g, 175 mmol) in a yield of 87%. The crystals were washed with tetrachloromethane and dried over silica under reduced pressure. A schematic representation of the reaction can be found in Scheme 1. IR (neat) 1762 cm⁻¹ (C=O).

2.2.2.2. Octan-2-yl 2,3,5-triiodobenzoate (**oil 1**)

To a solution of 2,3,5-triiodobenzoyl chloride (**1**, 90 g, 0.175 mol) in 450 mL of dichloromethane (DCM) stirred in an ice-water bath under nitrogen subsequently 2-octanol (30.5 mL, 0.192 mol), triethylamine (48.8 mL, 0.35 mol) and 4-*N,N*-dimethylaminopyridine (4.3 g, 35 mmol) were added drop wise. After stirring for 2 hours, the ice-water bath was removed and stirring was continued overnight. 700 mL of water was added and the organic layer was subsequently extracted with 600 mL HCl (1 N), 600 mL of a 10% NaHCO₃ solution and 500 mL brine. After drying over MgSO₄, the solvent was evaporated and the remaining oil was purified by elution with DCM over 660 g silica. 90.0 g of the racemic product (147 mmol, 84%) was obtained as a light yellowish viscous oil. A schematic representation of the reaction can be found in Scheme 1.

¹H NMR (CDCl₃, δ/ppm): 8.27 (d, $J = 1.9$ Hz, 1H, H²), 7.66 (d, $J = 1.9$ Hz, 1H, H⁶), 5.13 (m, $J = 6.4$ Hz, 2H, H⁸), 1.72 (m, 1H, H⁹), 1.60 (m, 1H, H⁹), 1.5-1.2 (m, 8H, H¹⁰, H¹¹, H¹² and H¹³), 1.36 (d, $J = 6.4$ Hz, 3H, H¹⁵), 0.88 (t, $J = 6.8$ Hz, 3H, H¹⁴). ¹³C NMR (CDCl₃, δ/ppm): 165.9 (C⁷), 148.4 (C⁶), 142.4 (C³), 136.5 (C²), 113.1 (C⁵), 106.2 (C⁴), 93.7 (C¹),

74.0 (C⁸), 35.8 (C⁹), 31.7 (C¹²), 29.1 (C¹¹), 25.4 (C¹⁰), 22.6 (C¹³), 19.8 (C¹⁵), 14.1 (C¹⁴). IR (neat) 1725 cm⁻¹ (C=O). MS(HRESI, *m/z*): Calcd for C₁₅H₁₉O₂I₃Na⁺ ([M+Na]⁺): 634.8417, Found: 634.8413. Density ρ = 1.8 g/cm³, refractive index n=1.628 (λ=589.3 nm).

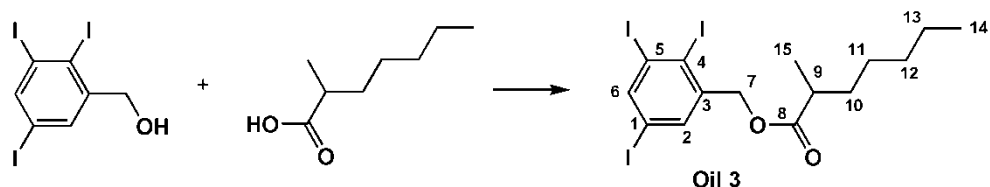


Scheme 1. Synthesis of octan-2-yl 2,3,5-triodobenzoate (**oil 1**) and 3,7-dimethyloctyl 2,3,5-triodobenzoate (**oil 2**).

2.2.2.3. 3,7-Dimethyloctyl 2,3,5-triodobenzoate (**oil 2**)

The synthesis of this compound is similar to that of octan-2-yl 2,3,5-triodobenzoate (**oil 1**) except that 2-octanol was replaced with 3,7-dimethyl-1-octanol (36.8 mL, 0.192 mol). 97.7 g of the racemic product (152 mmol, 87%) was obtained as a light yellow viscous oil. A schematic representation of the reaction can be found in Scheme 1.

¹H NMR (CDCl₃, δ/ppm): 8.29 (d, *J* = 2.0 Hz, 1H, H²), 7.70 (d, *J* = 2.0 Hz, 1H, H⁶), 4.36 (m, 2H, H⁸), 1.80 (m, 1H, H⁹), 1.63 (m, 1H, H¹⁰), 1.58 (m, 1H, H^{9'}), 1.52 (m, 1H, H¹⁴), 1.4-1.1 (m, 6H, H¹¹, H¹² and H¹³), 0.94 (d, *J* = 6.4 Hz, 3H, H¹⁵), 0.87 (d, *J* = 6.6 Hz, 6H, H¹⁶ and H¹⁷). ¹³C NMR (CDCl₃, δ/ppm): 165.4 (C⁷), 147.8 (C⁶), 141.2 (C³), 136.1 (C²), 112.5 (C⁵), 105.7 (C⁴), 92.9 (C¹), 64.1 (C⁸), 39.2 (C¹³), 37.1 (C¹¹), 35.3 (C⁹), 29.8 (C¹⁰), 28.0 (C¹⁴), 24.6 (C¹²), 22.7 (C¹⁷), 22.6 (C¹⁶), 19.5 (C¹⁵). IR (neat) 1729 cm⁻¹ (C=O). MS(HRESI, *m/z*): Calcd for C₁₇H₂₃I₃O₂Na⁺ ([M+Na]⁺): 662.8730, Found: 662.8719. Density ρ = 1.8 g/cm³, refractive index n=1.612 (λ=589.3 nm).



Scheme 2. Synthesis of 2,3,5-triodobenzyl 2-methylheptanoate (**oil 3**).

2.2.2.4. 2,3,5-Triiodobenzyl 2-methylheptanoate (**oil 3**)

N,N'-Diisopropylcarbodiimide (3.40 mL, 22.0 mmol) was added to a mixture of 2-methyl heptanoic acid (3.50 mL, 22.0 mmol), 4-N,N-dimethylaminopyridine (0.27 g, 2.2 mmol), 2,3,5-triiodobenzyl alcohol (10.7 g, 22.0 mmol) and 250 mL of DCM, stirred under nitrogen and cooled by an ice-water bath. After 2 hours the ice-water bath was removed and stirring was continued overnight at room temperature. The reaction mixture was filtered over a thin layer of silica with suction and evaporated. 12.1 g of the racemic product (19.8 mmol, 89%) was obtained as a yellow viscous oil after it had been eluted with DCM over 330 g of silica. A schematic representation of the reaction can be found in Scheme 2.

^1H NMR (CDCl_3 , δ/ppm): 8.16 (d, $J = 2.0$ Hz, 1H, H^6), 7.57 (d, $J = 2.0$ Hz, 1H, H^2), 5.07 (s, 2H, H^7), 2.56 (m, $J = 7.0$ Hz, 1H, H^9), 1.70 (m, 1H, C^{10}), 1.47 (m, 1H, C^{10}), 1.4-1.2 (m, 6H, H^{11} , H^{12} and H^{13}), 1.21 (d, $J = 7.0$ Hz, 3H, H^{15}), 0.88 (t, $J = 6.8$ Hz, 3H, H^{14}). ^{13}C NMR (CDCl_3 , δ/ppm): 175.9 (C^8), 146.3 (C^6), 143.3 (C^3), 136.3 (C^2), 112.0 (C^5), 110.9 (C^4), 94.4 (C^1), 71.7 (C^7), 39.6 (C^9), 33.8 (C^{10}), 31.7 (C^{12}), 26.9 (C^{11}), 22.6 (C^{13}), 17.2 (C^{15}), 14.1 (C^{14}). IR (neat) 1736 cm^{-1} ($\text{C}=\text{O}$). MS(HRESI, m/z): Calcd for $\text{C}_{15}\text{H}_{19}\text{O}_2\text{I}_3\text{Na}^+$ ($[\text{M}+\text{Na}]^+$): 634.8417, Found: 634.8418. Density $\rho = 1.8\text{ g/cm}^3$, refractive index $n=1.628$ ($\lambda=589.3\text{ nm}$).

2.2.2.5. Characterization

^1H and ^{13}C NMR spectra were obtained with a Bruker DPX-300 spectrometer. CDCl_3 chemical shifts are expressed in ppm downfield from tetramethylsilane (as internal standard).

High-resolution ESI (HRESI) mass spectra were recorded on an Agilent ESI-TOF mass spectrometer, measuring in the positive ion mode. FT-IR spectra were obtained on an ATI Mattson Genesis II spectrometer by Attenuated Total Reflection (ATR, SplitPea, Harrick Scientific). Log P values of the individual oils were calculated using Chemdraw v8.0 (CambridgeSoft, Cambridge, UK).

2.2.3. Preparation of iodinated stabilized nanoparticles

Emulsions were prepared from **oil 1**, **oil 2**, or **oil 3** (20% w/v) using 2 % w/w of the surfactant (1) lipids (DSPC, DSPE-PEG₂₀₀₀, cholesterol in a 61.7:5.0:33.3 molar ratio) (2) Pluronic F68 or (3) amphiphilic block PBD-PEO. In detail, 400 mg of surfactant was dissolved in 40 mL CHCl_3 (for lipids 4:1 v/v CHCl_3 :EtOH) in a round bottom flask. The solvent was slowly removed using a rotavap and a homogeneous lipid/polymeric film was formed on the glass surface. The film was hydrated with 15 mL THAM buffer (0.0252 % w/v THAM, 8.9 g/L NaCl, pH 7.4) at 70 °C for 2 hours. When polymers were used as emulsifiers, ten freeze-thaw cycles were performed in which the flask was frozen in liquid nitrogen and heated to 70 °C. Subsequently, 4.5 g iodinated oil was added and dispersed using an Ultrathurrax. The crude emulsion was homogenized for

3 minutes in a high-pressure microfluidizer (Microfluidizer M110S, Microfluidics, USA) at 1500 bar, which was preheated to 60 °C. The obtained emulsion was cooled down in an ice bath and subsequently filtered through a 0.45 µm sized sterile filter. The final emulsion contained 130 mg l/mL.

2.2.4. Determination of iodine concentration

The concentration iodine per sample was determined after Schöniger combustion using Inductively Coupled Plasma-Mass Spectrometry (ICP-MS).

2.2.5. Size distribution

The hydrodynamic radius and the fraction of particles with sizes >1.5 µm radius was measured as a function of time with dynamic light scattering (DLS) and Coulter Counter, respectively. Cryo-TEM was used to study the size and morphology of the emulsion. Before the first measurement at t=0, the emulsion was filtrated through a 450 nm filter. No further filtrations of the emulsion were performed throughout the entire experiment. In between measurements the samples were stored at room temperature.

2.2.5.1. Dynamic light scattering

The hydrodynamic radius and polydispersity of the emulsions was determined using dynamic light scattering (ALV/CGS-3 Compact Goniometer System, ALV-GmbH, Langen, Germany). Intensity correlation functions were measured at a scattering angle of $\theta=90^\circ$ using a wavelength of 632.8 nm. The diffusion coefficient (D) was obtained from cumulant fits of the intensity correlation function using ALV software. All reported hydrodynamic radii were calculated using the Stokes-Einstein equation $r_h=kT/(6\pi\eta D)$, where k is the Boltzmann constant, T is the absolute temperature and η is the solvent viscosity. Measurements were repeated 5 times and calculations were performed on the averaged correlation function of the 5 measurements.

2.2.5.2. Coulter Counter

A Beckman Coulter Counter (Multisizer 3) was used to measure the number of particles using a 50 µm aperture tube. Samples were measured 5, 30, 60, 90, 120, 150, 180, 240, 300, 360 and 420 minutes after filtration. For each measurement, 100 µL emulsion was mixed for 3 minutes with 50 mL of isotoniI (Beckman Coulter) from which 100 µL was analyzed in triplo in the diameter range of 1.1 to 30 µm. Of each sample, the background signal from pure isotoniI was substracted. The number of particles > 1.5 µm in radius in particle per million (ppm) was subsequently calculated by dividing the number of particles > 1.5 µm by the total number of particles in the emulsion mixture. The latter number was estimated from the weight of sample added to the Coulter Counter.

2.2.5.3. Cryo-Transmission Electron Microscopy

Cryogenic transmission electron microscopy (cryo-TEM) pictures were obtained with a FEI TECNAI F30ST electron microscope operated at an accelerating voltage of 300 kV in low dose mode. Samples for TEM were prepared by placing the emulsion (2 μL) on a 300-mesh carbon-coated copper grid and subsequently plunge-freezing this grid into liquid ethane using a Vitrobot.

2.2.6. Cytotoxicity assay

Human epithelial carcinoma cell line A431 (ATCC, cat. no. CRL1555) were grown in Dulbecco's Modified Eagle's Medium (DMEM) supplemented with fetal bovine serum, GlutaMax, penicillin/streptavidin and HEPES. Cells were seeded in a 96-well plate at 3500 cells/well in 180 μL medium and incubated with varying concentrations of iodinated emulsions and Fenestra VC (ART, Saint-Laurent, Canada) for 24 hours. The iodine concentrations (mg I/mL) used were similar for all contrast agents in the assay. Next, the cells were washed with PBS and 1.67 mg/mL MTT (150 μL /well) was added followed by an incubation for 2 hours at 37 °C. Medium was aspirated and formazan crystals were dissolved in DMSO (100 μL). Absorbance was recorded at 570 nm using a plate reader (GENios Pro, Tecan AG) with a reference absorbance of 690 nm, and normalized with respect to the control populations. The average value and the standard deviation for cell proliferation were calculated from data obtained with five wells for each sample.

2.2.7. *In vivo* CT imaging

Healthy Swiss mice (Charles River, aged 14-20 wks) (n=5) were used in order to evaluate the *in vivo* contrast ability of the described iodinated emulsions. The mice were placed in an induction chamber with 4% isoflurane in air to induce anesthesia and were positioned in the scanner, where they were kept under anesthesia with 1.5 – 2.5 % isoflurane. In the study, 4 mL/kg body weight of (a) a lipid based emulsion (130 mg I/mL) or (b) a block-copolymer-stabilized emulsion (130 mg I/mL) was injected *via* the tail-vein leading to an injected dose of 520 mg I/kg body weight. Helical CT scans were acquired using a dedicated small animal SPECT/CT system (nanoSPECT/CT®, Bioscan, USA; 24 minute acquisition time with 360 projections; 45 keV; 177 μA ; 2000 ms exposure time) in consecutive scans over 4 hours. In another group of mice, scans were repeated 1 week post injection. Cone-beam filtered back projection with a Shepp Logan filter and 100 μm voxels was chosen for reconstruction. CT values are expressed in Hounsfield Units (HU) and were obtained per organ by drawing volumetric regions of interest (ROIs) using InVivoScope software (Bioscan). ROI volumes varied per organ between 5 mm^3 (spleen) and 50 mm^3 (kidneys). The average HU and the standard deviation were calculated from the data with 3 ROIs per organ. All animal experiments were performed according to the U.S. National Institutes of Health

principles of laboratory animal care [21] and were approved by the ethical review committee of the Maastricht University Hospital (the Netherlands). The maintenance and care of the experimental animals was in compliance with the guidelines set by the institutional animal care committee, accredited by the National Department of Health.

2.3. Results and discussion

Three different iodinated oils were synthesized and formulated into emulsions using lipids and amphiphilic polymers as stabilizers. All emulsions were prepared and characterized with respect to their material properties, stability, cell toxicity. A selection of emulsions was tested *in vivo* as CT contrast agents.

2.3.1. Synthesis

Octan-2-yl 2,3,5-triiodobenzoate (**oil 1**), 3,7-dimethyloctyl 2,3,5-triiodobenzoate (**oil 2**), and 2,3,5-triiodobenzyl 2-methylheptanoate (**oil 3**) were synthesized and characterized by ^1H and ^{13}C NMR, high resolution ESI, FT-IR. All oils are highly viscous and amorphous at room temperature with a density of $\rho = 1.8 \text{ g/cm}^3$. The hydrophobicity differs slightly according to the calculated log P values: **oil 1**: log P = 8.74, **oil 2**: log P = 9.50, **oil 3**: log P = 8.65. Upon degradation of the oils *in vivo*, we expect to recover a small iodinated molecule identical to an approved X-ray contrast agent and a non-toxic fatty acid and higher alcohols, thereby ensuring an acceptable toxicity profile. Nine emulsions of **oil 1**, **oil 2** and **oil 3** were prepared in combination with three different emulsifiers and investigated with respect to size and stability of the emulsion particles.

2.3.2. Size characterization

The hydrodynamic radii of the 9 types of emulsion were measured directly after preparation with DLS and summarized in Table 1. In general, PBD-PEO as a stabilizer yields smaller emulsions in combination with a certain oil, followed by lipids and then Pluronic.

Table 1. Hydrodynamic radii of emulsions in nm and its polydispersity index (PDI) prepared with different surfactant and oils, measured by DLS on the same day as the preparation.

	Lipids	Pluronic	PBD-PEO
oil 1	104.6 nm (PDI 0.011)	111.0 nm (PDI 0.082)	84.0 nm (PDI 0.037)
oil 2	81.7 nm (PDI 0.017)	98.8 nm (PDI 0.075)	75.9 nm (PDI 0.022)
oil 3	97.6 nm (PDI 0.097)	112.4 nm (PDI 0.090)	101.3 nm (PDI 0.042)

A typical size distribution of the PBD-PEO **oil 1** emulsion obtained with dynamic light scattering (DLS) is presented in Figure 2A showing a monomodal size distribution with a mean hydrodynamic radius of $r_h=84 \text{ nm}$. PBD-PEO **oil 1** filled emulsion particles are characterized by Cryo-TEM (Fig. 2B). All particles have a radius $<100 \text{ nm}$, typical for all samples and have an electron dense core correlating with the high iodine payload.

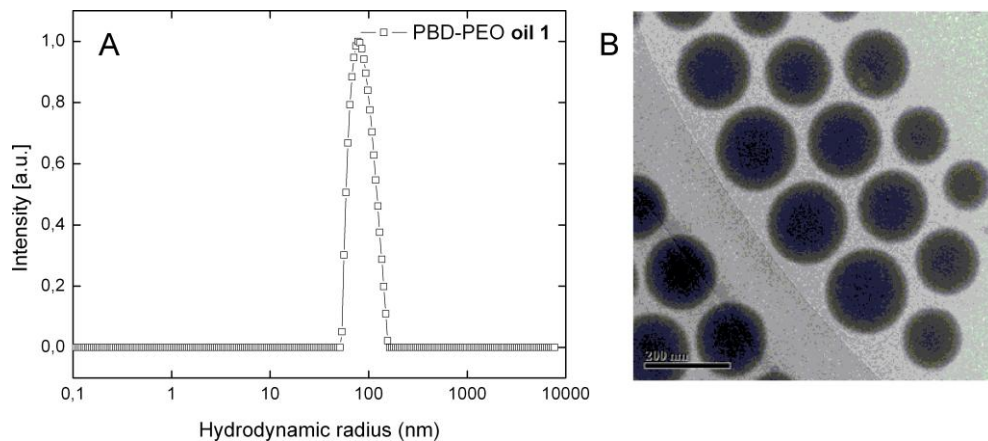


Figure 2. PBD-PEO oil 1 emulsion by (A) DLS, showing the unweighted size distribution and (B) Cryo-TEM.

The mean hydrodynamic radius of the PBD-PEO emulsions of **oil 1**, **oil 2**, and **oil 3** respectively, was measured over time with DLS (Fig. 3A). A different hydrodynamic radius with $r_h(\text{oil 2}) = 76 \text{ nm} < r_h(\text{oil 1}) = 84 \text{ nm} < r_h(\text{oil 3}) = 101 \text{ nm}$ was obtained shortly after preparation under identical processing conditions (Table 1). The hydrodynamic radius of these samples remained essentially constant over a period of at least a month (Fig. 3A).

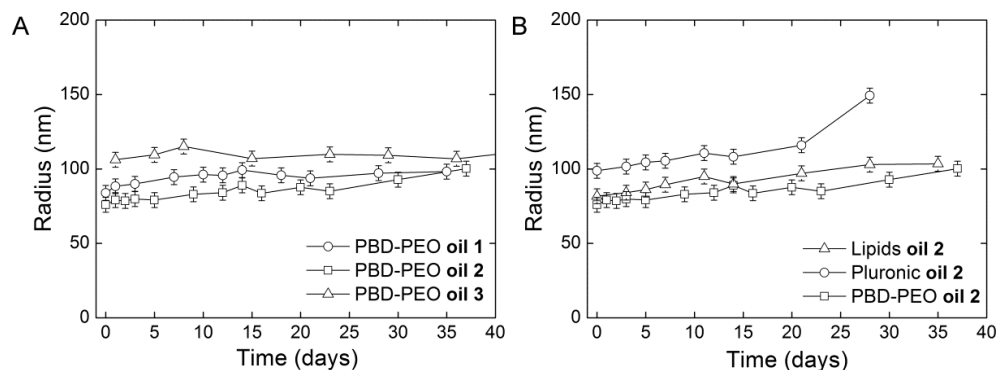


Figure 3. Size of nanoparticles measured over time by dynamic light scattering showing in (A) influence of iodinated oil in case of PBD-PEO surfactant; (B) influence of surfactant in case of **oil 2**.

The mean hydrodynamic radius of the emulsions of **oil 2**, stabilized with lipids, Pluronic or PBD-PEO are measured over time with DLS (Fig. 3B). A significant difference in radius was observed when using different surfactants i.e. for PBD-PEO: $r_h = 76 \pm 4 \text{ nm}$, for Pluronic: $r_h = 99 \pm 4 \text{ nm}$, while in case of lipids: $r_h = 82 \pm 4 \text{ nm}$. Emulsions formulated with lipids or PBD-PEO yielded a stable mean hydrodynamic radius over time, while the

mean size of emulsions stabilized with Pluronic steadily increases with time and even falls apart in two layers after day 28. Pluronic-stabilized emulsions were therefore not considered for any *in vivo* studies.

A comparison between the particles prepared with different oils and the calculated log P showed that smaller particles are obtained with the more hydrophobic **oil 2** (log P = 9.50) when compared to less hydrophobic oils (**oil 1**: log P = 8.74; **oil 3**: log P = 8.65). A similar relation between the log P of iodinated oil and the nanoparticle size can be observed for lipid-stabilized and Pluronic-stabilized emulsion droplets (Table 1). The hydrophobicity of the iodinated oil seems therefore of eminent importance to obtain smaller and therefore longer circulating emulsion particles.

The difference in radius observed for the three different emulsifiers when using the same oils can be explained by their different geometrical constraints imposed by the size ratio of the hydrophilic to hydrophobic part. For an amphiphilic molecule the ratio of the molecular weight of the hydrophilic part over the total molecular weight (f_{eo}), can be used to describe this geometrical constraint. For the PBD-PEO the total molecular weight of the hydrophilic part of the ethylene oxide is larger than the hydrophobic block ($f_{eo}=0.61$; $M_{w,phil}=2033$ g/mol; $M_{w,phob}=1305$ g/mol) inducing a higher surface curvature in the particles. The PEO part likely extends into the solution as surface grafted brush. Regular lipids self-assemble in more planar bilayers as the hydrophilic head group is smaller than the hydrophobic part ($f_{eo}=0.39$; $M_{w,phil}=312$ g/mol; $M_{w,phob}=478$ g/mol). The formulation used here contains 5% pegylated lipids ($f_{eo}\sim 0.8$), where the PEG molecules take a mushroom type configuration at the surface but do not induce higher curvature. It is more difficult to apply similar considerations to the triblock polymer Pluronic ($f_{eo}=0.8$, $M_{w,PEO}=3360$ g/mol; $M_{w,PPO}=1680$ g/mol; $M_{w,PEO}=3360$ g/mol). We suspect that the triblock is less efficient to stabilize more strongly curved surfaces leading to the largest particles compared to PBD-PEO and lipid stabilizers. Overall, this work shows that the hydrodynamic radius can be tuned with the chemical nature of the emulsifier and hydrophobic oil.

2.3.3. Cell viability

Acute cell toxicity of all emulsions was tested using a MTT assay and compared to the commercially available preclinical CT contrast agent Fenestra VC as a benchmark. The cell viability results obtained with **oil 2** in combination with lipids, Pluronic and PBD-PEO as emulsifiers in comparison to Fenestra VC is shown in Figure 4. No significant differences in cell viability were found between the different emulsions with formulations based on **oil 1-3** in combination with the different types of surfactant, in the case of **oil 2** formulations varying from a cell viability of 80 % at relative low concentrations (0.05 mg l/mL) to a cell viability of 40 % at high concentrations (5.0 mg l/mL). In all MTT assays after the 24 hour incubation, a thin white layer of emulsion particles was formed on top of the cells for all types of contrast agent due to the high density of the iodinated oils ($\rho = 1.8 \text{ g/cm}^3$). The MTT assay was repeated several times under different conditions (4 hour incubation time, shaking during incubation), all leading to similar results. It is likely that the observed increase in cell toxicity with increasing concentration was related to the fact that all emulsions sedimented to some extent on the cells, which may have lead to suffocation or a lack of medium available to the cells. Nevertheless, Fenestra VC led to significant lower cell viability already at concentrations of 0.5 mg l/mL indicating that the presented emulsions in this paper have a significantly lower impact on cell viability.

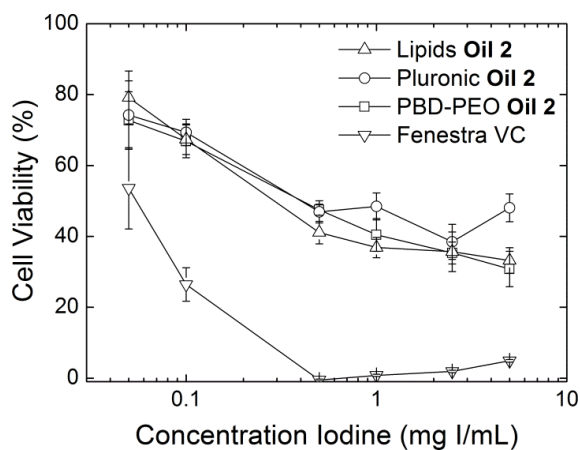


Figure 4. Cellular toxicity study; cell viability (human epithelial carcinoma cell line A431) as a function of iodine concentration, as determined by MTT.

2.3.4. *In vivo* CT imaging

The best candidate for the *in vivo* studies were the lipid-stabilized and PBD-PEO-stabilized emulsions of **oil 1** and **oil 2**, due to their prolonged stability compared to Pluronic and the generally smaller size of the obtained particles (see section 2.3.2.). *In vivo* contrast enhancement on CT scans was therefore investigated by bolus injection of freshly prepared emulsions Lipid **oil 1**, PBD-PEO **oil 1** and PBD-PEO **oil 2**, having sizes of $r_h=103$ nm (PDI 0.146), $r_h=96$ nm (PDI 0.0617) and $r_h=78$ nm (PDI 0.02), respectively.

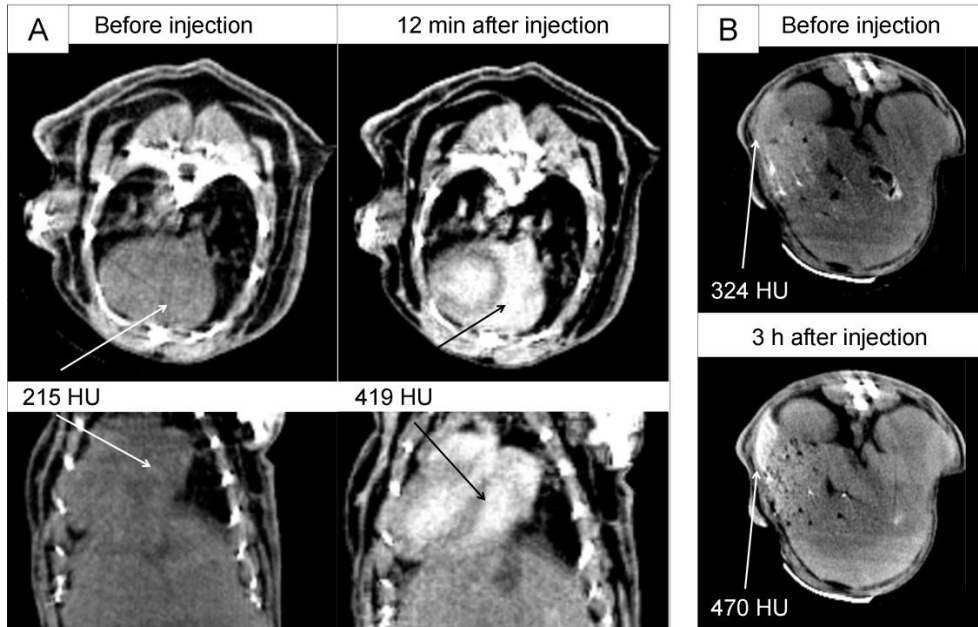


Figure 5. CT images and opacification (in HU) after iv injection of PBD-PEO **oil 2**; A) in the heart 12 min post-injection, transversal (top row) and coronal (bottom row) B) 3 hours post-injection in the spleen.

The injected dose was 520 mg l/kg in all cases. Contrast change (Δ HU) of different organs, i.e. blood, liver, spleen, kidney and urine, was measured on consecutive CT scans over a period of 3 hours after intravenous injection. As a representative example, the transversal and coronal slices of a CT scan acquired before and 12 min after injection of PBD-PEO **oil 2** are shown in Figure 5A.

The highest contrast change was observed for PBD-PEO **oil 2** in blood reaching on average Δ HU=190 directly after injection (Fig. 6A). The decrease of contrast in blood for Lipids **oil 1** and PBD-PEO **oil 1** was more rapid compared to PBD-PEO **oil 2**. Spleen and liver showed significant increases in contrast for the three types of particles (Fig. 6B and 6C) while no contrast change was observed in kidneys and bladder (Fig. 6D).

PBD-PEO **oil 2** emulsions exhibited a higher uptake in the spleen compared to the liver (Fig. 6C), while spleen and liver uptake was comparable for Lipid **oil 1** and PBD-PEO **oil 1**. One week post-injection CT contrast had dropped to control levels in all organs indicating that all emulsion particles had been fully metabolized or excreted within 1 week. Pathology studies gave no indications for histological abnormalities in the heart, lung, liver and spleen as compared to mice without injection of contrast agent. For all organs, the iodine concentration was calculated from the change in HU (Fig. 7) and is given in Fig. 6 in mg I/mL as well as in % injected dose iodine per gram.

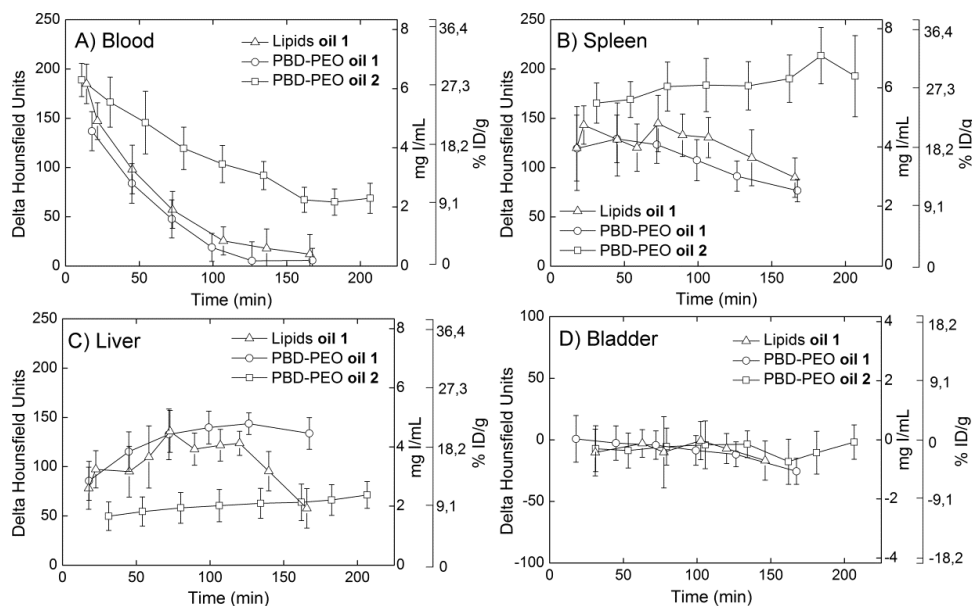


Figure 6. Increase in HU after injection of Lipid **oil 1**, PBD-PEO **oil 1**, PBD-PEO **oil 2** nanoparticles measured in A) Blood, B) Spleen, C) Liver, D) Bladder.

Blood circulation time can be described with a first order exponential time dependence with half-lives of Lipid **oil 1**: $t_{1/2}=0.9\pm 0.1$ h, PBD-PEO **oil 1**: $t_{1/2}=0.7\pm 0.1$ h and PBD-PEO **oil 2**: $t_{1/2}=2.7\pm 0.1$ h. Extrapolating the data to time of injection ($t=0$) using the exponential fit resulted consistently in a maximal contrast change in the blood compartment of $\Delta HU(t=0) = 220$ for all three emulsions corresponding to an iodine concentration of 7.3 mg I/mL. With an injected dose of 520 mg I/kg, this corresponds to a free volume of distribution of $v=71$ mL/kg (7% of total body weight) equaling the blood volume of 71 mL/kg in Swiss mice [22]. The fast uptake within the spleen and liver of all particles and the absence of any contrast change in the urine (Fig. 6D) indicates an excretion *via* the hepatobiliary pathway without any renal excretion. The decrease of HU in blood was in good quantitative correspondence with the uptake in liver and spleen.

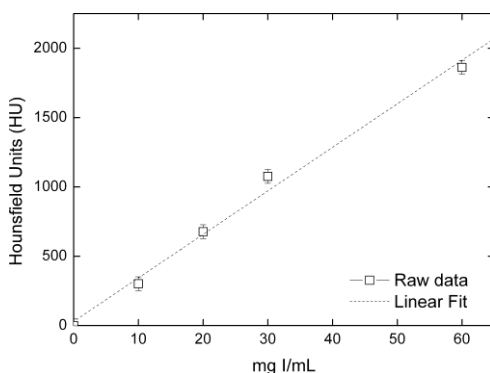


Figure 7. Calibration curve of the CT scanner showing the increase in HU as a function of the iodine concentration. A linear fit through the data points resulted in a slope of 31 ± 2 HU/(mg I/mL).

The differences in blood circulation time, and liver and spleen uptake between the three different formulations can be explained by the size difference between the emulsion particles. The opsonization process that mediates macrophage recognition and subsequent blood elimination is known to occur at a higher rate with an increased surface area of particles having a similar surface coating. We propose that this effect explains the longer blood half-life of PBD-PEO **oil 2** ($r_h=78$ nm) compared to the bigger particles of PBD-PEO **oil 1** ($r_h=96$ nm) and lipid **oil 1** ($r_h=103$ nm). A higher uptake in the spleen compared to liver for small particles was observed earlier for liposomes [23]. We therefore suggest that the differences in biodistribution observed in our study with respect to liver and spleen uptake were mainly caused by the different sizes and not by the nature of the surface coatings or the oils. Although the uptake (i.e. %ID Iodine/g) of PBD-PEO **oil 2** in the spleen was twice as high after 3 hours compared to the other two emulsions, it should be taken into account that the spleen is a relatively small organ (typically around 131 ± 38 mg for an 18 week old male mouse) as compared to the liver (1833 ± 252 mg) [24]. This probably explains why the total clearance *via* the hepatobiliary pathway is slower for the PBD-PEO **oil 2** particles (uptake in liver and spleen ~ 4.1 mg I after 2 h) compared to the lipid **oil 1** (~ 8.5 mg I after 2 h) and PBD-PEO **oil 1** particles (~ 9.3 mg I after 2 h). *In vivo* studies with **oil 1** emulsions stabilized with lipids led to sudden loss of animals in the first 3 hours post injection. For that reason, only one mouse was scanned for the full time period. As no signs of acute toxicity were observed, the most probable cause of death is an acute lung embolism caused by large aggregates that may have been formed *in vivo*.

As shown in Figure 3, neither large particles, nor any instability was observed in lipid-stabilized emulsions using DLS. As small number of large particle (approx.: $r_h > 2\lambda$; $\lambda=632.8$ nm) is difficult to detect within a large number of small particles using DLS, the

fraction of particles with a radius $r_h > 1.5 \mu\text{m}$ was determined using a Coulter Counter [25].

Emulsions of **oil 2** with lipids, or PBD-PEO as emulsifier were prepared, filtered through a 450 nm filter. Subsequently, the fraction of particles with radii in the range 1.5 - 15 μm was measured with a Coulter Counter as a function time. The number of particles with a radius $> 1.5 \mu\text{m}$ within the three different emulsions is shown in Figure 8A. Emulsion particles prepared with PBD-PEO as a surfactant did not contain a detectable fraction of particles with a radius $> 1.5 \mu\text{m}$ and also showed no formation of larger particles over time while emulsion prepared with lipids as a surfactant did exhibit an increasing number of large particles over time. The presence and formation of a low fraction of large particles obvious escaped detection by DLS. For comparison, Fig. 8B shows DLS data of a lipid-stabilized emulsion (same sample as used for Coulter Counter measurement) 3 days after filtration. One single peak was observed at $r_h=84 \text{ nm}$ and no aggregates were visible at larger sizes. Coulter Counter measurements demonstrated that lipid-based emulsion particles had a lower kinetic stability compared to the polymeric emulsion particles and tended to form larger particles, probably by coalescence [26,27]. It is likely that this process of increased number of particles over time depends on the interplay between the hydrophobicity of the interior oil and the nature of the surfactant [28,29]. The low kinetic stability of lipid-stabilized emulsions may become even more pronounced under *in vivo* conditions. Coulter Counter measurements are therefore a useful *in vitro* characterization method complementing DLS to check the kinetic stability of emulsions before performing *in vivo* tests. The emulsions stabilized with the amphiphilic polymeric diblock PBD-PEO showed high *in vitro* stability without any aggregate formations. The *in vivo* studies with these emulsions were performed without any loss of animals.

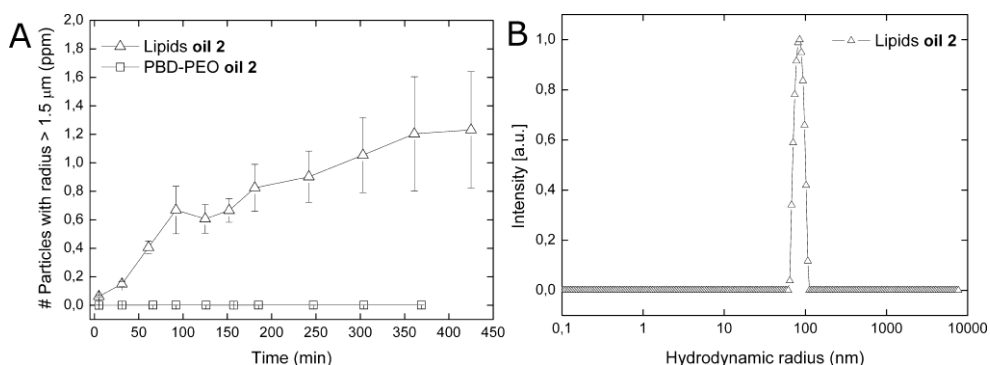


Figure 8. A) Effect of surfactant on the number of particles $> 1.5 \mu\text{m}$ as measured by Coulter Counter over a period of 7 hours. B) DLS measurement of nanoparticles prepared with lipids and **oil 2**, 3 days after filtration (unweighted data analysis, no additional baseline fit to the correlation function).

2.4. Conclusions

This work describes the synthesis, formulation and characterization of new radiopaque iodine-based emulsions as CT contrast agents. Three hydrophobic iodinated oils were formulated into emulsions using three different types of surfactants, namely lipids, Pluronic and PBD-PEO. *In vitro* stability studies showed that the exact nature of the iodine oil and, more importantly, the surfactant strongly affect the nanoparticle size as well as its stability. Coulter Counter appeared to be an essential tool to detect low numbers of large particles in the emulsion that remained undetectable with DLS measurements. The PBD-PEO **oil 2** emulsion produced excellent *in vivo* contrast enhancement and a prolonged circulation time without any signs of acute toxicity. As no contrast enhancement was visible in any organs one week after injection, the iodinated emulsions seemed to be excreted via the hepatobiliary pathway. The high iodine payload per mL allowed injecting small volume into mice while still generating sufficient CT contrast for clear organ delineation. Emulsions of the iodinated **oil 2** stabilized with PBD-PEO are therefore an excellent candidate as a long circulating contrast agent for CT imaging.

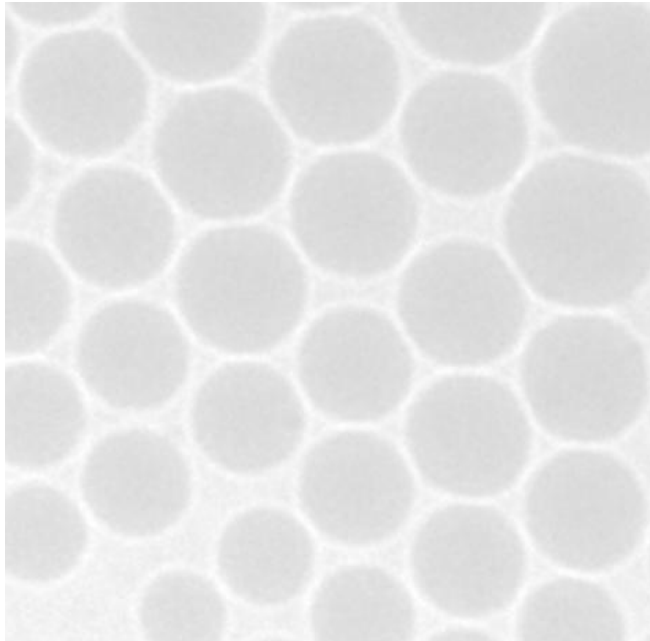
Acknowledgements

The authors acknowledge Susana Gonzales (Philips intern) and Wolter ten Hoeve (Syncom b.v.) for assistance with the organic synthesis. Furthermore we would like to thank Carlijn van Helvert, University Hospital Maastricht for performing the tail-vein injections and her animal handling expertise. The authors thank Sander Langereis (Philips) for helpful discussions and critically reviewing.

2.5. References

- [1] Kalender WA, Polacin A. Physical performance characteristics of spiral CT scanning. *Med Phys* 1991;18(5):910-915.
- [2] Kalender WA. X-ray computed tomography. *Phys Med Biol* 2006;51(13):R29-43.
- [3] Mattrey RF. Blood-pool contrast media are the ideal agents for computed tomography. *Invest Radiol* 1991;26 Suppl 1:S55-56; discussion S60-54.
- [4] Vera DR, Mattrey RF. A molecular CT blood pool contrast agent. *Acad Radiol* 2002;9(7):784-792.
- [5] Dawson P, Cosgrove DO, Grainger RG. X-ray contrast agents. In: *Textbook of contrast media*. Oxford: Isis medical Media Ltd 1999:61-71.
- [6] Mattrey RF, Aguirre DA. Advances in contrast media research. *Acad Radiol* 2003;10(12):1450-60.
- [7] Choi HS, Lui W, Misra O, Tanaka E, Zimmer JP, Ipe IB, Bawendi MG, Frangioni JV. Renal clearance of quantum dots. *Nature Biotechnology* 2007;25(10):1165-1170.
- [8] Rabin O, Manuel Perez J, Grimm J, Wojtkiewicz G, Weissleder R. An X-ray CT imaging agent based on long-circulating bismuth sulphide nanoparticles. *Nat Mater* 2006;5(2):118-122.
- [9] Cai QY, Kim SH, Choi KS, Kim SY, Byun SJ, Kim KW, Park SH, Juhng SK, Yoon KH. Colloidal gold nanoparticles as a blood-pool contrast agent for X-ray computed tomography in mice. *Invest Radiol* 2007;42(12):797-806.
- [10] Bar-Ilan O, Albrecht RM, Fako VE, Furgeson DY. Toxicity assessments of multisized gold and silver nanoparticles in zebrafish embryos. *Small* 2009;5(16):1897-1910.
- [11] Chen YS, Hung YC, Liao I, Huang GS. Assessment of the In Vivo Toxicity of Gold Nanoparticles. *Nanoscale Res Lett* 2009;4(8):858-864.
- [12] Cho WS, Cho M, Jeong J, Choi M, Cho HY, Han BS, Kim SH, Kim HO, Lim YT, Chung BH, Jeong J. Acute toxicity and pharmacokinetics of 13 nm-sized PEG-coated gold nanoparticles. *Toxicol Appl Pharmacol* 2009;236(1):16-24.
- [13] Galperin A, Margel D, Baniel J, Dank G, Biton H, Margel S. Radiopaque iodinated polymeric nanoparticles for X-ray imaging applications. *Biomaterials* 2007;28(30):4461-4468.
- [14] Galperin A, Margel S. Synthesis and characterization of radiopaque magnetic core-shell nanoparticles for X-ray imaging applications. *J Biomed Mater Res B Appl Biomater* 2007;83(2):490-8.
- [15] Aviv H, Bartling S, Kiesling F, Margel S. Radiopaque iodinated copolymeric nanoparticles for X-ray imaging applications. *Biomaterials* 2009.
- [16] Hyafil F, Cornily JC, Feig JE, Gordon R, Vucic E, Amirbekian V, Fisher EA, Fuster V, Feldman LJ, Fayad ZA. Noninvasive detection of macrophages using a nanoparticulate contrast agent for computed tomography. *Nat Med* 2007;13(5):636-641.
- [17] Torchilin VP, Frank-Kamenetsky MD, Wolf GL. CT visualization of blood pool in rats by using long-circulating, iodine-containing micelles. *Acad Radiol* 1999;6(1):61-65.
- [18] Torchilin VP. Polymeric contrast agents for medical imaging. *Curr Pharm Biotechnol* 2000;1(2):183-215.
- [19] Weichert JP, Lee FT, Jr., Longino MA, Chosy SG, Counsell RE. Lipid-based blood-pool CT imaging of the liver. *Acad Radiol* 1998;5 Suppl 1:S16-19; discussion S28-30.
- [20] Parnaud G, Tache S, Peiffer G, Corpet DE. Pluronic F68 block polymer, a very potent suppressor of carcinogenesis in the colon of rats and mice. *Br J Cancer* 2001;84(1):90-93.
- [21] *Guide for the care and use of laboratory animals*. Washington, DC; Government Printing, Office 1985. NIH Publication:86-23.
- [22] Sluiter W, Oomens LW, Brand A, Van Furth R. Determination of blood volume in the mouse with 51chromium-labelled erythrocytes. *J Immunol Methods* 1984;73(1):221-225.
- [23] Drummond DC, Meyer O, Hong K, Kirpotin DB, Papahadjopoulos D. Optimizing liposomes for delivery of chemotherapeutic agents to solid tumors. *Pharmacol Rev* 1999;51(4):691-743.
- [24] Iwaki T, Yamashita H, Hayakawa T. A color atlas of sectional anatomy of the mouse. Japan: Adthree Publishing Co, Ltd 2001:Appendix p. 160-161.
- [25] Han J, Davis SS, Washington C. Physical properties and stability of two emulsion formulations of propofol. *Int J Pharm* 2001;215(1-2):207-220.
- [26] Fredrick E, Walstra P, Dewettinck K. Factors governing partial coalescence in oil-in-water emulsions. *Adv Colloid Interface Sci* 2009;153(1-2):30-42.
- [27] Malcolm AS, Dexter AF, Katakdhond JA, Karakashev SI, Nguyen AV, Middelberg AP. Tuneable control of interfacial rheology and emulsion coalescence. *Chem Phys Chem* 2009;10(5):778-781.
- [28] Georgieva D, Schmitt V, Leal-Calderon F, Langevin D. On the possible role of surface elasticity in emulsion stability. *Langmuir* 2009;25(10):5565-5573.
- [29] Urbina-Villalba G. An algorithm for emulsion stability simulations: account of flocculation, coalescence, surfactant adsorption and the process of oswald ripening. *Int J Mol Sci* 2009;10(3):761-804.

Alternating biodistribution of blood pool CT contrast agents by a co-injection of rapid RES-uptake material



Based on

Alternating biodistribution of blood pool CT contrast agents by a co-injection of rapid RES-uptake material

A. d. Vries, E. Custers, J. Lub, K. Nicolay and H. Grull

Submitted

Abstract

Nanoparticle-based approaches to design blood pool contrast agents for CT have been extensively investigated. Recently, iodinated emulsion-based CT contrast agents were prepared that remain in the blood pool for several hours and are excreted *via* the hepatobiliary pathway. If the RES mediated liver uptake of the nanoparticles could be slowed down, one could possibly obtain even further extended blood circulation times. Here, we investigate if the biodistribution and clearance of the iodinated emulsion can be shifted towards a longer circulation time in blood by a co-injection of either liposomes or soy bean oil emulsion. Blood circulation time and organ distribution of the nanoparticles were studied by CT, SPECT and dual-isotope γ -counting. No effect was found in case of co-injection with liposomes but a co-injection with soy bean oil emulsion resulted in a significant decrease in splenic uptake of the iodinated emulsion, though this effect did not lead to a significant increase in the iodine concentration in liver or blood circulation time. We conclude that subtle changes in the nanoparticle nature lead to an individual and characteristic opsonization process associated with a particular organ uptake, leaving the fate of other nanoparticles present largely unchanged.

3.1. Introduction

Computed tomography (CT) is one of the most frequently used imaging modalities in the clinic for diagnosis of a large variety of diseases. For medical research performed in small animals, CT is also frequently used either to obtain a morphology reference picture in multimodal imaging applications like SPECT/CT or PET/CT, and also as a “stand alone” imaging modality. The small feature size in rodents required the development of dedicated micro CT scanners that allow CT imaging with high resolution [1-3]. Like in the clinic, for many preclinical applications radiopaque CT contrast agents are used to enhance the soft tissue contrast [4-6].

Current clinical available CT contrast agents have a low molecular weight (<2000 Da) resulting in a rapid renal excretion and fast extravasation [7]. Applied in preclinical research, the fast metabolism and high heart rates of small animals complicates the use of these contrast agents since the contrast enhancement in blood is typically lost within minutes, which does not match the relatively long scanning times of many micro CT systems (5-90 minutes, depending on size and resolution).

Furthermore, the high volume of distribution and thus rapid extravasation complicates the visualization of the vascular system and delineation of blood vessels embedded in surrounding soft tissue. The need for alternatives stimulated research on long-circulating blood pool CT contrast agents. Most approaches make use of nanoparticles and constructs having sizes larger than 5 nm, which prohibits extravasation as well as renal excretion. Examples comprise iodinated liposomes [8,9], micelles [10,11], polymeric nanoparticles [12-14], as well as gold nanoparticles [15-17], solid bismuth or tantalum oxide particles [18,19]. Using agents of a size that prohibits renal excretion leads automatically to a removal from the blood stream via the reticuloendothelial system (RES) with spleen and liver as the main uptake organs. Depending on the exact nature of the agent and eventual metabolism or hepatobiliary excretion, the retention time in these target organs strongly varies. Uptake by the RES system can be slowed down by an appropriate particle surface design, which prevents recognition by opsonizing proteins (e.g. apolipoprotein-E) and therefore leads to longer circulation time. Surface coatings of polyethyleneglycol (PEG) perform particularly well in preventing adsorption of opsonins, which was exploited for the development of “stealth liposomes” [20-22].

We recently applied a similar approach in the design of iodinated emulsions that were fully coated with a pegylated polymer brush. This CT contrast agent showed a circulation time of 2.7 hours with clearance *via* liver and spleen [23]. Iodine concentrations in the liver stabilized during the first 4 hours due to a balance between

uptake and hepatobiliary excretion. With liver being the main clearing organ, an even higher administered dose of CT agent would only be feasible if the RES mediated liver uptake could be slowed down, i.e. leading to an extended blood circulation time, while ongoing hepatobiliary excretion keeps the liver concentration limited to non-toxic levels. Here, we investigate if the RES mediated clearance of our iodinated-emulsion can be slowed down by co-injecting non-toxic nanoparticles such as polymer-stabilized soybean emulsions and liposomes. The rationale of the approach is based on several earlier reports that the circulation lifetime of liposomes increases with increasing dose [24-26]. Though not fully understood, the underlying mechanism of dose dependency is probably a result of a saturation of phagocytic capacity of RES macrophages or of a saturation of opsonising proteins (e.g. complement C3 fragment or β_2 -glycoprotein) [27-29]. However, for pegylated liposomes also contradictory findings were reported, showing that the circulation time is independent of the injected dose [22]. In general, liposomal circulation time and biodistribution has been reported to be influenced additionally by its composition and melting transition of the lipid bilayer (T_m) [30,31], size [32-34] and charge [35-37]. For particles having a 100% pegylated surface like polymersomes or polymeric emulsions stabilized with a PEG diblock polymer, no experimental studies were performed so far.

In this study, we investigate the biodistribution of a polymeric stabilized iodinated CT contrast agent upon co-injection of either physiological salt (control), DPPC-based liposomes, or soy bean oil emulsion in mice, using CT and SPECT imaging as well as dual-isotope γ -counting. The addressed research question is how co-injection of rapidly cleared DPPC liposomes or slower clearing soy bean emulsions affects biodistribution and blood half-life of the iodine containing CT contrast agent. Furthermore, the radiolabeling of polymeric soybean and iodinated emulsions is described, which required the synthesis of a DOTA-chelate functionalized poly(ethylene-glycol)-poly(butadiene) diblock (PBD-PEO-DOTA).

3.2. Materials and Methods

3.2.1. Materials

All solvents were obtained from Merck. 1,2-Dipalmitoyl-*sn*-glycero-3-phosphocholine (DPPC) and cholesterol were obtained from Avanti Polar Lipids (Alabaster, AL, USA). 1,2-distearoyl-*sn*-glycero-3-phosphoethanolamine-tetraazacyclododecane tetraacetic acid (DOTA-DSPE) was provided by SyMO-Chem (Eindhoven, The Netherlands). Poly(butadiene(1,2 addition)-*b*-ethylene oxide) (P-5842; $M_{w,PEO}=1800$ g/mol; $M_{w,PBD}=1220$ g/mol) (PBD-PEO) was purchased from Polymersource Inc. (Montreal, Canada) and was synthetically modified to form DOTA-functionalized PBD-PEO. Soy bean oil was purchased from Lipoid (Germany). $^{111}\text{Indium}$ and $^{177}\text{Lutetium}$ were obtained from Perkin Elmer (Boston, MA, USA). All other chemicals were obtained from Sigma-Aldrich (St. Louis, MO, USA) and were of analytical grade or the best grade available.

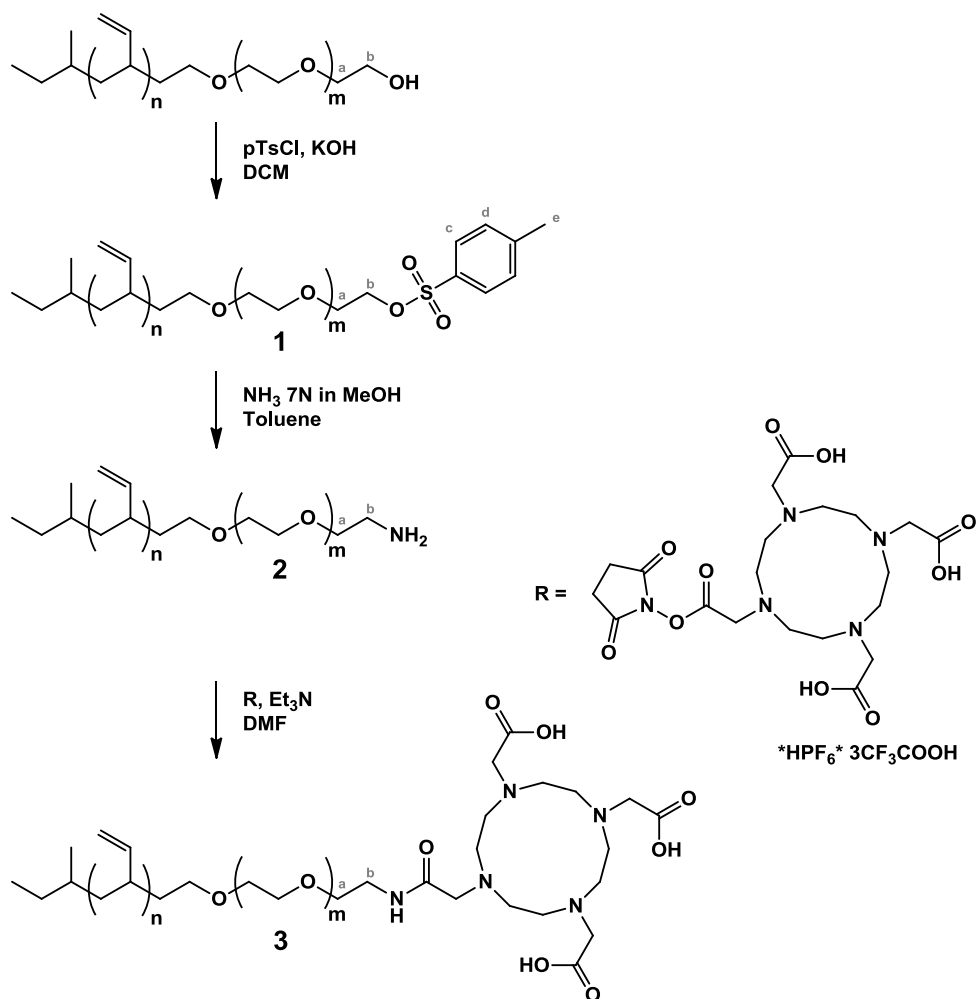
3.2.2. Synthesis of PBD-PEO-DOTA

The polybutadiene part of PBD-PEO consists for 88% of repeating units derived from 1,2-butadiene and the remain from 1,4-butadiene derived units. For reasons of simplicity the polymers are drawn as consisting of repeating units derived from 1,2-butadiene only .

A schematic representation of the synthesis of PBD-PEO-DOTA is shown in scheme 1. During the modification, changes in chemical shift of the signals belonging to H^a , H^b , C^a and C^b are observed. The other signals of PBD-PEO are not informative of the reaction and therefore not described.

3.2.2.1. PBD-PEO tosylate (**1**)

To a solution of PBD-PEO (3.37 gram, 0.89 mmol) in 15 mL of dichloromethane stirred in an ice-water bath under nitrogen 4-toluenesulfonyl chloride (342 mg, 1.79 mmol) was added. After stirring for 30 min at 0 °C, KOH (440 mg, 7.84 mmol) was added. The mixture was stirred overnight under nitrogen while the temperature slowly rose to room temperature. It was extracted subsequently with water (2x) and brine (2x). After drying over MgSO_4 , the solvent was evaporated *in vacuo* and the product PBD-PEO tosylate (**1**) was obtained (3.20 gram, 0.81 mmol, 91%) as a solid. ^1H NMR (CDCl_3 , δ/ppm): 7.81(d, H^c , 2H), 7.34 (d, H^d , 2H), 4.15 (m, H^b , 2H), 2.45 (s, H^e , 3H). ^{13}C DEPT NMR (CDCl_3 , δ/ppm): 129.8 (C^c), 128.0 (C^d), 69.2 (C^a), 68.7 (C^b), 21.6 (C^e).



Scheme 1. Synthesis of PBD-PEO-DOTA from PBD-PEO.

3.2.2.2. PBD-PEO-NH₂ (**2**)

PBD-PEO tosylate (**1**) (3.20 gram, 0.81 mmol) dissolved in 12 mL toluene was divided into three ace pressure tubes (15 mL size) and ammonia in methanol (total 12 mL of 7N NH₃ in MeOH, 84 mmol) was added. Closed tubes were heated at 50 °C for 63 hrs and after cooling down to room temperature the solvent was evaporated *in vacuo*. The residue was dissolved in DCM and was extracted subsequently with water (2x), brine(2x) and with a 10% NaHCO₃ solution. After drying over MgSO₄, the solvent was evaporated and the product pBd-PEO-NH₂ (**2**) was obtained (1.19 gram, 0.31 mmol,

38%). ^1H NMR (CDCl_3 , δ/ppm): 2.95-3.04 (H^b , 2H). ^{13}C DEPT NMR (CDCl_3 , δ/ppm): , 41.3 (C^b) .

3.2.2.3. PBD-PEO-DOTA (**3**)

PBD-PEO-NH₂ (**2**) (1.19 gram, 0.31 mmol) was dissolved in 12 mL dimethyl formamide, DOTA-mono-NHS ester (347 mg, 0.35 mmol) and triethylamine (0.9 mL, 6.47 mmol) were added. The mixture was stirred for 26 hrs at room temperature under nitrogen. The solvent was evaporated *in vacuo* and the product PBD-PEO-DOTA (**3**) was obtained (1.36 gram, 0.30 mmol, 97%). A broad signal from 1.5-4.5 ppm was observed from the H-signals of the DOTA-moiety. ^{13}C DEPT NMR (CDCl_3 , δ/ppm): The ^{13}C signals of the DOTA-moiety could not be observed due to broadening of the peaks.

3.2.3. Liposome preparation

200 nm-diameter liposomes containing DPPC, DOTA-DSPE and cholesterol at a molar ratio of 0.66/0.01/0.33 were produced by lipid film hydration and extrusion (240 μmol in total). In short, the lipids were dissolved in a 1:4 *v/v* methanol:chloroform mixture. A lipid film was formed by removing the organic solvents *in vacuo*. The lipid film was hydrated at 60 °C using 5.0 mL THAM buffer (0.0252 % *w/v* THAM, 8.9 g/L NaCl, pH 7.4). The lipid suspension was extruded at 60 °C, twice through a 400 nm polycarbonate membrane (Whatman, Kent, UK) and 5 times through a 200 nm polycarbonate membrane. Chelex (1.5 g in 5 mL of liposome solution) was added to remove residual free metals. After stirring for 72 hours at room temperature, the solution was filtrated over a sterile 0.45 μm filter.

3.2.4. Emulsion preparation

Iodinated emulsions were prepared according to a literature procedure of de Vries *et al.* [23]. The surfactant consisted of 1 mol% DOTA-functionalized PBD-PEO (**3**) (P-5842) and 99 mol% of PBD-PEO (P-5842). 3,7-Dimethyloctyl 2,3,5-triiodobenzoate (density $\rho = 1.8 \text{ g/cm}^3$) was used as the hydrophobic iodine oil and soy bean oil (density $\rho = 0.92 \text{ g/cm}^3$) was used for the preparation of the soy bean oil emulsion. Chelex (1.5 g in 5 mL of emulsion solution) was added to remove residual free metals. After stirring for 72 hours at room temperature, the solution was filtrated over a sterile 0.45 μm filter.

3.2.5. Characterization

Lipid concentration was measured by phosphate determination according to Rouser *et al.* [38]. The hydrodynamic radius and polydispersity of the nanoparticles was determined using dynamic light scattering (ALV/CGS-3 Compact Goniometer System, ALV-GmbH, Langen, Germany). Intensity correlation functions were measured at a scattering angle of $\theta=90^\circ$ using a wavelength of 632.8 nm. The diffusion coefficient (D) was obtained from cumulant fits of the intensity correlation function using ALV software. All reported hydrodynamic radii were calculated using the Stokes-Einstein equation

$r_h = kT / (6\pi\eta D)$, where k is the Boltzmann constant, T is the absolute temperature and η is the solvent viscosity. Measurements were repeated 5 times and calculations were performed on the averaged correlation function of the 5 measurements. Cryogenic transmission electron microscopy (cryo-TEM) pictures were obtained with a FEI TECNAI F30ST electron microscope operated at an accelerating voltage of 300 kV in low dose mode. Samples for cryo-TEM were prepared by placing the nanoparticle solution (4 μ L) on a 300-mesh carbon-coated copper grid and subsequently plunge-freezing this grid into liquid ethane using a Vitrobot.

3.2.6. Radiolabeling

The DOTA-functionalized iodine emulsion was radiolabeled with 111 indium (^{111}In). In detail, 300 μ L ammonium acetate buffer (2M NH_4OAc , pH 4.5) was added to 3.0 mL emulsion together with 10 μ L of ^{111}In (75 MBq) and the pH was adjusted to 5.0. The samples were stirred at 50 $^\circ\text{C}$ for 60 min (500 rpm). Liposomes were labeled with 177 lutetium (^{177}Lu). More specifically, a 1.5 mL liposomal solution was mixed with 150 μ L ammonium acetate buffer and 0.5 μ L of ^{177}Lu (22 MBq) and the pH was adjusted to 6.0. The mixture was stirred at 40 $^\circ\text{C}$ for 180 min. The soy bean oil emulsion was labeled with ^{177}Lu . A 2.0 mL soy bean emulsion solution was mixed with 200 μ L ammonium acetate buffer and 1.0 μ L of ^{177}Lu (35 MBq) and the pH was adjusted to 6.0. The mixture was stirred at 50 $^\circ\text{C}$ for 300 min.

Free DTPA (10 μ L/500 μ L nanoparticle solution, 10 mM) was added to the reaction mixtures for 15 min to scavenge free radionuclides. The radiochemical purities were checked on silica TLC using 200 mM EDTA as mobile phase and analyzed using a Phosphor Imager (FLA-7000, Fujifilm, Tokyo, Japan) and were typically 80-100 %. Samples were purified using a Zeba spin desalting column (column size 5 mL, 7 kDa MWCO) (GE Healthcare). After purification, the radiochemical purities were > 95% for all samples. ^{111}In and ^{177}Lu content was measured using a γ -counting wizard (Wizard 1480 3" Wallac counter, Perkin Elmer, Groningen, The Netherlands). After radioactive decay of the isotopes, the samples were analyzed using ICP-MS to determine the iodine and phosphorous concentrations.

3.2.7. Preparation of Mixtures for co-injection experiments

Mixtures were prepared in a 1:1 v/v ratio right before *i.v.* injection to prevent the polymeric monolayer of the iodine containing oil to have any interaction and possible exchange with the lipids of DPPC liposomes or polymeric layer of the SB oil emulsion. Iodine concentrations of the mixtures were confirmed using ICP-MS after radioactive decay of ^{111}In and ^{177}Lu .

3.2.8. Imaging and biodistribution

Healthy Swiss mice (Charles River, aged 12-18 wks) (n=5) were used in order to evaluate the *in vivo* CT contrast agents circulation time and biodistribution. All animal experiments were performed according to the U.S. National Institutes of Health

principles of laboratory animal care [39] and were approved by the ethical review committee of Maastricht University (the Netherlands). The care and maintenance of the experimental animals was in compliance with the guidelines set by the institutional animal care committee, accredited by the National Department of Health. 2 mL/kg body weight of iodinated contrast agent (130 mg I/mL) together with 2 mL/kg body weight of i) physiological salt (n=10) (control) (Group A) ii) liposomes (n=5) (Group B) and iii) SB oil emulsion (n=5) (Group C) was injected, leading to an injected dose of 260 mg I/kg body weight. Fenestra VC (50 mg I/mL) (n=5) was injected with a dose of 4 mL/kg body weight (200 mg I/kg body weight) (Group D). The mice were placed in an induction chamber with 4 % isoflurane in air to induce anesthesia and were positioned in the scanner, where they were kept under anesthesia with 1.5-2.5 % isoflurane.

Helical CT scans were acquired pre-injection (reference) and up to 3 hours post-injection using a dedicated small animal SPECT/CT system (nanoSPECT/CT®, Bioscan, USA; 24 min acquisition time with 360 projections; 45 keV; 177 μ A; 2000 ms exposure time). Solutions were mixed 1:1 v/v within 30 minutes before *in vivo* injection. Cone-beam filtered back projection with a Shepp Logan filter and 100 μ m voxels was chosen for reconstruction. CT values are expressed in Hounsfield Units (HU) and were obtained per organ by drawing volumetric regions of interest (ROIs) using InVivoScope software (Bioscan). ROI volumes varied per organ between 5 mm³ (spleen) and 200 mm³ (liver). The average HU and the standard deviation were calculated from the data with 6 ROIs per organ.

Post-mortem, the uptake of ¹¹¹In and ¹⁷⁷Lu in dissected organs was measured using a γ -counting wizard. Two mice (one injected with ¹¹¹In-labeled CT contrast agent and one injected with ¹¹¹In-labeled CT contrast agent and ¹⁷⁷Lu-labeled SB oil emulsion) were, prior to dissection, scanned using a SPECT/CT protocol (nanoSPECT/CT®, Bioscan, USA; 8 hour scan, 36 projections, 400 seconds/projection) acquiring a 20% window around 171 keV (from 153.9 keV to 188.1 keV) and a 15% window around 245 keV (226.6 - 263.4 keV) for ¹¹¹In-acquisition, and when combined with ¹⁷⁷lutetium we acquired an extra set of two 20% windows around 113 keV (101.7 - 124.3 keV) and 208 keV (187.2 - 228.8 keV) for ¹⁷⁷Lu-acquisition.

3.3. Results and discussion

3.3.1. Synthesis

The synthesis of PBD-PEO-DOTA (**3**) is outlined in Scheme 1. This DOTA derived copolymer of butadiene and ethylene oxide was prepared by converting the hydroxyl endgroup of the commercial copolymer (PBD-PEO) into a tosylate group (polymer (**1**)). This polymer was easily converted into PBD-PEO-NH₂ (**2**) that contains a primary amine group by reaction with ammonia in methanol. After reaction of PBD-PEO-NH₂ (**2**) with the N-hydroxyaminosuccinimidyl derivative of DOTA the final polymeric product PBD-PEO-DOTA (**3**) was obtained. Analysis of this product by means of NMR is rather difficult due to the broad signals of polybutadiene and of the DOTA derived moiety. Maldi spectroscopy of the product is not possible due to the different masses of the monomeric units of both polymeric parts. No signals were observed. Maldi Analysis of the reaction products 5 and 6 of the same reaction sequence but using mPEG-OH (homopolymer instead of the copolymer) gave spectra that indisputable could be assigned to these products. Because the replacement of the polybutadiene group by a methyl group will not alter the reactivity of the hydroxyl group of the poly(ethylene glycol) moiety it is assumed that the same conversions had occurred with the copolymer PBD-PEO as with mPEG-OH. Synthesis and Maldi Analysis of mPEG-DOTA is described in Appendix A at the end of this chapter.

3.3.2. Nanoparticle characterization

The hydrodynamic radius of the different nanoparticles was determined directly after preparation with dynamic light scattering. All samples showed a monomodal and narrow size distribution with a radius of 90.4 nm (polydispersity index (PDI) = 0.02) for the iodine containing emulsion, 109.1 nm (PDI = 0.10) and 132.52 nm (PDI = 0.09) for DPPC liposomes and the soy bean (SB) oil emulsion, respectively (Fig. 1). The commercial contrast agent Fenestra VC had a hydrodynamic radius of 116.3 nm (PDI = 0.06) (Fig. 1D). The lipid concentration based on the concentration of phosphorous in the DPPC liposomes was 44 mM and in Fenestra VC 36 mM.

The DOTA-functionalized iodine emulsion was radiolabeled with ¹¹¹In and the DOTA-functionalized DPPC liposomes and SB oil emulsion with ¹⁷⁷Lu resulting in high radiochemical purities of >95%. The final obtained activities were 18.2 MBq ¹¹¹In/mL for the iodine containing emulsion, 13.6 MBq ¹⁷⁷Lu/mL in case of the liposome solution, and 16.6 MBq ¹⁷⁷Lu/mL for the SB oil emulsion. The ¹¹¹In-labeled iodine containing emulsion was mixed 1:1 v/v with physiological salt (A), DPPC liposomes (B), or SB oil emulsion (C).

The total number of injected iodine particles and soy bean oil particles was estimated based on the iodine concentration, density of the iodine and soy bean oil and its volume as determined by DLS. For liposomes, this number was estimated based on phosphorous concentration and assuming that lipids have an average surface area per lipid of 0.6 nm^2 . The number of particles that were injected per group is summarized in Table 1.

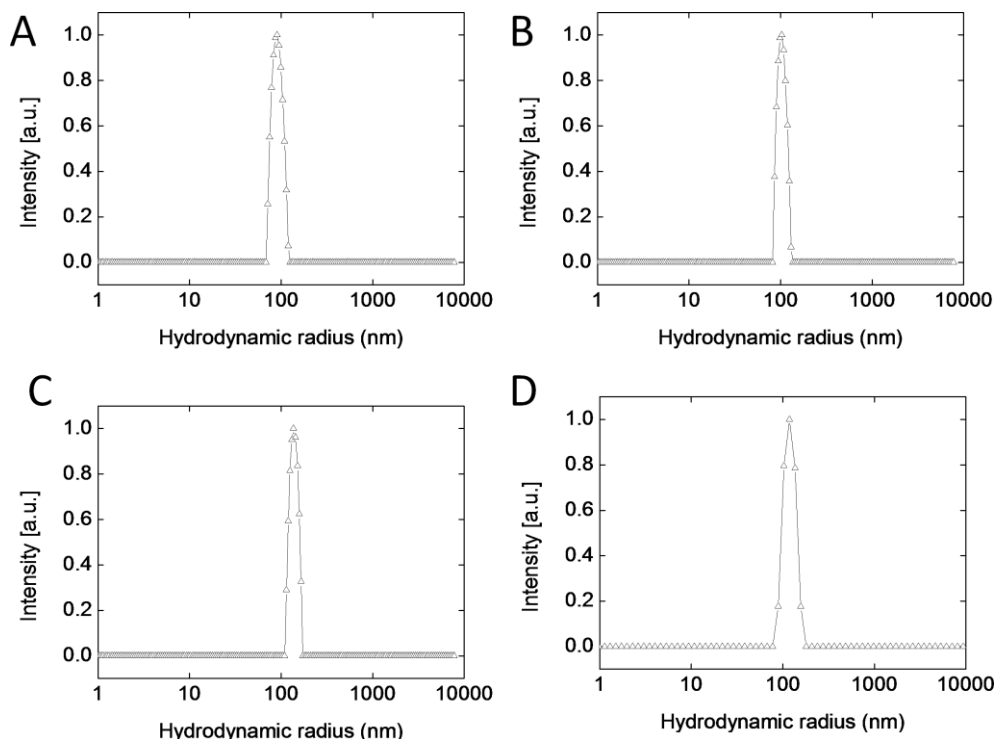


Figure 1. DLS measurements of (A) the iodine containing emulsion, (B) DPPC liposomes, (C) SB oil emulsion, and (D) Fenestra VC. (unweighted data analysis, no additional baseline fit to the correlation function).

All mixtures were prepared in a 1:1 v/v ratio. The cryo-TEM images of the nanoparticle solutions A, B and C are shown in Figure 2. The iodinated nanoparticles appear in TEM with a particularly strong contrast due to their electron dense core (Fig. 2A) and can be easily distinguished in mixtures from liposomes (Fig. 2B) or soy bean emulsion particles (Fig. 2C). Fenestra VC shows a high polydispersity as well as a large degree of liposomes with various morphologies, like partly coalescence between liposomes and iodinated particles (Fig. 2D).

Table 1. Three experimental animal groups were defined: Animals in Group A received an injection of iodine containing emulsion as a CT contrast mixed with physiological salt, Group B was injected with iodine containing emulsion and DPPC liposomes, and Group C received an injection of iodine containing emulsion mixed with SB oil emulsion. The numbers represent the total number of particles per injection.

Group	Numer of iodine particles	Number of DPPC liposomes	Numer of soy bean particles	Total number of injected nanoparticles
A	$4.5 * 10^{12}$	-	-	$4.5 * 10^{12}$
B	$4.5 * 10^{12}$	$5.4 * 10^{12}$	-	$9.9 * 10^{12}$
C	$4.5 * 10^{12}$	-	$3.1 * 10^{12}$	$7.6 * 10^{12}$

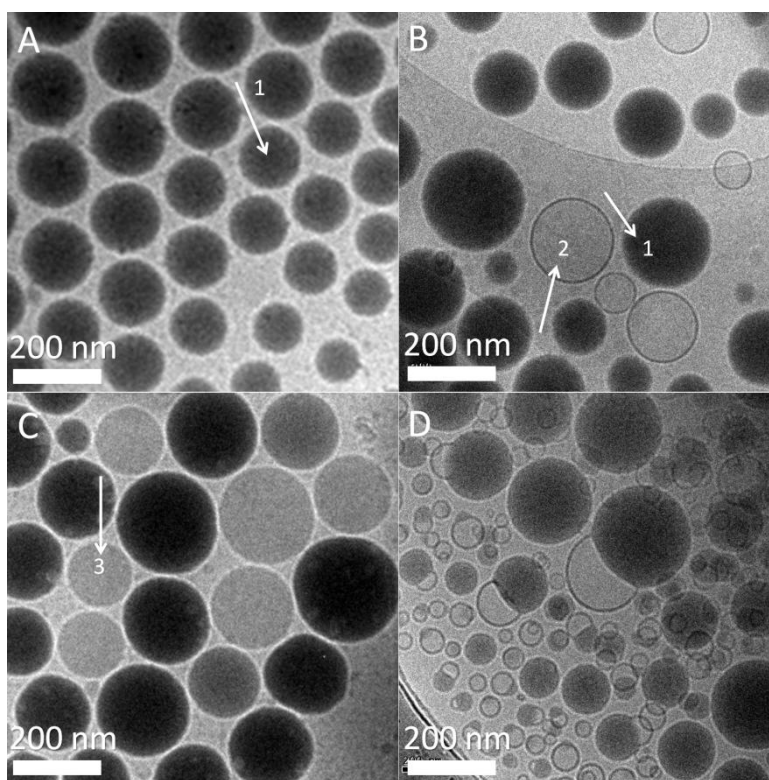


Figure 2. Cryo-TEM images of the mixtures used for injection of Group A (A), B (B) and C (C). All particles have a radius < 150 nm, typical for all samples. The iodine containing nanoparticles appear dark in TEM as they have an electron dense core indicated by the arrow 1. The lipid bilayer of the liposomes shows up as a grey rim with an aqueous core inside (arrow 2), whereas the SB oil emulsions stabilized with a polymeric monolayer have a grey core (arrow 3). In D, cryo-TEM images of Fenestra VC show a polydisperse mixture of emulsion droplets (dark core) as well as empty liposomes. Note that this image shows pure Fenestra VC to which no other particles or fluid was added.

3.3.3. *In vivo* studies

Mice received CT scans pre- and 3 hours post-injection of the dispersions. Twenty mice were divided into 3 groups (Group A (n=10), B (n=5) and C (n=5)), and injected with ^{111}In -radiolabeled iodinated emulsion only, ^{111}In -radiolabeled iodinated emulsion mixed with ^{177}Lu -radiolabeled DPPC liposomes and ^{111}In -radiolabeled iodinated emulsion mixed with ^{177}Lu -radiolabeled soy bean emulsion (Table 1). For reference, one group (n=5) (Group D) was injected with Fenestra VC. Full body CT scans were acquired as a function of time to follow the change in contrast in several organs.

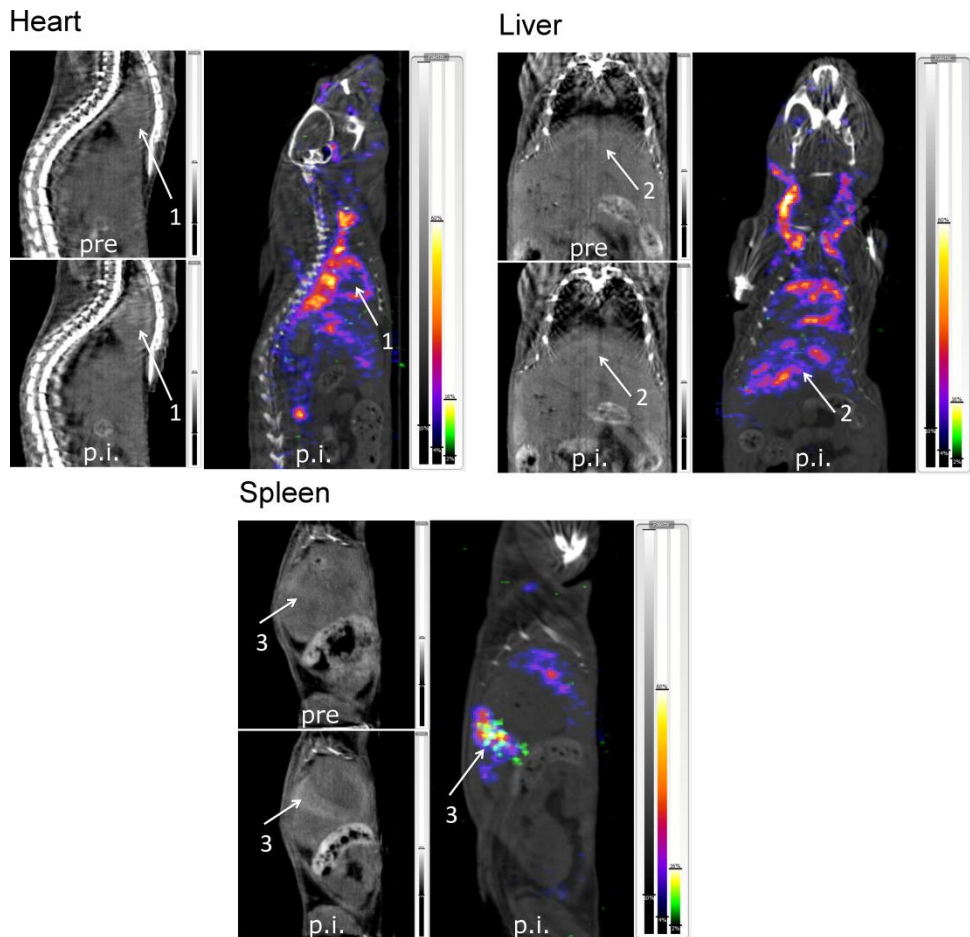


Figure 3. The CT and dual-isotope SPECT images of the heart, liver and spleen pre and post injection (p.i.) of iodine containing emulsion together with SB oil emulsion (Group C). The heart (arrow 1, 30 minutes p.i.) and spleen (arrow 3, 3 hours p.i.) show a strong increase in contrast in CT, while the liver (arrow 2) showed 3 hours p.i. only a weak contrast increase. On the right of all three panels, a dual-isotope SPECT scan shows in purple the biodistribution of the ^{111}In -labeled iodine emulsion and in green the ^{177}Lu -labeled soy bean oil emulsion.

Figure 3 shows an example of CT scans obtained from a mouse that was previously injected with a combination of iodinated emulsion and soy bean oil emulsion (Group C). The pre- and post-injection CT scans for the heart (30 min post-injection), the liver (3 hours post-injection) and spleen (3 hours post-injection) show a clear contrast increase in the heart and spleen, while the contrast increase in the liver is only minor. Furthermore, a post mortem dual-isotope SPECT scan was acquired, revealing a biodistribution of the ^{111}In -labeled iodinated emulsion in the blood circulation, liver and spleen, whereas the ^{177}Lu -labeled soy bean emulsion was mostly observed in the spleen. No signal was observed in the bladder.

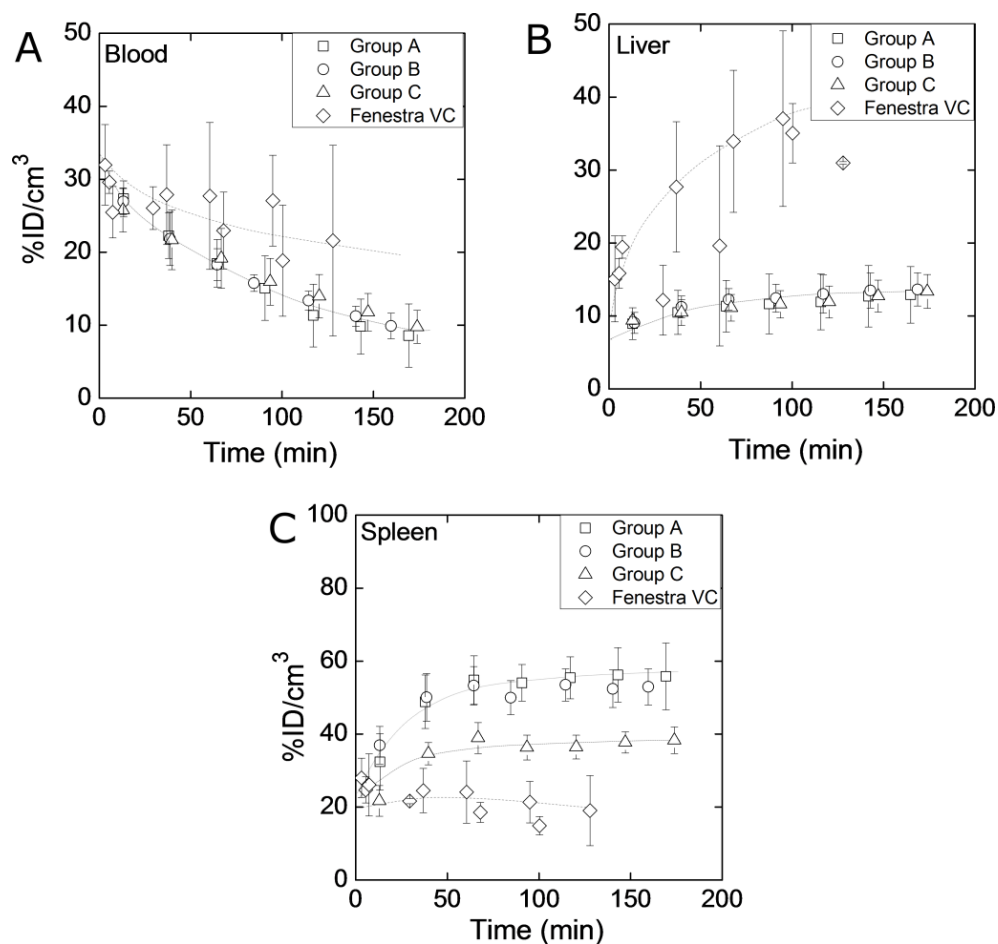


Figure 4. Iodine biodistribution in $\%ID/cm^3$ upon injection of iodine containing emulsion together with (i) physiological salt (Group A), (ii) liposomes (Group B), or (iii) SB oil emulsion (Group C) in (A) blood, (B) liver and (C) spleen over a period of 3 hours post-injection. Data represent mean \pm SD.

For blood, liver and spleen, the iodine concentrations were calculated from the change in Hounsfield Units on the *in vivo* CT scans using a standard iodine calibration of the HU measured on our system (page 43, Fig. 7). The amount of iodine is given in Figure 4 (A-C) in % injected dose iodine per cm^3 (%ID/ cm^3). Note, that %ID/ cm^3 is a relative number, which expresses the absolute iodine concentration per unit volume found in an organ as a percentage of injected dose. This allows comparing biodistribution data of iodinated emulsions that were injected at different doses. For example, Fenestra VC is injected at a lower iodine dose. This leads in general to lower absolute iodine concentrations in all organs, but to comparable values when expressed in %ID/ cm^3 .

The graph of Figure 4A shows a rapid increase up to 35 %ID/ cm^3 of the amount iodine in the blood after injection ($t=0$) for all formulations. Blood circulation time can be described with a first order exponential time dependence with half-lives of Group A: $t_{1/2}=87 \pm 20$ minutes, Group B: $t_{1/2}=99 \pm 12$ minutes and Group C: $t_{1/2}=116 \pm 15$ minutes. These $t_{1/2}$ values were statistically not significantly different. Fenestra VC on the other hand showed a longer circulation time: $t_{1/2}=210 \pm 60$ minutes. For the Groups A, B and C, the amounts of iodine in the liver (Fig. 4B) throughout the 3 hour period showed no significant differences. The iodine levels stabilized after approximately 80 minutes post-injection at a mean value of 14 ± 2 %ID/ cm^3 . For the spleen (Fig. 4C), co-injection of DPPC liposomes had no effect on the uptake of iodinated emulsions leading to similar tissue iodine concentrations (Group A: 56 ± 9 %ID/ cm^3 ; Group B: 53 ± 5 %ID/ cm^3). However, co-injection of soy bean oil emulsions (Group C) caused a significantly lower uptake of the iodine particles (38 ± 4 %ID/ cm^3). Fenestra VC shows a relatively high liver uptake (37 ± 12 %ID/ cm^3) (Fig. 4B) and a significantly lower spleen uptake (19 ± 10 %ID/ cm^3) (Fig. 4C).

Three hours post-injection, the biodistribution of the radiolabeled nanoparticles (Groups A, B, C) was quantified in dissected organs using dual-isotope γ -counting with the iodinated emulsion being always radiolabeled with ^{111}In , while the co-injected DPPC liposomes or soy bean emulsions were labelled with ^{177}Lu . The biodistribution of the iodinated emulsions alone, and of all nanoparticles in co-injection experiments is shown in Figure 5 for blood, heart, lung, liver, spleen and kidney. The iodine containing emulsion showed in all groups, regardless of co-injection of DPPC liposomes or soy bean emulsions, a similar biodistribution in blood as well as all organs, except for the spleen (Fig. 5C). Spleen uptake of the iodinated emulsion was in general highest of all organs reaching values of 26-42 %ID/g. However, spleen uptake was significantly reduced by co-injection of soy bean emulsion (Group C). DPPC liposomes were taken up by the liver (29 %ID/g) and spleen (67 %ID/g) in a higher concentration compared to the co-injected iodine containing emulsion (liver 12 %ID/g and spleen 36 %ID/g). While the SB oil emulsion showed a comparable liver uptake (18 %ID/g), the spleen uptake

was remarkably high at 79 %ID/g. This was accompanied by a suppressed uptake of the iodinated emulsion as mentioned above.

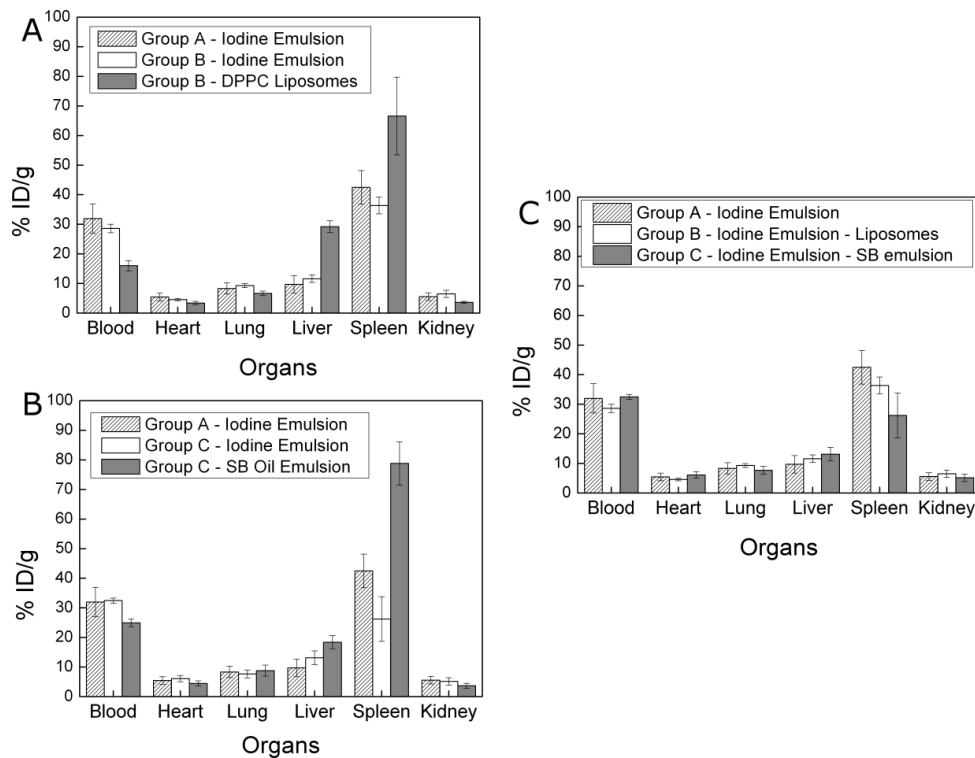


Figure 5. Biodistribution in dissected organs, three hours post injection shown in %ID/g of organ mass (A) Group A (^{111}In -labeled iodine emulsion) compared to Group B (^{111}In -labeled iodine emulsion and ^{177}Lu -labeled DPPC liposomes); (B) Group A (^{111}In -labeled iodine emulsion) compared to uptake of Group C (^{111}In -labeled iodine emulsion and ^{177}Lu -labeled SB oil emulsion); (C) iodinated emulsion in Groups A, B, C. Each bar represent mean \pm SD, (n=5).

3.4. Discussion

In general, the maximum tolerated dose of CT contrast agents is capped by iodine peak concentrations in vital organs because of their toxicity profile. Especially nanoparticle based CT blood pool agents suffer from liver toxicity problems at higher doses as they are mainly cleared *via* RES mediated uptake in the liver and spleen. As the liver peak concentration is determined by the uptake rate of CT agents from the blood on the one side, and the hepatobiliary excretion rate on the other, liver levels could potentially be maintained at tolerable levels by prolonging blood circulation and allowing for sufficient hepatobiliary excretion in the mean time.

We recently published a new type of CT blood pool contrast agent based on a polymer-stabilized iodinated emulsion [23]. This contrast agent showed blood circulation times of 2.7 ± 0.1 hours with clearance via liver and spleen, and a complete hepatobiliary excretion over 2 days. In this study, we investigated if the blood circulation time as well as organ uptake of this polymer-stabilized iodinated emulsion can be modulated by co-injecting a high payload of non-iodinated nanoparticles. Our hypothesis is that an increased payload of nanoparticles could deplete the blood from opsonins and reduce the RES mediated blood clearance similar to earlier findings with liposomes [24-26] but also iron oxide nanoparticles [40,41] leading to prolonged blood circulation. We therefore compared the blood circulation time and organ uptake of the novel iodine containing blood pool CT contrast agent while being co-injected with (i) physiological salt (Group A), (ii) DPPC liposomes (Group B), or (iii) soy bean oil emulsion (Group C). As reference, a Group D was injected with the commercial preclinical CT contrast agent Fenestra VC. The dynamics of iodine concentration in blood, spleen and liver described in $\%ID/cm^3$ was derived from CT scans prior to injection followed by consecutive post injection (p.i.) CT over a time span of 3 hours.

Furthermore, the biodistribution ($\%ID/g$) of all nanoparticles in Group A, B, C was assessed 3 hours p.i. with dual-isotope γ -counting after organ dissection. Our measurements showed that neither co-injection of DPPC liposomes (Group B) nor SB oil emulsion (Group C), doubling the amount of nanoparticles present in the blood (table 1), led to a statistically prolonged blood circulation time of the iodinated polymeric emulsion (Group A) (Fig. 4A). From earlier published studies with liposomes, we had expected that the number of co-injected nanoparticles of $3.1-5.4 \cdot 10^{12}$ particles of SB emulsions (Group C) or DPPC liposomes (Group B) would lead to an observable difference in circulation time of the iodinated nanoparticles [24-26,42]. On the other hand, experiments with pegylated liposomes did not always show dose dependence as strong as observed for non-pegylated liposomes [22]. Furthermore, as our iodinated emulsion particles are 100% pegylated, they are more comparable to polymersomes

that were recently studied *in vivo* [43-45]. However, no literature is currently available describing the clearance of polymeric nanoparticles, and their exact fate *in vivo* remains unclear.

A closer look upon the biodistribution data is needed to get a better understanding on the relative uptake in different organs. Uptake by the spleen and liver (Fig. 4) was observed within all three groups, indicating an excretion of the iodine containing emulsion *via* the hepatobiliary pathway, in agreement with previous data [23]. The uptake of iodine containing emulsion in the liver, spleen or other organs was relatively insensitive to a co-injection with DPPC or SB oil emulsion, the only exception being a reduced splenic uptake induced by a co-injection of SB oil emulsion (Fig. 4B). Dual-isotope γ -counting showed that DPPC liposomes were present mainly in the liver (29 %ID/g) and spleen (67 %ID/g), indicating that these nanoparticles were excreted *via* the hepatobiliary pathway as well. In comparison, SB oil emulsions were observed to a lower degree in the liver (18 %ID/g), but higher in the spleen (79 %ID/g) (Fig. 5). Though the high splenic uptake of SB emulsions reduced the uptake of the iodinated emulsion particles from 42 %ID/g to 26%ID/g, it left the blood circulation and liver uptake of the iodinated emulsion particles basically unchanged within the statistical errors. As the spleen is a relatively small organ (131 ± 38 mg, [46]) compared to blood (± 3.0 mL for 18 week old male Swiss mice; 7% of bodyweight) and liver (ca. 1833 ± 252 mg for an 18 week old male Swiss mouse [46]), the 16 %ID/g decrease in spleen uptake would lead to a maximal 1.2 %ID/g increase in liver uptake or blood concentration, which both are below the statistical variance of our experiment. We therefore conclude that even the most efficient blocking of splenic uptake is insufficient to significantly increase blood concentrations simply due to the small size of the spleen compared to the blood volume or size of the liver.

It is intriguing to look at the different nature and material properties of the iodinated polymer-stabilized nanoparticles compared to the DPPC liposomes and the polymer stabilized soy-bean emulsion in order to find a rational for above observed biodistribution. Important material parameters are size, surface coating, charge and attractive long-range interactions; which affect the interactions of the nanoparticles with blood components such as opsonins, which are mediating the recognition by the RES system and subsequent uptake in liver and spleen. DPPC liposomes are non-charged and furthermore no pegylated lipids were incorporated in the lipid bilayer. Previous studies showed for these non-pegylated liposomes fast liver and spleen uptake, while the blood circulation time increased with injected dose (i.e. lipid concentration) [24-26]. Consistent with these results, we also observed fast clearance of DPPC liposomes from blood and high spleen and liver uptake (Fig. 4C), though this obviously had no effect on the blood circulation and biodistribution of the iodinated emulsion. We

therefore assume that different and independent opsonins are involved in the recognition of liposomes compared to polymeric emulsions. This different handling profile of the liposomes may be furthermore influenced by their higher flexibility [29] compared to the more rigid oil-filled emulsion particles or the hydrophobicity of their lipid surface [47]. This is further supported by the observation that an injection of a two times higher dose of the CT agent (520 mg l/kg body weight), corresponding to ca. $9 \cdot 10^{12}$ nanoparticles, led to a circa two times longer blood half-life of 162 min [23] compared to the 87 min found in our study. Obviously, the hypothesis of extended blood circulation at high nanoparticle payload holds in our case only for exactly identical particles.

Nanoparticle sizes were 90.4 nm, 109.1 nm, and 132.5 nm for the iodine emulsion, DPPC liposomes and SB emulsion, respectively. The larger sized SB emulsions are preferentially taken up in the spleen compared to the smaller iodinated oil, a finding sometimes also observed for liposomes of different diameters [33]. For the DPPC liposomes it was shown that the uptake by the liver depends on the degree of opsonisation which is known to increase with size [27,29]. We therefore conclude that other factors must have a more important role in determining the observed biodistribution of SB and iodinated emulsion.

The soy-bean oil emulsions were chosen as they have the exact same surface as the iodinated oil containing emulsions. For both, the surface is made up from a non-charged pegylated polymer diblock PBD-PEO that forms a 100% pegylated polymer brush at the oil water interface. Thus, these particles differ from the iodinated CT agents only with respect to the oil compound in the interior. Importantly, the iodinated oil has a much higher refractive index and is therefore much more polarizable (higher Hamaker constant [48]), which can lead to different long-range interactions with compounds present in the blood. This observation is quite intriguing, as so far the surface coating of particles was considered most important for any possible interactions between nanoparticles and blood constituents. We speculate that these subtle differences are sufficient to trigger a different opsonisation process directing the uptake mainly towards the spleen for the SB emulsion and the liver for the iodinated emulsion. In direct competition during the co-injection experiment, the high splenic uptake of the SB emulsion seems to saturate this organ, thereby reducing the uptake of the iodinated emulsion.

FenestraTM vascular contrast (VC; ART, Quebec, Canada) is based on iodinated triglyceride - poly ethylene glycol (ITG-PEG) [49,50], having a circulation half-time of over 7 hours (for an injected dose of 500 mg l/kg) [51] or 3.5 hours for an injected dose of 200 mg l/kg body weight as demonstrated in our study. Despite its low iodine

concentration (50 mg I/mL), Fenestra has been frequently used over the last decade as a preclinical CT contrast agent [3,52-54]. Fenestra VC nanoparticles have a lipid monolayer containing pegylated phospholipids and regardless of its relatively large size (116 nm radius) it shows a relatively long circulation time (Fig. 3). Cryo-TEM images of Fenestra (Fig. 2) indicate the presence of emulsions as well as a high degree of liposomal structures. However, we do not know if the liposomal bilayer and the lipid monolayer of the emulsions are made up of the same lipids. In contrast to our polymeric iodinated emulsion, Fenestra showed a strong uptake in the liver and a low uptake in the spleen. Most likely, the liposomes are recognized by the same opsonins as the iodinated particles and reduce efficiently the subsequent uptake of the iodinated particles in the liver. While the lipid concentration of Fenestra VC (36 mM) is even lower than that of the DPPC liposomes in our co-injection experiment (54 mM), the DPPC liposomes were not able to prolong the circulation time of the iodine containing emulsion, underlining our initial suggestion that DPPC liposomes and polymer-stabilized emulsions are recognized and cleared by very different pathways. However, the injection of twice the dose of the same CT contrast agent led to a doubling of the blood half-life.

Our experiments show that recognition of nanoparticles present in the blood by opsonins and the subsequent uptake in organs like liver and spleen, strongly depend on the specific material properties. Minute differences in surface chemistry, charge, size, rigidity or even the interior phase can trigger different excretion pathways, which translate into different blood circulation times as well as biodistributions. A dose dependency of the blood half-life is indeed observed for identical CT contrast agent particles. In future experiments, the pharmacokinetics of polymeric nanoparticles and dose dependency will be investigated in more detail, which is of significant importance to in vivo applications of polymeric nanoparticles as, for example, MRI contrast agents [55] or as drug delivery vehicles [56,57].

3.5. Conclusion

The blood circulation time of a polymer-stabilized iodinated emulsion as well as its biodistribution remained unchanged in co-injection experiments with liposomes and polymer-stabilized soy bean emulsions. Our experiments suggest that each type of particle is recognized by different opsonins and that this determines their particular organ uptake, depending on the nature and material properties of the nanoparticle. Even the subtle change in the material properties of the two emulsions such as the exchange of the interior oil phase while leaving the surface unaltered is enough to lead to a completely different organ uptake. An increase of blood circulation time with dose of the same type of CT emulsion nanoparticle was indeed observed. However, no evidence was obtained for the generalized conclusion that an increasing nanoparticle load, regardless of the exact nature of the particles, leads to an increased blood circulation by depletion of opsonins from the blood.

Acknowledgements

The authors acknowledge Carlijn van Helvert, University Hospital Maastricht, for performing the tail-vein injections and her animal handling expertise. The authors thank Sander Langereis (Philips) for helpful discussions and critically reviewing the manuscript.

3.6. References

- [1] Almajdub M, Nejjari M, Poncet G, et al. In-vivo high-resolution X-ray microtomography for liver and spleen tumor assessment in mice. *Contrast Media Mol Imaging*. 2007;2:88-93.
- [2] Kim HW, Cai QY, Jun HY, Chon KS, Park SH, Byun SJ, et al. Micro-CT imaging with a hepatocyte-selective contrast agent for detecting liver metastasis in living mice. *Acad Radiol*. 2008;15:1282-90.
- [3] Schambach SJ, Bag S, Groden C, Schilling L, Brockmann MA. Vascular imaging in small rodents using micro-CT. *Methods*. 2010;50:26-35.
- [4] Stacul F. Current iodinated contrast media. *Eur Radiol*. 2001;11:690-7.
- [5] Cademartiri F, Mollet NR, van der Lugt A, McFadden EP, Stijnen T, de Feyter PJ, et al. Intravenous contrast material administration at helical 16-detector row CT coronary angiography: effect of iodine concentration on vascular attenuation. *Radiology*. 2005;236:661-5.
- [6] Christiansen C. X-ray contrast media - an overview. *Toxicology*. 2005;209:185-7.
- [7] Bourin M, Jolliet P, Ballereau F. An overview of the clinical pharmacokinetics of x-ray contrast media. *Clin Pharmacokinet*. 1997;32:180-93.
- [8] Mukundan S, Jr., Ghaghada KB, Badea CT, Kao CY, Hedlund LW, Provenzale JM, et al. A liposomal nanoscale contrast agent for preclinical CT in mice. *AJR Am J Roentgenol*. 2006;186:300-7.
- [9] Montet X, Pastor CM, Vallee JP, Becker CD, Geissbuhler A, Morel DR, et al. Improved visualization of vessels and hepatic tumors by micro-computed tomography (CT) using iodinated liposomes. *Invest Radiol*. 2007;42:652-8.
- [10] Trubetsky VS, Gazelle GS, Wolf GL, Torchilin VP. Block-copolymer of polyethylene glycol and polylysine as a carrier of organic iodine: design of long-circulating particulate contrast medium for X-ray computed tomography. *J Drug Target*. 1997;4:381-8.
- [11] Torchilin VP, Frank-Kamenetsky MD, Wolf GL. CT visualization of blood pool in rats by using long-circulating, iodine-containing micelles. *Acad Radiol*. 1999;6:61-5.
- [12] Galperin A, Margel D, Baniel J, Dank G, Biton H, Margel S. Radiopaque iodinated polymeric nanoparticles for X-ray imaging applications. *Biomaterials*. 2007;28:4461-8.
- [13] Kong WH, Lee WJ, Cui ZY, Bae KH, Park TG, Kim JH, et al. Nanoparticulate carrier containing water-insoluble iodinated oil as a multifunctional contrast agent for computed tomography imaging. *Biomaterials*. 2007;28:5555-61.
- [14] Aviv H, Bartling S, Kiesling F, Margel S. Radiopaque iodinated copolymeric nanoparticles for X-ray imaging applications. *Biomaterials*. 2009;30:5610-6.
- [15] Hainfeld JF, Slatkin DN, Focella TM, Smilowitz HM. Gold nanoparticles: a new X-ray contrast agent. *Br J Radiol*. 2006;79:248-53.
- [16] Cai QY, Kim SH, Choi KS, Kim SY, Byun SJ, Kim KW, et al. Colloidal gold nanoparticles as a blood-pool contrast agent for X-ray computed tomography in mice. *Invest Radiol*. 2007;42:797-806.
- [17] Cormode DP, Skajaa T, van Schooneveld MM, Koole R, Jarzyna P, Lobatto ME, et al. Nanocrystal core high-density lipoproteins: a multimodality contrast agent platform. *Nano Lett*. 2008;8:3715-23.
- [18] Rabin O, Manuel Perez J, Grimm J, Wojtkiewicz G, Weissleder R. An X-ray computed tomography imaging agent based on long-circulating bismuth sulphide nanoparticles. *Nat Mater*. 2006;5:118-22.
- [19] Oh MH, Lee N, Kim H, Park SP, Piao Y, Lee J, et al. Large-scale synthesis of bioinert tantalum oxide nanoparticles for X-ray computed tomography imaging and bimodal image-guided sentinel lymph node mapping. *J Am Chem Soc*. 2011;133:5508-15.
- [20] Klibanov AL, Maruyama K, Torchilin VP, Huang L. Amphipathic polyethyleneglycols effectively prolong the circulation time of liposomes. *FEBS Lett*. 1990;268:235-7.
- [21] Klibanov AL, Maruyama K, Beckerleg AM, Torchilin VP, Huang L. Activity of amphipathic poly(ethylene glycol) 5000 to prolong the circulation time of liposomes depends on the liposome size and is unfavorable for immunoliposome binding to target. *Biochim Biophys Acta*. 1991;1062:142-8.
- [22] Allen TM, Hansen C. Pharmacokinetics of stealth versus conventional liposomes: effect of dose. *Biochim Biophys Acta*. 1991;1068:133-41.

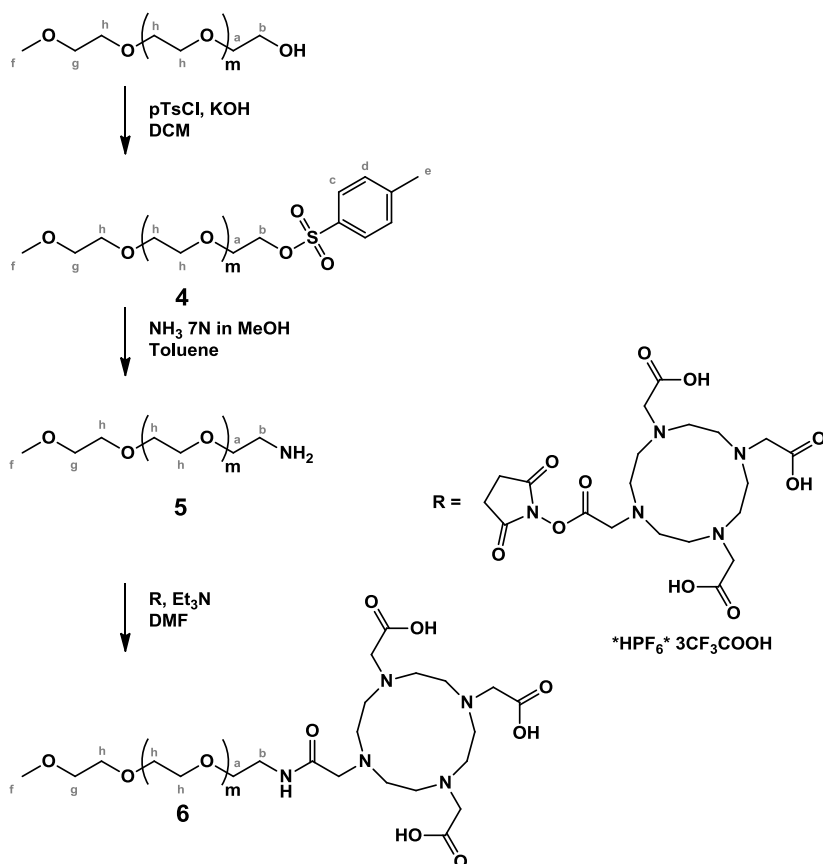
- [23] de Vries A, Custers E, Lub J, van den Bosch S, Nicolay K, Grull H. Block-copolymer-stabilized iodinated emulsions for use as CT contrast agents. *Biomaterials*. 2010;31:6537-44.
- [24] Beaumier PL, Hwang KJ, Slattery JT. Effect of liposome dose on the elimination of small unilamellar sphingomyelin/cholesterol vesicles from the circulation. *Res Commun Chem Pathol Pharmacol*. 1983;39:277-89.
- [25] Senior JH. Fate and behavior of liposomes in vivo: a review of controlling factors. *Crit Rev Ther Drug Carrier Syst*. 1987;3:123-93.
- [26] Harashima H, Yamane C, Kume Y, Kiwada H. Kinetic analysis of AUC-dependent saturable clearance of liposomes: mathematical description of AUC dependency. *J Pharmacokinet Biopharm*. 1993;21:299-308.
- [27] Harashima H, Sakata K, Funato K, Kiwada H. Enhanced hepatic uptake of liposomes through complement activation depending on the size of liposomes. *Pharm Res*. 1994;11:402-6.
- [28] Chonn A, Semple SC, Cullis PR. β_2 glycoprotein I is a major protein associated with very rapidly cleared liposomes in vivo, suggesting a significant role in the immune clearance of "non-self" particles. *J Biol Chem*. 1995;270:25845-9.
- [29] Ishida T, Harashima H, Kiwada H. Liposome clearance. *Biosci Rep*. 2002;22:197-224.
- [30] Gregoriadis G, Senior J. The phospholipid component of small unilamellar liposomes controls the rate of clearance of entrapped solutes from the circulation. *FEBS Lett*. 1980;119:43-6.
- [31] Litzinger DC, Huang L. Amphipathic poly(ethylene glycol) 5000-stabilized dioleoylphosphatidylethanolamine liposomes accumulate in spleen. *Biochim Biophys Acta*. 1992;1127:249-54.
- [32] Liu D, Mori A, Huang L. Role of liposome size and RES blockade in controlling biodistribution and tumor uptake of GM1-containing liposomes. *Biochim Biophys Acta*. 1992;1104:95-101.
- [33] Litzinger DC, Buiting AM, van Rooijen N, Huang L. Effect of liposome size on the circulation time and intraorgan distribution of amphipathic poly(ethylene glycol)-containing liposomes. *Biochim Biophys Acta*. 1994;1190:99-107.
- [34] Boerman OC, Oyen WJ, van Bloois L, Koenders EB, van der Meer JW, Corstens FH, et al. Optimization of technetium-99m-labeled PEG liposomes to image focal infection: effects of particle size and circulation time. *J Nucl Med*. 1997;38:489-93.
- [35] Senior JH, Trimble KR, Maskiewicz R. Interaction of positively-charged liposomes with blood: implications for their application in vivo. *Biochim Biophys Acta*. 1991;1070:173-9.
- [36] Devine DV, Wong K, Serrano K, Chonn A, Cullis PR. Liposome-complement interactions in rat serum: implications for liposome survival studies. *Biochim Biophys Acta*. 1994;1191:43-51.
- [37] Levchenko TS, Rammohan R, Lukyanov AN, Whiteman KR, Torchilin VP. Liposome clearance in mice: the effect of a separate and combined presence of surface charge and polymer coating. *Int J Pharm*. 2002;240:95-102.
- [38] Rouser G, Fkeischer S, Yamamoto A. Two dimensional thin layer chromatographic separation of polar lipids and determination of phospholipids by phosphorus analysis of spots. *Lipids*. 1970;5:494-6.
- [39] Guide for the care and use of laboratory animals. Washington D.C. Government Printing Office. 1985;NIH publication 86-23.
- [40] Wagner S, Schnorr J, Pilgrimm H, Hamm B, Taupitz M. Monomer-coated very small superparamagnetic iron oxide particles as contrast medium for magnetic resonance imaging: preclinical in vivo characterization. *Invest Radiol*. 2002;37:167-77.
- [41] Bourrinet P, Bengel HH, Bonnemain B, Dencausse A, Idee JM, Jacobs PM, et al. Preclinical safety and pharmacokinetic profile of ferumoxtran-10, an ultrasmall superparamagnetic iron oxide magnetic resonance contrast agent. *Invest Radiol*. 2006;41:313-24.
- [42] Drummond DC, Meyer O, Hong K, Kirpotin DB, Papahadjopoulos D. Optimizing liposomes for delivery of chemotherapeutic agents to solid tumors. *Pharmacol Rev*. 1999;51:691-743.
- [43] Photos PJ, Bacakova L, Discher B, Bates FS, Discher DE. Polymer vesicles in vivo: correlations with PEG molecular weight. *J Control Release*. 2003;90:323-34.
- [44] Murdoch C, Reeves KJ, Hearnden V, Colley H, Massignani M, Canton I, et al. Internalization and biodistribution of polymersomes into oral squamous cell carcinoma cells in vitro and in vivo. *Nanomedicine (Lond)*. 2010;5:1025-36.

- [45] Jain JP, Jatana M, Chakrabarti A, Kumar N. Amphotericin-B-loaded polymersomes formulation (PAMBO) based on (PEG)-PLA copolymers: an in vivo evaluation in a murine model. *Mol Pharm.* 2011;8:204-12.
- [46] Iwaki T, Yamashita H, Hayakawa T. A color atlas of sectional anatomy of the mouse Japan:Adthree Publishing Co.,Ltd. 2001:Appendix p. 160-1.
- [47] Senior J, Delgado C, Fisher D, Tilcock C, Gregoriadis G. Influence of surface hydrophilicity of liposomes on their interaction with plasma protein and clearance from the circulation: studies with poly(ethylene glycol)-coated vesicles. *Biochim Biophys Acta.* 1991;1062:77-82.
- [48] Norde W, Gage D. Interaction of bovine serum albumin and human blood plasma with PEO-tethered surfaces: influence of PEO chain length, grafting density, and temperature. *Langmuir.* 2004;20:4162-7.
- [49] Weichert JP, Lee FT, Jr., Longino MA, Chosy SG, Counsell RE. Lipid-based blood-pool CT imaging of the liver. *Acad Radiol.* 1998;5 Suppl 1:S16-9; discussion S28-30.
- [50] Wisner ER, Weichert JP, Longino MA, Counsell RE, Weisbrode SE. A surface-modified chylomicron remnant-like emulsion for percutaneous computed tomography lymphography: synthesis and preliminary imaging findings. *Invest Radiol.* 2002;37:232-9.
- [51] Ford NL, Graham KC, Groom AC, Macdonald IC, Chambers AF, Holdsworth DW. Time-course characterization of the computed tomography contrast enhancement of an iodinated blood-pool contrast agent in mice using a volumetric flat-panel equipped computed tomography scanner. *Invest Radiol.* 2006;41:384-90.
- [52] Badea CT, Hedlund LW, De Lin M, Boslego Mackel JF, Johnson GA. Tumor imaging in small animals with a combined micro-CT/micro-DSA system using iodinated conventional and blood pool contrast agents. *Contrast Media Mol Imaging.* 2006;1:153-64.
- [53] Badea CT, Hedlund LW, Mackel JF, Mao L, Rockman HA, Johnson GA. Cardiac micro-computed tomography for morphological and functional phenotyping of muscle LIM protein null mice. *Mol Imaging.* 2007;6:261-8.
- [54] Drangova M, Ford NL, Detombe SA, Wheatley AR, Holdsworth DW. Fast retrospectively gated quantitative four-dimensional (4D) cardiac micro computed tomography imaging of free-breathing mice. *Invest Radiol.* 2007;42:85-94.
- [55] Gröll H, Langereis S, Messenger L, Delli Castelli D, Sanino A, Torres E, et al. Block copolymer vesicles containing paramagnetic lanthanide complexes: a novel class of T_1 - and CEST MRI contrast agents *Soft Matter.* 2010;6:4847-50.
- [56] Ahmed F, Discher DE. Self-porating polymersomes of PEG-PLA and PEG-PCL: hydrolysis-triggered controlled release vesicles. *J Control Release.* 2004;96:37-53.
- [57] Haag R. Supramolecular drug-delivery systems based on polymeric core-shell architectures. *Angew Chem Int Ed Engl.* 2004;43:278-82.

Appendix A

Synthesis of mPEG-DOTA

A schematic representation of the synthesis of mPEG-DOTA is shown in Scheme S1.



Scheme S1. Synthesis of mPEG-DOTA (**6**) from mPEG-OH.

1. mPEG tosylate (**4**)

To a solution of mPEG-OH (1.99 gram, 0.97 mmol) in 10 mL of dichloromethane stirred in an ice-water bath under nitrogen 4-toluenesulfonyl chloride (494 mg, 2.59 mmol) was added. After stirring the solution for 30 min at 0 °C, KOH (492 mg, 8.77 mmol) was added. The mixture was stirred overnight under nitrogen while the temperature slowly rose to room temperature. The mixture was extracted subsequently with water (2x) and

brine (2x). After drying over MgSO_4 , the solvent was evaporated *in vacuo* and the product mPEG tosylate (**4**) was obtained (1.92 gram, 0.87 mmol, 90%) as a solid.

^1H NMR (CDCl_3 , δ/ppm): 7.80 (d H^c , 2H), 7.34 (d H^d , 2H), 4.15 (t, H^b , 2H) 3.47-3.81 (H^a , H^g , H^h), 3.38 (s, H^f , 3H), 2.45 (s H^e , 3H). ^{13}C DEPT NMR (CDCl_3 , δ/ppm): 129.8 (C^c), 128.0 (C^d), 71.9 (C^g), 70.0-70.9 (C^h), 69.2 (C^a), 68.7 (C^b), 59.0 (C^f), 21.5 (C^e).

2. mPEG-NH₂ (**5**)

mPEG tosylate (**4**) (1.88 gram, 0.85 mmol) dissolved in 5 mL toluene was divided into three ace pressure tubes (5 mL size) and ammonia in methanol (total 10 mL of 7N NH_3 in MeOH, 70 mmol) was added. Closed tubes were heated at 50 °C for 66 hrs and after cooling down to room temperature the solvent was evaporated *in vacuo*. The residue was dissolved in DCM and was subsequently extracted with water (2x), brine (2x) and with a 10% NaHCO_3 solution. After drying over MgSO_4 , the solvent was evaporated and the product mPEG-NH₂ (**5**) was obtained (0.95 gram, 0.85 mmol, 54%).

^1H NMR (CDCl_3 , δ/ppm): 3.47-3.81 (H^a , H^g , H^h), 3.38 (s, H^f , 3H), 3.0 (m H^b , 2H). ^{13}C DEPT NMR (CDCl_3 , δ/ppm): 71.9 (C^g), 70.0-70.9 (C^a , C^h), 59.0 (C^f), 41.2 (C^b). Maldi analysis: calculated for MNa^+ with $m=50$ ($\text{C}_{105}\text{H}_{213}\text{O}_{52}\text{NNa}$)⁺ 2344.40. Found: 2344.24 (Fig. S1).

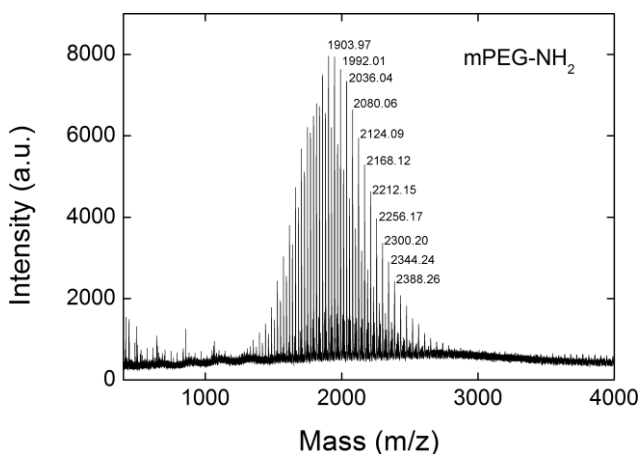


Figure S1. Maldi spectrum of mPEG-NH₂. $[\text{M}+\text{H}]^+$ and $[\text{M}+\text{Na}]^+$ was observed in the Maldi spectrum.

3. mPEG-DOTA (**6**)

mPEG-NH₂ (**5**) (0.80 gram, 0.40 mmol) was dissolved in 12 mL dimethyl formamide and DOTA-mono-NHS ester (200 mg, 0.20 mmol) and triethylamine (0.9 mL, 6.47 mmol) were added. The mixture was stirred for 14 hrs at room temperature under nitrogen. The solvent was evaporated *in vacuo* and the product mPEG-DOTA (**6**) was obtained (0.91 gram, 0.38 mmol, 95%).

^1H NMR (CDCl_3 , δ/ppm): 3.31-4.06 (H^a , H^g , H^h), 3.25 (s, H^f , 3H), Signals of H^b and the DOTA-moiety could not be assigned, but there is a very broad signal present from 1.0-5.5 ppm. ^{13}C DEPT NMR (CDCl_3 , δ/ppm): 72.2 (C^g), 69.80-71.7 (C^a , C^h), 59.2 (C^f). Signals of C^b and the DOTA-moiety could not be assigned due to broadening of the signals. Maldi analysis: calculated for MH^+ with $m=38$ ($\text{C}_{97}\text{H}_{192}\text{O}_{47}\text{N}_5$) $^+$ 2179.28. Found: 2179.75, (Fig. S2 and Fig. S3).

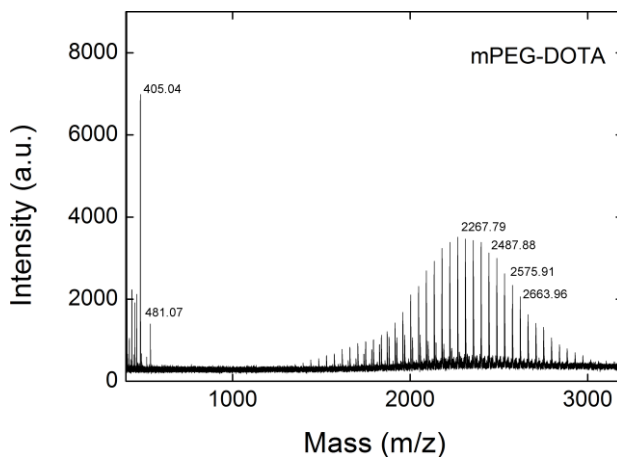


Figure S2. Maldi spectrum of mPEG-DOTA. $[\text{M}+\text{H}]^+$ was observed in the Maldi spectrum.

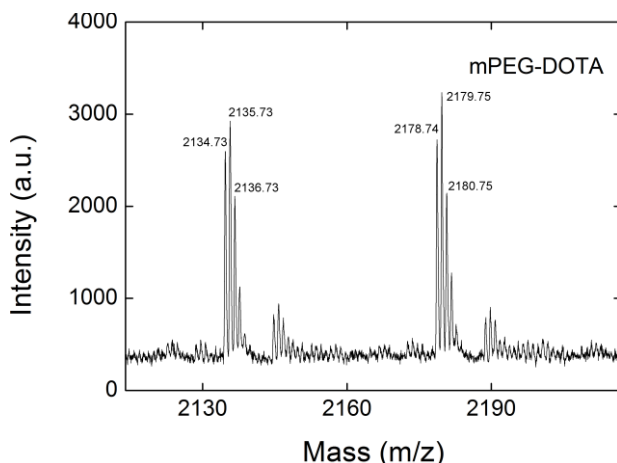
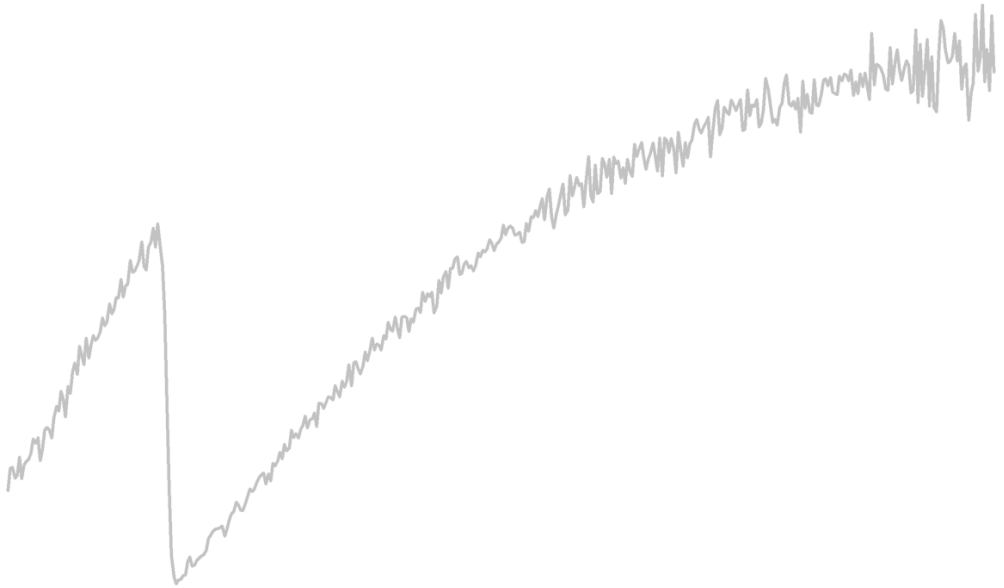


Figure S3. Maldi spectrum of mPEG-DOTA, zoomed in.

Quantitative Spectral K-edge imaging



Based on

Quantitative Spectral K-edge imaging in Preclinical Photon-Counting X-ray Computed Tomography

A. d. Vries, E. Roessl, A. Thran, J.P. Schlomka, B. Brendel, G. Martens, R. Proksa, K. Nicolay and H. Gröll

Submitted

Abstract

Purpose: Investigate the feasibility of preclinical spectral computed tomography (Spectral CT) to retrieve accurate information on the concentration and localization of high attenuation, iodine-based contrast agents in mice.

Materials and Methods: All animal procedures were performed according to the U.S. National Institutes of Health principles of laboratory animal care and were approved by the ethical review committee of the Maastricht University Hospital (the Netherlands). Healthy Swiss mice (n=4) were injected with an iodinated blood pool CT contrast agent radiolabeled with ^{111}In . CT and SPECT scans were acquired for 1 hour using a dedicated small animal SPECT/CT system. Subsequently, scans were performed with a preclinical Spectral CT scanner equipped with a photon-counting detector and six energy threshold levels. Quantitative data analysis of SPECT and Spectral CT scans was obtained using 3D volumes-of-interest drawing methods. Inductively coupled plasma mass spectrometry (ICP-MS) on dissected organs was performed to determine iodine uptake per organ and was compared with the amounts determined from Spectral CT and SPECT.

Results:

Spectral CT provides quantitative information on iodine biodistribution in mice. Iodine concentrations obtained with image processed Spectral CT data correlate well with data obtained either with non-invasive SPECT imaging (slope 0.96, $R^2=0.84$, $r=0.75$), or with ICP-MS (slope 0.99, $R^2=1.0$, $r=0.89$) in tissue samples.

Conclusion:

Spectral CT applying an empirical data decomposition method provides quantitative information of high-Z element biodistribution. Benchmarked against ICP-MS data, Spectral CT is comparable to SPECT based quantification.

4.1. Introduction

Computed Tomography (CT) is one of the most frequently used imaging modalities in the clinic, providing high-spatial-resolution anatomical images with very short acquisition times. CT has proved invaluable as a diagnostic tool for many clinical applications varying from trauma [1-3] to osteoporosis screening [4,5] and cancer diagnosis [6]. The role of CT increased further when CT contrast agents were clinically introduced for applications such as for cardiac angiography [7-9], urography [10], tumor characterization, staging and follow up [11-13].

Contrast enhanced CT is a qualitative imaging technique as CT contrast expressed in Hounsfield Units cannot directly be related to contrast agent concentration in tissue. However, quantitative analysis is necessary for the accurate characterization of diseases such as pancreatic [14] or hepatocellular carcinomas (HCC) [15-23] since the dynamic properties of contrast agent concentrations are required for exact staging. Yet another though related challenge is to differentiate between CT contrast coming from different elements. The latter is important for example to differentiate between CT contrast agents and calcification in coronary arteries in atherosclerotic plaque detection [24,25].

CT contrast agents are based on heavy nucleus atoms with a high number of electrons (high-Z elements) like iodine that show a typical discontinuous increase in their absorption coefficient for photons with energies just above the “K-edge”, which is the binding energy of the K-shell electrons (e.g. iodine: $Z=53$, K-edge energy: 33.2 keV). High-Z elements can thus be identified and quantified by their K-edge associated absorption in CT, provided an energy resolving detector is used. This method is termed Spectral CT. The feasibility of quantitative K-edge CT imaging was established in phantoms [26,27] and recent studies showed that Spectral CT improves luminal depiction and plaque characterization in mice [28,29]. However, quantification of high-Z elements *in vivo* yet needs to be demonstrated and requires optimization of the underlying data acquisition chain as well as performance improvements of the algorithms handling spectral decomposition and reconstruction.

The purpose of this study was to investigate contrast agent quantification with Spectral CT in mice. Using a radiolabeled iodinated contrast agent, tissue concentrations determined with Spectral CT can be compared to quantification based on SPECT in a dual-modality imaging approach. Furthermore, imaging-based quantification is compared to biodistribution data obtained with inductively coupled plasma mass spectrometry (ICP-MS) in tissue specimens. For improving quantification, Spectral CT

data were processed using an empirical material decomposition method first introduced for dual energy CT [30] which was recently extended to Spectral CT [31].

4.2. Materials and Methods

4.2.1. Materials

Poly(butadiene(1,2 addition)-*b*-ethylene oxide) (PBD-PEO) was purchased from Polymersource Inc. (Montreal, Canada) and was synthetically modified to form DOTA-functionalized PBD-PEO (see Chapter 3, 3.3.2., page 49). A 1.0 molar iodine solution (NaI) was obtained from Sigma-Aldrich.

4.2.2. Nanoparticle Preparation and Characterization

Iodinated emulsions were prepared and characterized as previously described [32]. Here, the iodinated oil was stabilized with 95 mol% of PBD-PEO and 5 mol% DOTA-PBD-PEO for radiolabeling with ^{111}In (^{111}In) (Perkin Elmer, Boston, Ma, USA). The hydrodynamic radius and polydispersity of the emulsions was determined using dynamic light scattering (DLS) (ALV/CGS-3 Compact Goniometer System, ALV-GmbH, Langen, Germany). Intensity correlation functions were measured at a scattering angle of $\theta=90^\circ$ using a wavelength of 632.8 nm. Hydrodynamic radii and size distributions were derived from cumulant fits of the intensity autocorrelation function, applying the Stokes-Einstein relation. Cryogenic transmission electron microscopy (cryo-TEM) pictures were obtained with a FEI TECNAI F30ST electron microscope operated at an accelerating voltage of 300 kV in low dose mode. Samples for cryo-TEM were prepared by placing the emulsion (2 μL) on a 300-mesh carbon-coated copper grid and subsequently plunge-freezing this grid into liquid ethane using a Vitrobot. The iodine concentration per sample was determined after Schöniger combustion using Inductively Coupled Plasma-Mass Spectrometry (ICP-MS).

Nanoparticles were labeled with ^{111}In (^{111}In) (Perkin Elmer, Boston, Ma, USA). In detail, 20 μL ammonium acetate buffer (2M NH_4OAc , pH 4.5) was added to a 520 μL CT contrast agent solution together with 6 μL of ^{111}In (60 MBq) and the pH was adjusted to 5.0. The sample was stirred at 60 $^\circ\text{C}$ for 60 min. Free DTPA (5 μL , 10 mM) was added to the reaction mixture for 15 min to scavenge free radionuclides. Labeling efficiency was checked on silica TLC using 200 mM EDTA as mobile phase and analyzed using a Phosphor Imager (FLA-7000, Fujifilm, Tokyo, Japan). Samples were purified using a PD-10 column (GE Healthcare). Pure fractions were collected and concentrated to its original concentration using a N_2 flow. Radiochemical purities obtained were $> 95\%$ and the ^{111}In content was measured using a γ -counting wizard (Wizard 1480 3" Wallac counter, Perkin Elmer, Groningen, The Netherlands). After radioactive decay of ^{111}In , the samples were analyzed using ICP-MS to determine iodine concentrations.

4.2.3. Spectral CT

Spectral CT images were acquired with a prototype scanner developed for preclinical use. A KEVEX micro-focus X-ray tube and a planar, single-row, 1024 pixel, 3 mm thick CdTe detector (Gamma Medica - Ideas, Fornebu, Norway) were mounted on a rotating gantry in fan beam geometry. The effective CdTe pixel height was collimated to 1.2 mm and the average pixel pitch was 400 μm , achieving an in-plane spatial resolution of 100 μm in the high-resolution configuration. The front-end readout electronics performs pulse amplification and shaping as well as pulse-height discrimination in six independently adjustable energy thresholds for each individual pixel of 25, 34, 39, 44, 49 and 55 keV. A total of 565 axial slices of the mouse (thickness: 200 μm) were acquired in sequential mode, resulting in a total coverage along the scanner rotation axis of about 11 cm. The tube voltage was set to 70 kVp and the anode tube current to 200 μA . The detector was placed at a distance of 600 mm from the focal spot, the iso-center at a distance of 100 mm. Per slice, 1250 projections were acquired over 360° with a rotation time of 300 s/revolution. The recorded counts were registered in six different 16-bit counters. Spectral CT data were processed using an empirical material decomposition method first introduced for dual energy CT [26,27,30] which was recently extended to energy sensitive photon-counting CT [31]. Finally the decomposed data were reconstructed to obtain images of the attenuation caused by the photoelectric effect, the Compton effect and the concentration of iodine on a voxel grid of 100x100x200 μm^3 .

4.2.4. Phantom Experiments

A set-up consisting of a high-purity germanium detector (Φ 20 mm x 12 mm, N₂ (liq.) cooled) (Detector Systems GmbH Mainz, Germany) combined with a multi-channel analyzer system (Target Systemelectronic GmbH, Solingen, Germany) and a X-ray source (source target: 1 μm thin tungsten target; focus size 3 mm; tube voltage 100 kVp) provided an energy resolution (FWHM) of <600eV at 122keV and was used to measure transmitted X-ray spectra to determine the K-edge absorption as a function of iodine concentration in 5 sodium iodide solutions (NaI in mol/L: 0.01, 0.04, 0.09, 0.44, 0.87, 1.0). These solutions were subsequently used for calibration studies with Spectral CT as required by the empirical decomposition method [30]. The iodine concentrations were confirmed with ICP-MS.

4.2.5. Animal Experiments

The animal procedures were performed according to the U.S. National Institutes of Health principles of laboratory animal care and approved by the local ethical review committee. All animal handlings were performed by experienced personnel (4 years experience). Healthy male Swiss mice (n=4) (Charles River) were injected with ¹¹¹In-radiolabeled nanoparticles with 520 mg of iodine per kilogram of bodyweight per mouse

and sacrificed 60-90 minutes post-injection. A post-mortem conventional helical CT scan (360 projections; 45 keV; 177 μ A; 2000 ms exposure time) and SPECT scan (36 projections; 640 sec/projection) were performed using a small animal SPECT/CT system (nanoSPECT/CT®, Bioscan, USA). Sacrificed mice were frozen in liquid nitrogen, followed by Spectral CT scans on frozen specimens at T=-5°C. Data were reconstructed using a polynomial algorithm [27,30,31]. Subsequently, mice were dissected and iodine concentrations per organ were determined using ICP-MS.

4.2.6. Image Processing

Scans were analyzed using the Philips IMALYTICS Translational Research Workstation. Volumes-of-interest (VOI) were drawn in 3D following the outer contours of the organs as visualized in CT. VOIs were drawn (A.d.V., 4 years experience) in all mice for the organs; i.e. heart, lung, liver, spleen, left kidney, right kidney, and bladder. All VOIs were defined prior to retrieval of the iodine concentrations per organ to avoid operator bias. After obtaining the iodine concentrations, no adjustments of the VOIs were made.

4.3. Results

4.3.1. Nanoparticle Preparation and Characterization

The emulsification process of an iodinated oil with the amphiphilic diblock polymer PEO-PBD yielded iodinated nanoparticles (Fig. 1A) with a mean hydrodynamic radius of $r_h=95.0$ nm and a narrow size distribution (Fig. 1B), as determined by dynamic light scattering (DLS). Cryo-TEM shows particles having a radius < 100 nm with an electron-dense core due to the high iodine payload (Fig. 1C). Subsequent radiolabeling yielded a multimodal SPECT/(Spectral) CT contrast agent, containing on average 0.5 MBq of ^{111}In per mg iodine at the time of injection.

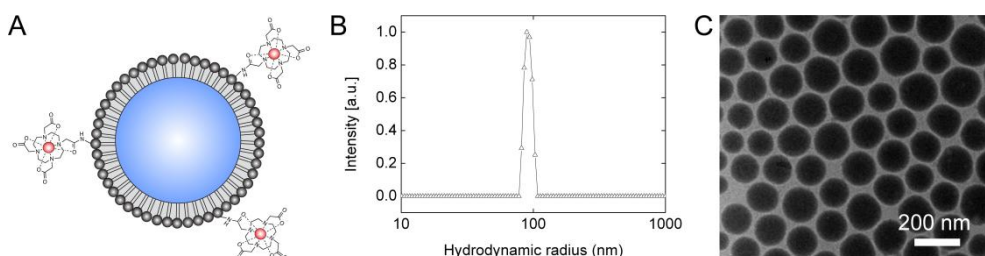


Figure 1. (A) Schematic representation of a multimodal contrast agent for CT (iodine filled core) and SPECT (^{111}In -radiolabeled surface). (B) Hydrodynamic radius (nm) measured by DLS, unweighted size distribution. (C) Cryo-TEM image.

4.3.2. Phantom Experiments

The transmission spectrum of an iodine containing sample can be obtained using previously described methods [27] (Fig. 2A). Based on the transmitted intensity (I) right above and below the K-edge, the change in mass attenuation at the K-edge of $\Delta(\mu/\rho) = 29.27$ cm^2/g [33] can be related to the line-integral of the iodine density A_{iodine} (g/cm^2) along the beam:

$$\ln\left(\frac{I_{\text{Above}}}{I_{\text{Below}}}\right) = -\Delta \frac{\mu}{\rho} * A_{\text{iodine}} \quad (\text{eq. 1})$$

Calibration experiments were performed using a high purity germanium detector (HPGe) on 5 iodine solutions of known iodine concentrations (determined with ICP-MS). The logarithm of the transmission ratio (I_{ratio}) and the iodine concentration show a linear relation with a slope 3.85 L/mol ($R^2 = 0.999$), having a Pearson's coefficient $r = 1.0$ (Fig. 2C). Utilizing the previously performed calibration, a vial containing the iodinated CT contrast agent was scanned to determine its iodine concentration. The spectrally determined iodine concentration of 0.98 M iodine was consistent with the value 1.0 ± 0.08 M determined by ICP-MS.

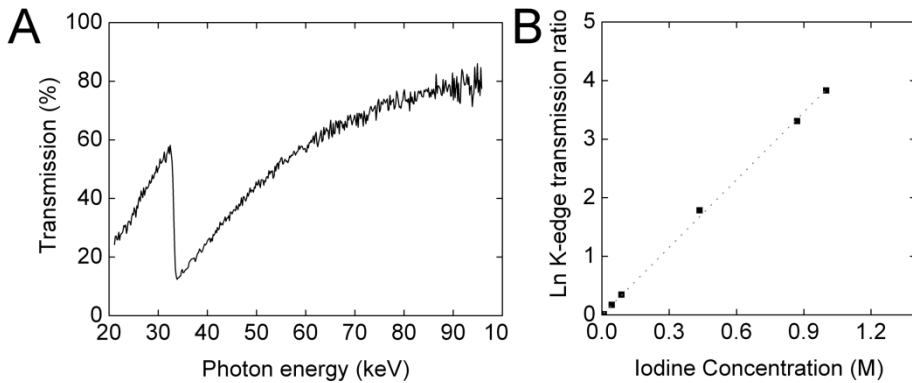


Figure 2. (A) Transmission spectrum of an iodine sample showing a K-edge at 33.2 keV; (B) Spectral CT calibration curve resulting in a linear fit: $\text{Ln}(I_{\text{ratio}}) = 3.85 (L/\text{mol}) * \text{iodine concentration (M)}$.

As the energy resolution of the CdTe detector in the preclinical Spectral CT scanner is lower compared to the HPGe, the spectral decomposition is less accurate and requires a separate calibration. To examine the quantitative capabilities of the preclinical Spectral CT scanner, we prepared a concentration series of sodium iodide of five samples, ($\text{NaI}(\text{mol/L}) = 0.02, 0.02, 0.11, 0.13, \text{ and } 0.47$). The 6 individual thresholds for the measured energy have been set to 25, 34, 39, 44, 49 and 55 keV for optimal iodine quantification (33.2 keV) [26]. Spectral CT data were processed and reconstructed using an empirical material decomposition method which was recently extended to energy sensitive photon-counting CT [31] and provided voxel-based iodine concentrations in molar (M) for each vial. Figure 3 shows a linear correlation of the iodine concentrations determined with Spectral CT with the iodine concentrations as measured with ICP-MS having a slope of 1.20 ± 0.03 ($R^2=0.99$, Pearson's correlation coefficient $r=1.0$).

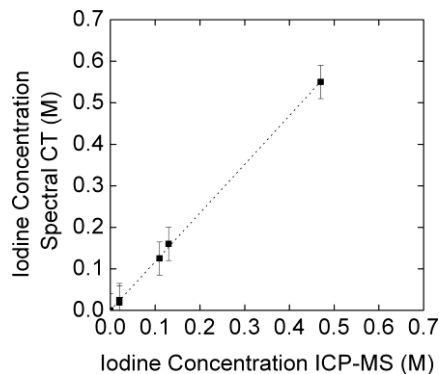


Figure 3. Quantification of iodine concentration (M) by Spectral CT and ICP-MS indicate a linear correlation between the two methods.

4.3.3. Animal Experiments

In an *in vivo* study, Spectral CT-based quantification of iodine in various tissues is compared to quantification obtained with SPECT imaging and ICP-based biodistribution data. Healthy Swiss mice were to this aim injected with a multimodal ^{111}In -radiolabeled iodine-containing blood pool contrast agent for SPECT and (Spectral) CT. The organ distribution of the multimodal contrast agent was visualized and quantified with a post-mortem SPECT scan as the γ -radiation of ^{111}In is related to the amount of iodine in the tissue (1.9 mg I/MBq ^{111}In). Next, the organ distribution of the multimodal contrast agent was investigated by Spectral CT, exploiting the K-edge absorption of iodine. Finally, mice were dissected and organs were analyzed for their iodine content by ICP-MS.

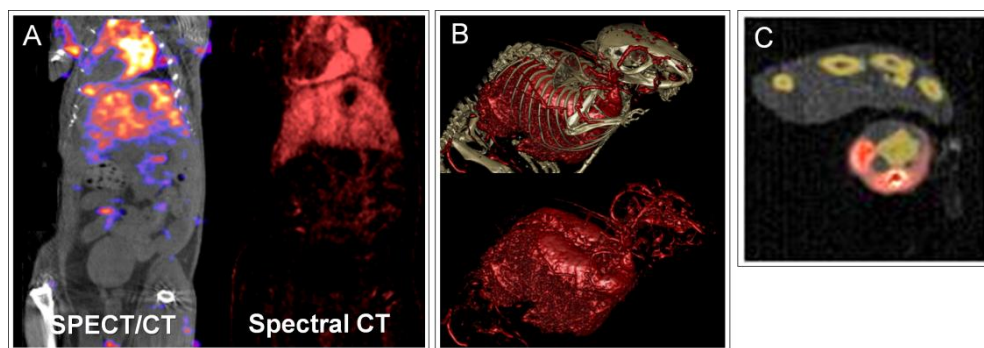


Figure 4. Mice injected with a multimodal blood pool contrast agent for SPECT and CT. (A) Comparison of a SPECT/CT scan (left) with an iodine Spectral CT (right) (*ex vivo*). (B) A Spectral CT scan showing the discrimination of attenuation derived from iodine (red) (bottom) and bone (top). (C) Spectral CT slice at the injection site (tail vein), showing bone (yellow) and iodine (red).

On the SPECT/CT scans of these mice, areas of high ^{111}In activity were observed in the blood vessels, heart, liver and spleen (Fig. 4A), indicating the presence of the multimodal contrast agent in these organs. The bladder showed hardly any signal in the SPECT scans. A similar distribution was observed with Spectral CT (Fig. 4A), showing a high iodine payload in the heart (i.e. blood) and liver. We also noted that the gallbladder showed up as a signal void in SPECT as well as in Spectral CT scans.

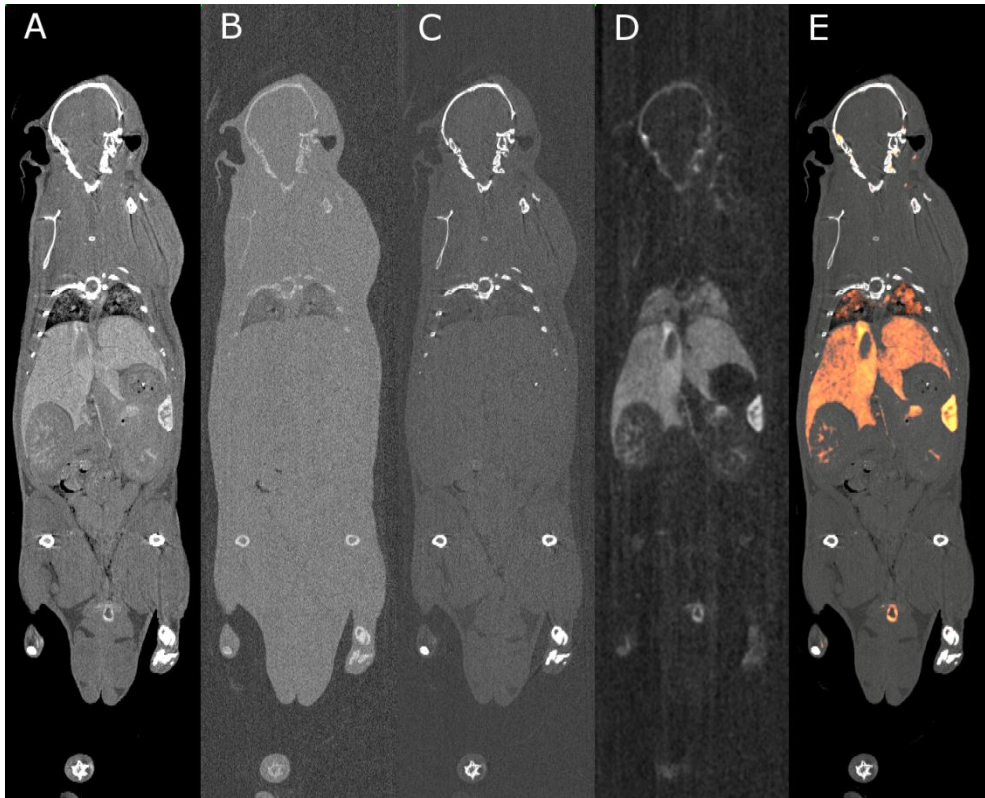


Figure 5. *Ex vivo* coronal images of a Swiss mouse previously injected with the iodine containing emulsion. (A) Quasi-mono-energetic image at an energy of 40 keV, (B) Compton image, (C) photo-effect based image, (D) iodine based image, and (E) color-overlay of the iodine image on the quasi-monoenergetic image. The iodine distribution is shown in shades of red. Iodine concentrations were highest in the liver and spleen.

As the contrast agent is predominantly retained within the vascular system due to its size, the vascular system could be delineated from bone tissue (Fig. 4B), making it even possible to observe blood vessels going through bone structures, like the Circle of Willis. Moreover, we were able to observe elevated iodine concentrations at the injection site in the tail vein of the mouse (Fig. 4C) separate from bone signal. From the raw Spectral CT data of energies between 25-40 keV, a quasi-monoenergetic CT image can be derived (Fig. 5A). Moreover, three separate images can be reconstructed showing the contributions of Compton effect (Fig. 5B), the photo-electric effect (Fig. 5C), and iodine content (Fig. 5D) to the photon absorption. The combined image of the attenuation of the photo-electric effect (bone) and iodine is shown in Figure 5E. Combining the information of the photo-effect based image and the iodine image, Spectral CT enables a well-defined discrimination between iodine attenuation and attenuation from calcium (bone).

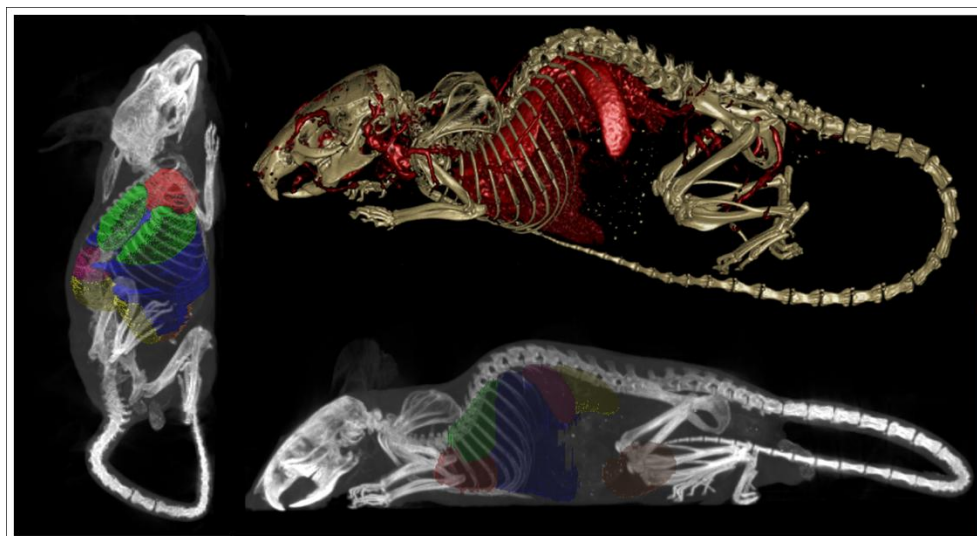


Figure 6. Volumes-of-interest (VOIs) defined in a SPECT/CT scan (left and bottom) showing the VOI of the heart (red), lung (green), liver (blue), spleen (pink), left kidney (yellow), right kidney (yellow), bladder (orange). The corresponding Spectral CT scan is shown in the top image.

3D VOIs were drawn following the exact contours in CT of the organs (Fig. 6) to determine the quantitative iodine concentrations in mice with Spectral CT and SPECT. Spectral CT quantification is based on the calibration obtained with samples of known iodine concentrations (IC) (Fig. 3). Finally, ICP-MS was performed on the dissected organs as a gold standard. The quantification results of Spectral CT, SPECT and ICP-MS per organ for each individual mouse are compared to investigate their mutual correlation (Fig. 7). Raw data are shown in Table 1.

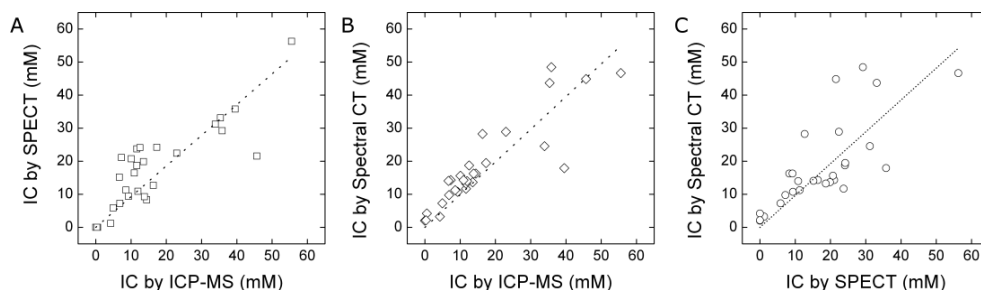


Figure 7. Quantification of iodine concentrations (IC) (mM) in different organs of mice post-injection of blood pool contrast agent. (A) Comparison of quantification by SPECT and ICP-MS (Slope=0.93, $R^2=0.88$, $r=0.85$) (B) Comparison of quantification of Spectral CT and ICP-MS (Slope=0.99, $R^2=1.0$, $r=0.89$) (c) Comparison of quantification of Spectral CT and SPECT (Slope=0.96, $R^2=0.84$, $r=0.75$).

SPECT-based quantification shows a good correlation with iodine concentration determined by the “gold standard” ICP-MS with a slope of 0.93 (Fig. 7A). The iodine concentrations per organ as determined by Spectral CT scales linearly with ICP-MS based concentrations (slope = 0.99; Fig. 7B), and additionally, the slope of the linear fit of the quantification *via* Spectral CT versus SPECT was 0.96 (Fig. 7C). In the lower iodine concentration range (<18 mM) no outliers are observed, indicating a reliable iodine quantification using Spectral CT. In the higher iodine concentrations range found for example in liver and spleen samples, more outliers are observed although in general a good correlation is found with the SPECT or biodistribution data.

Table 1. Iodine concentrations (mM) obtained from Spectral CT, SPECT and ICP-MS of the heart, lung, liver, spleen, kidneys and bladder of all four mice.

	Spectral CT	SPECT	ICP-MS
	Iodine conc. (mM)	Iodine conc. (mM)	Iodine conc. (mM)
Heart	14.3 ± 0.7	21.1 ± 2.4	7.3 ± 0.4
Lung	17.9 ± 1.3	35.8 ± 3.0	39.5 ± 2.0
Liver	24.6 ± 1.4	31.2 ± 3.4	33.9 ± 1.7
Mouse 1 Spleen	46.6 ± 3.6	56.2 ± 11.9	55.6 ± 2.8
Kidney (left)	11.7 ± 0.9	23.7 ± 1.9	11.7 ± 0.6
Kidney (right)	13.6 ± 1.1	19.9 ± 1.8	13.6 ± 0.7
Bladder	2.0 ± 0.2	0.0 ± 0.0	0.0 ± 0.0
Heart	13.2 ± 0.7	18.7 ± 2.7	11.7 ± 0.6
Lung	18.7 ± 1.9	24.1 ± 3.2	12.5 ± 0.6
Liver	28.2 ± 1.7	12.7 ± 1.8	16.4 ± 0.8
Mouse 2 Spleen	44.8 ± 4.2	21.5 ± 4.4	45.7 ± 2.3
Kidney (left)	10.8 ± 0.8	9.4 ± 1.0	9.3 ± 0.5
Kidney (right)	14.0 ± 1.2	10.9 ± 1.0	12 ± 0.6
Bladder	3.2 ± 0.4	1.2 ± 0.1	4.3 ± 0.2
Heart	15.6 ± 1.0	20.7 ± 2.8	10.1 ± 0.5
Lung	19.5 ± 1.8	24.2 ± 3.5	17.3 ± 0.9
Liver	28.9 ± 1.8	22.4 ± 3.1	23.0 ± 1.1
Mouse 3 Spleen	48.5 ± 4.6	29.2 ± 5.5	35.9 ± 1.8
Kidney (left)	11.3 ± 0.8	11.3 ± 1.6	8.6 ± 0.4
Kidney (right)	14.3 ± 1.1	16.4 ± 1.9	11.0 ± 0.5
Bladder	4.2 ± 0.5	0.0 ± 0.0	0.6 ± 0.0
Heart	14.0 ± 0.8	15.2 ± 1.6	6.7 ± 0.3
Lung	16.3 ± 1.6	8.3 ± 0.9	14.5 ± 0.7
Liver	16.3 ± 0.9	9.2 ± 0.5	13.8 ± 0.7
Mouse 4 Spleen	43.7 ± 4.2	33.1 ± 8.0	35.4 ± 1.8
Kidney (left)	7.3 ± 0.6	5.9 ± 1.1	5.0 ± 0.2
Kidney (right)	9.8 ± 0.5	7.2 ± 0.6	6.9 ± 0.3
Bladder	2.1 ± 0.2	0.0 ± 0.0	0.3 ± 0.0

4.4. Discussion and conclusion

In this study, we demonstrated the feasibility of Spectral CT for quantification of iodine in mice. Our approach comprised a multimodal imaging approach using a radiolabeled iodinated blood pool agent for image-based quantification with SPECT and Spectral CT. The radiolabeled iodinated emulsion allows relating ^{111}In activity quantified with SPECT to amounts of iodine, while Spectral CT and ICP-MS determine directly the iodine concentration. Good correlations were observed between all three quantification methods over a concentration range of 0.2 mM < [iodine] < 60 mM found in different tissues. At lower concentrations (<18 mM), we observe a high correlation between iodine quantification by Spectral CT and ICP-MS, indicating that Spectral CT has a high quantitative accuracy and is able to detect iodine tissue concentrations as low as 2 mM. Concentrations lower than 2 mM were difficult to determine due to noise in the transmission spectrum.

For higher iodine concentrations, a number of outliers were observed for Spectral CT compared to ICP-based data and as well for SPECT-based quantification, though for different specimens (Fig. 7). We believe that more practical rather than systematic reasons lead to this finding. For imaging based quantification, the VOIs were drawn around entire organs therefore including also major blood vessels within the organs. However, for ICP based quantification, the tissue specimen should match the organ defined by the VOI, which in practice appeared very challenging especially at the border of the vascular system and organs. Furthermore, cutting through blood vessels during dissection leads to a loss of blood from the specimen, resulting in an error, since dissection then alters the concentration of iodine measured in the organs by ICP-MS. Above affects mainly quantification in organs with high iodine uptake such as liver and spleen and may explain the deviations observed in Figure 7. Furthermore, the size distribution of the radiolabeled iodinated emulsion leads to an increase of iodine to ^{111}In ratio for increasing particle size and affects as well the organ uptake. Smaller particles are in general cleared and taken up to a higher extent by the spleen compared to larger nanoparticles that are preferentially taken up in the liver. Above effects related to particle size distribution will cause a mismatch between the quantification of SPECT compared to Spectral CT as well as ICP-MS data. Potential errors coming from the employed empirical calibration method are considered negligible as the fit of the calibration only showed minor deviations (Fig. 3).

Spectral CT does not require the acquisition of a pre-injection image comparable to the nuclear imaging modalities SPECT and PET. Though nuclear imaging techniques allow tracer quantification with pico- to nanomolar sensitivity, they suffer from very low spatial resolution as well as the lack of morphological information [34]. Consequently, nuclear

modalities are combined with imaging techniques such as CT or MRI for a high resolution anatomical overlay. Spectral CT has the ability to obtain in a single scan anatomical information at high resolution together with the ability to quantify contrast agents though higher contrast agent concentrations are required as compared to nuclear techniques. In this study, an iodine containing blood pool contrast agent was used for a proof of concept to gather experimental evidence for above statement on Spectral CT based quantification. Iodine is the most common clinically used element for contrast enhanced CT imaging. For preclinical research, its K-edge properties are suitable for small animal imaging [35], but translating the K-edge imaging of iodine to a clinical setting is challenging due to photon starvation at low energies. Nevertheless, we believe that the here shown results on quantification of iodine will be applicable to other high-Z elements that are more promising as spectrally detectable contrast agents such as gadolinium [26], gold [29,36] or bismuth [37], suffering to a much smaller extent from photon starvation due to their higher K-edge energies (50.2 keV, 80.7 keV and 90.5 keV, respectively).

We demonstrated the capability of the Spectral CT system in the discrimination between highly attenuating bone (calcium) and iodine. Although the latter has been previously demonstrated in dual energy CT [38], we would like to emphasize that Spectral CT is able to differentiate not only bone from iodine, but simultaneously also other high-Z elements in a single Spectral CT scan. Moreover, and contrary to the dual energy approach, the iodine concentration maps acquired with Spectral CT can be obtained free from artifacts induced by bones or calcified calcifications. The latter is of special importance to image and characterize atherosclerotic plaques.

Currently, the most important shortcoming of Spectral CT is the long scanning time of the used Spectral CT prototype scanner and needs to be improved to be able to perform *in vivo* studies. Several options exist: 1) Increasing the count-rate capability of the detection system. The highest reported count rate achieved in photon-counting detectors of 150 Mcps/mm² (ChromAIX ASIC [39]) is already about 1000 times faster than the detector used in this study, but is still significantly lower than the count rates in state-of-the-art clinical scanners. 2) Increasing the number of detector rows [24]. Already the use of large area detectors with several hundreds of detector rows, as it is common practice in pre-clinical CT, would reduce the scanning time to more acceptable levels; 3) Reduction of the detector pixel size to distribute counts over a larger number of electronic channels; 4) Use of bow-tie filters to reduce the dynamic range requirements for the detector array; 5) Introduction of pileup models in reconstruction to avoid image artifacts from data acquired at high-flux [40].

All options are currently being investigated making it quite likely that future Spectral CT systems are able to handle the clinically used X-ray fluxes. Additional benefits of Spectral CT in clinical use would be a reduction in the radiation dose administered to the patient in comparison with conventional CT due to the much improved dynamic range in the low flux region and by means of spectral, iterative image reconstruction techniques.

In summary, we demonstrated that Spectral CT is able to quantify iodine concentrations in different organs of mice and allows differentiating between high-Z elements such as calcium or iodine. Benchmarked against ICP-MS data, Spectral CT quantification is comparable to SPECT based quantification. We expect that Spectral CT is by no means restricted to the mentioned clinical applications and will find a broader application in near future.

Practical applications

Spectral CT is a technique that enables delineation between high attenuating atoms such as calcium and CT contrast agents by using energy resolved photon-counting detectors. It furthermore is able to quantify high-Z elements in a single scan. Spectral CT has a favorable dynamic range in the low flux region which holds the potential to reduce the radiation patient dose, which is additionally reduced by the fact that Spectral CT does not the acquisition of a pre-injection image. We emphasize applications in calcification scoring in atherosclerotic plaque detection in the presence of contrast agents and in other diseases such as bowel disease and staging of carcinomas.

Acknowledgements

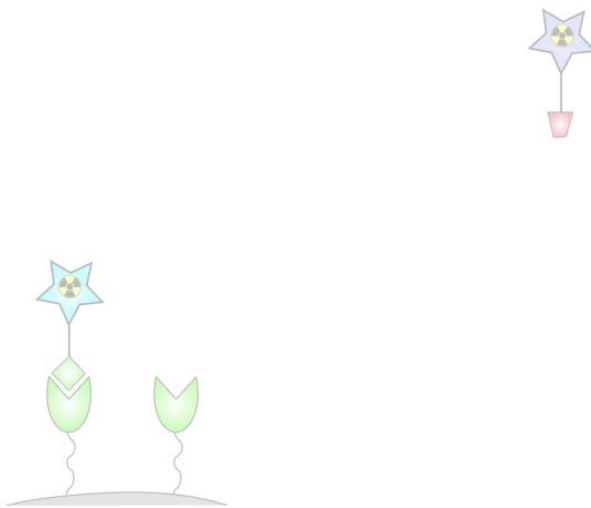
We would like to acknowledge Carlijn van Helvert and Katia Donato for their help in the experiments and data analysis and Johan Lub and Erica Custers for their help in the synthesis of the DOTA-PBD-PEO block copolymer. We also thank Alexander Fischer, Eike Gegenmantel and Timo Paulus of Philips Research Laboratories in Aachen (Germany) for their help with the Philips IMALYTICS Translational Research Workstation. Furthermore, we would like to acknowledge Marcel Verheijen for the cryo-TEM images and Carry Hermans for her invaluable help in the ICP-MS analysis of the iodine samples.

4.5. References

- [1] Novelline RA, Rhea JT, Bell T. Helical CT of abdominal trauma. *Radiol Clin North Am.* 1999;37:591-612, vi-vii.
- [2] Blackmore CC, Ramsey SD, Mann FA, Deyo RA. Cervical spine screening with CT in trauma patients: a cost-effectiveness analysis. *Radiology.* 1999;212:117-25.
- [3] Huber-Wagner S, Lefering R, Qvick LM, Korner M, Kay MV, Pfeifer KJ, et al. Effect of whole-body CT during trauma resuscitation on survival: a retrospective, multicentre study. *Lancet.* 2009;373:1455-61.
- [4] Boehm HF, Link TM. Bone imaging: traditional techniques and their interpretation. *Curr Osteoporos Rep.* 2004;2:41-6.
- [5] Singer A. Osteoporosis diagnosis and screening. *Clin Cornerstone.* 2006;8:9-18.
- [6] Swensen SJ, Jett JR, Hartman TE, Midthun DE, Mandrekar SJ, Hillman SL, et al. CT screening for lung cancer: five-year prospective experience. *Radiology.* 2005;235:259-65.
- [7] Nieman K, Oudkerk M, Rensing BJ, van Ooijen P, Munne A, van Geuns RJ, et al. Coronary angiography with multi-slice computed tomography. *Lancet.* 2001;357:599-603.
- [8] Johnson PT, Pannu HK, Fishman EK. IV contrast infusion for coronary artery CT angiography: literature review and results of a nationwide survey. *AJR Am J Roentgenol.* 2009;192:W214-21.
- [9] Weininger M, Barraza JM, Kemper CA, Kalafut JF, Costello P, Schoepf UJ. Cardiothoracic CT angiography: current contrast medium delivery strategies. *AJR Am J Roentgenol.* 2011;196:W260-72.
- [10] O'Connor OJ, Maher MM. CT urography. *AJR Am J Roentgenol.* 2010;195:W320-4.
- [11] Iyer RB, Silverman PM, Tamm EP, Dunnington JS, DuBrow RA. Diagnosis, staging, and follow-up of esophageal cancer. *AJR Am J Roentgenol.* 2003;181:785-93.
- [12] Albani JM, Ciaschini MW, Streem SB, Herts BR, Angermeier KW. The role of computerized tomographic urography in the initial evaluation of hematuria. *J Urol.* 2007;177:644-8.
- [13] Sohaib SA, Koh DM, Husband JE. The role of imaging in the diagnosis, staging, and management of testicular cancer. *AJR Am J Roentgenol.* 2008;191:387-95.
- [14] Catalano C, Laghi A, Fraioli F, Pediconi F, Napoli A, Danti M, et al. Pancreatic carcinoma: the role of high-resolution multislice spiral CT in the diagnosis and assessment of resectability. *Eur Radiol.* 2003;13:149-56.
- [15] Zhao H, Zhou KR, Yan FH. Role of multiphase scans by multirow-detector helical CT in detecting small hepatocellular carcinoma. *World J Gastroenterol.* 2003;9:2198-201.
- [16] Sahani DV, Holalkere NS, Mueller PR, Zhu AX. Advanced hepatocellular carcinoma: CT perfusion of liver and tumor tissue - initial experience. *Radiology.* 2007;243:736-43.
- [17] Zhao H, Yao JL, Wang Y, Zhou KR. Detection of small hepatocellular carcinoma: comparison of dynamic enhancement magnetic resonance imaging and multiphase multirow-detector helical CT scanning. *World J Gastroenterol.* 2007;13:1252-6.
- [18] Rubinshtein R, Halon DA, Lewis BS. Prognostic value of non-invasive coronary computed tomography angiography: where are we now? *Int J Cardiovasc Imaging.* 2010.
- [19] Leoni S, Piscaglia F, Golfieri R, Camaggi V, Vidili G, Pini P, et al. The impact of vascular and nonvascular findings on the noninvasive diagnosis of small hepatocellular carcinoma based on the EASL and AASLD criteria. *Am J Gastroenterol.* 2010;105:599-609.
- [20] Ayyappan AP, Jhaveri KS. CT and MRI of hepatocellular carcinoma: an update. *Expert Rev Anticancer Ther.* 2010;10:507-19.
- [21] Ippolito D, Sironi S, Pozzi M, Antolini L, Ratti L, Alberzoni C, et al. Hepatocellular carcinoma in cirrhotic liver disease: functional computed tomography with perfusion imaging in the assessment of tumor vascularization. *Acad Radiol.* 2008;15:919-27.
- [22] Ippolito D, Sironi S, Pozzi M, Antolini L, Invernizzi F, Ratti L, et al. Perfusion CT in cirrhotic patients with early stage hepatocellular carcinoma: assessment of tumor-related vascularization. *Eur J Radiol.* 2010;73:148-52.
- [23] Goetti R, Leschka S, Desbiolles L, Klotz E, Samaras P, von Boehmer L, et al. Quantitative computed tomography liver perfusion imaging using dynamic spiral scanning with variable pitch: feasibility and initial results in patients with cancer metastases. *Invest Radiol.* 2010;45:419-26.
- [24] Rubin GD. MDCT imaging of the aorta and peripheral vessels. *Eur J Radiol.* 2003;45 Suppl 1:S42-9.
- [25] Budoff MJ, Achenbach S, Blumenthal RS, Carr JJ, Goldin JG, Greenland P, et al. Assessment of coronary artery disease by cardiac computed tomography: a scientific statement from the American Heart Association Committee on Cardiovascular Imaging and Intervention, Council on Cardiovascular Radiology and Intervention, and Committee on Cardiac Imaging, Council on Clinical Cardiology. *Circulation.* 2006;114:1761-91.

- [26] Schlomka JP, Roessl E, Dorscheid R, Dill S, Martens G, Istel T, et al. Experimental feasibility of multi-energy photon-counting K-edge imaging in pre-clinical computed tomography. *Phys Med Biol*. 2008;53:4031-47.
- [27] Roessl E, Proksa R. K-edge imaging in X-ray computed tomography using multi-bin photon counting detectors. *Phys Med Biol*. 2007;52:4679-96.
- [28] Feuerlein S, Roessl E, Proksa R, Martens G, Klass O, Jeltsch M, et al. Multienergy photon-counting K-edge imaging: potential for improved luminal depiction in vascular imaging. *Radiology*. 2008;249:1010-6.
- [29] Cormode DP, Roessl E, Thran A, Skajaa T, Gordon RE, Schlomka JP, et al. Atherosclerotic plaque composition: analysis with multicolor CT and targeted gold nanoparticles. *Radiology*. 2010;256:774-82.
- [30] Stenner P, Berkus T, Kachelriess M. Empirical dual energy calibration (EDEC) for cone-beam computed tomography. *Med Phys*. 2007;34:3630-41.
- [31] Brendel B, Roessl E, Schlomka JP, Proksa R. Empirical, projection-based basis-component decomposition method. *Medical Imaging 2009: Physics of medical Imaging. Proceedings of SPIE 2009;7258:72583Y1-Y8*.
- [32] de Vries A, Custers E, Lub J, van den Bosch S, Nicolay K, Gröll H. Block-copolymer-stabilized iodinated emulsions for use as CT contrast agents. *Biomaterials*. 2010;31:6537-44.
- [33] Hubbell JH, Seltzer SM. "Tables of X-ray mass attenuation coefficients and mass energy absorption coefficients (Table 3)," (National Institute of Standards and Technology, Gaithersburg, MD, 2011). <http://physics.nist.gov>.
- [34] Pysz MA, Gambhir SS, Willmann JK. Molecular imaging: current status and emerging strategies. *Clin Radiol*. 2010;65:500-16.
- [35] Riederer SJ, Mistretta CA. Selective iodine imaging using K-edge energies in computerized X-ray tomography. *Med Phys*. 1977;4:474-81.
- [36] Roessl E, Cormode DP, Brendel B, Engel KJ, Martens G, Thran A, et al. Preclinical spectral computed tomography of gold-nanoparticles. *Nuclear Instruments and Methods in Physics Research A*. 2010;doi: 10.1016/j.nima.2010.11.072.
- [37] Pan D, Roessl E, Schlomka JP, Caruthers SD, Senpan A, Scott MJ, et al. Computed tomography in color: NanoK-enhanced spectral CT molecular imaging. *Angew Chem Int Ed Engl*. 2010;49:9635-9.
- [38] Johnson TR, Krauss B, Sedlmair M, Grasruck M, Bruder H, Morhard D, et al. Material differentiation by dual energy CT: initial experience. *Eur Radiol*. 2007;17:1510-7.
- [39] Steadman R, Herrmann C, Mühlens O, Maeding DG, Colley J, Firlit T, et al. ChromAIX: A high-rate energy-resolving photon-counting ASIC for Spectral Computed Tomography. *Medical Imaging 2010: Physics of medical Imaging. Proceedings of SPIE 2010;7622:762220-1-8*.
- [40] Taguchi K, Frey EC, Wang X, Iwanczyk JS, Barber WC. An analytical model of the effects of pulse pileup on the energy spectrum recorded by energy resolved photon counting X-ray detectors. *Med Phys*. 2010;37:3957-69.

Dual-isotope $^{111}\text{In}/^{177}\text{Lu}$ SPECT imaging as a tool in molecular imaging tracer design



Based on

Dual-isotope $^{111}\text{In}/^{177}\text{Lu}$ SPECT imaging as a tool in molecular imaging tracer design

N.M. Hijnen, A. d. Vries, K. Nicolay and H. Gröll

Accepted for publication in Contrast Media & Molecular Imaging

Abstract

The synthesis, design, and subsequent pre-clinical testing of new molecular imaging tracers are topic of extensive research in healthcare. Quantitative dual-isotope SPECT imaging is proposed here as a tool in the design and validation of such tracers, as it can be used to quantify and compare the biodistribution of a specific ligand and its non-specific control ligand, labeled with two different radionuclides, in the same animal. Since the biodistribution results are not blurred by experimental or physiological inter-animal variations, this approach allows determining the ligands net targeting effect. However, dual-isotope quantification is complicated by cross-talk between the two radionuclides used and the radionuclides should not influence the biodistribution of the tracer. Here, we developed a quantitative dual-isotope SPECT protocol using combined ^{111}In and ^{177}Lu and tested this tool for a well-known angiogenesis specific ligand (cRGDfK peptide) in comparison to a potential non-specific control (cRADfK peptide). Dual-isotope SPECT imaging of the peptides showed a similar organ and tumor uptake as single-isotope studies (cRGDfK-DOTA: 1.5 ± 0.8 %ID/cm³, cRADfK-DOTA: 0.2 ± 0.1 %ID/cm³) but with higher statistical relevance (p-value: 0.007, $n = 8$). This demonstrated that for the same relevance, 7 animals were required in case of a single-isotope test design as compared to only 3 animals when a dual-isotope test was used. Interchanging radionuclides did not influence the biodistribution of the peptides. Dual-isotope SPECT after simultaneous injection of ^{111}In and ^{177}Lu labeled cRGD and cRAD was shown to be a valuable method for paired testing of the *in vivo* target specificity of ligands in molecular imaging tracer design.

5.1. Introduction

Molecular imaging aims at earlier and more specific detection by imaging disease-related molecular and cellular processes that precede morphological changes. Key are molecular imaging tracers that specifically home in on disease related molecular markers and render them detectable with one of the diagnostic imaging techniques. Consequently, synthesis and design of new molecular imaging tracers, their subsequent pre-clinical testing and clinical validation is a topic of extensive research [1].

Disease-related markers typically have expression levels in the pM to nM range, leading to similar concentrations of bound imaging agents [2]. Therefore, sensitive optical techniques or nuclear techniques like Positron Emission Tomography (PET) and Single Photon Emission Computed Tomography (SPECT) seem to be the most suited modalities for molecular imaging as they allow detection of tracers in the pM to nM range [2]. While PET imaging is currently more sensitive than SPECT and allows more absolute quantification, SPECT has an advantage over PET when it comes to simultaneous imaging of two different radionuclides, i.e. dual-isotope imaging. The cameras used in SPECT scanners are equipped with energy resolved detectors that can distinguish between different γ -emitting radionuclides based on their differences in emission energies. Simultaneous detection of multiple probes with different spectral characteristics is also possible with optical imaging, however direct quantification is more difficult in optical imaging due to absorption and light scattering.

Though there are several clinical examples of dual-isotope SPECT in cardiac imaging [3], brain imaging [4], or osteomyelitis [5,6], broad clinical adoption is still lacking. In pre-clinical research, a dual-isotope approach recently showed its value to investigate organ function [7] or to unravel biological mechanisms, for example the activation of peptide-based molecular imaging probes *in vivo* [8]. We expect that quantitative dual-isotope imaging also holds great potential as a tool in the design and validation of new molecular imaging tracers, since it can be used to quantify and compare the biodistribution of a specific ligand and its non-specific control ligand, labeled with two different γ -emitting radionuclides, simultaneously in the same animal. Here, we present a dual-isotope imaging approach that enables the investigation of the net uptake of a tracer by eliminating any inter-animal differences and physiological changes (Fig. 1). This paired design leads to less degrees of freedom compared with the usually performed unpaired testing and therefore to a decrease in the amount of animals that will be required to obtain a statistically relevant result.

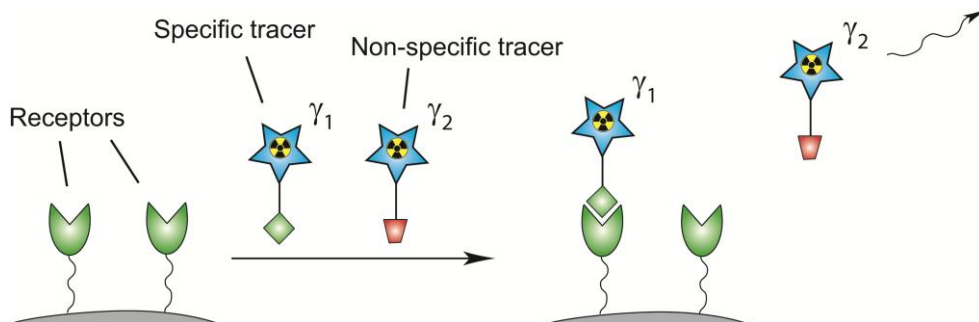


Figure 1. Specific and non-specific tracer simultaneously in one animal, to be imaged with dual-isotope SPECT.

One of the reasons that broad clinical application of dual-isotope SPECT is lacking is the challenge to obtain quantitative information from dual-isotope SPECT scans [9,10]. Overlap in the emission spectra of the two respective radionuclides as well as Compton scattering will result in crosstalk between the signals coming from these radionuclides. Crosstalk is defined as the detection of photons originating from one radionuclide in the acquisition window of the other, and results in artefacts and quantification errors [9,11]. Therefore, quantitative dual-isotope imaging requires the development of new protocols as compared with conventional single-isotope imaging to compensate for crosstalk effects. Examples of such methods include the use of additional energy windows that allow quantification of the extent of the crosstalk followed by subtraction or model-based methods [9,12]. Another approach is to minimize crosstalk effects by re-positioning the acquisition energy window and careful choice of the radionuclide combination used (Table 1). To date, the radionuclide combinations that are used most often for dual-isotope imaging include combined $^{123}\text{I}/^{99\text{m}}\text{Tc}$ [4], $^{201}\text{Tl}/^{99\text{m}}\text{Tc}$ [13], $^{131}\text{I}/^{99\text{m}}\text{Tc}$ [14], and $^{111}\text{In}/^{99\text{m}}\text{Tc}$ [15]. However, for the purpose of comparing the biodistribution of a specific ligand directly to its non-specific control, the choice of radionuclides is restricted since both radionuclides have to be suited for radiolabeling the ligands via the same chelator. The latter is of great importance since the chelator itself could change the biodistribution of the tracer, thereby hindering direct comparison of the ligands. Herein, the DOTA chelator (1,4,7,10-tetraazacyclododecane-N,N',N'',N''' tetraacetic acid) is the preferred choice since its macrocyclic structure in general forms more stable chelates than the DTPA chelator (diethylene triamine pentaacetic acid) [16]. Furthermore, the radionuclides itself should not have a different effect on the biodistribution, or influence the binding affinity of the ligands. Finally, the radionuclides require a half-life that is similar to each other and suitable for the study duration. Above requirements led us to choose ^{111}In and ^{177}Lu as a radionuclide couple, though we are aware that ^{177}Lu is not ideal for use in diagnostic clinical imaging studies due to its beta emission.

In this work, we developed and optimized a quantitative $^{111}\text{In}/^{177}\text{Lu}$ dual-isotope SPECT imaging protocol to establish it as a tool in pre-clinical tracer design. For this methodological study, we decided to use the well characterized angiogenesis-specific ligand cyclic arginine-glycine-aspartate peptide (cRGD) [17] in direct comparison to cyclic arginine-alanine-aspartate peptide (cRAD) that serves as internal control. The cRGD peptide is known to have a high affinity for the $\alpha_v\beta_3$ cell surface integrin, which is over-expressed on specific tumor cells and endothelial cells in angiogenic blood vessels [18-24]. In cRAD, the glycine residue is changed into alanine, and it was suggested that with this mutation the affinity for $\alpha_v\beta_3$ -integrin is lost [25,26]. As a proof of concept, we carried out a dual-isotope SPECT study to investigate how this minor difference in chemical structure translates into loss of specificity and potential changes in the biodistribution. As dual-isotope allows the direct comparison in the same animal, we expect to come to statistical relevant data with less animals compared with the classical approach using an unpaired study design.

Table 1. Radiochemical properties of γ -emitting radionuclides used for SPECT imaging.

Radionuclide	$t_{1/2}$ (days)	Peak 1 (abundance)	Peak 2 (abundance)	Peak 3 (abundance)	Chelate
$^{99\text{m}}\text{Technetium}$	0.3	141 keV (89%)	-	-	DTPA
$^{111}\text{Indium}$	2.8	171 keV (91%)	245 keV (94%)	-	DTPA, DOTA
$^{123}\text{Iodine}$	0.6	159 keV (83%)	-	-	Covalent
$^{125}\text{Iodine}$	59.4	35 keV (7%)	-	-	Covalent
$^{131}\text{Iodine}$	8.0	80 keV (3%)	284 keV (6%)	365 keV (81%)	Covalent
$^{177}\text{Lutetium}$	6.7	57 keV (X-ray 5%)	113 keV (6%)	208 keV (11%)	DOTA
$^{201}\text{Thallium}$	3.0	72 keV (Hg X-ray 94%)	167 keV (10%)	-	DTPA

5.2. Materials and Methods

5.2.1. Dual-isotope optimization

The $^{111}\text{In}/^{177}\text{Lu}$ combination was analyzed and optimized, measuring crosstalk severity and sensitivity for different energy window settings. All measurements were performed on a small animal SPECT/CT system (nanoSPECT/CT®, Bioscan, USA) equipped with four detector heads and converging 9-pinhole collimators (pinhole diameter: 1 mm, max. resolution: 0.8 mm). The amount of initially measured crosstalk was minimized by optimizing the acquisition energy windows for both radionuclides. The crosstalk was quantified in form of a crosstalk factor, which was defined as:

$$\gamma_1' = \gamma_1 - A\gamma_2 \quad \text{and} \quad \gamma_2' = \gamma_2 - B\gamma_1$$

with A and B being crosstalk factors from radionuclide γ_2 to radionuclide γ_1 and γ_1 to γ_2 respectively. The factors used for phantom studies were determined by placing a known amount of one radionuclide in the scanner (γ_2 , approximately 20 MBq, >100 kcounts per projection in 120 to 360 seconds), and acquire the signal using the energy window settings for both radionuclides. The crosstalk factor (A) was defined as the ratio between the amount of counts measured in the window for radionuclide γ_1 and the amount of counts measured in the window of radionuclide γ_2 . Besides overlap of the emission peaks, the crosstalk factors depend on the amount of Compton scattering. As Compton scattering and attenuation effects increase under *in vivo* conditions, the crosstalk factors were determined again in mice to allow *in vivo* studies.

Table 2. Phantom and *in vivo* crosstalk factors (cc-factor) from γ_1 to γ_2 ($\gamma_1 \rightarrow \gamma_2$) and *vice versa* as measured on the SPECT/CT.

Setting [#]	Phantom cc-factor $^{177}\text{Lu} \rightarrow ^{111}\text{In}$	Phantom cc-factor $^{111}\text{In} \rightarrow ^{177}\text{Lu}$	In vivo cc-factor $^{177}\text{Lu} \rightarrow ^{111}\text{In}$	In vivo cc-factor $^{111}\text{In} \rightarrow ^{177}\text{Lu}$
1	0.0682 ± 0.0004*	0.1489 ± 0.0003*	0.1253 ± 0.0134*†	0.2034 ± 0.0022*†
2	0.0913 ± 0.0009*	0.0273 ± 0.0002*	0.1798 ± 0.0220*†	0.0400 ± 0.0003*†

[#] The acquisition energy windows settings corresponding to setting 1 and 2 are stated in the text.

* Measured in threefold using static planar scans, acquiring > 100 kcounts per projection (mean value ± SD).

† Measured in BALB/c nu/nu mice (average weight: 24 g).

The crosstalk factors measured for the $^{111}\text{In}/^{177}\text{Lu}$ settings that were optimal in sensitivity and minimized in crosstalk in both phantoms and *in vivo* are shown in Table 2. The first setting consisted of four separate energy windows: a 20% window around 171 keV (from 153.9 keV to 188.1 keV) and a 15% window around 245 keV (226.6 - 263.4 keV) for ^{111}In -acquisition, and two 20% windows around 113 keV (101.7 - 124.3 keV) and 208 keV (187.2 - 228.8 keV) for ^{177}Lu -acquisition. In the second acquisition setting, the ^{177}Lu energy window around 113 keV was removed since this window was

highly affected by the ^{111}In signal. Furthermore, all windows were reduced in size to 10% around 171 keV (162.5 - 179.6 keV), 10% around 245 keV (232.8 - 257.3 keV) and 10% around 208 keV (197.6 - 218.4 keV). As expected, in the second acquisition setting, the sensitivity for both radionuclides was reduced compared with the first acquisition setting by 81% and 38% for ^{111}In and ^{177}Lu respectively. In order to compensate for the loss in sensitivity, the scan-times were increased when using setting 2. The crosstalk remaining after adjusting the energy acquisition windows was partly removed using proprietary crosstalk removal software of the manufacturer (InVivoScope version 1.39, background clean function disabled, Bioscan, USA), which utilized the user defined crosstalk factors to subtract counts originating from radionuclide γ_1 in the acquisition window of radionuclide γ_2 and vice versa.

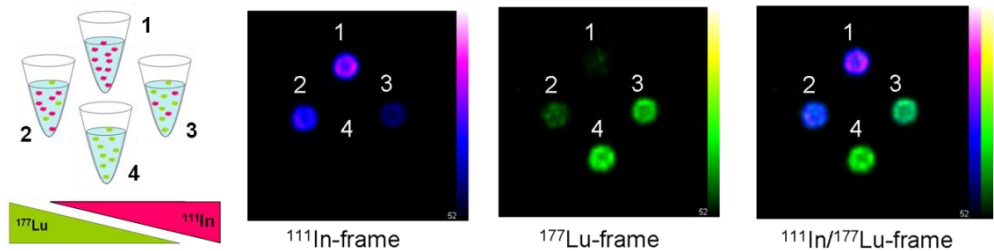


Figure 2. Schematic drawing of the phantom setup used for optimization of the dual-isotope acquisition settings. The phantom consists of four Eppendorf® vials containing different amounts of activity dissolved in a constant volume of water.

The dual-isotope acquisition and crosstalk removal protocols were tested in phantoms by simultaneous scanning of four phantoms containing known amounts of mixed ^{111}In and ^{177}Lu (vial 1: 100% ^{111}In (≈ 7.7 MBq), vial 2: 78% ^{111}In and 25% ^{177}Lu , vial 3: 75% ^{177}Lu and 25% ^{111}In , vial 4: 100% ^{177}Lu (≈ 25.7 MBq), (Fig. 2). The separate activities detected by SPECT were quantified before and after crosstalk removal. The quantification error was calculated for each setting. Based on these results, energy window setting 2 was considered favourable over energy window setting 1 and was therefore used during further experiments (Fig. 3).

The dual-isotope protocol was tested *in vivo* in BALB/c nu/nu mice using free radionuclides as tracer. The biodistribution of ^{111}In and ^{177}Lu was measured separately in single-isotope SPECT studies and compared with the biodistribution measured with dual-isotope SPECT after co-injection. The radiopharmaceuticals were dissolved in physiological tris(hydroxymethyl)aminomethane buffer (100 μL , pH 7.38) or in phosphate buffered saline (PBS, 100 μL) and injected into the tail vein. In case of the dual-isotope scans, the radionuclides were either pre-mixed and co-injected (100 μL) or administered with two separate injections (50 μL each) into the same tail vein.

For ^{177}Lu -scans, approximately 40 MBq activity was injected as opposed to 10 MBq for ^{111}In -scans to compensate for the difference in γ -abundance. Animals were sacrificed by cervical dislocation three hours post-injection and imaged post-mortem to have a direct comparison between imaging and biodistribution data at this time-point.

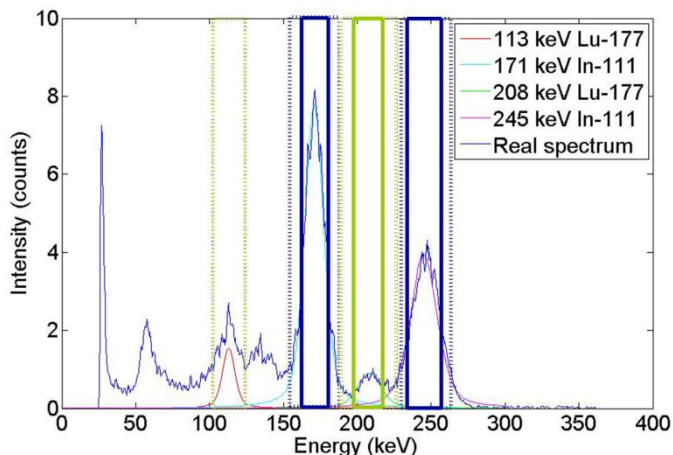


Figure 3. Energy spectrum of $^{111}\text{In}/^{177}\text{Lu}$ dual-isotope SPECT. Dashed rectangles indicate the energy windows as used in single-isotope acquisition (setting 1), solid rectangles indicate the energy windows as in optimal dual-isotope acquisition (setting 2). Green: ^{177}Lu windows, blue: ^{111}In windows.

After image reconstruction, volumes of interest (VOIs) were selected around selected organs and tissues using both SPECT and CT data. All VOIs were drawn in threefold and averaged to minimize drawing variation. Detected counts in the VOIs were converted to Becquerel using a quantification factor that was calculated at the start of each study using a known amount of the radionuclide of interest. The biodistribution results from SPECT were expressed as percent injected dose per volume ($\%ID/\text{cm}^3$). After scanning, the animals were dissected and the radioactivity in blood, heart, lung, liver, spleen, left kidney, muscle and thigh bone was measured in a γ -counter (Wizard 1480, Perkin Elmer, NL) using the multiple isotope counting mode. Control experiments showed that the average deviation in dual-isotope $^{111}\text{In}/^{177}\text{Lu}$ counting from single-isotope ^{111}In or ^{177}Lu counting was $< 2\%$ for both radionuclides. Radioactivity uptake in the tissues was calculated as percent injected dose per gram of tissue ($\%ID/\text{g}$). These values were compared with the radioactive uptake as quantified from SPECT imaging.

5.2.2. DOTA-peptide Conjugation

DOTA was conjugated to cRGDfK and cRADfK for radiolabeling. Acetyl-protected cRGDfK or cRADfK (2 mg, 2.6 μmol in 400 μL H_2O) (Absinth Services B.V., NL) was deacetylated using hydroxylamine solution (1M, 1.9 mL). After 30 minutes at room temperature, the deacetylated cRGDfK or cRADfK was combined with maleimido-mono-amide-DOTA solution (4 mg, 5.2 μmol in 2.7 mL H_2O) (Macrocyclics, USA). The reaction mixture was shaken overnight at room temperature to form cRGDfK-DOTA or cRADfK-DOTA. The desired product was purified using preparative reversed phase high performance liquid chromatography (RP-HPLC) to a purity of > 98%, freeze-dried and dissolved in Millipore-purified water.

5.2.3. Radiolabeling

An aliquot of cRGDfK-DOTA or cRADfK-DOTA solution (1.9 μL , 1.4 nmol) was added to $^{177}\text{LuCl}_3$ (100 MBq) or $^{111}\text{InCl}_3$ (50 MBq) in ammonium acetate buffer or sodium acetate buffer respectively (300 μL , 0.2 M, pH 5.5). The crude mixture was shaken at $T = 353$ K for 30 min before the reaction was quenched by adding 10 μL of a 10 mM EDTA solution. Typically, in these conditions approximately 80% labeling yield was obtained for both peptides with both radionuclides. The radiolabeled peptides were purified by solid phase extraction on C_8 Sep-Pak cartridges (Waters, USA). The product was eluted in two 100 μL fractions of 30% ethanol in Millipore-purified water. The fractions were pooled and concentrated to 80 μL under a stream of nitrogen. Ammonium acetate buffer (0.25 M, pH 8.0) was added to adjust the pH to 7.2.

Both radiotracers solutions exhibited > 95% radiochemical purity at the time of injection, as confirmed by radio-TLC and radio-HPLC. Radio-TLC was performed on ITLC-SG plates (Pall, USA) eluted in a 200 mM EDTA in physiological saline solution and analyzed on a phosphor imager (FLA-7000, Fujifilm, Japan). Under these conditions, ^{111}In -EDTA and ^{177}Lu -EDTA migrated with $R_f = 0.9$ while the radiolabeled peptides remained at the origin ($R_f = 0.0$). Radio-HPLC analysis was carried out on an Agilent 1100 system equipped with a UV detector and a radioactivity Gabi detector (Raytest, Germany). The analyte was loaded on a C18 column (Agilent, Eclipse XDB C18, 150 \times 4.6 mm, 5 μm particle size) which was eluted with a linear elution gradient of 5-40% (v/v) acetonitrile in water with 0.1% formic acid (1 mL/min for 11 minutes), starting with 3 minutes of 5% acetonitrile in water. Free radionuclide eluted from the column after 2.2 minutes, radiolabeled cRGDfK-DOTA and cRADfK-DOTA after 9.5 minutes. The solutions injected in mice contained 1.32 nmol of one peptide for single-isotope experiments (100 μL) or 1.32 nmol of each peptide (100 μL in total) for dual-isotope experiments.

5.2.4. Xenograft Model

The dual-isotope protocol was tested *in vivo* in healthy BALB/c nu/nu mice. The specific $\alpha_v\beta_3$ targeting effect of cRGD was assessed and compared with the cRAD-peptide as the non-binding control. cRGDfK-DOTA and cRADfK-DOTA were both radiolabeled with ^{111}In and ^{177}Lu achieving > 95% radiochemical purity and subsequently injected into tumor-bearing mice. The tumor cell line U87MG was chosen to establish tumor xenografts in nude mice as this cell line is known to show significant over-expression of $\alpha_v\beta_3$ -integrin receptors [27]. Therefore, BALB/c nu/nu mice (male, 11-15 weeks old) were injected with approximately $5 \cdot 10^6$ U87MG cells (human, glioblastoma-astrocytoma, ATCC, Manassas, USA) in phosphate buffered saline (100 μL) subcutaneously on the left or right flank. The mice were imaged when the tumor reached a size of approximately 40 to 60 mm^3 .

The *in vivo* studies performed are listed in Table 2. Both peptides were labeled with both radionuclides to study possible effects of the respective radionuclide on tumor uptake and biodistribution. Two different peptide doses were assessed using ^{177}Lu as radiolabel during the single-isotope studies (0.26 and 1.32 nmol). For the single-isotope studies with ^{111}In and the dual-isotope studies with both ^{111}In and ^{177}Lu 1.32 nmol peptide was used since this was the minimum dose required to obtain sufficiently high activity for SPECT imaging using ^{111}In as radiolabel. The optimal imaging time-point was determined to be one hour after injection based on dynamic scans of the tumor uptake of ^{177}Lu -DOTA-cRGDfK and ^{177}Lu -DOTA-cRADfK. During further experiments, mice were sacrificed at this time-point and imaged post-mortem to have a direct comparison between imaging and biodistribution data at this time-point.

After SPECT and γ -counting, the homogeneity of the activity-uptake in the tumor was assessed by autoradiography using a phosphor imaging system. Two tumors harvested from mice administered with ^{177}Lu -DOTA-cRGDfK were sliced (slice thickness ± 1 mm) and placed on a phosphor imaging plate for two hours. The activity distribution was imaged with 100 μm resolution using the same phosphor imager as for the ITLC plates. All animal experiments were approved by the animal welfare committee of the Maastricht University (the Netherlands) and were performed according to the U.S. National Institutes of Health principles of laboratory animal care [28] and the Dutch national law "Wet op de Dierproeven" (Std 1985, 336).

5.3. Results and discussion

The $^{111}\text{In}/^{177}\text{Lu}$ couple was chosen for dual-isotope imaging based on their radiochemical and physical characteristics. Both radionuclides have a half-life suitable for the study duration, and allow radiolabeling of a ligand via a DOTA chelator. Furthermore, these radionuclides have minimal overlap in the γ -emission energy spectra. The ^{177}Lu radionuclide is, besides a γ -emitter, also a β -emitter used for therapy. Therefore, the $^{111}\text{In}/^{177}\text{Lu}$ radionuclide combination is primarily suitable for use in short-term pre-clinical biodistribution studies where possible radiotoxic effects are not of main importance, although short-term effects on the uptake of other tracers cannot be fully excluded [29].

5.3.1. Dual-isotope optimization

To allow for quantitative $^{111}\text{In}/^{177}\text{Lu}$ SPECT imaging, the acquisition settings were optimized to minimize the amount of crosstalk by adjusting the acquisition energy windows settings. Optimizing the acquisition settings to three 10% energy windows around 171, 208, and 245 keV, resulted in a reduction of the mean error on ^{111}In -quantification of 3.6% to 2.9% and for ^{177}Lu -quantification from 38.0% to 13.9% error in phantoms (Fig. 4A). Crosstalk from ^{111}In to ^{177}Lu was more severe than *vice versa*. Part of the remaining crosstalk could be removed by using a subtraction-based software correction method that made use of a crosstalk calibration factor. After the software correction, the mean error on ^{111}In -quantification in phantoms increased slightly from 2.9% to 3.6%, while the mean error on ^{177}Lu -quantification reduced from 13.9% to 2.3% (Fig. 4B).

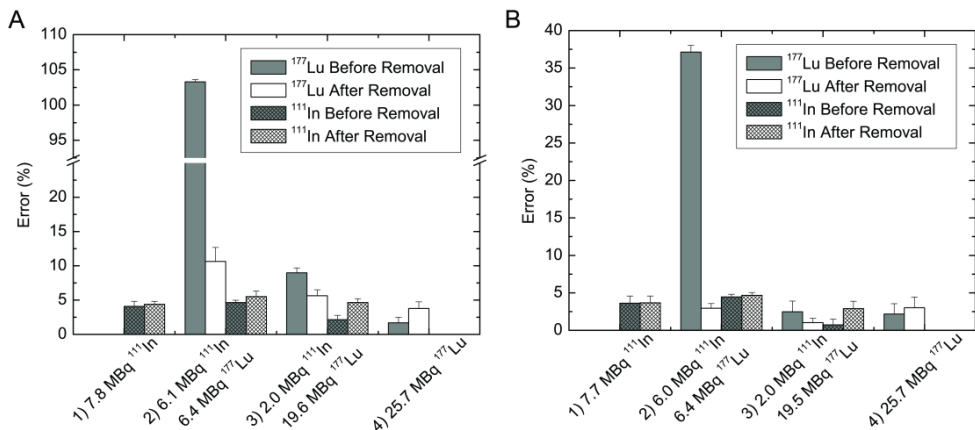


Figure 4. Quantification error percentages for dual-isotope $^{111}\text{In}/^{177}\text{Lu}$ SPECT imaging in phantoms using (A) energy window setting 1 and (B) energy window setting 2.

The dual-isotope protocol was tested in an *in vivo* experiment by studying the biodistribution of the free radionuclides with both single- and dual-isotope acquisition (Fig. 5). The biodistribution of both radionuclides determined with single-isotope SPECT studies corresponded with earlier results reported in literature. In fact, non-carrier-added (n.c.a.) ^{111}In is known to bind to transferrin and other proteins in blood [30] leading to an uptake in liver, while the remaining ^{111}In is eliminated by the kidneys. N.c.a. ^{177}Lu acts as calcium mimic *in vivo* and accumulates in bone [31]. A comparable biodistribution was found for simultaneous injecting both isotopes using dual-isotope SPECT studies and applying crosstalk removal, with no significant ^{111}In related activity detected in the bones, and no significant ^{177}Lu related activity in the kidneys and liver. A linear correlation was found between the biodistribution quantified from single- and dual-isotope SPECT studies (^{111}In : $R^2 \approx 0.94$ and ^{177}Lu : $R^2 \approx 0.92$), supporting the use of dual-isotope $^{111}\text{In}/^{177}\text{Lu}$ SPECT for *in vivo* quantification.

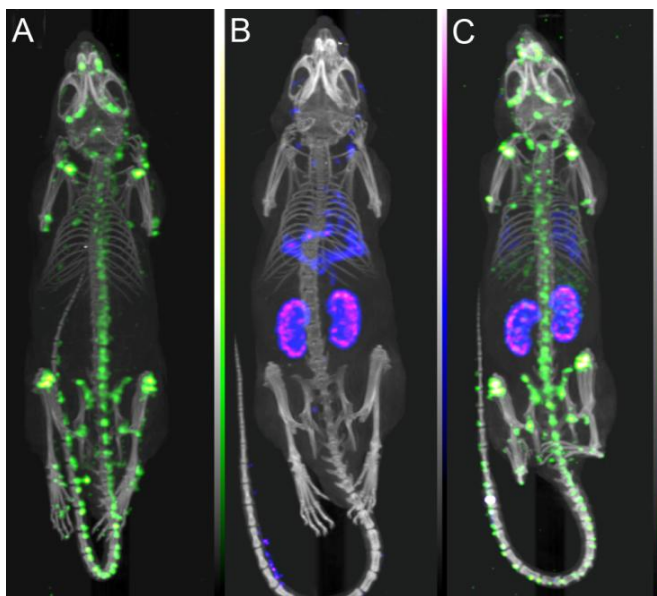


Figure 5. SPECT/CT images of single-isotope acquisition of (A) ^{177}Lu (green), (B) ^{111}In (blue/purple) and (C) dual-isotope simultaneous acquisition of ^{177}Lu (green) and ^{111}In (blue/purple) (all 3 hours circulation time).

5.3.2. Single-isotope

Single-isotope studies showed specific tumor uptake of ^{177}Lu -DOTA-cRGDfK (0.97 ± 0.19 %ID/cm³, Fig. 6A). Most of the injected peptide was eliminated through the urinary system, as confirmed by the presence of high activity in the bladder and some residual activity in the kidneys. No ^{177}Lu activity was found in bone, suggesting tracer stability *in vivo*. The highest tumor uptake was found after injection of low amounts of cRGD (γ -

counting: 6.5 ± 1.9 %ID/g post-injection of 0.26 nmol peptide instead of 1.32 nmol peptide). This finding was in line with previous research in which saturation of the $\alpha_v\beta_3$ -receptors was reported to occur at RGD peptide doses > 0.26 nmol [32], resulting in lower uptake percentages of the injected dose and increased non-specific uptake in the intestines. However, to obtain a sufficiently high activity for SPECT imaging using ^{111}In as radiolabel a minimum peptide dose of 1.32 nmol was required. For exact comparison the same amount of peptide dose should be used for both the specific tracer and the non-specific control. Therefore, 1.32 nmol of each peptide was used during further experiments for both radiolabels, unless otherwise stated.

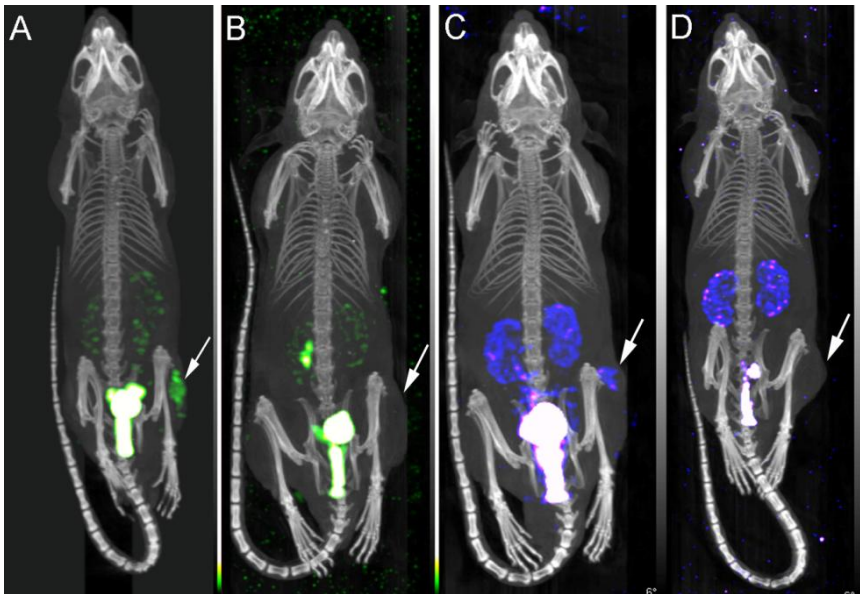


Figure 6. Combined SPECT/CT images of tumor bearing mice 1 hour after injection of (A) 1.32 nmol ^{177}Lu -DOTA-cRGDfK, (B) 1.32 nmol ^{177}Lu -DOTA-cRADfK, (C) 1.32 nmol ^{111}In -DOTA-cRGDfK and (D) 1.32 nmol ^{111}In -DOTA-cRADfK. The white arrows point at the tumor locations.

A similar biodistribution was found with SPECT and γ -counting (linear correlation, $R^2 \approx 0.74$), although quantification of the tissue-uptake from SPECT data consistently resulted in lower uptake percentages than quantification using γ -counting (2.41 ± 0.56 %ID/g tumor uptake using γ -counting compared with 0.97 ± 0.19 %ID/cm³ using SPECT, Fig. 7). Apart from the differences in tissue density that is present in the %ID/cm³ (SPECT) compared with the %ID/g (γ -counter) data, this difference was caused by the method of VOI selection during SPECT analysis. In this method a cylindrical volume was drawn around the tissue of interest, causing an overestimation of the tissue volume which translates to an underestimation in %ID/cm³.

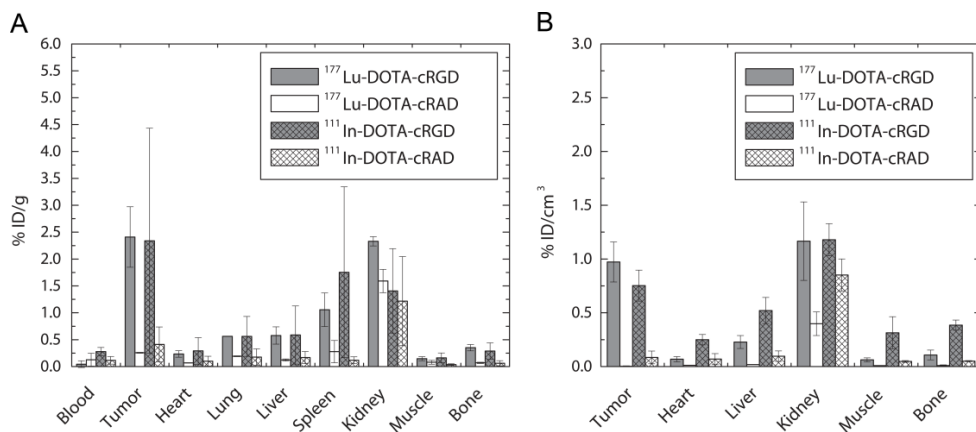


Figure 7. Biodistribution results 1 hour after injection of 1.32 nmol ¹⁷⁷Lu-DOTA-cRGDfK ($n=2$), 1.32 nmol ¹⁷⁷Lu-DOTA-cRADfK ($n=2$), 1.32 nmol ¹¹¹In-DOTA-cRGDfK ($n=2$) and 1.32 nmol ¹¹¹In-DOTA-cRADfK ($n=2$) from (A) γ -counting (%ID/g) and (B) SPECT (%ID/cm³).

Post-injection of ¹⁷⁷Lu-DOTA-cRADfK, no significant tumor uptake was found with both SPECT (0.00 ± 0.00 %ID/cm³) and γ -counting (0.26 ± 0.01 %ID/g) (Fig. 6B, 7B). Apart from the tumor tissue, the biodistribution of ¹⁷⁷Lu-DOTA-cRADfK was similar to that of ¹⁷⁷Lu-DOTA-cRGDfK. The above experiments were repeated for DOTA-cRGDfK and DOTA-cRADfK labeled with ¹¹¹In instead of ¹⁷⁷Lu to assess the influence of the radionuclide on the tracer biodistribution. No difference in biodistribution was observed between ¹¹¹In- and ¹⁷⁷Lu- labeled peptides (Fig. 6C, 6D). As expected, tumor uptake was observed for ¹¹¹In-DOTA-cRGDfK (SPECT: 0.75 ± 0.14 %ID/cm³, γ -counting: 2.34 ± 2.09 %ID/g) but not for ¹¹¹In-DOTA-cRADfK (SPECT: 0.08 ± 0.06 %ID/cm³, γ -counting: 0.41 ± 0.33 %ID/g). The difference in tumor uptake between radiolabeled DOTA-cRGDfK and DOTA-cRADfK was significant based on both the SPECT and γ -counter data separately (1.32 nmol peptide, $n = 8$, P-value ≈ 0.0209 , Kruskal-Wallis test). Taking all single-isotope targeting studies together an even higher significance was obtained (1.32 nmol and 0.26 nmol peptide, $n = 12$, P-value ≈ 0.0039 , Kruskal-Wallis test).

5.3.3. Dual-isotope

For the dual-isotope study, five mice were co-injected with ¹⁷⁷Lu-DOTA-cRGDfK and ¹¹¹In-DOTA-cRADfK (Fig. 8A, 9A). The mice were imaged using the energy windows of setting 2 (10 % windows around 171, 208 and 245 keV) and crosstalk was removed. The ¹⁷⁷Lu-frame showed tumor uptake of the ¹⁷⁷Lu-DOTA-cRGDfK while no tumor uptake of ¹¹¹In-DOTA-cRADfK was visible in the ¹¹¹In-frame. The biodistribution for both tracers was similar to the biodistribution found during single-isotope studies with 1.32 nmol peptide. Tumor uptake of cRGD (SPECT: 1.54 ± 0.92 %ID/cm³, γ -counting: $3.40 \pm$

0.47 %ID/g) and cRAD (SPECT: 0.17 ± 0.08 %ID/cm³, γ -counting: 0.18 ± 0.13 %ID/g) was comparable with the tumor uptake found in single-isotope studies (Table 3). This indicated that co-injection of the tracers did not influence the accumulation of the specific tracer at the target, which is a pre-requisite for using the dual-isotope approach as suggested.

Table 3. Summary of *in vivo* experiments.

DOTA-cRGDfK	DOTA-cRADfK	Amount of peptide (nmol)	<i>n</i> [†]	Tumour-uptake (%ID/cm ³)	Tumour-uptake (%ID/g)
¹⁷⁷ Lu		0.26	2	$1.21 \pm 0.28^*$	$6.46 \pm 1.86^*$
¹⁷⁷ Lu		1.32	2	$0.97 \pm 0.19^*$	$2.41 \pm 0.56^*$
	¹⁷⁷ Lu	0.26	2	$0.11 \pm 0.09^*$	$0.17 \pm 0.16^*$
	¹⁷⁷ Lu	1.32	2	$0.00 \pm 0.00^*$	$0.26 \pm 0.01^*$
¹¹¹ In		1.32	2	$0.75 \pm 0.14^*$	$2.34 \pm 2.09^*$
	¹¹¹ In	1.32	2	$0.08 \pm 0.06^*$	$0.41 \pm 0.33^*$
¹⁷⁷ Lu	¹¹¹ In	1.32	5	$1.54 \pm 0.92^*$; $0.17 \pm 0.08^*$	$3.40 \pm 0.47^*$; $0.18 \pm 0.13^*$
¹¹¹ In	¹⁷⁷ Lu	1.32	4	$1.50 \pm 0.72^*$; $0.26 \pm 0.05^*$	$2.94 \pm 0.31^*$; $0.24 \pm 0.13^*$
¹⁷⁷ Lu, ¹¹¹ In		1.32	2	$1.80 \pm 0.44^*$; $1.58 \pm 0.41^*$	$2.54 \pm 0.91^*$; $2.65 \pm 1.21^*$

* Value \pm SD

[†] *n* = number of animals

Subsequently, four mice were co-injected with ¹¹¹In-DOTA-cRGDfK and ¹⁷⁷Lu-DOTA-cRADfK, in order to investigate any possible changes in biodistribution or binding affinity following radionuclide interchange (as was previously shown to be the case for DOTA-conjugated somatostatin analogues [33]). The mice were imaged one-hour post-injection using the same protocol as for the first group. SPECT dual-isotope showed tumor uptake of ¹¹¹In-DOTA-cRGDfK, while no tumor uptake could be visualized in the corresponding ¹⁷⁷Lu-frame (Fig. 8B). Apart from the tumor-site, the biodistribution of both ligands was similar (Fig. 9B). The quantified tumor uptake corresponded with previous single- and dual-isotope studies (cRGD SPECT: 1.50 ± 0.72 %ID/cm³, cRGD γ -counting: 2.94 ± 0.31 %ID/g; cRAD SPECT: 0.26 ± 0.05 %ID/cm³, cRAD γ -counting: 0.24 ± 0.13 %ID/g; Table 3). Again quantification of the tissue-uptake from SPECT data consistently resulted in lower uptake percentages than quantification using γ -counting. However, the strength of dual-isotope SPECT studies is that the same VOI can be used to quantify both the cRGD and cRAD biodistribution, eliminating this effect in direct comparison. The difference in tumor uptake between radiolabeled DOTA-cRADfK and radiolabeled DOTA-cRGDfK was significant based on both the SPECT and γ -counter data from the dual-isotope studies (1.32 nmol peptide, *n* = 9, P-value: 0.0045, Signed-Rank test).

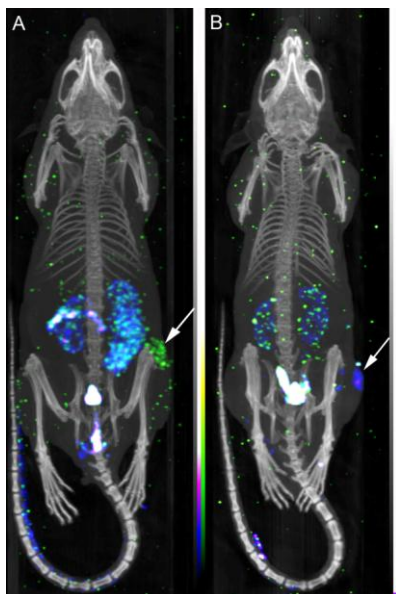


Figure 8. Dual-isotope SPECT/CT images of tumor bearing mice, 1 hour post co-injection of (A) 1.32 nmol ^{177}Lu -DOTA-cRGDfK (yellow-green colormap) and 1.32 nmol ^{111}In -DOTA-cRADfK (blue-purple colormap) and (B) 1.32 nmol ^{111}In -DOTA-cRGDfK (blue-purple colormap) and 1.32 nmol ^{177}Lu -DOTA-cRADfK (yellow-green colormap). The white arrows point at the tumor locations.

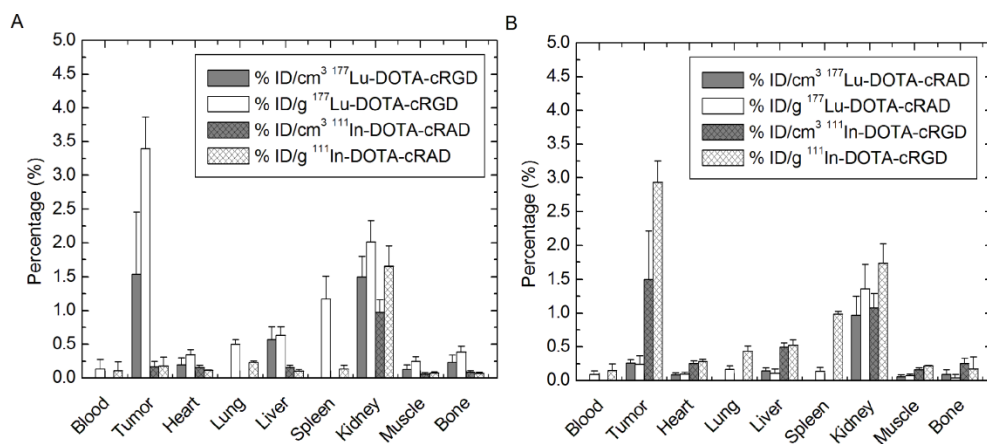


Figure 9. Biodistribution results 1 hour post co-injection of (A) 1.32 nmol ^{177}Lu -DOTA-cRGDfK and 1.32 nmol ^{111}In -DOTA-cRADfK ($n=5$) and (B) 1.32 nmol ^{177}Lu -DOTA-cRADfK and 1.32 nmol ^{111}In -DOTA-cRGDfK ($n=4$) from SPECT (%ID/cm³) and γ -counting (%ID/g).

As final control, two mice were co-injected with ^{177}Lu -DOTA-cRGDfK and ^{111}In -DOTA-cRGDfK. No significant difference between tumor uptake of both tracers was observed (^{177}Lu SPECT: 1.80 ± 0.44 %ID/cm³, ^{177}Lu γ -counting: 2.54 ± 0.91 %ID/g; ^{111}In SPECT: 1.58 ± 0.41 %ID/cm³, ^{111}In γ -counting: 2.65 ± 1.21 %ID/g; Table 3).

5.3.4. Statistics

There are less degrees of freedom when a pair of tracers is assessed in one animal, resulting in a statistical benefit requiring less experiments, and therefore less animals, to obtain a statistically relevant result. In Table 4, an approximation of this effect is illustrated for normally distributed data with equal variances, showing that for the same statistical relevance, 7 animals are required in case of an independent (single-isotope) test design, compared with 3 animals when a paired (dual-isotope) test design is used.

Ranked testing was performed to analyse our data because a normal distribution with equal variances could not be ensured due to the limited sampling size ($n = 8$) (Kruskal-Wallis test for single-isotope (unpaired) and the Signed-Rank test for dual-isotope (paired)). Based on the single-isotope studies, a statistical relevant difference between tumor uptake of radiolabeled cRGD and cRAD was obtained with a P-value of 0.0209 in 8 experiments. With the same amount of experiments in dual-isotope setting, a decrease in P-value was obtained to a P-value of 0.0071. The same statistical relevance was obtained for the single- and dual-isotope data quantified from SPECT imaging and γ -counting, showing that the difference in tissue-uptake percentages between the two methods does not influence the statistics when ranked testing is used. In this paper we show that by using of the dual-isotope approach, the amount of animal studies required for quantification of the net-targeting effect of new molecular imaging tracers can be significantly reduced.

Table 4. Statistical benefit of paired design testing*

Test design	Required sampling size (n)	Example:
Independent	$n = \frac{2(z_\alpha + z_\beta)^2 s^2}{d^2} \ddagger$	$n = \frac{2(1.65 + 1.28)^2 \cdot 0.6^2}{1^2} = 6.18 \ddagger$
Paired	$n = \frac{(z_\alpha + z_\beta)^2 s_d^2}{d^2} \ddagger$	$n = \frac{(1.65 + 1.28)^2 \cdot 0.5^2}{1^2} = 2.15 \ddagger$

* For normally distributed data with equal variances. The formulas only give an approximation when a small sampling size is used (like in this example).

‡ n = sampling size / number of animals

z = z-statistic

α = significance level, for example 5%

$1-\beta$ = power of the test, for example 90% $\rightarrow \beta = 10\%$

s = standard deviation, for example 0.6 %ID/g

s_d = standard deviation of observed differences, for example 0.5 %ID/g

d = relevant effect, for example 1 %ID/g

‡ [34]

5.4. Conclusion

We developed a dual-isotope SPECT protocol on a preclinical SPECT system and tested it for quantification of the biodistribution and tumor uptake of the angiogenesis tracer cRGD compared with its control cRAD. Single- and dual-isotope SPECT imaging as well as biodistribution data obtained with γ -counting showed tumor uptake of cRGD and no significant tumor uptake of cRAD. While having comparable organ uptake, it is concluded that cRAD is a valid non-specific control for cRGD with respect to specific targeting of the $\alpha_v\beta_3$ receptor. Furthermore, the radionuclide used for radiolabeling of both peptides did not influence the biodistribution or binding affinity of the tracer. Using dual-isotope SPECT, the biodistribution of a non-specific control can be quantified simultaneously with the specific tracer in the same animal. Provided that co-injection of both tracers does not affect their individual biodistribution, this approach provides an ideal internal reference and excludes any inter-animal variations and physiological changes, as well as reducing the amount of animals required. We recently showed the value of this dual-isotope approach in the design of matrix metalloproteinase tracers [8] and currently apply it in the development of new molecular imaging ligands.

Acknowledgements

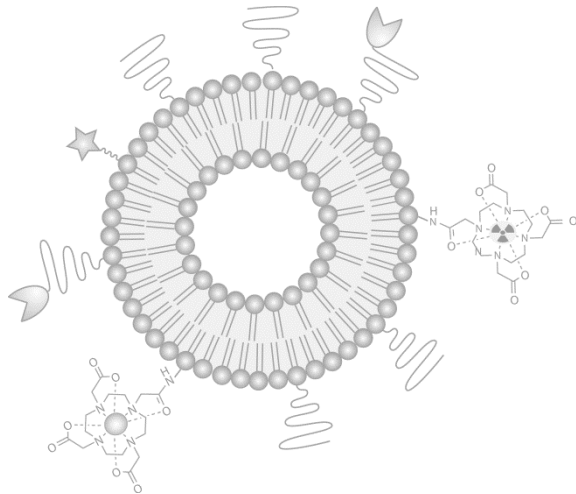
The authors acknowledge Caren van Kammen, Maastricht University for her animal handling expertise, Suzanne Kivits for analyzing SPECT and CT data and Monique Berben (Life Science Facilities, Philips Research) for her help with the biodistribution studies. The authors especially thank Raffa Rossin (Philips Research) for fruitful discussions.

5.5. References

- [1] Weissleder R RB, Rehemtulla A, Gambhir SS. *Molecular Imaging Principles and Practice*. Shelton: People's Medical Publishing House-USA; 2010.
- [2] Blankenberg FG. Molecular imaging: The latest generation of contrast agents and tissue characterization techniques. *J Cell Biochem*. 2003;90:443-53.
- [3] Berman DS, Kang X, Tamarappoo B, Wolak A, Hayes SW, Nakazato R, et al. Stress thallium-201/rest technetium-99m sequential dual-isotope high-speed myocardial perfusion imaging. *JACC Cardiovasc Imaging*. 2009;2:273-82.
- [4] Hsieh PC, Lee IH, Yeh TL, Chen KC, Huang HC, Chen PS, et al. Distribution volume ratio of serotonin and dopamine transporters in euthymic patients with a history of major depression - a dual-isotope SPECT study. *Psychiatry Res*. 2010;184:157-61.
- [5] van der Bruggen W, Bleeker-Rovers CP, Boerman OC, Gotthardt M, Oyen WJ. PET and SPECT in osteomyelitis and prosthetic bone and joint infections: a systematic review. *Semin Nucl Med*. 2010;40:3-15.
- [6] Heiba SI, Kolker D, Mocherla B, Kapoor K, Jiang M, Son H, et al. The optimized evaluation of diabetic foot infection by dual-isotope SPECT/CT imaging protocol. *J Foot Ankle Surg*. 2010;49:529-36.
- [7] Melis M, de Swart J, de Visser M, Berndsen SC, Koelewijn S, Valkema R, et al. Dynamic and static small-animal SPECT in rats for monitoring renal function after 177Lu-labeled Tyr3-octreotate radionuclide therapy. *J Nucl Med*. 2010;51:1962-8.
- [8] van Duijnhoven SM, Robillard MS, Nicolay K, Grull H. Tumor targeting of MMP-2/9 activatable cell-penetrating imaging probes is caused by tumor-independent activation. *J Nucl Med*. 2011;52:279-86.
- [9] Du Y, Frey EC. Quantitative evaluation of simultaneous reconstruction with model-based crosstalk compensation for 99mTc/123I dual-isotope simultaneous acquisition brain SPECT. *Med Phys*. 2009;36:2021-33.
- [10] Kao PF, Wey SP, Yang AS. Simultaneous 99mTc and 123I dual-isotope brain striatal phantom single photon emission computed tomography: validation of 99mTc-TRODAT-1 and 123I-IBZM simultaneous dopamine system brain imaging. *Kaohsiung J Med Sci*. 2009;25:601-7.
- [11] Sanchez-Crespo A, Petersson J, Nyren S, Mure M, Glenn RW, Thorell JO, et al. A novel quantitative dual-isotope method for simultaneous ventilation and perfusion lung SPET. *European journal of nuclear medicine and molecular imaging*. 2002;29:863-75.
- [12] Kadmas DJ, Frey EC, Tsui BM. Simultaneous technetium-99m/thallium-201 SPECT imaging with model-based compensation for cross-contaminating effects. *Phys Med Biol*. 1999;44:1843-60.
- [13] Heo J, Wolmer I, Kegel J, Iskandrian AS. Sequential dual-isotope SPECT imaging with thallium-201 and technetium-99m-sestamibi. *J Nucl Med*. 1994;35:549-53.
- [14] Ceccarelli C, Bianchi F, Trippi D, Brozzi F, Di Martino F, Santini P, et al. Location of functioning metastases from differentiated thyroid carcinoma by simultaneous double isotope acquisition of I-131 whole body scan and bone scan. *J Endocrinol Invest*. 2004;27:866-9.
- [15] Zhu X, Park MA, Gerbaudo VH, Moore SC. Quantitative simultaneous In-111/Tc-99m planar imaging in a long-bone infection phantom. *Phys Med Biol*. 2007;52:7353-65.
- [16] Port M, Idee JM, Medina C, Robic C, Sabatou M, Corot C. Efficiency, thermodynamic and kinetic stability of marketed gadolinium chelates and their possible clinical consequences: a critical review. *Biometals*. 2008;21:469-90.
- [17] Haubner R, Wester HJ, Reuning U, Senekowitsch-Schmidtke R, Diefenbach B, Kessler H, et al. Radiolabeled alpha(v)beta3 integrin antagonists: a new class of tracers for tumor targeting. *J Nucl Med*. 1999;40:1061-71.
- [18] Avraamides CJ, Garmy-Susini B, Varnier JA. Integrins in angiogenesis and lymphangiogenesis. *Nat Rev Cancer*. 2008;8:604-17.
- [19] Brooks PC, Clark RA, Cheresch DA. Requirement of vascular integrin alpha v beta 3 for angiogenesis. *Science*. 1994;264:569-71.
- [20] Haubner R, Wester HJ, Burkhart F, Senekowitsch-Schmidtke R, Weber W, Goodman SL, et al. Glycosylated RGD-containing peptides: tracer for tumor targeting and angiogenesis imaging with improved biokinetics. *J Nucl Med*. 2001;42:326-36.
- [21] Janssen M, Frielink C, Dijkgraaf I, Oyen W, Edwards DS, Liu S, et al. Improved tumor targeting of radiolabeled RGD peptides using rapid dose fractionation. *Cancer Biother Radiopharm*. 2004;19:399-404.

- [22] Beer AJ, Niemeyer M, Carlsen J, Sarbia M, Nahrig J, Watzlowik P, et al. Patterns of alphavbeta3 expression in primary and metastatic human breast cancer as shown by 18F-Galacto-RGD PET. *J Nucl Med.* 2008;49:255-9.
- [23] Ferl GZ, Dumont RA, Hildebrandt IJ, Armijo A, Haubner R, Reischl G, et al. Derivation of a compartmental model for quantifying 64Cu-DOTA-RGD kinetics in tumor-bearing mice. *J Nucl Med.* 2009;50:250-8.
- [24] Sugahara KN, Teesalu T, Karmali PP, Kotamraju VR, Agemy L, Girard OM, et al. Tissue-penetrating delivery of compounds and nanoparticles into tumors. *Cancer Cell.* 2009;16:510-20.
- [25] Kok RJ, Schraa AJ, Bos EJ, Moorlag HE, Asgeirsdottir SA, Everts M, et al. Preparation and functional evaluation of RGD-modified proteins as alpha(v)beta(3) integrin directed therapeutics. *Bioconjug Chem.* 2002;13:128-35.
- [26] Mulder WJ, Strijkers GJ, Habets JW, Bleeker EJ, van der Schaft DW, Storm G, et al. MR molecular imaging and fluorescence microscopy for identification of activated tumor endothelium using a bimodal lipidic nanoparticle. *Faseb J.* 2005;19:2008-10.
- [27] Zhang X, Xiong Z, Wu Y, Cai W, Tseng JR, Gambhir SS, et al. Quantitative PET imaging of tumor integrin alphavbeta3 expression with 18F-FRGD2. *J Nucl Med.* 2006;47:113-21.
- [28] Guide for the use and care of laboratory animals. In: NIH, editor. Washington, DC: National Academy Press; 1985.
- [29] Boyd M, Sorensen A, McCluskey AG, Mairs RJ. Radiation quality-dependent bystander effects elicited by targeted radionuclides. *J Pharm Pharmacol.* 2008;60:951-8.
- [30] Proffitt RT, Williams LE, Presant CA, Tin GW, Uliana JA, Gamble RC, et al. Tumor-imaging potential of liposomes loaded with In-111-NTA: biodistribution in mice. *J Nucl Med.* 1983;24:45-51.
- [31] Breeman WA, van der Wansem K, Bernard BF, van Gameren A, Erion JL, Visser TJ, et al. The addition of DTPA to [177Lu-DOTA0,Tyr3]octreotate prior to administration reduces rat skeleton uptake of radioactivity. *Eur J Nucl Med Mol Imaging.* 2003;30:312-5.
- [32] Dijkgraaf I, Kruijtz JA, Frielink C, Soede AC, Hilbers HW, Oyen WJ, et al. Synthesis and biological evaluation of potent alphavbeta3-integrin receptor antagonists. *Nucl Med Biol.* 2006;33:953-61.
- [33] Antunes P, Ginj M, Zhang H, Waser B, Baum RP, Reubi JC, et al. Are radiogallium-labelled DOTA-conjugated somatostatin analogues superior to those labelled with other radiometals? *Eur J Nucl Med Mol Imaging.* 2007;34:982-93.
- [34] Zielhuis GA. Handleiding medisch-wetenschappelijk onderzoek. Maarssen: Elsevier Gezondheidszorg; 2000. p. 87-98.

Multimodal liposomes for SPECT/MR imaging as a tool for *in situ* relaxivity measurements



Based on

Multimodal liposomes for SPECT/MR imaging as a tool for *in situ* relaxivity measurements

A. d. Vries, M.B. Kok, H.M.H.F. Sanders, K. Nicolay and H. Gröll

Accepted for publication in *Contrast Media & Molecular Imaging*

Abstract

One of the major challenges of MR imaging is the quantification of local concentrations of contrast agents. Cellular uptake strongly influences different parameters such as the water exchange rates and the pool of water protons and results in an altering of the contrast agent's relaxivity, therefore making it difficult to determine contrast agent concentrations based on the MR signal only. Here, we propose a multimodal radiolabeled paramagnetic liposomal contrast agent that allows simultaneous imaging with SPECT and MRI. As SPECT-based quantification allows determining the gadolinium concentration, the MRI signal can be deconvoluted to get an understanding of the cellular location of the contrast agent. The here presented cell experiments indicated a reduction of the relaxivity from $2.7 \pm 0.1 \text{ mM}^{-1}\text{s}^{-1}$ to a net relaxivity of $1.7 \pm 0.3 \text{ mM}^{-1}\text{s}^{-1}$ upon cellular uptake for RGD targeted liposomes by means of the contrast agent concentration as determined by SPECT. This is not observed for nontargeted liposomes that serve as controls. We show that receptor targeted liposomes in comparison to nontargeted liposomes are taken up into cells faster and into subcellular structures of different size. We suggest that the here presented multimodal contrast agent provides a functional readout of its response to the biological environment and is furthermore applicable in *in vivo* measurements. As this approach can be extended to several MRI based contrast mechanisms, we foresee a broader use of multimodal SPECT/MRI nanoparticles to serve as an *in vivo* sensor in biological or medical research.

6.1. Introduction

Magnetic Resonance Imaging (MRI) plays an important role in diagnosis of diseases thanks to its superb soft tissue contrast and high spatial resolution. MR Image generation is based on the proton concentration and on the water protons' magnetic properties that are tissue specific. MR contrast between tissues can be further enhanced with contrast agents (CA) that decrease the longitudinal or transversal relaxation times of water protons (T_1 and T_2 respectively). Clinically used T_1 contrast agents commonly are based on gadolinium (Gd) chelates [1] while T_2 agents are based on iron (Fe) oxides [2]. For applications in molecular imaging [3], drug delivery [4] or cell tracking [5], accurate means to assess tissue concentrations of CA are essential. MRI-based quantification of CA concentration can be approached by measurement of the pre to post CA-induced changes in the T_1 or T_2 relaxation times. In aqueous media, the relaxivity $r_{1,2}$ [$\text{mM}^{-1}\text{s}^{-1}$] relates CA concentration (i.e. expressed in terms of Gd or Fe concentration) to the measured relaxation times $T_{1,2}$ [s]. *In vivo*, the situation becomes more complex as CA may bind to biological compounds or undergo compartmentalization and internalization which modulates parameters such as the tumbling and water exchange rates as well as the pool of water protons that can interact with the CA. These effects lead to an agent relaxivity that is different compared to the *in vitro* relaxivity [6-8]. In this situation, the apparent disadvantage of MRI can be utilized as a tool to investigate the localization of the CA, provided that the local concentration of CA is known. Any approach to quantitative imaging of contrast agents with MRI and the analysis of the *in vivo* relaxivity of MR agents requires *a priori* a determination of the contrast agent concentration by independent means. Gd concentration measurements in tissue by inductively coupled plasma (ICP) are the gold standard, but can obviously only be applied post-mortem, which restricts this method to fundamental research. Dual modal nanoparticles like fluorine based emulsions that carry a high payload of Gd-chelates conjugated to the lipid monolayer offer an elegant way to determine the Gd-concentration based on the fluorine signal quantified with MRI [9,10]. In principle, this approach is well suited for *in vivo* use in order to probe the effective relaxivity, although it suffers from the low MRI sensitivity for fluorine.

Here we propose a radiolabeled paramagnetic liposome (Fig. 1) as a multimodal agent for SPECT/MRI measurements, where the radiolabel allows quantification of the Gd concentration based on SPECT imaging. This type of multimodal nanoparticle can be employed as a tool to investigate interactions between agent and the biological environment providing the relaxivity as read-out. We tested this concept *in vitro* with multimodal nanoparticles carrying cyclic cRGD peptides to target the $\alpha_v\beta_3$ receptor in comparison to nontargeted liposomes. The $\alpha_v\beta_3$ receptor is typically overexpressed on endothelial cells in angiogenic blood vessels of tumors and is considered a biomarker

for cancer [11]. Consequently, our *in vitro* study was performed in cell assays using proliferating human umbilical vein derived endothelial cells (HUVECs) as a model system. Earlier cell studies performed with targeted and nontargeted liposomes as well as multimodal fluorine-based emulsions revealed a systematic decrease of the relaxivity for targeted particles upon uptake into HUVECs due to compartmentalization. Here, liposomes were prepared by thin film hydration and subsequent extrusion following earlier published procedures [12]. The liposomal bilayer contained amphiphilic Gd-chelates, a fluorescently labeled lipid based on rhodamine, and an amphiphilic DOTA ligand conjugated to a lipid construct, which later was used for radiolabeling with indium-111 (^{111}In) for SPECT. A maleimide-lipid was furthermore incorporated in the lipid bilayer as a handle to covalently couple cyclic RGD on the liposomal surface for targeting (RGD-liposomes; non RGD containing liposomes were used as nontargeted controls and will be further referred to as NT-liposomes). Agent quantification based on SPECT was compared to γ -counting and ICP-MS and used to derive cell-associated relaxivities from relaxation time measurements. Confocal laser scanning microscopy (CLSM) was employed to follow the fate and intracellular localization of the agents.

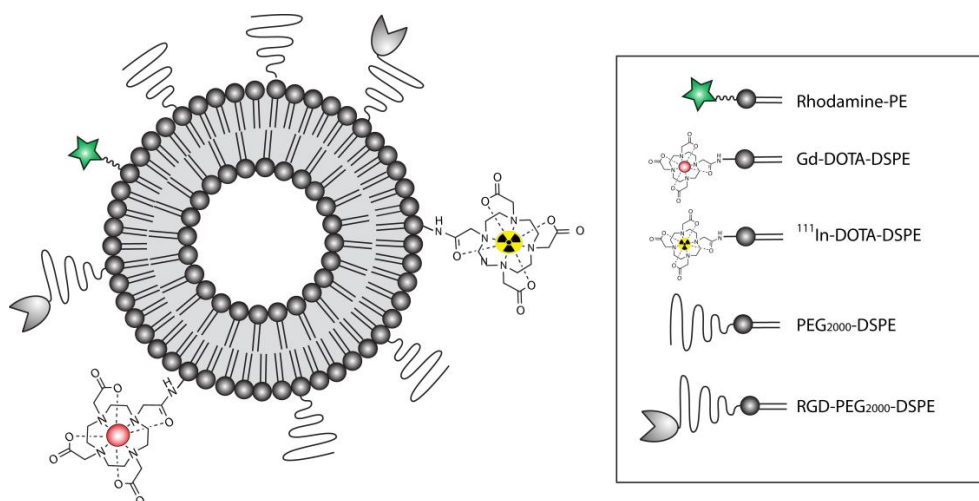


Figure 1. Schematic representation of a multimodal RGD-conjugated liposomal contrast agent. The nanoparticle contains an MR label (Gd-DOTA-DSPE), a radiolabel for SPECT (^{111}In -DOTA-DSPE) and a fluorescent label (Rhodamine-PE).

6.2. Materials and Methods

6.2.1. Materials

1,2-Distearoyl-*sn*-glycero-3-phosphocholine (DSPC), cholesterol, 1,2-distearoyl-*sn*-glycero-3-phosphoethanolamine-N-[methoxy(polyethyleneglycol)-2000] (PEG₂₀₀₀-DSPE), 1,2-distearoyl-*sn*-glycero-3-phosphoethanolamine-N-[maleimide (polyethyleneglycol)-2000] (Mal-PEG₂₀₀₀-DSPE) and 1,2-dipalmitoyl-*sn*-3-phosphoethanolamine-N-[lissamine rhodamine B sulfonyl] (rhodamine-PE) were obtained from Avanti Polar Lipids (Alabaster, AL, USA). 1,2-distearoyl-*sn*-glycero-3-phosphoethanolamine-[tetraazacyclododecane tetraacetic acid] (Gd-DOTA-DSPE) and DOTA-DSPE were purchased from SyMO-Chem (Eindhoven, The Netherlands). Endothelial Growth Medium-2 (EGM-2) and human umbilical vein derived endothelial cells (HUVECs) were ordered with Lonza Bioscience (Switzerland). Monoclonal mouse anti-human CD31 antibody was obtained from Dakocytomation (Glostrup, Denmark). Alexa Fluor 488 conjugated goat anti-mouse secondary antibody was obtained from Molecular Probes Europe BV (Leiden, The Netherlands). Cyclic RGD, c(RGDf(-S-acetylthioacetyl)K) was synthesized by Ansynth Service BV (Roosendaal, The Netherlands). ¹¹¹In originated from Perkin Elmer, Boston, Ma, USA. All other chemicals were obtained from Sigma (St. Louis, MO, USA) and were of analytical grade or the best grade available.

6.2.2. Liposome preparation and characterization

200 nm-diameter liposomes containing Gd-DOTA-DSPE, DOTA-DSPE, DSPC, cholesterol, PEG₂₀₀₀-DSPE and Mal-PEG₂₀₀₀-DSPE at a molar ratio of 0.72/0.03/1.10/1/0.075/0.075 were produced by lipid film hydration and extrusion (400 μmol lipids in total). In short, the lipids were dissolved in a 1:5 v/v methanol:chloroform mixture. As a fluorescent marker, 0.1 mole percent of rhodamine-PE was added. A lipid film was created by drying *in vacuo*. The lipid film was hydrated at 67 °C using a HEPES buffered saline solution (HBS), containing 20 mM HEPES and 135 mM NaCl (pH 6.7). The lipid suspension was extruded at 67 °C, twice through a single 200 nm polycarbonate membrane (Whatman, Kent, UK) and 6 times through a double 200 nm polycarbonate membrane. After extrusion, half of the liposome suspension was modified with a cyclic RGD-peptide (6 μg/μmol total lipid) to target the α_vβ₃-integrin. The cyclic RGD-peptide was deacetylated and coupled to the distal end of Mal-PEG₂₀₀₀-DSPE. After incubation overnight at 4 °C, both batches of liposomes were centrifuged at 310,000 g for 45 min in order to remove possible unconjugated RGD-peptide for the batch containing RGD-liposomes. The pellets were resuspended in HBS (pH 7.4). Lipid concentration was measured by phosphate determination according to Rouser *et al.* [13]. Size and polydispersity index (PDI) of the liposomes were determined with dynamic light scattering (DLS) (Zetasizer Nano, Malvern, UK). Cryogenic transmission electron microscopy (cryo-TEM) pictures were obtained with a FEI TECNAI F30ST electron microscope operated at an accelerating voltage of 300 kV. Sample preparation

was performed by applying a 4 μL droplet of suspension to a holey carbon film and subsequently plunge-freezing this sample into liquid ethane using a Vitrobot. Both the longitudinal and transverse relaxivity were determined at 6.3 T (20°C) by fitting R_1 ($1/T_1$) and R_2 ($1/T_2$) values as a function of the Gd concentration of the liposome suspension as determined using inductively coupled plasma atomic mass spectroscopy (ICP-MS) by Philips Research (Eindhoven, The Netherlands), using the least squares method.

6.2.3. ^{111}In labeling

RGD-liposomes and NT-liposomes were labeled with ^{111}In (Perkin Elmer, Boston, Ma, USA). In detail, 100 μL ammonium acetate buffer (2M NH_4OAc , pH 4.5) was added to a 2.6 mL liposomal solution together with 25 μL of ^{111}In (50 MBq) and the pH was adjusted to 5.0. The sample was stirred at 50 °C for 90 min. Free DTPA (10 μL , 10 mM) was added to the reaction mixture for 15 min to scavenge free radionuclides. Labeling efficiency was checked on silica TLC using 200 mM EDTA as mobile phase and analyzed using a Phosphor Imager (FLA-7000, Fujifilm, Tokyo, Japan). Radiochemical purities obtained were >95% for the RGD-liposomes as well as the NT-liposomes.

6.2.4. Cell culture

Human umbilical vein derived endothelial cells (HUVECs) were used for all the experiments. Cells were stored in liquid nitrogen upon arrival. Before use, the cells were quickly thawed in a water bath ($T=37\text{ }^\circ\text{C}$) and divided over 2 gelatin coated T75 TCPS flasks (VWR, West Chester, PA, USA). Cells were cultured in a humidified incubator at 37 °C with 5% CO_2 . The EGM-2 medium was replaced every 2-3 days. Cells were subcultured at 80-90% confluency according to procedures provided by Lonza Bioscience (Switzerland).

6.2.5. Experimental setup

Cells of passage 3 or 4 were used for all experiments at 80-90% confluency. Incubation was carried out on both gelatin-coated coverslips, for CLSM analysis, and in gelatin-coated T75 TCPS culture flasks, for MRI, FACS and ICP-MS analysis. Samples for CLSM were incubated with liposomes that were not labeled with ^{111}In . All measurements were done in triplicate for both types of liposomes and each incubation time. To start the experiment, medium was replaced by either RGD-liposome or NT-liposome containing medium at a concentration of 1.2 μmol total lipid per mL. 4 mL of liposome containing medium was added to the T75 gelatin-coated TCPS flasks and 0.5 mL of medium was added to the gelatin-coated coverslips. The incubation time with liposomes containing medium was varied between 0 and 8 hr. After incubation, the cells were washed three times with 5 mL pre-warmed (37 °C) HEPES-buffered saline solution to remove non-adherent liposomes. After these washing steps, the cells grown

on coverslips were fixed using 4% PFA for 15 min at room temperature. Cells in culture flasks were detached using 2 mL 0.25% trypsin 1 mM EDTA-4Na (Lonza Bioscience, Switzerland). The trypsin solution was neutralized using 4 mL trypsin neutralizing solution (Lonza Bioscience, Basel, Switzerland). Cells were spun down at 220 g and the supernatant was removed. The cell pellet was resuspended in 200 μ L 4% paraformaldehyde solution in PBS and transferred to a 300 μ L Eppendorf cup. A loosely-packed cell pellet was formed by centrifugation at 10 g for 5 min. The 51 cell pellets (3 control, 24 NT-liposome containing and 24 RGD-liposome containing cell pellets) were stored at room temperature in the dark.

6.2.6. Magnetic resonance imaging

The T_1 and T_2 relaxation times and the volume of the 51 pellets were measured using a 6.3 T horizontal bore animal MR scanner (Bruker, Ettlingen, Germany). Samples were measured approximately 3 months after initial labeling. After this period the radioactivity was reduced to safe levels for handling. All measurements were carried out at room temperature. Longitudinal and transverse relaxation times were measured in a 3 cm diameter send and receive quadrature-driven birdcage coil (Rapid Biomedical, Rimpar, Germany). The Eppendorf tubes containing the loosely-packed cell pellets were placed in a custom made holder (4 tubes at a time) that was filled with HEPES buffered saline solution to facilitate shimming. T_1 was measured using a fast inversion recovery segmented FLASH sequence with an echo time (TE) of 1.5 ms, a repetition time (TR) of 3.0 ms, a flip angle of 15°, and an inversion time (TI) ranging from 67 ms to 4800 ms in 80 steps. Overall repetition time was 20 s. Field of view (FOV) was 3x2.18 cm², using a matrix size of 128x128, a slice thickness of 0.75 mm and 2 averages. T_2 was measured using a multi-slice multi-echo sequence with TE ranging between 9 and 288 ms in 32 steps and a TR of 1000 ms. FOV was 3x2.2 cm², slice thickness was 0.75 mm using a matrix size of 128x128. Number of averages was 4. From the images a T_1 - and T_2 -map were calculated using Mathematica (Wolfram Research Inc, Champaign, IL, USA). T_1 and T_2 of the different cell pellets were determined by selecting a ROI within the pellet. T_1 -weighted images were measured using a multi-slice spin-echo sequence with TE = 10.3 ms and TR = 500 ms. FOV was 3x2.18 cm², slice thickness was 0.75 mm using a matrix size of 256x192. Number of averages was 1. The volume of the cell pellet was determined for each sample separately in a 0.7 cm diameter solenoid coil using a 3D FLASH sequence with TE = 3.2 ms, TR = 25 ms and a flip angle of 30°. FOV was 1.6x1.6x1.6 cm³, matrix size was 128x128x128. Number of averages was 1. A threshold value was determined manually to select the voxels inside the pellet, which were multiplied by the voxel volume to obtain the total volume of the pellet. The concentration of Gd in each cell pellet was determined by dividing the gadolinium content by the pellet volume.

6.2.7. SPECT imaging and quantification

Measurements were performed on 17 cell pellets (1 control, 8 NT-liposome containing- and 8 RGD-liposome containing cell pellets) using the Bioscan nanoSPECT/CT system (Washington, USA). Due to the radioactive decay of $^{111}\text{Indium}$ we were limited to measure only a part of the 51 cell pellets. For the helical SPECT scan 48 projections were obtained with 960 seconds/projection using 20% windows centered at 171 keV and a 15% window centered at 245 keV. Subsequently, a helical CT scan was made for overlay using 45 keV, 177 μA , 2000 ms, 360 projections, and a pitch of 1. After reconstruction voxel sizes were obtained of 1.2 mm^3 (SPECT) and 0.5 mm^3 (CT). Cellular uptake of $^{111}\text{Indium}$ was determined by drawing at least three different volumetric regions of interest (ROIs) around the cell pellets using InVivoScope software (Bioscan). The background was determined by using exact copies of the ROIs drawn around the cell pellets (at least 3 per vial), but now in an area without any measurable radioactivity. Quantitative cellular uptake was obtained after a subtraction of the obtained SPECT signal within the cell pellets with the background signal. Calculated errors were typically 10 - 15 % of the total signal and were derived from the signal error of the ROIs within the vial and the background error. All 51 cell pellets were furthermore measured using a γ -counting wizard (Wizard 1480 3" Wallac counter, Perkin Elmer, Groningen, The Netherlands) as a control measurement for quantitative analysis. Also here a background correction is performed.

6.2.8. Statistical analysis

For the correlation of the different quantification techniques, Pearson's correlation coefficient (r) was computed. ANOVA tables were used to calculate the p-values of the three correlation plots, determining whether there is a statistically significant relationship between SPECT vs. ICP-MS, γ -counting vs. ICP-MS and SPECT vs. γ -counting quantification at the 95 % confidence interval. No outliers were removed. The relaxivity values of the RGD-liposomes in cells (Fig. 5A) were compared to the calculated r_1 using a two-sided student's t-test with a 95 % confidence interval.

6.2.9. Determination of the phosphorus and gadolinium concentration

Phosphorus and Gd concentrations of the liposome mixtures as well as those from the obtained cell pellets were determined by means of Inductively Coupled Plasma-Mass Spectrometry (ICP-MS, DRCII, Perkin Elmer) after destruction with nitric acid at 180 °C.

6.2.10. Confocal laser scanning microscopy

After fixation, the coverslips with HUVECs incubated with liposomes were stained using a mouse anti-human CD31 antibody to visualize the cellular membrane. The cells were rinsed for 5 min with PBS followed by 60 min of incubation with the primary mouse anti-human CD31 antibody (1:40 dilution). Subsequently the cells were washed 3x 5 min with PBS followed by 30 min of incubation with a secondary Alexa Fluor 488 goat anti-mouse IgG antibody (1:200 dilution). The cells were washed 3 x 5 min with PBS and

the nuclei were stained for 5 min with DAPI. After staining of the nuclei the cells were rinsed 3x5 min with PBS and subsequently mounted on a microscopy slide using Mowiol mounting medium. Confocal fluorescence images were recorded at room temperature on a Zeiss LSM 510 META system using a Plan-Apochromat® 63x/1.4 NA oil-immersion objective. Alexa Fluor 488 and rhodamine-PE were excited using the 488 and 543 nm line of a HeNe laser, respectively. The fluorescence emission of Alexa Fluor 488 was recorded with photomultiplier tubes (Hamamatsu R6357) after spectral filtering with a NFT 490 nm beam splitter followed by a 500-550 nm bandpass filter. Rhodamine-PE emission was analyzed using the Zeiss Meta System in a wavelength range of 586-704 nm. DAPI staining of nuclei was visualized by two-photon excitation fluorescence microscopy performed on the same Zeiss LSM 510 system. Excitation at 780 nm was provided by a pulsed Ti:Sapphire laser (Chameleon™; Coherent, Santa Clara, CA, USA), and fluorescence emission was detected with a 395-465 nm bandpass filter. All experiments were combined in multitrack mode and acquired confocally.

6.3. Results and discussion

Typically, the final lipid concentration after preparation of the liposomal formulation was approximately 50 mM as determined by phosphate determination according to Rouser *et al.* [13]. Size control is of high importance since it may be a critical parameter in the cellular uptake process [14]. Dynamic light scattering showed a single peak of 182 nm and 178 nm for RGD- and NT-liposomes with a polydispersity index (PDI) of 0.18 and 0.16 respectively. High resolution cryo-TEM images (Fig. 2) revealed spherical unilamellar vesicles, typical for liposomes, as well as a few micelles as was observed previously [15]. The longitudinal (r_1) and transverse (r_2) relaxivities were determined in a HEPES buffered saline solution at a field strength of 6.3 T and at a temperature of 20°C, resulting in $r_1 = 2.7 \pm 0.1 \text{ mM}^{-1}\text{s}^{-1}$ and $3.4 \pm 0.1 \text{ mM}^{-1}\text{s}^{-1}$ and $r_2 = 16.2 \pm 0.1 \text{ mM}^{-1}\text{s}^{-1}$ and $16.1 \pm 0.1 \text{ mM}^{-1}\text{s}^{-1}$ for RGD-liposomes and NT-liposomes respectively.

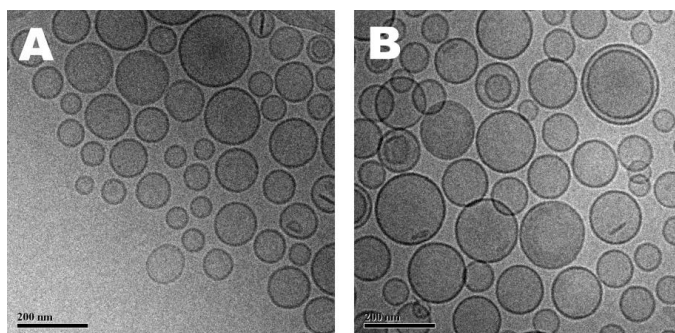


Figure 2. Cryo-TEM images of (A) RGD-liposomes and (B) NT-liposomes. Bar = 200 nm.

To investigate cellular uptake of the multimodal RGD- or NT-liposomes, cultured HUVEC cells were incubated with a liposome-containing medium at a concentration of 1.2 μmol total lipid per mL for 1 up to 8 hours. Next, cells were thoroughly washed, collected and centrifuged to obtain loosely-packed cell pellets and subsequently imaged with MRI and SPECT/CT. Figure 3 shows MRI, SPECT and overlaid SPECT/CT images of pellets containing HUVECs that were incubated for 8 hours with NT-liposomes (Fig. 3A), RGD-liposomes (Fig. 3B) and control HUVECs that were not incubated with contrast agent (Fig. 3C). T_1 -weighted MR images show that the pellet containing control HUVECs is essentially iso-intense with the medium above, whereas pellets containing NT- or RGD-incubated HUVECs can easily be distinguished from buffer as a consequence of the reduced T_1 . The RGD-incubated cells show higher signal compared to cells incubated with NT-liposomes. Accordingly, SPECT imaging showed a low signal coming from HUVECs incubated with NT-liposomes, a brighter signal for cells incubated with RGD-liposomes, whereas no activity was found in control HUVECs.

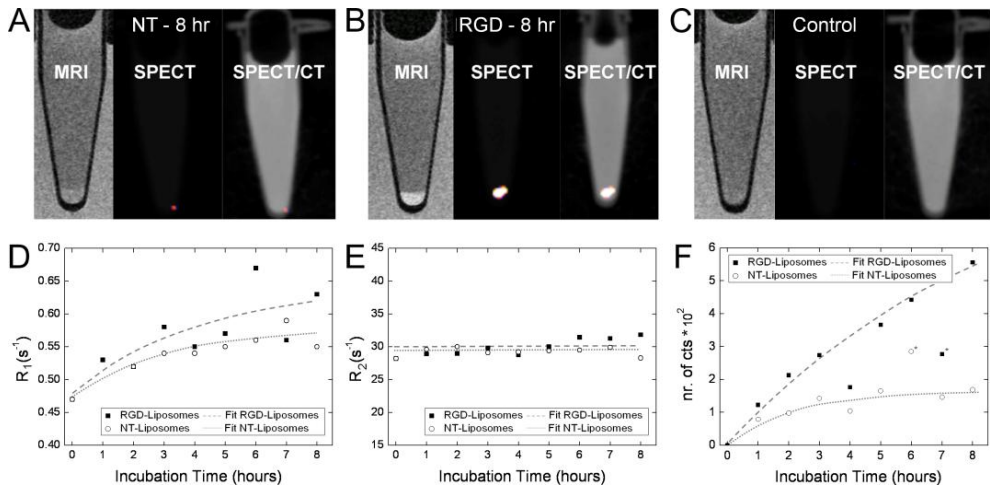


Figure 3. Upper row: T_1 -weighted MRI, SPECT and combined SPECT/CT images of pellets of HUVECs incubated for 8 hr with NT-liposomes (Fig. 3A), RGD-liposomes (Fig. 3B) and control HUVECs without contrast agent (Fig. 3C). The pellets are situated at the bottom of the Eppendorf cups. Below: Uptake of contrast agent as described by R_1 -MRI (Fig. 3D), R_2 -MRI (Fig. 3E) and the number of counts (Fig. 3F) in SPECT (background subtracted) as a function of time for HUVECs incubated with RGD-liposomes (solid squares) or NT-liposomes (open circles). All measurements had a typical error of 10-15% (for more details, see Materials and Methods section in the supplementary information). An exponential fit to the data ($y=y_0+A*e^{-t/x}$) is provided as a dashed line. Two data points marked with asterisks were not included in the exponential fit.

The longitudinal relaxation rates ($R_1=1/T_1$) of the cell pellets (Fig. 3D) increased faster after incubation with RGD-liposomes when compared to NT-liposomes, while these differences remain small for the transverse relaxation rate relaxation rates ($R_2=1/T_2$) (Fig. 3E). However, earlier studies showed that R_1 or R_2 do not allow to determine the intracellular concentration of the paramagnetic nanoparticle [6,7]. Compartmentalization into cell organelles may decrease the intracellular relaxivity, which manifests itself in a nonlinear dependence of R_1 on cell-associated contrast agent concentration [8,16]. This becomes immediately evident when comparing the MRI data (Fig. 3D) to corresponding SPECT data (Fig. 3F), which shows the activity per cell pellet after different incubation times with RGD- and NT-liposomes. The cellular uptake of the targeted contrast agent as analyzed with SPECT indicates a faster uptake compared to the apparent uptake kinetics as deduced from the MRI data (Fig. 3D). The SPECT data indicate a 3.3 times higher uptake of RGD-liposomes compared to NT-liposomes (Fig. 3F), whereas the R_1 values of Figure 3D show merely a factor of 2.1, pointing to a systematic decrease of the net relaxivity of targeted liposomes upon cellular uptake. The transverse relaxation rate (Fig. 3E) for both RGD- and NT-liposomes showed similar values throughout the incubation-time range.

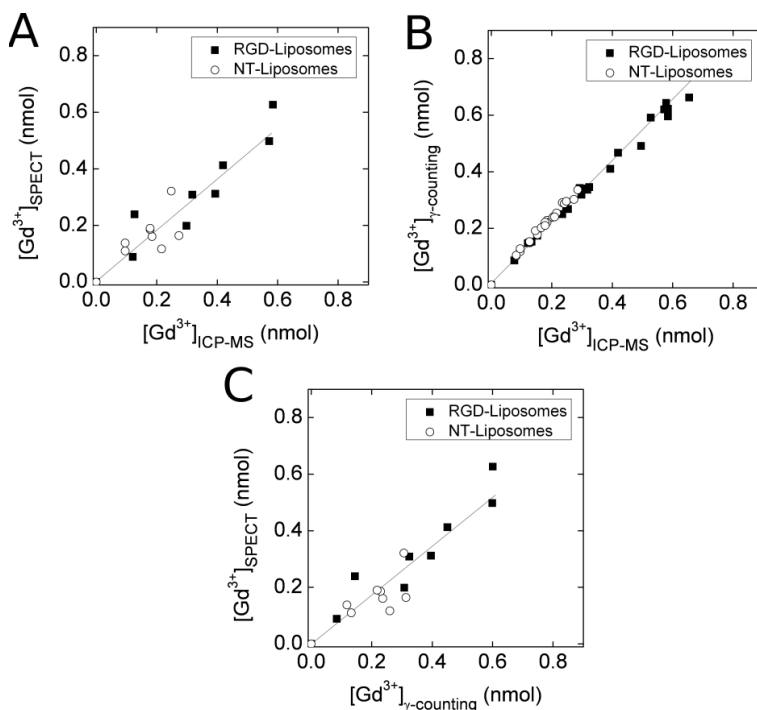


Figure 4. Gadolinium content calculated from SPECT (A), γ -counting (B) as a function of the amount of gadolinium determined by ICP-MS; amount of gadolinium calculated from SPECT correlated to gadolinium content as calculated from γ -counting data (C) for HUVECs incubated with RGD-liposomes (solid squares) or NT-liposomes (open circles). The solid line is a linear fit to all experimental data resulting in $Gd^{3+}_{SPECT} = 0.96 \cdot Gd^{3+}_{ICP-MS}$, ($R^2 = 0.95$, Pearson's correlation coefficient (r) = 0.93, $p = 0.000$), $Gd^{3+}_{\gamma-counting} = 0.97 \cdot Gd^{3+}_{ICP-MS}$, ($R^2 = 0.99$, $r = 0.99$, $p = 0.000$) and $Gd^{3+}_{SPECT} = 0.87 \cdot Gd^{3+}_{\gamma-counting}$, ($R^2 = 0.95$, $r = 0.93$, $p = 0.000$).

For a more detailed analysis, the Gd concentration needed to be related to the activity of ^{111}In . In a dilution series of ^{111}In -labeled liposomes, the ^{111}In signal was measured using scintillation counting of γ -photons, while the Gd concentration was determined with inductively coupled plasma mass spectrometry (ICP-MS). For our multimodal agent, 900 cts from ^{111}In corresponded to 1 nmol Gd allowing a direct quantification on the amount of Gd within the cells based on the SPECT signal. Beforehand, the SPECT system was calibrated with an ^{111}In source to relate counts to activity (1000 cts corresponded to 2.2 kBq ^{111}In at our reference time). It should be noted that the amount of ^{111}In atoms present in this study was a factor of 10^6 lower than Gd, reflecting the higher sensitivity of SPECT compared to MRI. Nevertheless, the acquired SPECT data (Fig. 3F) suffer from a low signal-to-noise ratio due to the overall low activity present in the cell pellets. To verify whether SPECT imaging yields reliable quantitative information in this experiment, the cell pellets were analyzed by ICP and γ -counting for reference. Figure 4 shows the correlation between the Gd content based on SPECT

imaging (Fig. 4A) and γ -counting (Fig. 4B) as a function of the Gd content as determined by ICP-MS; a combination of all data finally leads to Figure 4C, showing that SPECT imaging indeed allows a reliable quantification of Gd within the cell pellets. In detail, the correlations resulted in $Gd^{3+}_{SPECT} = 0.96 \cdot Gd^{3+}_{ICP-MS}$, ($R^2 = 0.95$, Pearson's correlation coefficient ($r = 0.93$, $p = 0.000$), $Gd^{3+}_{\gamma\text{-counting}} = 0.97 \cdot Gd^{3+}_{ICP-MS}$, ($R^2 = 0.99$, $r = 0.99$, $p = 0.000$) and $Gd^{3+}_{SPECT} = 0.87 \cdot Gd^{3+}_{\gamma\text{-counting}}$, ($R^2 = 0.95$, $r = 0.93$, $p = 0.000$). Applying this concept in vivo would require an application that leads to sufficient uptake of the dual modal liposome and to an activity in the lesion that can be reliably quantified with SPECT.

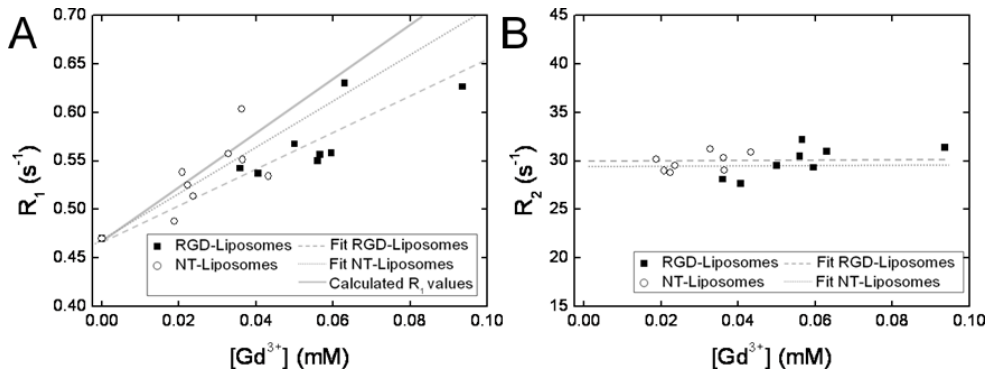


Figure 5. 1H relaxometry measurements for pellets of HUVECs incubated with RGD-liposomes (solid squares) or NT-liposomes (open circles). R_1 (A) and R_2 (B) as a function of the concentration of gadolinium as determined by SPECT. Data fits are provided as a dashed (RGD-liposomes) and dotted (NT-liposomes) line. The solid line in Figure 4A represents the calculated R_1 values that should have been observed if the relaxivity was not quenched and was found significantly different from the RGD-liposomes in HUVECs ($p < 0.05$).

For RGD-liposomes a faster uptake kinetic was observed leading to 0.63 nmol of Gd per cell pellet after 8 hours of incubation compared to 0.19 nmol for NT-liposomes. This 3-fold difference was previously impossible to detect based on the R_1 signal as shown in Figure 3D. The SPECT, ICP-MS and γ -counting calibration (Fig. 4) now allowed analyzing changes of R_1 and R_2 in cells upon incubation with targeted and nontargeted liposomes as a function of the Gd concentration, as measured indirectly with SPECT (Fig. 5A) and volume measurements of the cell pellets by MR. The expected R_1 values as a function of Gd concentration are plotted based on the intrinsic liposomal relaxivity of $r_1 = 2.7 \pm 0.1 \text{ mM}^{-1}\text{s}^{-1}$ that was previously determined in HBS buffer (Fig. 5A, solid line). Clearly, all values for R_1 are lower than expected indicating a reduced intracellular longitudinal relaxivity. The slope taken from the corresponding linear fits allows to compute the apparent intracellular relaxivity for RGD and NT-liposomes ($1.73 \pm 0.3 \text{ mM}^{-1}\text{s}^{-1}$ versus $2.34 \pm 0.7 \text{ mM}^{-1}\text{s}^{-1}$), revealing a pronounced reduction of the longitudinal relaxivity for targeted liposomes.

The underlying mechanism for the observed effect is the different uptake of targeted and nontargeted liposomes. Internalization by the $\alpha_v\beta_3$ receptor is faster and also leads to a different localization of the targeted nanoparticle compared to nontargeted liposomes [7]. No significant R_2 differences were observed between RGD- and NT-liposomes treated cells at any time point.

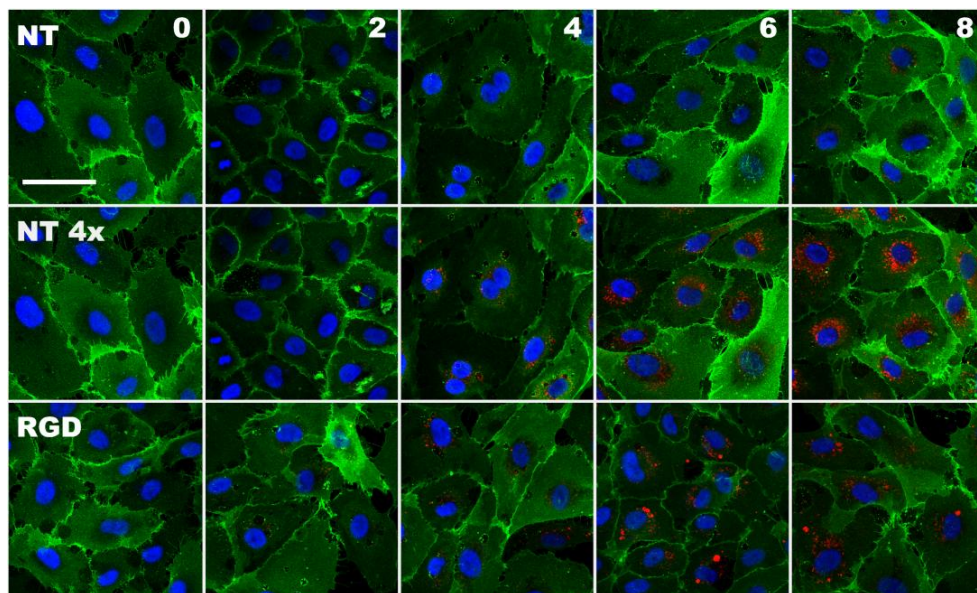


Figure 6. CLSM images of HUVECs incubated with RGD-liposomes (RGD) or NT-liposomes (NT). Blue = DAPI, red = rhodamine, green = CD31, bar = 50 μm . The number shown in the top right corner of each column refers to the incubation time in hours. Note that the laser intensity used to obtain NT 4x images (middle row) was fourfold higher than the intensity used to obtain the other images (bottom and top row).

The cellular location of the liposomal contrast agent was determined using confocal laser scanning microscopy (CLSM), by utilizing the rhodamine fluorophore present in the bilayer of the liposomes. Figure 6 shows confocal images of HUVECs grown on gelatin-coated coverslips. Both RGD- and NT-liposomes accumulated in the perinuclear region. Up to 8 hours of incubation, both the RGD- and NT-liposomes were mainly found in sharply delineated spherical 0.4-1.0 μm diameter structures inside the cytoplasm. No detectable association of liposomes with the cellular membrane was observed for both RGD- and NT-liposomes. Clear differences in uptake between RGD- and NT-liposomes were visible. For HUVECs incubated with RGD-liposomes, many significantly larger vesicular structures with a diameter of 1-5 μm were observed, indicating concentrated spots of RGD-liposomes. On the other hand, incubation with NT-liposomes resulted in a perinuclear intracellular distribution in smaller 0.4 - 1.0 μm diameter vesicles. A three-compartment exchange model as previously published by

Strijkers *et al.* [8] showed that the lower surface-to-volume ratio for larger sized vesicles compared to small vesicles results in a reduced water exchange across the vesicular membrane, which again translates into a reduced longitudinal relaxivity. This observed reduction can be ascribed to the endocytotic uptake of RGD targeted liposomes into larger vesicles (Fig. 6).

6.4. Conclusions

Previously, liposomes have been investigated as a combined SPECT and MRI contrast agent [17-21], however, these studies did not address quantification to aid in the interpretation of MRI parameter changes. In our study, we demonstrated that dual modal nanoparticles can be utilized in SPECT to measure the particle concentration. The characteristics of the MR imaging data in combination with SPECT can be used to assess cellular uptake and intracellular trafficking of the nanoparticles. This approach may be easily extended to multimodal SPECT/MRI and also PET/MRI nanoparticles to measure other functional MR-based signals as was previously demonstrated for pH-mapping [22,23]. Other examples range from smart MR probes to report temperature and enzyme activity based on different concepts such as CEST agents [24,25], enzyme-responsive paramagnetic liposomal contrast agents [26] to MR image-guided drug delivery systems [4,27] and cellular trafficking [5], where the alterations in the MRI signal are a convolution of MR contrast agent concentration and a response to the environment. As this approach is noninvasive and applicable *in vivo* in longitudinal studies, a broad utility of this concept can be expected in imaging-based analyses in biological and medical research.

Acknowledgements

This study was funded in part by the BSIK program entitled Molecular Imaging of Ischemic Heart Disease (project number BSIK03033), the Integrated EU Project MEDITRANS (FP6-2004-NMP-NI-4/IP 026668-2) and the EC-FP6-project DiMI, LSHB-CT-2005-512146. This study was performed in the framework of the European Cooperation in the field of Scientific and Technical Research (COST) D38 Action Metal-Based Systems for Molecular Imaging Applications. The authors would like to express their thanks to Jeannette Smulders for the ICP-MS analysis and Sander Langereis for helpful discussions.

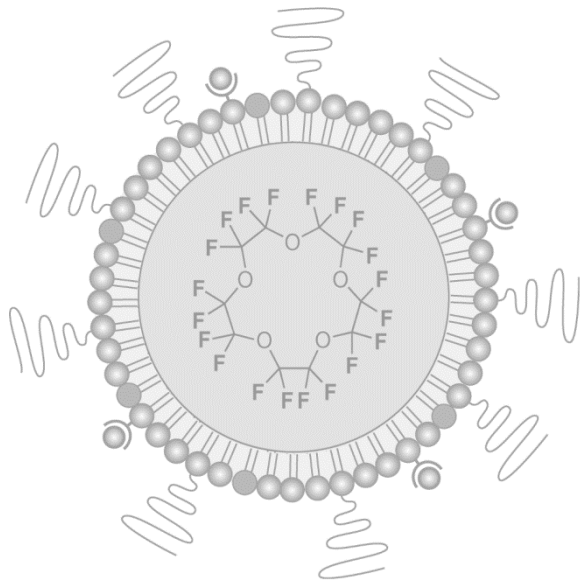
6.5. References

- [1] Caravan P, Ellison JJ, McMurry TJ, Lauffer RB. Gadolinium(III) Chelates as MRI Contrast Agents: Structure, Dynamics, and Applications. *Chem Rev.* 1999;99:2293-352.
- [2] Laurent S, Forge D, Port M, Roch A, Robic C, Vander Elst L, et al. Magnetic iron oxide nanoparticles: synthesis, stabilization, vectorization, physicochemical characterizations, and biological applications. *Chem Rev.* 2008;108:2064-110.
- [3] Terreno E, Castelli DD, Viale A, Aime S. Challenges for molecular magnetic resonance imaging. *Chem Rev.* 2010;110:3019-42.
- [4] Hynynen K. MRI-guided focused ultrasound treatments. *Ultrasonics.* 2010;50:221-9.
- [5] Bulte JW. In vivo MRI cell tracking: clinical studies. *AJR Am J Roentgenol.* 2009;193:314-25.
- [6] Geninatti Crich S, Cabella C, Barge A, Belfiore S, Ghirelli C, Lattuada L, et al. In vitro and in vivo magnetic resonance detection of tumor cells by targeting glutamine transporters with Gd-based probes. *J Med Chem.* 2006;49:4926-36.
- [7] Kok MB, Hak S, Mulder WJ, van der Schaft DW, Strijkers GJ, Nicolay K. Cellular compartmentalization of internalized paramagnetic liposomes strongly influences both T1 and T2 relaxivity. *Magn Reson Med.* 2009;61:1022-32.
- [8] Strijkers GJ, Hak S, Kok MB, Springer CS, Jr., Nicolay K. Three-compartment T1 relaxation model for intracellular paramagnetic contrast agents. *Magn Reson Med.* 2009;61:1049-58.
- [9] Kok MB, de Vries A, Abdurrahim D, Prompers JJ, Grull H, Nicolay K, et al. Quantitative (1)H MRI, (19)F MRI, and (19)F MRS of cell-internalized perfluorocarbon paramagnetic nanoparticles. *Contrast Media Mol Imaging.* 2010.
- [10] Morawski AM, Winter PM, Yu X, Fuhrhop RW, Scott MJ, Hockett F, et al. Quantitative "magnetic resonance immunohistochemistry" with ligand-targeted (19)F nanoparticles. *Magn Reson Med.* 2004;52:1255-62.
- [11] Brooks PC, Clark RA, Cheresh DA. Requirement of vascular integrin alpha v beta 3 for angiogenesis. *Science.* 1994;264:569-71.
- [12] Mulder WJM, Strijkers GJ, Griffioen AW, van Bloois L, Molema G, Storm G, et al. A Liposomal System for Contrast-Enhanced Magnetic Resonance Imaging of Molecular Targets. *Bioconjugate Chemistry.* 2004;15:799-806.
- [13] Rouser G, Fkeischer S, Yamamoto A. Two dimensional thin layer chromatographic separation of polar lipids and determination of phospholipids by phosphorus analysis of spots. *Lipids.* 1970;5:494-6.
- [14] Allen TM, Austin GA, Chonn A, Lin L, Lee KC. Uptake of liposomes by cultured mouse bone marrow macrophages: influence of liposome composition and size. *Biochim Biophys Acta.* 1991;1061:56-64.
- [15] Hak S, Sanders HM, Agrawal P, Langereis S, Grull H, Keizer HM, et al. A high relaxivity Gd(III)DOTA-DSPE-based liposomal contrast agent for magnetic resonance imaging. *Eur J Pharm Biopharm.* 2009;72:397-404.
- [16] Delli Castelli D, Dastru W, Terreno E, Cittadino E, Mainini F, Torres E, et al. In vivo MRI multicontrast kinetic analysis of the uptake and intracellular trafficking of paramagnetically labeled liposomes. *J Control Release.* 2010;144:271-9.
- [17] Li D, Patel AR, Klibanov AL, Kramer CM, Ruiz M, Kang BY, et al. Molecular imaging of atherosclerotic plaques targeted to oxidized LDL receptor LOX-1 by SPECT/CT and magnetic resonance. *Circ Cardiovasc Imaging.* 2010;3:464-72.
- [18] Lijowski M, Caruthers S, Hu G, Zhang H, Scott MJ, Williams T, et al. High sensitivity: high-resolution SPECT-CT/MR molecular imaging of angiogenesis in the Vx2 model. *Invest Radiol.* 2009;44:15-22.
- [19] Torchilin VP. Surface-modified liposomes in gamma- and MR-imaging. *Adv Drug Deliv Rev.* 1997;24:301-13.
- [20] Zielhuis SW, Seppenwoolde JH, Mateus VA, Bakker CJ, Krijger GC, Storm G, et al. Lanthanide-loaded liposomes for multimodality imaging and therapy. *Cancer Biother Radiopharm.* 2006;21:520-7.
- [21] Hu G, Lijowski M, Zhang H, Partlow KC, Caruthers SD, Kiefer G, et al. Imaging of Vx-2 rabbit tumors with alpha(nu)beta3-integrin-targeted 111In nanoparticles. *Int J Cancer.* 2007;120:1951-7.
- [22] Frullano L, Catana C, Benner T, Sherry AD, Caravan P. Bimodal MR-PET agent for quantitative pH imaging. *Angew Chem Int Ed Engl.* 2010;49:2382-4.
- [23] Gianolio E, Maciocco L, Imperio D, Giovenzana GB, Simonelli F, Abbas K, et al. Dual MRI-SPECT agent for pH-mapping. *Chem Commun (Camb).* 2011;47:1539-41.
- [24] Terreno E, Castelli DD, Aime S. Encoding the frequency dependence in MRI contrast media: the emerging class of CEST agents. *Contrast Media Mol Imaging.* 2010;5:78-98.

- [25] Yoo B, Raam MS, Rosenblum RM, Pagel MD. Enzyme-responsive PARACEST MRI contrast agents: a new biomedical imaging approach for studies of the proteasome. *Contrast Media Mol Imaging*. 2007;2:189-98.
- [26] Figueiredo S, Moreira JN, Geraldés CF, Aime S, Terreno E. Supramolecular protamine/Gd-loaded liposomes adducts as relaxometric protease responsive probes. *Bioorg Med Chem*. 2010.
- [27] de Smet M, Heijman E, Langereis S, Hijnen NM, Grull H. Magnetic resonance imaging of high intensity focused ultrasound mediated drug delivery from temperature-sensitive liposomes: An in vivo proof-of-concept study. *J Control Release*. 2010.

Chapter 7

Relaxometric studies of gadolinium-functionalized perfluorocarbon nanoparticles for MR imaging



Based on

Relaxometric studies of gadolinium-functionalized perfluorocarbon nanoparticles for MR imaging

A. d. Vries, R. Moonen, M. Yildirim, S. Langereis, R. Lamerichs, J.A. Pikkemaat, S. Baroni, E. Terreno, K. Nicolay, G.J. Strijkers and H. Gröll

Submitted

Abstract

Fluorine MRI (^{19}F MRI) is receiving an increasing attention as a viable addition to proton-based MRI for dedicated application in molecular imaging. The fluorine nucleus has a high gyromagnetic ratio, a natural abundance of 100%, and is furthermore almost completely absent in human tissues allowing hot spot imaging. Fluorinated emulsions have been shown to be suitable for *in vivo* use with good safety profile and tolerability. The applicability of ^{19}F MRI as a molecular and cellular imaging technique has been demonstrated in a number of studies ranging from *in vivo* cell tracking to detection and imaging of tumors in small animals. Besides applications, the development of new contrast materials with improved relaxation properties has also been a core research topic in the field of ^{19}F MRI, since the inherently low longitudinal relaxation rates of PFC compounds result into relatively low imaging efficiency. Borrowed from ^1H MRI, the incorporation of lanthanides, specifically Gd(III)-complexes, as signal modulating ingredients into the nanoparticle formulation has emerged as a promising approach towards improvement of the ^{19}F MR acquisition. Three different perfluorocarbon emulsions were investigated at five different magnetic fields. Perfluoro-15-crown-5-ether was used as the core material and Gd(III)DOTA-DSPE, Gd(III)DOTA-C6-DSPE and Gd(III)DTPA-BSA as the relaxation altering components. While Gd(III)DOTA-DSPE and Gd(III)DOTA-C6-DSPE are favorable constructs for ^1H NMR, Gd(III)DTPA-BSA showed the strongest increase in $^{19}\text{F}R_1$. These results show the potential of the use of paramagnetic lipids to increase $^{19}\text{F}R_1$.

7.1. Introduction

MRI is a powerful molecular imaging tool as it provides high-resolution images and excellent soft-tissue contrast without the need for ionizing radiation. Quantitative molecular imaging of cellular disease markers has been found essential for the characterization of disease processes. A promising quantitative technique is ^{19}F MR imaging. Among the advantages of ^{19}F MRI is the fact that the ^{19}F nucleus has a 100 % natural abundance, a nuclear spin of $\frac{1}{2}$ and a sensitivity close to that of ^1H NMR. The lack of background signal quantification of the fluorine content. However, sensitivity remains an issue as the local ^{19}F concentration by far cannot approach the ^1H content of the human body. Contrast agents providing high local densities of ^{19}F are required to reach detectable ^{19}F concentrations. Over the last decade, extensive studies on perfluorocarbon nanoparticles were performed demonstrating their use amongst others in quantitative molecular imaging of fibrin-targeted clots in atherosclerosis [1], $\alpha_v\beta_3$ -targeting of angiogenesis in diseased aortic valve leaflets [2] and VCAM-1 targeted renal inflammation [3]. Next to molecular imaging, perfluorocarbon nanoparticles have been investigated in cell trafficking where they enable quantitative assessment of the biodistribution of labeled neural stem cells [4] and T-cells [5-7]. Quantitative ^{19}F MRI of perfluorocarbons was furthermore extensively explored for in the *in vivo* mapping of tumor oxygenation [8,9].

Attempts have been made to increase the ^{19}F sensitivity in MR as this would decrease the necessary probe concentration at the imaging site of interest. Previously, it has been shown that the vicinity of the lanthanide Gadolinium (Gd) significantly increases the fluorine longitudinal relaxation rate ($^{19}\text{F}R_1$, (s^{-1})) [10,11]. The influence of a gadolinium-functionalized lipid (Gd(III)DTPA-BOA) in the perfluoro-15-crown-5-ether (PFCE) emulsion monolayer on the $^{19}\text{F}R_1$ and $^{19}\text{F}R_2$ was recently investigated, showing not only the Gd concentration dependence on fluorine relaxation but also that the $^{19}\text{F}R_1$ relaxation rate decreased upon increased field strength and *vice versa* for $^{19}\text{F}R_2$ [12]. Intuitively one would assume that the Gd, incorporated in the Gd(III)DTPA-BOA lipid is situated on the outside of the nanoparticle monolayer as the Gd(III)DTPA head group is hydrophilic and insoluble in PFCE. The results of Neubauer *et al.* however suggest that the Gd is in close enough proximity of ^{19}F to still increase relaxation of the perfluoro-15-crown-5-ether (PFCE) inside the emulsion. Taking the Solomon-Bloembergen-Morgen theory of relaxivity as a basis, the underlying mechanism must be related to outer sphere relaxation as any direct contact between the fluorinated molecules inside the emulsion droplet and the Gd-chelate head group is prohibited by the lipid monolayer in between. Secondly, the effect must increase with the amount of Gd in the monolayer, and decrease with increasing volume of the emulsion droplet. The latter is a logical consequence of the increasing distance each fluorinated molecule has to diffuse inside

the emulsion droplet to get close to the surface layer in order to experience the dipolar interactions with the paramagnetic head-group. Above intuitive rational was worked out recently in more detail by Hu *et al.* giving a theoretical model and first experimental data [13].

An increase in sensitivity for ^{19}F MRI would be beneficial for ^{19}F applications in clinical practice. Gd-functionalized nanoparticles are currently investigated for use in molecular imaging applications as they create an increased proton R_1 and allow a delineation of the diseased tissue using proton MR. FDA approval for all Gd-related nanoparticulate contrast agents is however complicated as they are taken up *via* the reticulo endothelial system (RES), which may lead to a prolonged retention time of Gd-compounds *in vivo*. The latter may lead to nephrogenic systemic fibrosis (NSF), which is mostly observed in patients with impaired renal excretion after injection of Gd contrast agents based on a bisamide chelate. Most likely, the lower stability of Gd bisamide complexes compared to DTPA or DOTA complexes in combination with the long body retention time leads to considerable transchelation of Gd inducing toxicity [14-16]. As Gd-DOTA constructs show a much higher kinetic stability and lower transmetallation rate than Gd(III)DTPA-bisamide constructs [17,18], Gd-DOTA is the more favorable chelate to incorporate in the lipid bilayer of fluorine nanoparticles. Whether the influence on the relaxation rate of fluorine persists when Gd(III)DOTA is used instead of Gd(III)DTPA is unclear.

Here, we investigate the influence of three different gadolinium-lipids on the water proton relaxivities and fluorine relaxation rates $^{19}\text{F}R_1$ and $^{19}\text{F}R_2$ of a PFCE nanoparticle (Fig. 1). Gd(III)DOTA-DSPE, Gd(III)DOTA-C6-DSPE and Gd(III)DTPA-BSA are employed in our formulations as relaxation agents. This allowed us to investigate not only the difference between Gd(III)DOTA-DSPE and Gd(III)DTPA-BSA, but also whether an aliphatic spacer of approximately 6 Å (Gd(III)DOTA-C6-DSPE) alters the influence of Gd on fluorine relaxation rates. These three fluorine emulsions (FE) will from here on be referred to as FE-DOTA, FE-C6-DOTA and FE-DTPA. ^1H NMRD measurements are performed on all Gd-constructs to define the positioning and movement of gadolinium on the constructs. All fluorine $^{19}\text{F}R_1$ and $^{19}\text{F}R_2$ measurements are performed at 5 different field strengths and are compared to the results of two controls being a PFCE emulsion without any Gd incorporated (referred to as FE) and a PFCE emulsion having Gd only present in the aqueous solution as Gd(III)HPDO3A (further referred to as FE + HPDO3A).

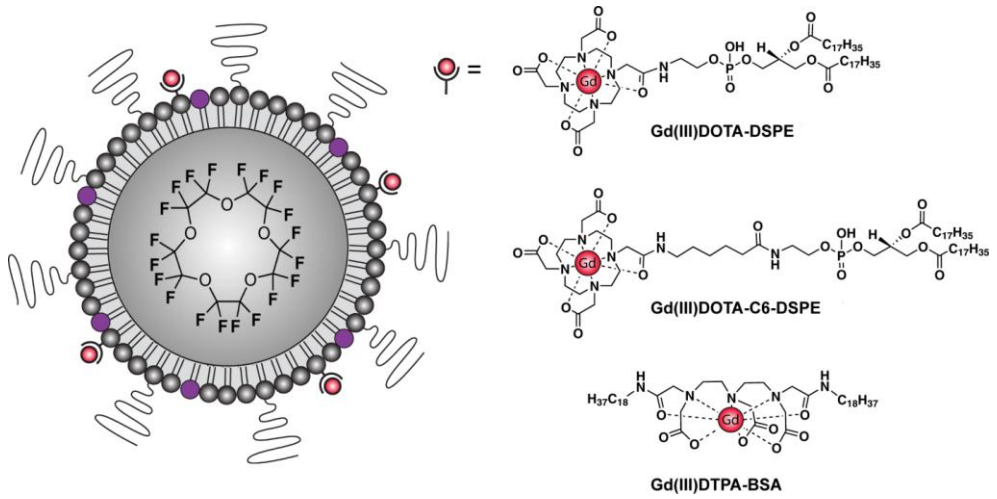


Figure 1. Schematic representation of a Gadolinium-functionalized PFCE emulsion which was prepared using either Gd(III)DOTA-DSPE, Gd(III)DOTA-C6-DSPE or Gd(III)DTPA-BSA as paramagnetic lipids embedded in the nanoparticle monolayer.

7.2. Materials and Methods

7.2.1. Materials

1,2-Distearoyl-*sn*-glycero-3-phosphocholine (DSPC), cholesterol and 1,2-distearoyl-*sn*-glycero-3-phosphoethanolamine-*N*-[methoxy(-polyethyleneglycol)-2000] (DSPE-PEG₂₀₀₀) were obtained from Lipoid (Germany). 1,2-dipalmitoyl-*sn*-3-phosphoethanolamine-*N*-[lissamine rhodamine B sulfonyl] (rhodamine-PE) was obtained from Avanti Polar Lipids (Alabaster, AL, USA). Gd(III)DOTA-DSPE, Gd(III)DOTA-C6-DSPE and Gd(III)DTPA-bis(stearylamide) (Gd(III)DTPA-BSA) were synthesized by SyMO-Chem (Eindhoven, the Netherlands). All other commercial chemicals were purchased from Sigma-Aldrich in the highest available quality.

7.2.2. Emulsion preparation

Perfluorocarbon nanoparticles were composed of 20% (w/v) perfluoro-15-crown-5-ether, 2% (w/v) surfactant in THAM buffer (0.0252% w/v trishydroxymethyl aminomethane and 8.9 g/L NaCl, pH 7.4). The surfactant comprised DSPC, DSPE-PEG₂₀₀₀, Gd(III)DOTA-DSPE / Gd(III)DOTA-C6-DSPE / Gd(III)DTPA-BSA, rhodamine-PE and cholesterol in a molar ratio of 1.55:0.15:0.3:0.003:1 while the composition of Gd-free nanoparticles consisted of DSPC, DSPE-PEG₂₀₀₀, rhodamine-PE and cholesterol in a molar ratio of 1.85:0.15:0.003:1. In detail, 600 mmol total lipids were dissolved in 50 mL of a 2:1 v/v CHCl₃:MeOH mixture. As a fluorescent marker, 0.1 mol% rhodamine-PE was included. This solution was evaporated to dryness using rotation evaporation at 10 mbar and 40 °C. The lipid film was put under a nitrogen flow overnight to remove traces of organic solvents. Subsequently, the lipid film was heated to 70 °C and hydrated with 15 mL THAM buffer for 30 minutes. PFCE (4.5 g) was added to the lipid mixture and the crude emulsion was processed for 3 min in a high-pressure microfluidizer (M-110S, Microfluidics, USA) at 1500 bar, preheated to 70 °C and with the interaction chamber cooled with an ice bath. The final emulsion was cooled down in an ice bath for 5 minutes and stored in the dark at room temperature. The gadolinium-free emulsion was split into two batches. One of them was replenished with HPDO3A to come to an equal concentration of Gd as the gadolinium containing samples (as determined by ICP-AES).

7.2.3. Characterization

Phospholipid concentrations of the liposomal dispersions were determined using two techniques. The first method was a phosphate determination according to Rouser after destruction with nitric acid at 180 °C [19]. The second method made use of inductively coupled plasma atomic emission spectrometry (ICP-AES, DRCII, Perkin-Elmer, Philips Research Materials Analysis, Eindhoven, the Netherlands). Destruction of the samples was performed with nitric acid at 180 °C. In order to determine the longitudinal

relaxivities, Gd(III) concentrations were determined using ICP-AES as well. Fluorine content was determined by high field NMR spectroscopy.

The hydrodynamic radius and polydispersity of the emulsions was determined using dynamic light scattering (ALV/CGS-3 Compact Goniometer System, ALV-GmbH, Langen, Germany). Intensity correlation functions were measured at a scattering angle of $\theta=90^\circ$ using a wavelength of 632.8 nm. The diffusion coefficient (D) was obtained from cumulant fits of the intensity correlation function using ALV software. All reported hydrodynamic radii were calculated using the Stokes-Einstein equation $r_h=kT/(6\pi\eta D)$, where k is the Boltzmann constant, T is the absolute temperature and η is the solvent viscosity. Measurements were repeated 5 times and calculations were performed on the averaged correlation function of the 5 measurements.

The zeta potential of the emulsions was determined with the microelectrophoretic method using the Malvern Zetasizer Nano ZS apparatus. Measurements were performed at 20 °C in THAM buffer (0.0252% w/v trishydroxymethyl aminomethane and 8.9 g/L NaCl) at pH 7.4. Each zeta potential was an average from 1000 measurements.

Cryogenic transmission electron microscopy (cryo-TEM) pictures were obtained with a FEI TECNAI F30ST electron microscope operated at an accelerating voltage of 300 kV in low dose mode. Samples for TEM were prepared by placing the emulsion (2 μ L) on a 300-mesh carbon-coated copper grid and subsequently plunge-freezing this grid into liquid ethane using a Vitrobot.

7.2.4. ^1H Nuclear Magnetic Relaxation Dispersion (NMRD)

^1H NMRD profiles were measured on a Stellar Spinmaster FFC-2000 fast-field cycling relaxometer (Mede, Italy) in a magnetic field range from 2.4×10^{-4} to 0.47 T (corresponding to proton Larmor frequencies of 0.01-20 MHz). Additional T_1 relaxation times were obtained on a Stellar SpinMaster Spectrometer (Stellar S.n.c., Mede (PV), Italy) equipped with a tunable probe (in the range 0.47-1.6 T), by means of the standard inversion recovery method with a 90° pulse width of 3.5 μ s, using 16 experiments of 4 scans each. The T_1 reproducibility was within 5%. The temperature was controlled with a Stellar VTC-91 airflow heater equipped with a calibrated copper constantan thermocouple (precision of 0.1 °C). Measurements were performed at 25 °C and 37 °C. The longitudinal relaxivity r_1 was calculated taking into account the diamagnetic contributions of the buffer. The NMRD profiles were analyzed according to the Solomon–Bloembergen–Morgan equations modified according to the Lipari-Szabo model free approach. The number of coordinating water molecules (q), the water proton paramagnetic center distance (r), the distance of closest approach (a) and the diffusion coefficient (D) were kept constant at $q = 1$, $r = 3.1 \text{ \AA}$, $a = 3.8 \text{ \AA}$ and $D = 2.2 \times 10^{-5} \text{ cm}^2\text{s}^{-1}$

at 25 °C. The global and local rotational correlation times (global and local τ_r), the correlation time for tensor fluctuation (τ_v), the water residence lifetime (τ_m), the order parameter (S^2) and the square of the transient of the zero field splitting of the electronic spin states (Δ^2) were allowed to vary.

7.2.5. Relaxivity measurements of fluorine

Relaxation measurements ($^{19}\text{F}R_1$ and $^{19}\text{F}R_2$) were performed at 5 different field strengths (1.4 T, 3.0 T, 6.3 T, 9.4 T, 14.0 T) at room temperature ($T=293$ K). The effect of nanoparticle concentration was assessed by evaluating a concentration-series of each emulsion formulation for their T_1 and T_2 values. The PFCE concentration of these samples were 0.45, 0.33, 0.22, 0.11 M and 43.2, 22.5 and 3.8 mM as determined at 14.0 T by using hexafluoropropanol as a reference. Protocols for $^{19}\text{F}R_1$ and $^{19}\text{F}R_2$ were optimized for all field strengths and curves were fitted using a single-exponential decay function.

1.4 T: Measurements were performed according to Henoumont *et al.* [20]. The longitudinal relaxation rate was monitored using a Bruker Minispec mq60 with a dedicated ^{19}F probe kindly provided by Bruker Optics (Delft, The Netherlands). An inversion recovery sequence with four averages was used. Ten inversion times ranging in an exponential fashion from 5 ms to at least 5 times the T_1 of the solution were used. The recycle delay was also set to at least 5 times the T_1 of the solution. For T_2 , a Carr-Purcell-Meiboom-Gill (CPMG) NMR pulse sequence was performed, obtaining 2048 data points with at least 16 averages using $\tau = 1.0$ s and a recycle delay of 7.0 s.

3.0 T: Measurements were conducted on a 3.0 T Philips Achieva clinical scanner (Philips Healthcare, Best, the Netherlands) equipped with a special design $^1\text{H}/^{19}\text{F}$ small bore coil. Longitudinal relaxation was measured by means of a single voxel spectroscopy sequence consisting of a 180° inversion pulse and a 90° excitation pulse, both wideband and tuned to the NMR offset of PFCE, and a sampling phase where the free induction decay (FID) signal generated by the fluorine nuclei was acquired. The time interval between inversion and excitation was altered over a range from 1.5 ms to 10 s with 44 time points. The repetition time of the measurements was kept long, i.e. 20 s, in order to ensure complete relaxation after each acquisition.

6.3 and 9.4 T: Two horizontal bore small animal scanners (Bruker Biospin, Ettlingen, Germany) with dedicated ^{19}F solenoid coils were used for experiments at 6.3 T and 9.4 T. T_1 and T_2 measurements were performed using a Rapid Acquisition with Relaxation Enhancement (RARE) sequence with RARE factor 2, 8 echo images (echo time (TE) 12 ms to 180 ms) and 8 different repetition times (TR) of 375 ms to 5000 ms yielding saturation recovery times of 189 ms to 4814 ms. T_1 was determined by exponential fitting of the mean signal intensity versus the saturation recovery time in a region of interest (ROI) encompassing the entire sample, using only the first echo image (TE 12 ms). T_2 was determined by exponential fitting of the mean ROI signal intensity over all

echo images at maximum TR.

14.0 T: T_1 measurements were performed using an inversion recovery NMR pulse sequence modified with magnetic-field gradients in order to suppress radiation damping. Inversion-recovery curves (NMR signal intensity versus inversion recovery time) were calculated from the integrals of the PFCE ^{19}F -NMR signals. T_2 measurements were performed using a CPMG NMR pulse sequence. Decay curves (NMR signal intensity versus signal decay time) were calculated from the integrals of the PFCE ^{19}F -NMR signals. Actual T_1 and T_2 values were obtained from the inversion-recovery curves and decay curves respectively, using the Levenberg-Marquard non-linear least-squares fitting procedure of the Bruker TOPSPIN NMR software.

7.3. Results and discussion

7.3.1. Nanoparticle characterization

The size of FE-DOTA, FE-C6-DOTA, FE-DTPA, FE and FE + HPDO3A was 92.4 nm (polydispersity index (PDI) of 0.14), 97.3 nm (PDI 0.15) and 87.1 nm (PDI 0.23), 87.3 nm (PDI 0.14) and 87.0 nm (PDI 0.11) in radius respectively, as evidenced by dynamic light scattering measurements. Cryo-TEM revealed spherical nanoparticles with an electron dense core that can be attributed to the high concentration of PFCE (Fig. 2). Liposomes were observed in some cases, though the number was estimated to be less than 3% of the total amount of nanoparticles.

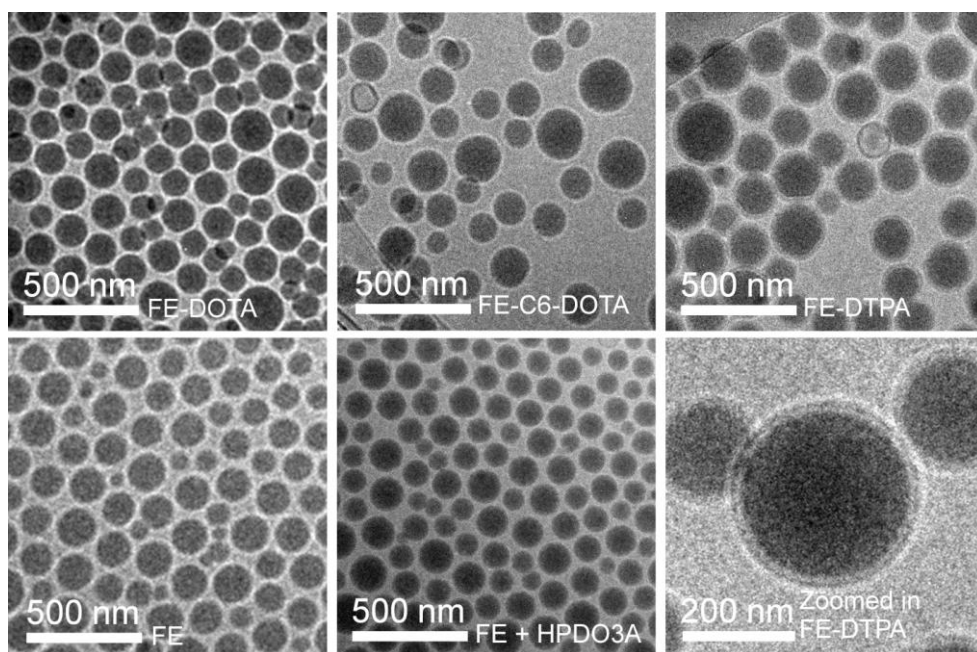


Figure 2. Cryo-TEM images of the PFCE emulsions show nanoparticles with sizes of around 180 nm in diameter. The last sample (FE-DTPA) at a higher magnification shows the paramagnetic lipid monolayer of the PFCE nanoparticle.

Phospholipid concentrations were 37 ± 4 mM for all samples and gadolinium content of the gadolinium-containing emulsions (including FE + HPDO3A) was 2.2 ± 0.1 mM as determined by ICP-AES. Zeta potential measurements revealed a surface charge close to zero (-2.0 to 0 mV) for all nanoparticle formulations.

7.3.2. ^1H Nuclear Magnetic Relaxation Dispersion (NMRD)

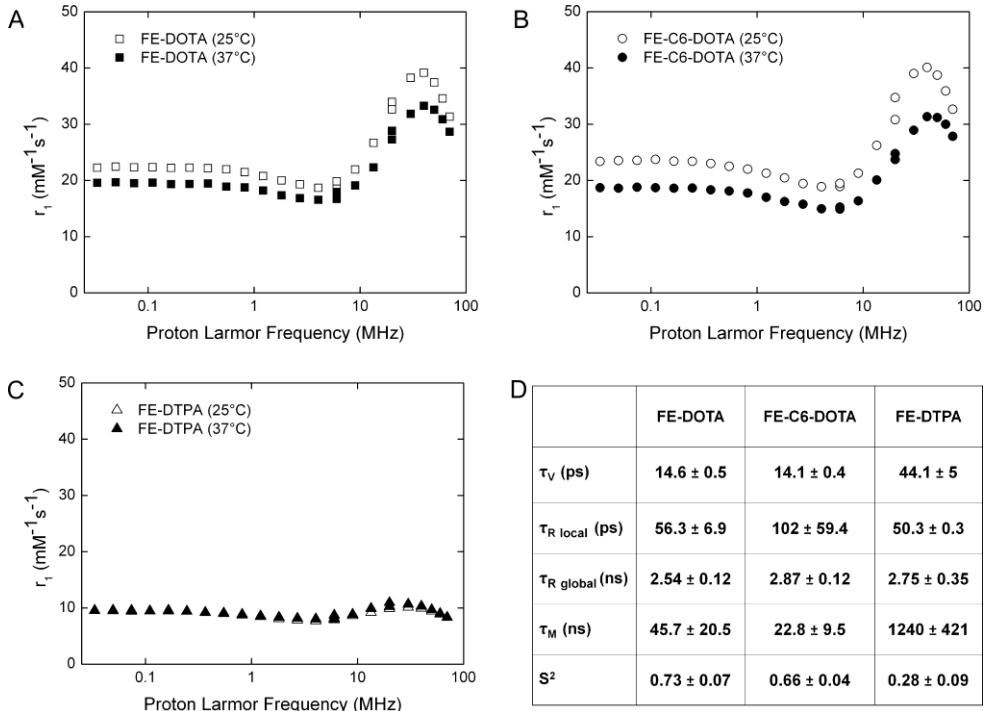


Figure 3. ^1H -NMRD profiles of A) FE-DOTA; B) FE-C6-DOTA; C) FE-DTPA measured at at 25 °C and 37 °C. D) Best fitting values of the correlation time for tensor fluctuation τ_V , the local rotational correlation time $\tau_{R \text{ local}}$, the global rotational correlation time $\tau_{R \text{ global}}$, the water residence lifetime τ_M and the local motion correlation factor S^2 , obtained from fitting the SBM-LS model at high frequencies (1-70 MHz) for optimal fitting.

^1H NMRD curves of the FE-DOTA, the FE-C6-DOTA and FE-DTPA were measured at 25 °C and 37 °C (Fig. 3). At 1.41 T, close to the typical clinical imaging field strength of 1.5 T, the longitudinal relaxivities r_1 at 25 °C were $34.6 \text{ mM}^{-1}\text{s}^{-1}$, $35.9 \text{ mM}^{-1}\text{s}^{-1}$ and $8.9 \text{ mM}^{-1}\text{s}^{-1}$ respectively. The here reported longitudinal relaxivities are the average ionic relaxivities of the Gd(III) ions on the lipid surface. The relaxivity per emulsion droplet is much higher as one emulsion typically contains 40,000 Gd(III) ions, based on a calculation of an emulsion with a diameter of 200 nm and a lipid surface area of 0.6 nm^2 . The peaks in the NMRD curves around 30 MHz are characteristic for macromolecules but is less pronounced for FE-DTPA. ^1H NMRD profiles were recorded at two different temperatures to facilitate modeling of the Solomon-Bloembergen-Morgan (SBM) equation. Data were analyzed in the high field portion only for optimal curve fitting (1-70 MHz). This approach has been demonstrated useful because of the lack of an adequate model for properly describing the low-field relaxation of the

unpaired electrons of the metal ion, especially if the paramagnetic system is subjected to a slow rotational tumbling [21-23]. The fitting quality of the fitting performed with the Lipari-Szabo (SBM-LS) model was better than the SBM model only (data not shown). The estimated parameters are presented in Fig. 3D. The main difference among the three samples is represented by the much longer residence lifetime of the metal bound water molecule for the bis-amide derivative of the FE-DTPA (1240 ns) as compared to FE-DOTA and FE-C6-DOTA which both have similar relaxometric efficacies (<100 ns). The local rotational correlation time is rather short (50-100 ps) for all the systems with the highest τ_r local for FE-C6-DOTA, whereas the global motion was very similar in the three cases (correlation times 2.5-2.9 ns). Particular relevance in the Lipari-Szabo model is played by the order parameter S^2 , which provides information about the correlation between the two motions ($S^2 = 0$ local motion uncorrelated with the global one, $S^2 = 1$ local motion fully correlated to the global one). The order parameter for the FE-C6-DOTA ($S^2=0.66$) was slightly smaller than the analogous non spaced system ($S^2=0.73$). However, the value obtained for the Gd(III)DTPA-functionalized emulsion is much smaller ($S^2=0.28$) than that of the DOTA-functionalized nanoparticles.

7.3.3. Relaxivity measurements of fluorine

In order to study the relationship of gadolinium construct and the $^{19}\text{F}R_1$ and $^{19}\text{F}R_2$ at different field strengths, five different fluorine emulsions were all measured at 1.4, 3.0, 6.3, 9.4 and 14.0 T. Three gadolinium-functionalized emulsions consisted of 1) a PFCE emulsion with 10 mol% Gd(III)DOTA-DSPE on its surface (FE-DOTA), 2) a PFCE emulsion with 10 mol% Gd(III)-DOTA-C6-DSPE (FE-C6-DOTA) and 3) a PFCE emulsion with 10 mol% Gd-DTPA-BSA (FE-DTPA). Two emulsions: FE (a PFCE emulsion without any gadolinium) and FE + HPDO3A (a PFCE emulsion with HPDO3A added in the aqueous solution) served as controls.

All emulsions were measured in a concentration series of at least 5 different nanoparticle concentrations. No significant differences in $^{19}\text{F}R_1$ were observed for different concentrations (data not shown) and these were used to compute the average $^{19}\text{F}R_1$ and its standard deviations. These $^{19}\text{F}R_1$ values of the 5 emulsions as a dependence on the magnetic field are depicted in Figure 4. Upon higher field strengths, the $^{19}\text{F}R_1$ of FE increased going from $^{19}\text{F}R_1 = 0.89 \pm 0.02 \text{ s}^{-1}$ at 1.4 T to $1.49 \pm 0.03 \text{ s}^{-1}$ at 14.0 T. The relationship between $^{19}\text{F}R_1$ and magnetic field (B) can be described in a linear fit as $^{19}\text{F}R_1=0.046*B+0.85 \text{ s}^{-1}$, $R^2=0.98$. Adding HPDO3A to the aqueous solution did not alter the longitudinal relaxation of fluorine as compared to FE and a similar linear behavior was observed with $^{19}\text{F}R_1=0.045*B+0.85 \text{ s}^{-1}$, $R^2=0.99$. Moreover, pure PFCE measured at these field strengths resulted in $^{19}\text{F}R_1$ values similar to that of FE and FE + HPDO3A (data not shown). The effect of gadolinium on $^{19}\text{F}R_1$ is pronounced at especially the lower field region. FE-DOTA as well as FE-C6-DOTA

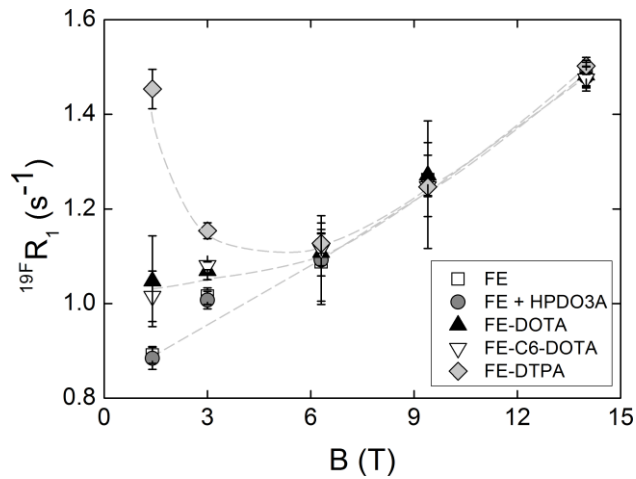


Figure 4. $^{19}\text{F}R_1$ (s^{-1}) measured for FE, FE + HPDO3A, FE-DOTA, FE-C6-DOTA and FE-DTPA at different field strengths. A general increase in $^{19}\text{F}R_1$ is observed for higher field strengths with FE-DTPA having the most prominent influence of the gadolinium construct on $^{19}\text{F}R_1$. Data represent mean \pm SD ($n=5$). The dashed lines are guides to the eye.

showed increased $^{19}\text{F}R_1$ values as compared to FE at 1.4 T ($1.05 \pm 0.10 \text{ s}^{-1}$ and $1.02 \pm 0.05 \text{ s}^{-1}$ respectively versus $0.89 \pm 0.02 \text{ s}^{-1}$) and were also statistically significantly different from that of FE at 3.0 T ($1.07 \pm 0.02 \text{ s}^{-1}$ and $1.08 \pm 0.01 \text{ s}^{-1}$ versus $1.02 \pm 0.02 \text{ s}^{-1}$) though the differences were less prominent than at 1.4 T. The increase in $^{19}\text{F}R_1$ of FE-DOTA and FE-C6-DOTA upon higher field strengths was relatively small at the lower field region but follows the same trend as FE at 6.3 T and higher where no longer any influence of Gd on the longitudinal relaxation rate of fluorine was observed.

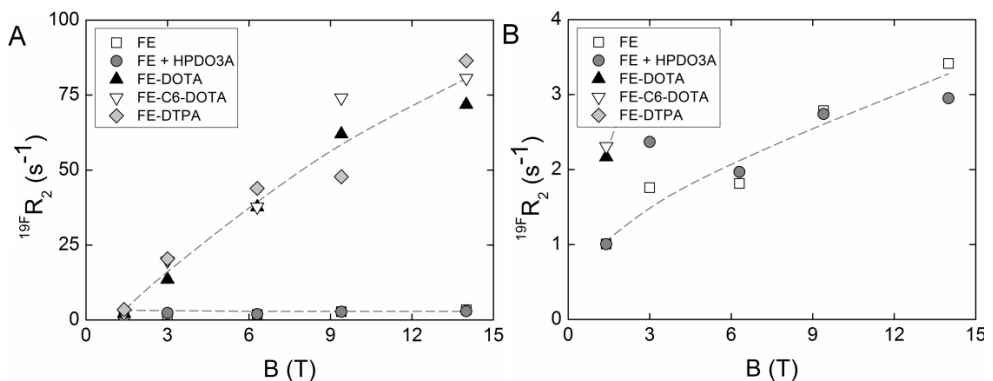


Figure 5. $^{19}\text{F}R_2$ (s^{-1}) measured for FE, FE + HPDO3A, FE-DOTA, FE-C6-DOTA and FE-DTPA at different field strengths. An increase in $^{19}\text{F}R_2$ was observed for higher magnetic fields especially for the gadolinium-functionalized emulsions but can also be observed for FE and FE + HPDO3A. The dashed lines are guides to the eye.

The strongest benefit of including gadolinium in a fluorine emulsion for ^{19}F imaging was observed for FE-DTPA. The $^{19}\text{F}R_1$ of FE-DTPA of $1.45 \pm 0.04 \text{ s}^{-1}$ is much higher than that of FE or the DOTA-functionalized nanoparticles at 1.4 T and comparable to its $^{19}\text{F}R_1$ at 14 T ($1.50 \pm 0.02 \text{ s}^{-1}$). At 3.0 T the $^{19}\text{F}R_1$ dropped to $1.15 \pm 0.04 \text{ s}^{-1}$ but remains statistically higher than that of FE or FE-DOTA. The minimum $^{19}\text{F}R_1$ value for FE-DTPA was found at a magnetic field of 6.3 T ($1.13 \pm 0.02 \text{ s}^{-1}$) and from that point increased with similar values for $^{19}\text{F}R_1$ as FE.

Transversal relaxation rates $^{19}\text{F}R_2$ were measured for gadolinium-functionalized PFCE nanoparticles and the controls. $^{19}\text{F}R_2$ values decreased with a lower concentration of emulsion. Therefore, for a good comparison, only the values measured with the highest concentration sample are shown (0.45 M PFCE). There was a field-dependent increase in $^{19}\text{F}R_2$ for the gadolinium-functionalized emulsions as can be observed in Fig. 5A. Especially for higher fields, the increased R_2 was up to a 25-fold higher than the non-functionalized emulsions. Taking a closer look at FE and FE + HPDO3A, a similar increase in $^{19}\text{F}R_2$ upon higher fields was observed, although to a much smaller extend (Fig. 5B).

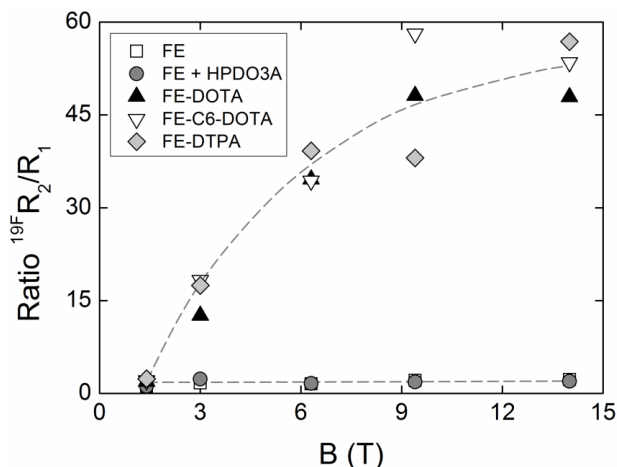


Figure 6. $^{19}\text{F}R_2/R_1$ ratios for different magnetic fields. The dashed lines are guides to the eye.

To visualize in more detail the effect of Gd on fluorine relaxation, the $^{19}\text{F}R_2/R_1$ ratio was plotted against the magnetic field (Fig. 6). For FE and FE + HPDO3A, the $^{19}\text{F}R_2/R_1$ ratio increased only slightly upon higher fields, but this effect was more pronounced for the gadolinium-functionalized emulsions. Already at 3.0 T, measured $^{19}\text{F}R_2/R_1$ ratios reached values above 5-10, indicating a severe influence of $^{19}\text{F}R_2$ effects. The $^{19}\text{F}R_2/R_1$ ratio increased up to around 58 for 14.0 T, while for FE, the $^{19}\text{F}R_2/R_1$ ratio at 14.0 T was only 2.2.

7.4. Discussion

Two macrocyclic gadolinium-functionalized lipids (Gd(III)DOTA-DSPE, Gd(III)DOTA-C6-DSPE) and one linear gadolinium-functionalized lipid (Gd(III)DTPA-BSA) were investigated for their capability to increase the fluorine relaxation rates of PFCE emulsions to generate a higher signal from the ^{19}F nuclei. Neubauer *et al.* previously demonstrated that a Gd-DTPA chelate increases the $^{19}\text{F}R_1$, despite the hydrophilic nature of the gadolinium-chelate which reduces the chances of interaction of gadolinium with the perfluorocarbon core [12]. Here, we investigated whether macrocyclic chelates are favorable for increasing the relaxivity of $^{19}\text{F}R_1$. This might become clinically relevant with respect to Gd induced toxicity and nephrogenic systemic fibrosis (NSF) as Gd-DOTA chelates are known for their higher Gd binding affinity as compared to Gd-DTPA-bisamides resulting in lower chances of inducing the development of NSF.

7.4.1. NMRD Measurements

^1H NMRD curves were determined for the gadolinium-functionalized constructs to investigate their influence on proton R_1 and the flexibility and localization on the lipid monolayer. The emulsions with Gd(III)DOTA-based lipids showed a significantly increased longitudinal relaxivity compared to the Gd(III)DTPA-BSA-based emulsion. The peaks in the NMRD profiles around 30 MHz are characteristic for macromolecular complexes as was also observed for gadolinium-functionalized liposomal MR contrast agents [18]. Using the SBM-LS model, estimations of the correlation time for tensor fluctuation τ_v , the local rotational correlation time $\tau_{r \text{ local}}$, the global rotational correlation time $\tau_{r \text{ global}}$, the water residency time τ_m and the local motion correlation factor S^2 . The local rotational correlation times $\tau_{r \text{ local}}$ of FE-DOTA and FE-DTPA were similar (56.3, and 50.3 ps, respectively), whereas the τ_r of FE-C6-DOTA of 102 ps was significantly higher, likely caused by the increased flexibility from the incorporated C6-spacer. The water residence lifetime τ_m of FE-DOTA and FE-C6-DOTA are within the same order of magnitude (45.7 ns and 22.8 ns, respectively) whereas the τ_m of FE-DTPA was 1240 ns. This might be explained by the difference in their overall structure. In the case of FE-DTPA, the polar head group consists of the Gd(III)DTPA-BSA complex. Consequently, the Gd(III)DTPA-BSA is positioned at the interface between the lipid monolayer and the bulk water. For Gd(III)DOTA-DSPE, the Gd(III)DOTA chelate is conjugated to the primary amine of DSPE, where the phosphate group is presumably positioned at the interface of the lipid layer and the bulk water. We hypothesize that the Gd(III)DOTA complex extends from the membrane slightly further into the surrounding water, resulting in better access for water molecules to the paramagnetic complex compared to Gd(III)DTPA-BSA, which results in the higher r_1 of the DOTA-functionalized complexes. Similar observations were previously observed by Winter *et*

al. and Hak *et al.* [17-18]. S^2 for the FE-C6-DOTA was slightly smaller than the analogous non-spaced system, thus indicating the higher flexibility of the former complex. Surprisingly, the S^2 obtained for the Gd(III)DTPA-BSA-functionalized emulsion is much smaller indicative for a high mobility of this compound attached to the emulsion. It is feasible that this value was underestimated in the analysis because of the low relaxivity observed for this system that is mainly caused by the occurrence of a long T_M value.

7.4.2. Relaxivity measurements of fluorine

$^{19}\text{F}R_1$ and $^{19}\text{F}R_2$ measurements were performed at five different field strengths to determine the effect of 3 different paramagnetic lipids on the fluorine signal. An increase in $^{19}\text{F}R_1$ was observed with increasing magnetic fields for FE, FE + HPDO3A and for pure PFCE, a behavior also described in literature [11,12]. Moreover, their $^{19}\text{F}R_1$ values were similar at each individual field strength indicating that the encapsulation of fluorine into a nanoparticle and in addition adding HPDO3A to the aqueous solution does not influence the fluorine relaxation rate.

FE-DOTA and FE-C6-DOTA had significantly increased $^{19}\text{F}R_1$ values at 1.4 T and 3.0 T, but followed a similar trend as FE for higher field strengths. This behavior was even more apparent for FE-DTPA, showing an increase in $^{19}\text{F}R_1$ of a factor of 1.6 using only 10 mol% of Gd(III)DTPA-BSA in the lipid monolayer. The effect is strongest for 1.4 T and is much reduced for 3.0 T to follow at higher field strengths a similar trend as for FE. A possible explanation for the stronger effect of Gd(III)DTPA-BSA as compared to the paramagnetic DOTA-lipids can be found in the position of the chelate relative to the lipid monolayer. Using the SBM-LS model, relatively long water residency times were found of Gd(III)DTPA indicating relatively poor access to free water molecules as compared to the Gd(III)DOTA constructs. As this indicates that the Gd(III)DTPA is positioned closer to the nanoparticle core, it is likely that the Gd(III)DTPA constructs is in closer proximity to fluorine as compared to the Gd(III)DOTA construct and therefore shows a more pronounced influence on the relaxation rate. The most efficient $^{19}\text{F}R_1$ increase was observed at lower field strengths, which can be caused by a better matching to the Larmor frequency of the nucleus [12,24].

Transversal relaxation rates of FE and FE + HPDO3A showed only a minor increase upon higher field strengths. For FE-DOTA an increased $^{19}\text{F}R_2$ was observed which further enhanced when going to higher magnetic fields. FE-C6-DOTA and FE-DTPA showed a similar behavior as FE-DOTA. The reason why the DOTA constructs have a more pronounced influence on $^{19}\text{F}R_2$ as compared to $^{19}\text{F}R_1$ can be due to the fact that T_2 effects generally extend over longer distances than T_1 . For the paramagnetic samples, T_2 values were very short causing a relatively large variation on the measurement data.

Nonetheless, data from Figure 5 suggest a clear lanthanide induced fluorine relaxivity that should be taken into account before imaging as it influences the $^{19}\text{F}R_2/R_1$ ratio. Figure 6 indicated that the ratio $^{19}\text{F}R_2/R_1$ for FE and FE + HPDO3A increases slightly upon higher field strengths but is only minor when we compare it with the large increase in the $^{19}\text{F}R_2/R_1$ ratio for perfluorinated nanoparticles with paramagnetic lipids included in the lipid monolayer. Figure 6 shows that for many applications it is not advantageous for the signal-to-noise-ratio of regular fluorine MRI to incorporate paramagnetic lipids, especially at high field strengths, but also already severely influences the $^{19}\text{F}R_1$ at 1.4 T. However, some applications would benefit from paramagnetic lipids on the nanoparticle surface as they enhance the ^1H relaxation rate.

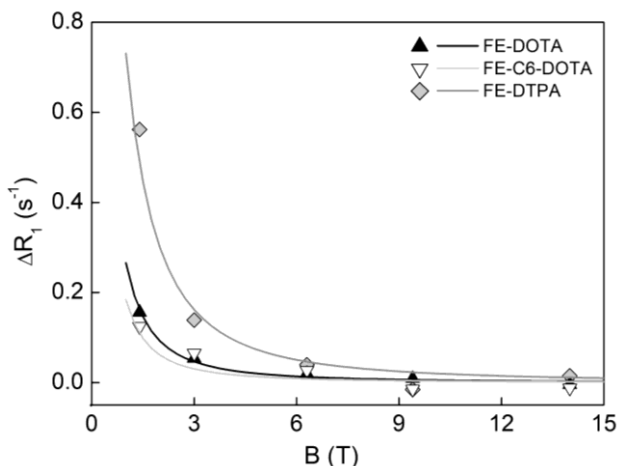


Figure 7. Relaxation enhancement $^{19}\text{F}R_1$ caused by gadolinium upon different magnetic fields, extracted from experimental data (symbols) and from the model prediction (lines) of FE-DOTA, FE-C6-DOTA and FE-DTPA.

Recently, a physical model was developed to understand the longitudinal ^{19}F relaxation enhancement by Gd^{3+} in perfluorocarbon emulsions [13]. Briefly, the model describes the influence of Gd^{3+} on the $^{19}\text{F}R_1$ by an outer-sphere relaxation mechanism, since the distance between gadolinium and fluorine is at least the distance of one hydrophobic tail (~ 1.5 nm). We have applied the model by Hu *et al.* to describe the field dependence of the increase in $^{19}\text{F}R_1$ by the incorporation of Gd^{3+} -containing chelates in our PFCE nanoparticles, as shown in Fig. 7. Model (solid lines) and data (symbols) are in good agreement using estimates of the distance of the closest approach between Gd^{3+} and ^{19}F of $d = 2.0$ nm, 2.2 nm, and 1.5 nm for FE-DOTA, FE-C6-DOTA, and FE-DTPA, respectively, while keeping all other model parameters constant. The value for FE-DTPA is higher than the one found by Hu *et al.* ($d = 0.9$ nm), which might be explained by the fact that we use 10 mol% Gd-DTPA-BSA in the lipid monolayer as compared to 30 mol% of Gd-DTPA-BOA. Our particles were also slightly larger (87 nm in radius compared to 75 nm) which could explain the overall lower increase in R_1 , as the

influence of Gd on $^{19}\text{F}R_1$ scales with 1/particle radius, related to the surface-to-volume ratio.

In this study, we showed the influence of three gadolinium-lipids on the water proton relaxivities and fluorine relaxation rates $^{19}\text{F}R_1$ and $^{19}\text{F}R_2$ of PFCE nanoparticles at 1.4, 3.0, 6.3, 9.4, and 14.0 T. Gd(III)DOTA-DSPE and Gd(III)DOTA-C6-DSPE are favorable as a contrast agent for proton NMR but the opposite holds for Gd(III)DTPA-BSA that showed the highest increase in $^{19}\text{F}R_1$, possibly due to its closer proximity to the fluorinated nanoparticle core as compared to the Gd(III)DOTA-constructs. For clinical applications this will result in a trade-off between SNR of fluorine and SNR of proton which will depend mostly on its exact application. Nonetheless, our data clearly show that for gadolinium-functionalized perfluorocarbon nanoparticles, the current clinical field strengths (1.5 - 3.0 T) are favorable for fluorine imaging as increased $^{19}\text{F}R_1$ values are observed. For higher field strengths in the range of 6.3 - 9.4 T, gadolinium is a disadvantage as it does not increase the $^{19}\text{F}R_1$ as compared to emulsions without gadolinium, but does increase significantly the $^{19}\text{F}R_2$. Instead of using gadolinium, the use of higher field strengths (14.0 T) is favorable as high $^{19}\text{F}R_1$ values can be obtained in the combination with low $^{19}\text{F}R_2$ values. Our data show that the most favorable situation for fluorine measurements are high magnetic fields without the inclusion of gadolinium constructs.

Acknowledgements

We kindly acknowledge Larry de Graaf for building the dedicated ^{19}F solenoid coil, Marcel Verheijen for performing Cryo-TEM analysis, Danielle Beelen for her help on the 14.0 T measurements and Marius van der Haven for kindly providing a ^{19}F coil for the Bruker Minispec mq60. We thank dr. L. Hu and prof. S.A. Wickline for help with the physical modeling of the field dependence of the Gd-induced relaxation enhancement. This research was performed within the framework of CTMM, the Center for Translational Molecular Medicine (www.ctmm.nl), project PARISK (grant 01C-202).

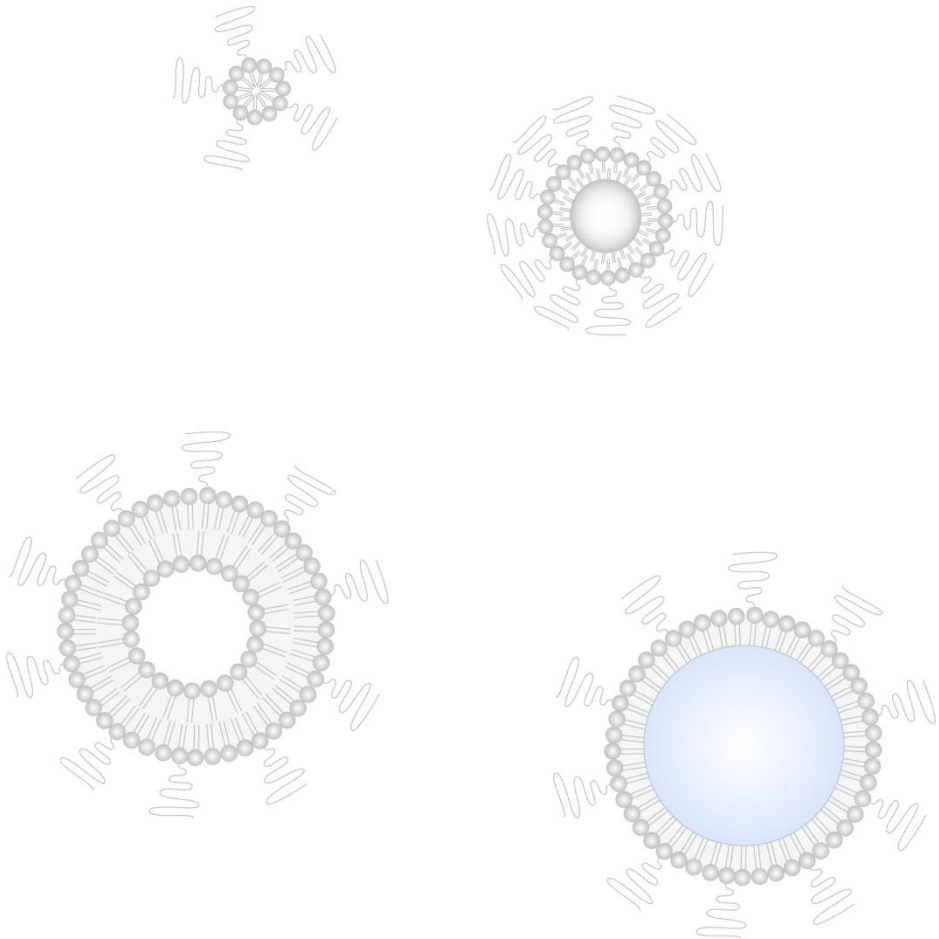
7.5. References

- [1] Morawski AM, Winter PM, Yu X, Fuhrhop RW, Scott MJ, Hockett F, *et al.* Quantitative "magnetic resonance immunohistochemistry" with ligand-targeted (19)F nanoparticles. *Magn Reson Med.* 2004;52:1255-62.
- [2] Waters EA, Chen J, Allen JS, Zhang H, Lanza GM, Wickline SA. Detection and quantification of angiogenesis in experimental valve disease with integrin-targeted nanoparticles and 19-fluorine MRI/MRS. *J Cardiovasc Magn Reson.* 2008;10:43.
- [3] Southworth R, Kaneda M, Chen J, Zhang L, Zhang H, Yang X, *et al.* Renal vascular inflammation induced by Western diet in ApoE-null mice quantified by (19)F NMR of VCAM-1 targeted nanobeacons. *Nanomedicine.* 2009;5:359-67. Epub 2009 Jan 19.
- [4] Ruiz-Cabello J, Walczak P, Kedziorek DA, Chacko VP, Schmieder AH, Wickline SA, *et al.* In vivo "hot spot" MR imaging of neural stem cells using fluorinated nanoparticles. *Magn Reson Med.* 2008;60:1506-11.
- [5] Srinivas M, Morel PA, Ernst LA, Laidlaw DH, Ahrens ET. Fluorine-19 MRI for visualization and quantification of cell migration in a diabetes model. *Magn Reson Med.* 2007;58:725-34.
- [6] Srinivas M, Turner MS, Janjic JM, Morel PA, Laidlaw DH, Ahrens ET. In vivo cytometry of antigen-specific t cells using 19F MRI. *Magn Reson Med.* 2009;62:747-53.
- [7] Janjic JM, Ahrens ET. Fluorine-containing nanoemulsions for MRI cell tracking. *Wiley Interdiscip Rev Nanomed Nanobiotechnol.* 2009;1:492-501.
- [8] Mason RP, Antich PP, Babcock EE, Gerberich JL, Nunnally RL. Perfluorocarbon imaging in vivo: a 19F MRI study in tumor-bearing mice. *Magn Reson Imaging.* 1989;7:475-85.
- [9] Kadayakkara DK, Janjic JM, Pusateri LK, Young WB, Ahrens ET. In vivo observation of intracellular oximetry in perfluorocarbon-labeled glioma cells and chemotherapeutic response in the CNS using fluorine-19 MRI. *Magn Reson Med.* 2010;64:1252-9.
- [10] Ratner AV, Quay S, Muller HH, Simpson BB, Hurd R, Young SW. 19F relaxation rate enhancement and frequency shift with Gd-DTPA. *Invest Radiol.* 1989;24:224-7.
- [11] Chalmers KH, De Luca E, Hogg NH, Kenwright AM, Kuprov I, Parker D, *et al.* Design principles and theory of paramagnetic fluorine-labelled lanthanide complexes as probes for (19)F magnetic resonance: a proof-of-concept study. *Chemistry.* 2010;16:134-48.
- [12] Neubauer AM, Myerson J, Caruthers SD, Hockett FD, Winter PM, Chen J, *et al.* Gadolinium-modulated 19F signals from perfluorocarbon nanoparticles as a new strategy for molecular imaging. *Magn Reson Med.* 2008;60:1066-72.
- [13] Hu L, Zhang L, Chen J, Lanza GM, Wickline SA. Diffusional mechanisms augment the fluorine MR relaxation in paramagnetic perfluorocarbon nanoparticles that provides a "relaxation switch" for detecting cellular endosomal activation. *J Magn Reson Imaging.* 2011;14:22656.
- [14] Kuo PH, Kanal E, Abu-Alfa AK, Cowper SE. Gadolinium-based MR contrast agents and nephrogenic systemic fibrosis. *Radiology.* 2007;242:647-9. Epub 2007 Jan 9.
- [15] Stratta P, Canavese C, Aime S. Gadolinium-enhanced magnetic resonance imaging, renal failure and nephrogenic systemic fibrosis/nephrogenic fibrosing dermopathy. *Curr Med Chem.* 2008;15:1229-35.
- [16] Aime S, Caravan P. Biodistribution of gadolinium-based contrast agents, including gadolinium deposition. *J Magn Reson Imaging.* 2009;30:1259-67.
- [17] Winter PM, Athey P, Kiefer G, Gulyas G, Frank K, Fuhrhop R, *et al.* Improved paramagnetic chelate for molecular imaging with MRI. *Journal of Magnetism and Magnetic Materials.* 2005;293:540-5.
- [18] Hak S, Sanders HM, Agrawal P, Langereis S, Grull H, Keizer HM, *et al.* A high relaxivity Gd(III)DOTA-DSPE-based liposomal contrast agent for magnetic resonance imaging. *Eur J Pharm Biopharm.* 2009;72:397-404. Epub 2008 Oct 10.
- [19] Rouser G, Fkeischer S, Yamamoto A. Two dimensional thin layer chromatographic separation of polar lipids and determination of phospholipids by phosphorus analysis of spots. *Lipids.* 1970;5:494-6.
- [20] Henoumont C, Laurent S, Vander Elst L. How to perform accurate and reliable measurements of longitudinal and transverse relaxation times of MRI contrast media in aqueous solutions. *Contrast Media Mol Imaging.* 2009;4:312-21.
- [21] Troughton JS, Greenfield MT, Greenwood JM, Dumas S, Wiethoff AJ, Wang J, *et al.* Synthesis and evaluation of a high relaxivity manganese(II)-based MRI contrast agent. *Inorg Chem.* 2004;43:6313-23.
- [22] Zhang Z, Greenfield MT, Spiller M, McMurry TJ, Lauffer RB, Caravan P. Multilocus binding increases the relaxivity of protein-bound MRI contrast agents. *Angew Chem Int Ed Engl.* 2005;44:6766-9.

- [23] Carniato F, Tei L, Dastru W, Marchese L, Botta M. Relaxivity modulation in Gd-functionalised mesoporous silicas. *Chem Commun (Camb)*. 2009:1246-8. Epub 2009 Jan 21.
- [24] Koenig SH, Brown RD, 3rd. Relaxation of solvent protons by paramagnetic ions and its dependence on magnetic field and chemical environment: implications for NMR imaging. *Magn Reson Med*. 1984;1:478-95.

Nanoparticles for quantitative imaging

Future perspectives



8.1. Nanoparticles as contrast agents

Imaging has revolutionized the medical world as it allows the physician to see diseases in the patient that, in the past, could often only be found by surgery or by autopsy. This non-invasive approach of disease recognition offers a huge clinical benefit for patients, but also less time consuming and often more specific in finding the diseased area. Currently, imaging modalities have advanced to a stage in which they are capable of finding diseases before the patient even experiences any physical discomforts or other symptoms. Much of that advances are thanks to contrast agents that have been developed for all imaging modalities to enhance the difference between healthy and diseased tissue.

The last two decades has witnessed unprecedented increase in the number of nanoparticles that are investigated for use as contrast agents. This is not without reason. Nanoparticles can be composed of different types of material, various contrast generating compounds can be incorporated and even targeting units can be attached. Also in this thesis we showed that nanoparticles can be tailored towards dedicated applications. Looking at the potential of nanoparticles, one might now wonder, why are nanoparticles not already introduced in the clinic?

8.2. Considerations before clinical use

Nanoparticulate contrast agents that are made up of endogenous material can potentially induce side effects upon intravenous injection, which needs to be carefully considered before clinical use. The first important aspect is the toxicity of the nanoparticles. Intravenously injected nanoparticles can circulate in the blood for extended periods of time as they are too big for renal excretion. The human immune system recognizes these particles, leading to clearance *via* the reticuloendothelial system with uptake in the liver and spleen. Here, these nanoparticles are metabolized or excreted *via* the gall bladder if they are biodegradable, but can also show extended tissue retention in case they are bio-inert. The time span for nanoparticle clearance from liver and spleen depends therefore strongly on the used materials, and varies from hours to weeks or even longer. Potential toxicity, carcinogenicity or other long term side effects are therefore of concern, especially when nanoparticles are used for pure diagnostic applications. The FDA is therefore cautious on accepting nanoparticles for clinical use in diagnostics. For example, emulsion based on perfluorodecalin failed in their final FDA approval because of their long organ retention and the slow clearance of the fluorinated oil. Currently, the only nanoparticles for diagnostic imaging on the

market are lipid based microbubbles for ultrasound imaging and iron oxides for MRI imaging [1]. However, the latter will be withdrawn from the market within near future.

The second consideration to be taken into account is the costs for clinical trials to get a new drug or contrast agent to approval. Clinical trials are extremely expensive and time consuming to perform. Costs comprise equipment, staff, the number of sites that are conducting the study and the number of recruited patients over a period as long as 5 to 10 years. While the higher reimbursements for drugs sets off these expenses even for applications with smaller patient numbers, the market for a novel contrast agent needs to be large enough to make it cost effective. It is therefore unlikely that many more new contrast agents will reach the clinical market as the current approved contrast agents meet to a large degree the current diagnostic needs.

Nanoparticles for therapeutic applications like Doxil® (Caelyx®) have been approved based on their increased safety profile and reduced side effects [2]. Current research aims to develop improved nanoparticulate drug formulations that locally deliver a drug at the diseased area and leave the healthy tissue unharmed. Decreasing the side effects per dosage of drugs would allow a treatment with higher dosages, thus extending the therapeutic window, which may result in higher efficacy. The need for such an agent is high, especially when it would be applicable to different diseases, e.g. different types of cancer. In drug delivery research, micelles, liposomes and polymersomes receive a lot of attention as they can be based on endogenous lipids or biodegradable polymers with little side effects, while offering a large versatility in surface modification and drug incorporation. For example, several *in vivo* applications of drug loaded polymersomes have been published. Discher *et al.* [3] and Ahmed *et al.* [4] showed shrinking of tumors upon injection of PEO-poly(lactic acid) (PLA) polymersomes loaded with the anti-cancer drugs doxorubicin and taxol, while injection of a cocktail of free doxorubicin and taxol did not result in shrinkage of the tumor. They confirmed tumor uptake of doxorubicin by *ex vivo* histology exploiting the fluorescent properties of doxorubicin. However, this approach does not provide any insight in the *in vivo* pharmacokinetics of polymersomes and dynamics of tumor uptake. Imaging-based approaches as presented in this thesis provide tools to follow and visualize the *in vivo* behavior of nanoparticles and can eventually be applied to drug delivery carriers. Imaging may therefore not only help in the rational design of new drug carriers but may provide a non-invasive mean to quantify drug release.

Recently, de Smet *et al.* published the use of thermo-sensitive liposomes for image-guided drug delivery [5]. The lipid bilayer of the liposomes consisted of lipids with a melting temperature slightly above body temperature and the aqueous core of the liposomes contained a mixture of doxorubicin and Prohance. Upon heating, the

liposomes release then not only the drug but also Prohance, which leads to an increase in R_1 . This MR signal change was found to scale with the amount of drug taken up in the tumor and can therefore be used as a direct feedback during treatment on the release and localization of the drug at the site of interest [6]. This approach is now investigated by several groups, among others the National Institute of Health (NIH). Thermo-sensitive liposomes filled with a drug and a paramagnetic MR contrast agent is perfect system for image-guided drug delivery. However, also here the potential long term risks associated with Gd payload inside the liposomes may make clinical use difficult.

8.3. Nanoparticles for research

Imaging allows gaining much more information about the interaction of nanoparticles with cells and the pharmacokinetics and dynamics *in vivo* in relation to the material properties. *Vice versa*, nanoparticles in combination with imaging can be applied as a research tool, for example to investigate the development of diseases and biological processes. We describe in chapter 2 and 3 the preparation of iodinated emulsions as a CT contrast agent and test its performance in preclinical CT studies. Subsequently, the blood kinetic is followed with imaging as a function of dose, and in co-injection experiments with other nanoparticles. These experiments revealed the impact of different surfactants on emulsions stability *in vivo*, providing useful information on how to prepare stable particles for (pre)clinical use. Furthermore, these particles are serving as a research tool as we demonstrate that the biological processes involved in the blood clearance and excretion of the nanoparticles is not so trivial and needs extended attention before understanding the exact proteins and pathways involved.

In chapter 4, these nanoparticles are used in a dual modality approach as a research tool for the development of Spectral CT in a benchmark study against SPECT. This approach allowed to gather biodistribution data from two modalities in rodents and led to a refinement of the reconstruction algorithms of spectral CT. We demonstrated that spectral CT is able to quantify iodine concentrations in different organs of mice and allows differentiating between high-Z elements such as calcium or iodine. Benchmarked against ICP-MS data, Spectral CT quantification was found comparable to SPECT based quantification.

Chapter 5 deals with setting up dual-isotope SPECT imaging as a tool to study two different tracers in the same animal. This method was investigated and established using a tumor targeted and a control peptide radiolabeled with ^{111}In and ^{177}Lu . Dual-isotope SPECT imaging of the peptides showed a similar organ and tumor uptake as

single-isotope studies but with higher statistical relevance. This demonstrated that for the same relevance, only 3 animals were required when a dual-isotope test was used instead of 7 for single isotope studies. Dual-isotope SPECT was shown to be a valuable method for paired testing of the *in vivo* target specificity of ligands in molecular imaging tracer design. Because of the picomolar sensitivity of SPECT, this modality does not require the use of nanoparticles as carriers. This however can easily be realized as is shown in chapter 6. In this chapter, a SPECT/MR liposomal contrast agent was used to obtain information for two imaging modalities. We showed that by combining this information, the presented multimodal contrast agent provides a functional readout of its response to the biological environment. In chapter 7, we showed that a small adjustment to a nanoparticle, the incorporation of a paramagnetic lipid, can have a strong influence on the contrast in ^{19}F MRI.

In all chapters, imaging is used in one way or the other for quantification of the biodistribution of nanoparticles. Quantitative imaging is the next step that can help nanoparticle research in the rational design of new constructs, as it helps to gain insights in biodistribution, the biological processes that are involved and its final fate in the body. Moreover, applications of nanoparticles for therapeutic purposes are increasing and require research insights for optimization. The combination of therapy and diagnostics (theranostics) opens new opportunities such as image-guided drug delivery using e.g. HIFU-MRI in combination with drug-filled temperature sensitive nanoparticles [7,8].

8.4. Conclusion

In this thesis the development and application of several multimodal nanoparticles for quantitative imaging are described. Nanoparticles are perfect research tools for biomedical imaging applications and their use will be extended to future nanoparticulate image-guided drug delivery systems.

8.5. References

- [1] Reimer P, Balzer T. Ferucarbotran (Resovist): a new clinically approved RES-specific contrast agent for contrast-enhanced MRI of the liver: properties, clinical development, and applications. *Eur Radiol.* 2003;13:1266-76. Epub 2002 Nov 1.
- [2] Alberts DS, Muggia FM, Carmichael J, Winer EP, Jahanzeb M, Venook AP, et al. Efficacy and safety of liposomal anthracyclines in phase I/II clinical trials. *Semin Oncol.* 2004;31:53-90.
- [3] Discher DE, Ortiz V, Srinivas G, Klein ML, Kim Y, Christian D, et al. Emerging application of polymersomes in delivery: From molecular dynamics to shrinkage of tumors. *Progress in polymer science.* 2007;32:838–57.
- [4] Ahmed F, Pakunlu RI, Brannan A, Bates F, Minko T, Discher DE. Biodegradable polymersomes loaded with both paclitaxel and doxorubicin permeate and shrink tumors, inducing apoptosis in proportion to accumulated drug. *J Control Release.* 2006;116:150-8. Epub 2006 Jul 20.
- [5] de Smet M, Langereis S, van den Bosch S, Grull H. Temperature-sensitive liposomes for doxorubicin delivery under MRI guidance. *J Control Release.* 2010;143:120-7. Epub 2009 Dec 5.
- [6] de Smet M, Heijman E, Langereis S, Hijnen NM, Grull H. Magnetic resonance imaging of high intensity focused ultrasound mediated drug delivery from temperature-sensitive liposomes: an in vivo proof-of-concept study. *J Control Release.* 2011;150:102-10. Epub 2010 Nov 6.
- [7] Kelkar SS, Reineke TM. Theranostics: Combining Imaging and Therapy. *Bioconjug Chem.* 2011;29:29.
- [8] Lammers T, Aime S, Hennink WE, Storm G, Kiessling F. Theranostic Nanomedicine. *Acc Chem Res.* 2011;5:5.

Summary

The scope of this thesis is research related to applications of nanoparticles in quantitative preclinical imaging. Nanoparticles are a versatile platform that can interact with biological systems at many different length scales and can furthermore be rendered visible for basically any medical imaging technique by modification with appropriate contrast providing moieties. Thus, nanoparticles can be used as a new class of contrast agents for basically all imaging modalities, e.g. as long circulating blood pool agents in CT, or as MRI contrast agents. *Vice versa*, non-invasive imaging techniques can be used to for example follow the biodistribution of nanoparticles *in vivo* and apply nanoparticles as a tool to investigate biological processes related to disease processes. Dual modal imaging applying multifunctional and dual-labeled nanoparticles offer new approaches to quantitative imaging, giving new insights into technology development on one side and biological read-outs on the other. For instance, quantification of biological processes that lie at the basis in the development of disease may lead to earlier detection and better disease diagnosis and treatment. Results and concepts presented in this thesis have high impact on therapeutic application of nanoparticles, for example when they are used as drug delivery systems. Imaging can provide valuable information on drug delivery and biodistribution in a quantitative manner, which may help in development of new therapeutic strategies.

Nanoparticles are promising structures for quantitative imaging. Its surface can be utilized to attach almost any desirable molecule. Nanoparticles are relatively large in size (typically 10-200 nm) and can for instance accommodate a high payload of contrast agent per particle on its surface or inside the particle, thereby increasing the signal/particle by five orders of magnitude. In addition, also multiple imaging probes for different imaging modalities can be incorporated providing a double read-out. For the understanding of biological processes, targeting ligands such as antibodies, proteins and peptides can be attached to its surface. Despite the wide variety of possibilities with nanoparticles, they have hardly been studied for quantitative imaging purposes. Therefore, the aim of the research described in this thesis was to explore and develop several nanoparticles for quantitative imaging by using existing or newly developed imaging techniques.

Chapter 1 gives a general introduction in the field of nanoparticles for quantitative imaging. Several imaging techniques are described such as CT, Spectral CT, SPECT and MRI, and how nanoparticles can play an important role in research.

Chapter 2 describes the development of a novel nanoparticulate CT contrast agent. Several amphiphilic molecules were investigated in this chapter in the combination with different iodinated oils for their influence on the size stability of the nanoparticles.

In **Chapter 3**, the dose dependent biodistribution of the nanoparticles is investigated as well as strategies to vary the biodistribution. The effect of a co-injection with liposomes and soy bean oil emulsions was investigated using CT, SPECT and γ -counting. The final optimized blood pool CT contrast agent from chapter 2 and 3 can be used for qualitative imaging in CT as well as in quantitative imaging in Spectral CT.

Chapter 4 describes the very first use of this novel imaging technique Spectral CT in quantitative imaging. For this, the nanoparticles of chapter 2 were extended to a multimodal nanoparticulate contrast agent for CT, Spectral CT and SPECT. Spectral CT quantification was compared to quantification using SPECT and ICP-MS to demonstrate the correlations and accuracy of the techniques.

In **Chapter 5**, the development is described of a dual-isotope SPECT imaging protocol as a tool for pre-clinical testing of new molecular imaging tracers. New molecular targeting probes are consistently investigated as a tool to enable target specific binding of nanoparticles to cellular surfaces of interest. Dual-isotope SPECT can be used in which the biodistribution of two different ligands labelled with two different radionuclides can be studied in the same animal, thereby excluding experimental and physiological inter-animal variations. The developed dual-isotope protocol was tested using a known angiogenesis specific ligand (cRGD peptide) in comparison to a potential non-specific control (cRAD peptide).

Chapter 6 describes the use of a multimodal radiolabeled paramagnetic liposomal contrast agent that allows simultaneous imaging with SPECT and MRI. A double read-out is then possible and demonstrates the additional advantages of the combination of the two techniques. SPECT can for instance quantify the nanoparticle concentration and MRI can spatially localize the nanoparticle. The combination however gives an indirect read-out of the water exchange, which in return reveals insights in biological processes and environments.

Chapter 7 describes a study that investigates the use of nanoparticles in the quantitative imaging technique fluorine MRI. The use of gadolinium-complexes as signal modulating ingredients into the nanoparticle formulation has emerged as a promising approach towards improvement of the fluorine signal. Paramagnetic lipids based on gadolinium complexes can be incorporated to increase the ^{19}F MR signal per particle. Here, 3 different paramagnetic lipids were investigated on its influence at five different field strengths. This furthermore also provides important insights in the dependency of the magnetic field on fluorine signal intensity.

The final **Chapter 8** describes the future perspectives of the use of multimodal nanoparticles for quantitative imaging.

List of Publications

International refereed journal publications

de Vries A, Custers E, Lub J, van den Bosch S, Nicolay K, Gröll H; Block-copolymer-stabilized iodinated emulsions as a novel CT contrast agent, **Biomaterials** 31(25) 2010, 6537-6544.

Kok MB^{*}, **de Vries A**^{*}, Abdurrachim D, Prompers JJ, Gröll H, Nicolay K, Strijkers GJ; Quantitative ¹H MRI, ¹⁹F MRI, and ¹⁹F MRS of cell-internalized perfluorocarbon paramagnetic nanoparticles, **Contrast media & molecular imaging** 398, 2010.

Gremse, F, Grouls C, Palmoski M, Lammers T, **de Vries A**, Gröll H, Das M, Mühlenbruch G, Akhtar S, Schober A, Kiessling F; Virtual Elastic Sphere Processing Enables Reproducible Quantification of Vessel Stenosis at CT and MR Angiography, **Radiology** 110069, 2011.

Hijnen NM, **de Vries A**, Burdinski D, Blange R, Gröll H; Synthesis and in vivo evaluation of ²⁰¹T(III)-DOTA complexes for applications in SPECT imaging, **Nuclear medicine and biology**, 38(4), 2011, 585-592.

Hijnen NM, **de Vries A**, Nicolay K, Gröll H; Dual-isotope ¹¹¹In/¹⁷⁷Lu SPECT imaging as a tool in molecular imaging tracer design, **Contrast media & molecular imaging** 2011, accepted.

de Vries A, Kok MB, Sanders HMHF, Nicolay K, Strijkers GJ, Gröll H; Multimodal liposomes for combined SPECT/MR imaging as a tool for in-situ relaxivity measurements, **Contrast media & molecular imaging** 2011, accepted

de Vries A, Roessl E, Schlomka JP, Proksa R, Nicolay K, Gröll H; Quantitative spectral K-edge imaging in preclinical photon-counting X-ray computed tomography, **Radiology**, submitted.

de Vries A, Custers E, Lub J, Nicolay K, Gröll H; Alternating biodistribution of blood pool CT contrast agents by a co-injection of rapid RES-uptake material, submitted.

de Vries A, Moonen RPM, Lamerichs R, Pikkemaat JA, Yildirim M, Strijkers GJ, Nicolay K, Gröll H; Relaxometric studies of gadolinium-modulated ¹⁹F nanoparticles for MR imaging, submitted.

Conference Proceedings

A. de Vries, J.P. Schlomka, E. Roessl, K. Nicolay, H. Grüll, *Iodinated emulsion for multimodality imaging using spectral CT and SPECT*, Hot Topics in Molecular Imaging 2008, Les Houches, France.

A. de Vries, J.P. Schlomka, E. Roessl, R. Proksa, K. Nicolay, H. Grüll, *Dual modality SPECT agents for quantification of CT*, World Molecular Imaging Meeting 2008, Nice, France.

A. de Vries, J.P. Schlomka, E. Roessl, R. Proksa, K. Nicolay, H. Grüll, *Multimodal imaging agents for Spectral CT and SPECT*, KNCV Weesp 2009.

A. de Vries, M.B. Kok, H. Grüll, G.J. Strijkers, K. Nicolay, *Quantitative imaging of a cell-internalized trimodal contrast agent*, World Molecular Imaging Meeting 2009, Montreal, Canada.

A. de Vries, J.P. Schlomka, E. Roessl, R. Proksa, K. Nicolay, H. Grüll, *Biodistribution of a radiolabeled CT contrast agent quantified by dual modality SPECT and Spectral CT*, World Molecular Imaging Meeting 2009, Montreal, Canada.

N.M. Hijnen, **A. de Vries**, K. Nicolay, H. Grüll, *Quantification of the net target specificity of cRGD tracer using dual isotope nanoSPECT/CT imaging*, World Molecular Imaging Meeting 2009, Montreal, Canada.

A. de Vries, J.P. Schlomka, E. Roessl, R. Proksa, K. Nicolay, H. Grüll, *Dual modality quantification of CT contrast agents by SPECT and spectral CT*, EuroNanoMedicine 2009, Bled, Slovenia.

S.J.C.G. Hectors, **A. de Vries**, G.J. Strijkers, K. Nicolay, H. Grüll, *Paramagnetic polymersomes and polymeric micelles for imaging and drug delivery*, 2nd ISMRM Benelux chapter meeting 2010, Utrecht, the Netherlands.

A. de Vries, J.P. Schlomka, E. Roessl, R. Proksa, K. Nicolay, H. Grüll, *Validation of the novel imaging technique Spectral CT using SPECT*, NVKF Woudschoten Meeting 2010.

A. de Vries, M. Yildirim, S. Langereis, R. Lamerichs, K. Nicolay, H. Grüll, *Novel nanoparticle formulations with enhanced ^{19}F relaxation*, ISMRM 18th Scientific Meeting & Exhibition, Stockholm, Sweden, 2010.

M. Yildirim, **A. de Vries**, M. Berben, C. van Cammen, K. Nicolay, H. Grüll, R. Lamerichs, *In vivo molecular imaging of angiogenesis in murine urogenital organs with targeted perfluorocarbon nanoparticles and ^{19}F ultrafast Turbo Spectroscopic Imaging (F-uTSI)*, ISMRM 18th Scientific Meeting & Exhibition, Stockholm, Sweden, 2010.

A. de Vries, K. Nicolay, H. Grüll, *Long circulating emulsion based CT contrast agents*, Fifth European Molecular Imaging Meeting 2010, Warsaw, Poland.

A. de Vries, E. Custers, J. Lub, K. Nicolay, H. Grüll, *A novel blood pool CT contrast agent*, Biomedica 2011, Eindhoven, the Netherlands.

Curriculum Vitae

Anke de Vries was born on Sunday August 22th 1982 in Eindhoven, the Netherlands. She completed the higher general secondary education (VWO) in 2000 at the Lorentz-Casimir Lyceum in Eindhoven. In the same year, she started studying Biomedical Engineering at the Eindhoven University of Technology. She obtained her Master degree in the group of Bert Meijer in 2006 where she studied the use of dendrimers as a carrier of multiple Gd(III)DTPA MRI contrast agents and proteins. In 2007 she started her PhD project at the Bio-Molecular Engineering group of Philips Research Eindhoven with Professor Holger Gröll as well as the Biomedical NMR group of Professor Klaas Nicolay at the Eindhoven University of Technology. During this period, she developed and tested contrast agents for various imaging modalities, with quantification as a general aspect. As of August 2011 she works at the Catharina Hospital in Eindhoven as a Medical Physicist trainee in the field of nuclear medicine.

Dankwoord

Een promotie bij een bedrijf lijkt voor veel mensen een lastig iets, omdat er zowel met de belangen van jezelf als wetenschapper maar ook met de belangen van het bedrijf rekening gehouden moet worden. Dit heb ik echter nooit zo gezien of ervaren. Door de samenwerking tussen de TU/e en Philips Research ben ik in een bijzonder bevoorrechte positie geweest waarin meer mogelijk was dan in menig ander promotieproject. Ik heb veel kunnen leren over het bedrijfsleven, genoten van een ontzettend luxe laboratorium, en ik had altijd de TU/e aan mijn zijde om me te helpen in de sturing van mijn promotietraject. Ik besef me heel goed hoeveel geluk ik hiermee heb gehad. Er stonden altijd zoveel mensen klaar om me op alle gebieden te helpen en ik wil graag iedereen bedanken die aan mijn mooie promotiejaren heeft bijgedragen. Een aantal mensen zou ik in het bijzonder willen bedanken.

Holger, ik weet niet hoe ik je ooit kan bedanken voor de geweldige tijd die ik heb gehad. Je lijkt wel een onuitputtelijke bron van creativiteit en energie! Je leert ons altijd zoveel, zowel over de wetenschap alsook de achtergrond van de wetenschap (hoe heeft men de structuur van DNA ontdekt?) en je brengt het met zoveel enthousiasme. Het verbaasde me dan ook niets dat je dit jaar tot beste docent van de TU/e bent uitgeroepen. Je bent een geweldig iemand om van te leren en je openheid maakt ons een hele hechte aio-groep. Het mooiste wat iemand zich kan wensen is dat hij geen spijt heeft van zijn keuzes in zijn leven. Nou Holger, ik heb nooit spijt gehad van mijn keuze promotieonderzoek bij je te gaan doen. De mooiste tijd van mijn leven en dat is grotendeels te danken aan jou. Bedankt! Ik wens je nog vele gelukkige wetenschappelijke jaren toe.

Beste Klaas, bedankt voor alles wat je voor me hebt gedaan. Niet alleen heb je het mogelijk gemaakt dat ik überhaupt aan deze promotie kon beginnen, maar bovenal heb je me altijd het gevoel gegeven dat je voor me klaar stond. Ik kon alles bespreken en heb veel gehad aan je sturing en adviezen. Daarnaast heb veel kunnen leren van je kritische blik en bovenal enthousiasme om goede wetenschap te bedrijven. Ik hoop van harte dat je nog vele jaren, en ook tijdens je pensioen, nog kan genieten van mooie wetenschap en vooral gelukkige jaren.

Beste Gustav. Toen ik aan een fluor-MRI-project begon was het duidelijk dat het niet eenvoudig zou gaan worden. Dat je meteen klaar stond om te helpen, ja daar was geen twijfel over mogelijk. Ik kon meteen bij je aankloppen en heb veel aan je hulp gehad, waarvoor veel dank. Maar daarnaast wil ik je ook bedanken voor alle momenten dat ik van je heb kunnen leren. Vooral tijdens de MIB

meetings heb ik genoten van je kritische blik en humor. Ga vooral zo door, want je bent een goede leermeester!

Ook de Biomedical NMR-groep wil ik bedanken. Ik heb veel gehad aan de gezelligheid die altijd in de groep te vinden was, en ik wil met name Hedwig erg bedanken voor haar geweldige werk altijd. Rik en Larry, ontzettend bedankt voor jullie hulp bij de fluormetingen! Ik ben benieuwd of de spoel nog in elkaar zit? Ook Maarten Kok wil ik erg bedanken voor de mooie samenwerking van ons (2 publicaties!) en de gezellige spelletjesavonden. Hopelijk komt het er snel weer eens van!

Daarnaast wil ik de leden van mijn promotiecommissie bedanken. Luc Brunsveld, Marion de Jong, Fabian Kiessling, Gert Storm en Gustav, bedankt voor de tijd die jullie hebben gestopt in het leeswerk en jullie deelname aan mijn promotiecommissie.

Mijn kantoor en lab waren voor 95% van de tijd bij Philips Research. Er zijn daar dan ook talrijke mensen die ik zou willen bedanken. Waarvan niet op de minste plaats Oliver Steinbach. Oliver, ik vond het heel bijzonder dat je me alle vrijheid gaf om gebruik te maken van het Philips-lab en om te leren van het bedrijfsleven. Het is een ontzettend leerzame tijd voor me geweest. Heel erg bedankt!

De dierenstudies beschreven in dit proefschrift hadden niet uitgevoerd kunnen worden zonder de hulp van een stel hele bijzondere vrolijke meiden. Carlijn, Caren, Melanie en Monique, wat hebben we hard gewerkt maar ook een lol gehad samen! Bedankt voor al jullie werk en uitstekende zorg voor de muizen. Ik zal jullie missen. Hetzelfde geldt voor Suzanne, Katia, Iris en Andy. Jullie waren meer op de achtergrond aan het werk, maar zonder jullie harde werk ligt al het werk op het RC-lab stil. Dat weten we heel goed en bedankt dat jullie alles draaiende houden! Ook de andere 'LSF'-mensen dragen bij aan het soepel verlopen van alle experimenten en ik wil dan ook Frenk, Dirk, Gerry, Roland, Christa en Anne hiervoor bedanken. Ook Inge de Roos wil ik erg bedanken voor haar bijdrage in de optimalisatie van de microfluidizer en emulsies.

In de Bio-Molecular Engineering groep zijn er talrijke mensen die ik wil bedanken. Roland, Sandra, Ceciel, Nicole, Erica, Rolf, Charles, Raquel, Dirk, Evelyn, Nico, David, Marcel, Zach en Tilman: Bedankt voor de leuke tijd die ik heb gehad. Marc, Raffa, Edwin, jullie stonden altijd klaar voor leuke discussies, bedankt voor alle leerzame momenten! Johan, je hebt me op allerlei vlakken hulp geboden. Zowel met zaken als pakjes versturen, maar ook met wetenschap en prachtige syntheses. Ontzettend bedankt voor alles. Ik zal jou en je humor erg missen!

Sander, je bent een bijzonder mens. Ik ken je al sinds mijn eerste jaren BMT waarin ik een OGO-project bij je heb gedaan op het gebied van dendrimeren en MRI. Daarna tijdens mijn afstuderen, maar ook in mijn promotiejaren ben je altijd in de buurt geweest om me te helpen. Je weet niet half hoe fijn het is iemand te hebben die op zo'n manier als jij mee kan denken over promotieonderzoek en waarbij je alles kwijt kan, lief en leed. Ontzettend bedankt voor alles wat je voor mij hebt gedaan en wat je voor de aio's doet. Na al die jaren scheiden helaas onze wegen, maar we nemen geen afscheid. Tot ziens.

Binnen andere afdelingen van Philips stonden ook mensen voor me klaar om te helpen bij allerlei analyses en ik wil Jeannette, Carry, Jeroen, Daniëlle en het cryo-TEaM Monja en Marcel ontzettend bedanken voor hun belangrijke bijdrages aan dit proefschrift.

Ich möchte mich auch gerne bei Ewald Roessl und Jens-Peter Schlomka bedanken für ihre Arbeit und ihrer Hilfe mit dem Spectral CT Projekt. Das war eine besondere Zeit für mich und ich habe viel von Euch gelernt. Ich danke Euch beiden sehr dafür. Alexander Fischer, Eike Gegenmatel und Timo Paulos möchte ich auch gerne danken für ihre Unterstützung mit der Imalytics Workstation.

Tijdens mijn promotieonderzoek heb ik meerdere studentes begeleid in hun afstudeeronderzoek. Niet alleen was dat altijd erg leuk om te doen, ik leerde ook veel over het onderzoek en dat sommige dingen niet altijd zo logisch zijn als dat ze na een tijd voor je lijken. Het feit dat het meeste werk van hen niet in mijn proefschrift staat doet niet onder aan de kwaliteit ervan en wat ik ervan heb geleerd. Stefanie, je was een geweldige studente om te begeleiden. Altijd recht op je doel af en erg ijverig. Ik weet zeker dat je proefschrift straks ook prachtig zal worden! Marije, wat hebben we een leuke tijd gehad samen! Alles wat je in handen kreeg vond je meteen leuk om te doen en ik weet zeker dat je enthousiasme je een geweldige carrière gaat geven. Bedankt allebei!

Je directe collega's zijn op het werk toch wel het belangrijkste. Mensen waar je ideeën kan uitwisselen, lol mee hebt en lief, leed en koekjes kan delen, maar ook die voor elkaar klaar staan wanneer je hulp nodig hebt. Duijntje, Pedro, Mariska, Nicole, Luc, Tiemen en Sin Yuin; ontzettend bedankt voor de leuke tijd. Ik zal jullie missen! De leuke lunches, de kerstmarktuitjes, de tips over belastingen, de smulpepi's (weten jullie de afkorting nog wel?), de kruimels van de rijstwafels, de schuimpjes van de Superkoop, en jullie altijd vrolijke insteek. Vooral Nicole wil ik erg bedanken. Je hebt een prachtig afstudeerproject bij me gedaan en we waren dan ook heel blij dat je je promotieonderzoek in dezelfde

groep wilde beginnen. Ik heb al die jaren veel van je geleerd en genoten van je gezelligheid, ongemakkelijkheid (wie kan er op zo'n manier een toetsenbord indrukken!?) en ik zal je zo ontzettend missen. Ik ben heel erg blij dat je mijn paranimf wilt zijn!

Mijn vriendinnen van BMT (Ellen, Karin, Karolien en Marjon) hebben me door de jaren heen vele leuke ontspannende momenten bezorgd. Skiën (hoewel dat voor mij niet echt ontspannen was!), Euro Disney, picknicken, Valencia, wandelingen en feestjes. Bedankt! We gaan gewoon zo door! Ook mijn andere vriendinnen wil ik bedanken, gewoon, omdat ik altijd op jullie kan rekenen. Julie, Karlijn en Marieke, bedankt voor al jullie begrip als ik het druk had! Sigrid wil ik in het bijzonder bedanken. We hebben zoveel lol samen en dat geeft een bijzondere band. Ik was je ceremoniemeester op de bruiloft van jou en Maarten en ik ben heel trots dat je mijn paranimf wil zijn. Dankjewel! Nu op naar een nieuwe WIDM serie! 1^e keer bij mij kijken?

Mijn familie staat altijd voor me klaar en het is heel bijzonder dat we zo'n goede band hebben met elkaar. Tante Marie-Louise (oftewel, ons muis (de jonge muis)) en Ome Kees wil ik vooral bedanken, omdat jullie er altijd voor ons zijn. Dennis en Jessica ben ik ook dankbaar, met jullie is het altijd lachen! Daarnaast wil ik mijn sissies en tevens beste vriendinnen, Debby en Marjolijn, heel erg bedanken voor al hun begrip en sissie-support van de afgelopen tijd. Remko, je bent een geweldige schoonbroer! Ook mijn schoonfamilie wil ik bedanken. Jan, Coriet, Marjol, Evert en opa en oma Rooze: jullie zijn schatten!

Papa en mama, zonder jullie had ik dit werk niet kunnen doen. Jullie mogen ontzettend trots zijn op jullie zelf. Geen mens had zich een mooiere en betere jeugd kunnen wensen dan die jullie ons gegeven hebben. De onvoorwaardelijke steun en liefde heeft ervoor gezorgd dat wij ons op alle vlakken konden ontwikkelen, wat we ook wilden. Heel erg bedankt.

Joost, ik weet niet wat ik zonder jou zou moeten. Je hebt zoveel bijgedragen aan dit boekje en staat altijd voor me klaar. Of ik nu gezellig ben of ontzettend gestressed, het is je nooit te gek. Dankjewel, voor alles. xxx

